Topology, Localization, and Quantum Information in Atomic, Molecular and Optical Systems

a dissertation presented
by
Norman Ying Yao
to
The Department of Physics

in partial fulfillment of the requirements
for the degree of
Doctor of Philosophy
in the subject of
Physics

Harvard University
Cambridge, Massachusetts
May 2014

Topology, Localization, and Quantum Information in Atomic, Molecular and Optical Systems

Abstract

The scientific interface between atomic, molecular and optical (AMO) physics, condensed matter, and quantum information science has recently led to the development of new insights and tools that bridge the gap between macroscopic quantum behavior and detailed microscopic intuition. While the dialogue between these fields has sharpened our understanding of quantum theory, it has also raised a bevy of new questions regarding the out-of-equilibrium dynamics and control of many-body systems. This thesis is motivated by experimental advances that make it possible to produce and probe isolated, strongly interacting ensembles of disordered particles, as found in systems ranging from trapped ions and Rydberg atoms to ultracold polar molecules and spin defects in the solid state. The presence of strong interactions in these systems underlies their potential for exploring correlated many-body physics and this thesis presents recent results on realizing fractionalization and localization. From a complementary perspective, the controlled manipulation of individual quanta can also enable the bottom-up construction of quantum devices. To this end, this thesis also describes blueprints for a room-temperature quantum computer, quantum credit cards and nanoscale quantum thermometry.

Contents

Listing of figures

Citations to previously published work

Most of the chapters of this thesis have appeared in print elsewhere. By chapter number, they are:

Chapter 2: "Many-body Localization with Dipoles", Norman Y. Yao, Chris R. Laumann, Sarang Gopalakrishnan, Michael Knap, Markus Mueller, Eugene A. Demler, Mikhail D. Lukin [arXiv:1311.7151] and "Interferometric probes of many-body localization" Max Serbyn, Michael Knap, S. Gopalakrishnan, Z. Papic, Norman Y. Yao, Chris R. Laumann, D. Abanin, Mikhail D. Lukin, Eugene A. Demler [arXiv:1403.0693]

Chapter 3: "Topological Flat Bands from Dipolar Spin Systems", Norman Y. Yao, Chris R. Laumann, Alexey V. Gorshkov, Steven D. Bennett, Eugene Demler, Peter Zoller, Mikhail D. Lukin [Phys. Rev. Lett. 109, 266804 (2012)] and "Realizing Fractional Chern Insulators with Dipolar Spins", Norman Y. Yao, Alexey V. Gorshkov, Chris R. Laumann, Andreas M. Lauchli, J. Ye, Mikhail D. Lukin [Phys. Rev. Lett. 110, 185302 (2013)]

Chapter 4: "Enhanced anti-ferromagnetic exchange between magnetic impurities in a superconducting host", Norman Y. Yao, Leonid I. Glazman, Eugene A. Demler, Mikhail D. Lukin, Jay D. Sau [arXiv:1309.2633] and "Phase diagram and excitations of a Shiba molecule", Norman Y. Yao, Pascu Moca, Irez Weymann, Jay D. Sau, Mikhail D. Lukin, Eugene A. Demler, Gergely Zarand [arXiv:1403.4611]

Chapter 5: "Robust quantum state transfer in random unpolarized spin chains", Norman Y. Yao, Liang Jiang, Alexey V. Gorshkov, Zhexuan Gong, Alex Zhai, Luming Duan, and Mikhail D. Lukin [Phys. Rev. Lett. 106, 040505 (2011)] and "Quantum Logic between Remote Quantum Registers", Norman Y. Yao, Zhexuan Gong, Chris R. Laumann, Steven D. Bennett, Luming Duan, Mikhail D. Lukin, Liang Jiang, and Alexey V. Gorshkov [Phys. Rev. A 87, 022306 (2013)] and "Long-range quantum gates using dipolar crystals", Hendrik Weimer, Norman Y. Yao, Chris R. Laumann, and Mikhail D. Lukin [Phys. Rev. Lett. 108, 100501 (2012)] and "Collectively enhanced interactions in solid-state spin qubits", Hendrik

Weimer, Norman Y. Yao, Mikhail D. Lukin [Phys. Rev. Lett. 110, 067601 (2013)]

Chapter 6: "Scalable Architecture for a Room Temperature Solid-State Quantum Information Processor", Norman Y. Yao, Liang Jiang, Alexey V. Gorshkov, Peter C. Maurer, Geza Giedke, J. Ignacio Cirac, and Mikhail D. Lukin [Nature Communications 3, 800 (2012)]

Chapter 7: "Topologically Protected Quantum State Transfer in a Chiral Spin Liquid", Norman Y. Yao, Chris R. Laumann, Alexey V. Gorshkov, Hendrik Weimer, Liang Jiang, J. Ignacio Cirac, Peter Zoller and Mikhail D. Lukin [Nature Communications 4, 1585 (2013)]

Chapter 8: "Unforgeable Noise-Tolerant Quantum Tokens", Fernando Pastawski, Norman Y. Yao, Liang Jiang, Mikhail D. Lukin and J. Ignacio Cirac [Proceedings of the National Academy of Sciences 109, 16079 (2012)] and "Phonon-induced spin-spin interactions in diamond nanostructures: application to spin squeezing", Steven D. Bennett, Norman Y. Yao, Johannes Otterbach, Peter Zoller, Peter Rabl, Mikhail D. Lukin [Phys. Rev. Lett. 110, 156402 (2013)] and "Timekeeping with electronic spin states in diamond", Jonathan S. Hodges, Norman Y. Yao, Dougal Maclaurin, Mikhail D. Lukin, Chaitanya Rastogi, Dirk Englund [Phys. Rev. A 87, 032118 (2013)] and "Nanoscale quantum thermometry in a living cell", Georg Kucsko, Peter Maurer, Norman Y. Yao, Minako Kubo, Hyun-Ji Noh, Peggy Lo, Hongkun Park, Mikhail D. Lukin [Nature 500, 54-58 (2013)]

To my parents Ruji Yao and Qiang Wang.

Acknowledgments

First and foremost, I'd like to acknowledge Prof. Mikhail Lukin, for being not only a tremendous advisor, but also a patient mentor, a brilliant collaborator and a compassionate friend. From Secretary Brezhnev stories to midnight curfews – imposed to ensure that I slept enough – Misha has made my years in graduate school some of the most memorable and productive of my life. I feel very blessed to have had him as my advisor.

I am also indebted to the other members of my thesis committee, Prof. Eugene Demler and Prof. Subir Sachdev. Much of my background in condensed matter comes from the three courses that I took with Eugene – my favorites at Harvard. His remarkable ability to always know the answer is superseded only by his fearless attitude toward any calculation. Our collaborations have been both fun and fruitful. Similarly, it was a final project in Subir's class that piqued my interest in exactly solvable models and led me to the work presented in Chapter 7.

The scientific atmosphere in the Lukin group and in the broader CMT/AMO universe at Harvard have been essential in shaping me as a scientist. I am especially grateful to Liang Jiang and Alexey Gorshkov who took me under their wings in my early years. I was lucky enough to share an office with Alexey as a G1 and every single day was an adventure. From spawning seemingly ingenious ideas at 5am (none of which ever worked) to listening to Russian songs, I remember that year with fondness. It has been a tremendous pleasure to work with all members of the Lukin group, including, Alexey Akimov, Darrick Chang, Kristiaan De Greve, Ruffin Evans, Sahand Hormoz, Lee Liu, Adi Pick, Jonathan Hodges, Dominik Wild, Jeronimo Maze, Tobias Tiecke, Dirk Englund, Jeff Thompson, Shimon Kolkowitz, Nick Chisholm, Sasha Zibrov, Nathalie de Leon, Ofer Firstenberg, Alex Kubanek, Alex Sushkov, Christian Latta, Mike Goldman, Peter Komar, Igor Lovchinsky, Arthur Safira, Alp Sipahigil, and Emre Togan. To this end, I would also like to thank Gilad Ben-Shach, Arijeet Pal, Johannes Otterbach, Debanjan Chowdhury, Liza Huijse, Philipp Strack, Dima Abanin, Peter Rabl, Misha Lemeshko, Dougal Maclaurin, and Markus Mueller. Finally, I would to acknowledge Peter Maurer and Georg Kucsko,

experimental wizards, for many fun and successful collaborations.

My graduate years have also benefited from numerous collaborations outside of Harvard. The keen insight and infectious enthusiasm of Prof. Peter Zoller have made my many visits to Innsbruck a highlight of graduate school. I thank him for teaching me to think creatively, to question diligently and to explore new topics boldly. I feel extremely lucky to be able to call Peter a friend and collaborator. I am also grateful to the members of his group for their hospitality, both scientific and otherwise (in particular, for organizing and watching football during the Superbowl); to this end, I would specifically like to mention Andreas Lauchli, Marcello Dalmonte, Hannes Pichler, Misha Baranov, Tomas Ramos, David Marcos, and Alexander Glatzle. I have also been amazingly fortunate to collaborate with Prof. Luming Duan. I thank Luming for sharing his sharp intuition and encouraging me during my very first project and also for his hospitality both at Michigan and half-way around the world at Tsinghua. I would also like to thank the members of his group, Zhexuan Gong, Dong-Ling Deng, Zhangqi Yin and Chong Zu, for enlightening discussions and fierce badminton rivalries. Finally, I have had the great pleasure of collaborating with Prof. Ignacio Cirac, who humor ("less Samba, more work") and insight are unmatched. Whether in Munich or Berkeley, it was rare that a discussion with Ignacio did not immediately pay dividends. From his group at the MPQ, I would like to specifically acknowledge, Fernando Pastawki, Eric Kessler, Oriol Romero-Isart, Mari-Carmen Banuls, and Geza Giedke.

The work presented here has been shaped and guided by many other friends and collaborators. Without their brilliance, humor, and intuition, this thesis would hardly exist at all. Most importantly, these relationships have developed into lasting friendships and have made the science extremely fun. I thank Prof. Leonid Glazman for teaching me the essentials of Russian phrases, for training me to never (ever) trust my gut, and for encouraging me to become a more precise scientist. I thank Prof. Jay Sau for imbuing me with the confidence to tackle complex calculations with his mantra, "If I can calculate it, I will". I thank Prof. Gergely Zarand for patiently correcting my mistakes, for teaching me a tremendous amount about Kondo physics and for hospitality during my visit to Budapest. From Gerge's group, I would also like to acknowledge Pascu Moca, Andras Palyi and Janos Asboth for many fun discussions. I thank Prof. Ana Maria Rey and Prof. Jun Ye for sharing with me their knowledge on topics ranging from polar molecules to group theory and for their never-ending hospitality during my visits to Boulder. From JILA, I would also like to thank Kaden Hazzard, Bo Yan, Steven Moses, and Rabin Paudel. I thank Joel Yuan-Zhou, Semion Saikin, and Prof. Alan Aspuru-Guzik for involving me in their projects and for patiently teaching me the chemistry of porphyrins. I thank Sarang Gopalakrishnan

and Michael Knap for being patient neighbors and always ready to listen to a crazy idea or two; I'd also like to thank Sarang's cat for providing innumerable hours of story-time and entertainment. I thank Hendrik Weimer for his patience in overcoming the "blob". I thank Prof. Florian Schreck for adventures in Innsbruck and Quebec.

Nearly eight years ago, I started my very first undergraduate research project at Harvard under the guidance of Prof. David Weitz. Since then, we have spent countless hours mulling over data, shared way to many Clover coffees, and have admired local talent all over the world. To me, Dave is the ultimate scientist. His curiosity never wanes (even at 4am) and his clarity of insight is matched only by the clarity of his writing. I have learned more about what it means to be a scientist from Dave than from anyone else. I thank him for more than words can hope to describe. I would also like to thank Prof. MacKintosh and his student Chase Broedersz for being wondrous collaborators and for their hospitality during my numerous trips to Amsterdam. In particular, I thank Chase for all the "nerdy fun" we've had from NYC to Asiadam to Princeton to Les Houches.

The challenges of graduate school have only been bearable because of the constant support I have received from my friends. I thank George Laffey for being the world's best "pro-bro" and for dominating tennis, table tennis, and frisbee outings. I thank David Laffey for countless screenplays which often made bed-time reading the best part of the day. I thank the members of Yaolympics, Jim Li, Nicolae Done, Patrick Wu, Jinbin Liu, and the Lieb for making me look forward to Labor day every year. I thank my chuvak, Brendan Shields, for teaching me about both life and billiards. I thank Michael Gullans for epic chest-bumps; I hope you still have terre battue on those tennis shoes, because after all, we both know what we're really in Paris to do. I thank Soonwon Choi for coming all the way from Caltech to oversee my exercise routine. I thank Steve Bennett for adventures in Bad Honnef and for de-gluten-freeing in the interest of Uncle Pete. I thank Quirin Unterreithmeier for all the delicious pasta nights. I thank Payal Kapadia for teaching me the meaning of friendship, for her constant advice in times of crisis and for all those slices of banana nut bread. I thank Nancy Chen, Sidd Viswanathan, Jeannie Tse and all the members of the Harvard Table Tennis club for unexpected adventures in Minnesota and Wisconsin. I thank Yiwen Chu for being my constant companion and confidant through all of graduate school. Her kindness is matched only by her supreme picture-taking skills. I thank her for all of the castles, for letting me row her around in every boat we could find and for keeping me grounded. I thank Chris Laumann for making the last three years of graduate school simply perfect. From Mario to tennis to long car rides everywhere, Chris has been the ultimate friend and collaborator. His enthusiasm for physics is matched only by his love of soup dumplings and I can only hope that he will continue to guide me in

both life and science. Above all, I thank Birgit Hausmann for inspiring me with the depth of her love and for teaching me the meaning of true magic. Du bist meine große Liebe and 我的最爱. Boy, I'm on a grand train  !

Finally, I would like to thank my parents, for their neverending love and support and for teaching me to be fearless, curious, and persistent in all that I choose to do.

Chapter 1

Introduction

1.1 Quantum many-body physics

Our modern understanding of quantum physics reduces to two flavors of questions: the one-body problem and the many-body problem. This is because, technically speaking, the two-body problem reduces to the one body case, while the three-body problem is already generally intractable [1]. The research of this thesis clusters around the relatively new field of controlled quantum many-body physics [2]. Typically, we think of many-body phenomena as both complex and difficult to probe. Indeed, isolating a particular effect or signal remains the most basic challenge in most condensed matter experiments; these signals are often swamped by noise, manifest only on sub-nanometer length scales, or occur imperceptibly fast. However, owing to recent experimental advances, it has become possible to assemble individual quantum mechanical building blocks into many-body systems. This approach has the virtue of enabling one to choose which elements of complexity to put in. Some of the most striking physics which can be accessed by such techniques involve the non-equilibrium behavior of isolated, or almost isolated, many-body systems [2].

It is fitting, then, that chapter 2 of this thesis explores one of the central assumptions in statistical mechanics. The assumption that an isolated, many-body quantum system,

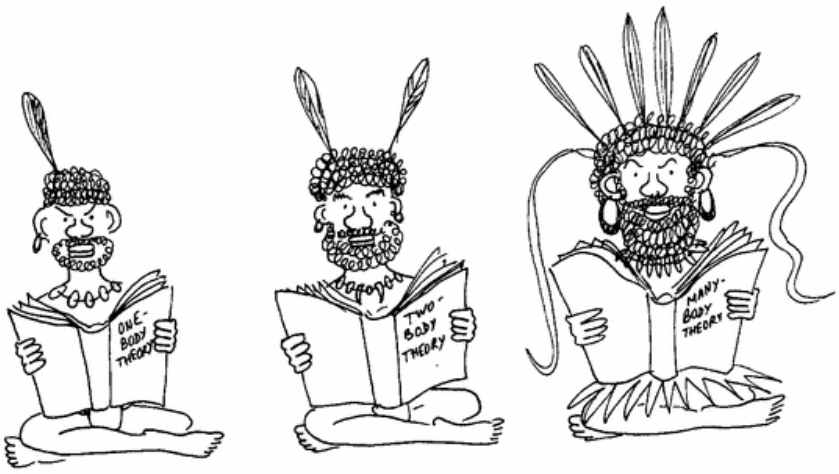

Figure 1: One, two, many-body theory [1].

establishes local equilibrium through interactions between its constituent particles . This notion underlies conventional kinetic and transport theories and governs our macroscopic intuition for heat and electrical flows. This ergodic hypothesis, however, was recently shown to fail in a class of disordered interacting systems [3–22]. Strong enough disorder can give rise to a many-body localized (MBL) phase, in which transport is absent and the system cannot act as a heat bath for its constituent parts. Although the MBL phase resembles a conventional, noninteracting Anderson insulator in that diffusion is absent, it has very different dynamical properties. Specifically, interactions between particles in the MBL phase can cause dephasing and generate long-range entanglement, leading to the slow growth of entanglement entropy [10, 11, 13–15]. Here, we will begin with a short introduction to localization, both at the single particle and many-body level.

1.1.1 Localization: from Anderson to Many-body

The story of localization begins with a seemingly simple and natural question: what is the role of disorder in the objects we see around us? We are taught to think of solids as ordered arrangements of atoms and molecules, but pick up any solid-state textbook, and one will find nuanced descriptions of countless lattice defects: interstitials, line defects, vacancies, substitutions, etc. In condensed matter physics, the importance of disorder was

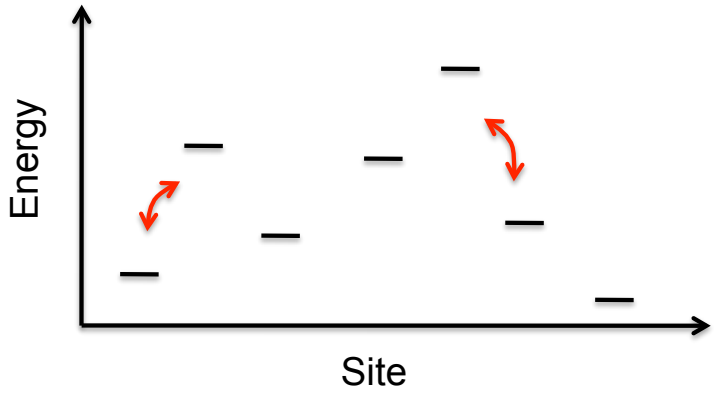

Figure 2: Schematic for Anderson localization

brought to the forefront by the seminal work of P. W. Anderson [23], who was able to show that the quantum mechanical wavefunction of a non-interacting particle is exponentially localized at all energies for sufficiently strong but finite disorder. As localized states do not carry currents over macroscopic length scales, this has dramatic consequences for the transport properties of a material.

The simplest schematic Hamiltonian for single-particle Anderson localization is,

$$H = \sum_{\langle ij \rangle} t_{ij} c_i^\dagger c_j + h.c. + \sum_i \mu_i n_i \tag{1.1}$$

where t_{ij} describes the hopping of a quantum particle in a background potential set by $\{\mu_i\}$. The intuition for Anderson localization lies in the simple schematic depicted in Fig. 2. The hopping amplitude between adjacent sites is not strong enough to hybridize two nearest-neighbor sites. To consider this more formally, let us take μ_i to be independent random variables in a box distribution of width W. For $W = 0$, there is no disorder, the eigenmodes of the Hamiltonian are simple Bloch waves and the system is metallic. Now, in the opposite limit, for $t = 0$, the eigenmodes are simply delta functions localized at each site. In the limit $W \gg t$, one can estimate the effect of t by utilizing perturbation theory, where eigenmodes take the form $|i\rangle + \sum_j \frac{t}{\mu_i - \mu_j} |j\rangle$. Anderson was able to show that this

perturbation theory converges in the thermodynamic limit, and hence, that there exists a regime where the eigenstates are localized (e.g. have wavefunctions that fall off in real space as $e^{-r/\xi}$ for some localization length ξ) and the system has vanishing DC conductivity at T = 0. Most interestingly, for sufficiently strong disorder, the entire band of eigenstates will all be localized.

The question of many body localization is what occurs when generic quartic operators are added to the original single-particle Hamiltonian. This more general question, was in fact, the goal of Anderson's original 1958 manuscript and has remained both open and controversial. The question of many-body localization received a jolt in 2005 when Basko, Aleiner and Altshuler published a calculation that purported to show localization even in the presence of interactions at finite energy density. Working in the basis of single-particle localized states they consider the effect of a generic quartic interaction,

$$H = \sum_{\alpha} c_{\alpha}^{\dagger} c_{\alpha} + \sum_{\alpha,\beta,\gamma,\delta} V_{\alpha,\beta,\gamma,\delta} c_{\alpha}^{\dagger} c_{\beta}^{\dagger} c_{\gamma} c_{\delta}. \tag{1.2}$$

Employing a self-consistent Born approximation, they calculate the explicit mixing between one-particle excitations and many-body states, ultimately finding a convergent perturbation theory. Follow-up numerical work by Huse, Oganesyan and Pal confirmed that a many-body localization transition seemed to be present in e.g. the spectral statistics of certain interacting 1D spin chains. In chapter 2, we describe a class of possible experimental realizations for MBL as well as methods for probing the localized phase. Finally, we ask the basic question: is disorder essential for MBL?

1.1.2 Fractional Chern Insulators

The development of ultra-cold atomic and molecular gases has raised the possibility of studying topological phases in out-of-equilibrium spin systems. Unlike traditional condensed matter systems, one cannot simply cool into a desired topological ground state

by decreasing the temperature of a surrounding bath. Rather, preparation must proceed coherently, e.g. by exploiting the quantum adiabatic theorem. This necessitates a detailed knowledge of the phase transitions separating topological states from their short-range-entangled neighbors. As such transitions are beyond the standard Ginzburg-Laudau paradigm, it is important to develop tools to characterize them. This requires understanding the interplay between topology, lattice symmetries and out-of-equilibrium dynamics. One particular context where lattice and topology meet is in the notion of fractional Chern insulators (FCI) – exotic phases, which arise when strongly interacting particles inhabit a flat topological bandstructure [24–31]. Particles injected into these exotic states of matter fractionalize into multiple independently propagating pieces, each of which carries a fraction of the original particle s quantum numbers. While similar effects underpin the fractional quantum Hall effect observed in continuum two dimensional electron gases [32, 33], fractional Chern insulators, by contrast, are lattice dominated. They have an extremely high density of correlated particles whose collective excitations can transform non-trivially under lattice symmetries. Chapter 3 of this thesis is devoted to describing the realization of a $\nu = 1/2$ fractional Chern insulator in ultracold polar molecules.

Since the FCI state generally competes with superfluid and crystalline orders, the resulting phase diagram exhibits both conventional and topological phases. The extent to which these neighboring phases enable the actual experimental preparation of the $\nu = 1/2$ fractional Chern insulator is an open question that is explored in the latter half of chapter 3. In particular, the adiabatic preparation of the FCI state from a superfluid requires that the boundary separating these phases is second order. Indeed, a first order transition would imply an exponentially small gap, suggesting that any adiabatic ramp would either need to be prohibitively slow or run the risk of generating a high density of quench defects. The final portion of chapter 3 postulates the idea that lattice symmetries, such as inversion, could protect a continuous transition.

1.1.3 Spins on a superconductor

Chapters 2 and 3 of this thesis focused on the quantum control of spin degrees of freedom. These controlled spins provide a remarkable platform for realizing exotic condensed matter phenomena such as many-body localization and fractional Chern insulators. However, uncontrolled spins often have a less desirable effect by contributing to magnetic noise. This is especially true in mesoscopic superconducting devices, where both the nature and origin of such noise remain a mystery. To this end, understanding the interactions between magnetic impurities on a superconductor is question of both fundamental and practical importance. Chapter 4 addresses this question in the context of Yu-Shiba-Rusinov bound states, where one finds that superconductivity induces a strong $1/r^2$ anti-ferromagnetic interaction that can dominate over conventional RKKY.

In this section, we introduce the basic theory behind Yu-Shiba-Rusinov bound states. To start we consider a single magnetic impurity on the surface of an S-wave superconductor. The impurity creates a local magnetic potential which scatters nearby conduction electrons via the usual s-d interaction,

$$H_{sd} = \frac{1}{2N} \sum_{k,k',\alpha,\beta} J(k-k') c^{\dagger}_{k,\alpha} \sigma_{\alpha\beta} c_{k',\beta} \cdot \mathrm{S} \tag{1.3}$$

where $J(k-k')$ characterizes the exchange interaction, σ is a Pauli matrix acting on the electron's spin degree of freedom and S is the impurity spin. Perturbatively, this type of s-d interaction mediates an indirect exchange between two neighboring magnetic impurities, the so-called RKKY interaction [34–36]. Intuitively, the first impurity $\mathrm{S}_{\mathbf{1}}$ scatters a conduction electron, while the second impurity $\mathrm{S}_{\mathbf{2}}$ sees the density of the scattered electron via its own s-d interaction. At second order, this generates an effective exchange interaction $J_{RKKY} S_1 \cdot S_2$ where one can imagine J_{RKKY} as being composed of two contributions. At distances $r \ll \xi$ (the superconducting coherence length), one does not see the effects of superconductivity and hence, in this limit, J_{RKKY} must reduce to the

same form as for a normal metal,

$$J_{RKKY}(r) = \frac{1}{8\pi r^3} J_{ex}^2 \rho_f \nu_0^2 \cos(2k_f r) \tag{1.4}$$

where J_{ex} is the strength of the exchange interaction, ρ_f is the density of states at the Fermi energy, ν_o is the volume per lattice site and k_f is the Fermi momentum. Meanwhile, at distances $r \gtrsim \xi$, the RKKY interaction obtains a superconducting correction and is expressed as,

$$J_{RKKY}^{SC}(r) = \frac{1}{8\pi r \xi^2} J_{ex}^2 \rho_f \nu_0^2 \cos(2k_f r) e^{-r/\xi}. \tag{1.5}$$

The fact that the superconductor is gapped enters in the exponential decay as well as the ξ^2 term of the denominator. It is worth it to point out that at $r \ll \xi$, the normal metal contribution wins by a factor of $(\xi/r)^2$ as expected. Plugging in for impurities on the surface of typical superconductors such as Niobium or Aluminum, one finds that at $r \sim 1$nm, the impurities interact with strength $J_{RKKY} \sim 100$MHz -1GHz. This indirect exchange is stronger than the bare magnetic dipolar interaction, but it decays just as rapidly within the coherence window and exponentially outside the window.

Working beyond the perturbative RKKY exchange, we now consider the appearance of bound mid-gap Shiba states in the superconductor [37–39]. Let us begin by recalling the Hamiltonian for an unperturbed BCS s-wave superconductor,

$$H_0 = \sum_{k,\alpha} \epsilon_k c_{k,\alpha}^\dagger c_{k,\alpha} + \Delta \sum_k [c_{k\uparrow}^\dagger c_{-k\downarrow}^\dagger + c_{-k\downarrow} c_{k\uparrow}]. \tag{1.6}$$

As a road map, we will be utilizing the T-matrix formalism to derive the perturbed Green's function (in the presence of classical magnetic impurities) and will ultimately obtain the energy and spatial wavefunction of the Shiba bound state [38]. Since the magnetic moment of the impurity spin is allowed to orient in any direction, we will work with 4-component spinors (Nambu-Gor'kov representation), $\Psi_k = (c_{k\uparrow}, c_{-k\downarrow}, c_{k\uparrow}^\dagger, c_{-k\downarrow}^\dagger)^T$, wherein H_0 can be

re-expressed as,

$$H_0 = \sum_k \Psi_k^\dagger(\epsilon_k\tau_3 + \Delta_k\tau_2\sigma_2)\Psi_k. \tag{1.7}$$

Both $\tau_{1,2,3}$ and $\sigma_{1,2,3}$ are Pauli matrices, but they are associated with different pieces of the Hilbert space. In particular, τ acts on the so-called particle-hole space spanned by $\{c_{k\uparrow}, c_{-k\downarrow}^\dagger\}$, while σ acts on the spin degree of freedom. By writing down the equations of motion (in the absence of impurities), one obtains the usual unperturbed single-particle BCS Green's function

$$G_0(k,\omega) = \frac{1}{i\omega - \epsilon_k\tau_3 - \Delta_k\tau_2\sigma_2}. \tag{1.8}$$

We can now solve for the new Green's function in the presence of an isolated magnetic impurity by using the usual T-matrix,
$G(k,k',\omega) = G_0(k,\omega)\delta(k-k') + G_0(k,\omega)T(k,k',\omega)G_0(k',\omega)$. For simplicity, let us assume that our magnetic potential is isotropic and spherically symmetric with $J(k-k') = J_{ex}$. In this particular case, the T-matrix reduces to a simple form

$$T(\omega) = \frac{1}{N}\frac{(SJ_{ex}/2)^2 g_0(\omega)}{1-(g_0(\omega)SJ_{ex}/2)^2} \tag{1.9}$$

where $g_0(\omega) = 1/N\sum_k G_0(k,\omega)$ is the local Green's function and S is the spin of the impurity. Summing over k yields,

$$g_0(\omega) = -\pi\rho_f\frac{\omega + \Delta\tau_2\sigma_2}{\sqrt{\Delta^2-\omega^2}}. \tag{1.10}$$

To obtain the energies of the Shiba bound states (e.g. $|E_b| < \Delta$), we need to find the poles of the T-matrix. This can be done analytically, by directly solving for the eigenvalues and determining the energies $\omega = E_b$ that correspond to poles; in particular, one finds that setting the denominator of the eigenvalues to zero,

$\Delta^2(-1+\pi^2(JS/2)^2\rho_f^2)-(\omega+\omega\pi^2(JS/2)^2\rho_f)^2=0$, yields

$$E_b=\Delta\frac{1-\pi^2(JS/2)^2\rho_f^2}{1+\pi^2(JS/2)^2\rho_f^2}. \tag{1.11}$$

One can check two very simple limits: (i) in the case where $J_{ex}\to 0$, $E_b\to\Delta$ and there does not exist an intra-gap state, (ii) in the case where $J_{ex}\to\infty$, $E_b\to-\Delta$ and the new "ground state" actually corresponds to an occupied Shiba state.

1.1.4 Quantum Primitives with Nitrogen-Vacancy Defects

The final four chapters of this thesis have a common theme in that they are motivated by recent experimental advances in the quantum control of Nitrogen-Vacancy defects in diamond. Nitrogen-Vacancy color centers stand out among other promising qubit implementations [40–43] in that their electronic spins can be individually polarized, manipulated and optically detected under room-temperature conditions. Each NV center constitutes an individual two-qubit quantum register as it also contains a localized nuclear spin. The nuclear spin, which has an extremely long coherence time, can serve as a memory qubit, storing quantum information, while the electronic spin can be used to initialize, read out, and mediate coupling between nuclear spins of adjacent registers. Magnetic dipole interactions allow for coherent coupling between NV centers spatially separated by tens of nanometers.

Single NV registers contain a spin triplet electronic ground state ($S=1$) and can be optically pumped and initialized to the $|0\rangle_e$ spin state, which has no magnetic dipole coupling with other NV registers or impurities. After optical initialization, the electronic spin of each register remains in the $|0\rangle_e$ state, unless coherently transferred to the $|1\rangle_e$ state by a resonant microwave (MW) pulse [44–47]. The nuclear spin associated with Nitrogen atoms ($I=1/2$ for ^{15}N) possesses an extremely long coherence time (^{13}C nuclear spins could also in principle be utilized); manipulation of the nuclear spin is accomplished with

RF pulses [48]. The Hamiltonian governing the electronic and nuclear spins of the NV register is

$$H_{e,n} = \Delta_0 S_z^2 + \mu_e B S_z + \mu_n B I_z + A S_z I_z, \tag{1.12}$$

with zero-field splitting $\Delta_0 = 2.87$GHz, electronic spin gyromagnetic ratio $\mu_e = -2.8$MHz/Gauss, nuclear spin gyromagnetic ratio $\mu_n = -0.43$ kHz/Gauss, and hyperfine coupling $A = 3.0$ MHz [44]. The application of a magnetic field along the NV-axis ($\hat{z}$) ensures full addressability of the two-qubit system and a universal set of two-qubit quantum operations can easily be achieved with only MW and RF controls [48].

Chapter 5 of this thesis describes a variety of mechanisms to achieve robust quantum gates between spatially separated quantum registers. This is especially important for Nitrogen-Vacancy based primitives since the bare interaction distance (e.g. tens of nanometers) is well below the optical wavelength used for initialization and read-out. Utilizing the techniques described in chapter 5, we propose a scalable architecture for a room-temperature NV quantum computer in chapter 6. The key challenge in realizing such a quantum processor is the inevitable presence of disorder in the NV diamond lattice. Such disorder typically causes localization which limits the fidelity of two-qubit quantum logic. Thus, in chapter 7, we propose to overcome disorder by implementing a topologically protected spin chain data bus that is robust to disorder. Finally, in chapter 8, we present a variety of other primitives enabled by the NV's long room temperature coherence properties such as quantum credit cards, atomic clocks, and spin squeezed metrology.

Chapter 2

Many-body localization

2.1 Realizing many-body localization with dipoles

Statistical mechanics is the framework that connects thermodynamics to the microscopic world. It hinges on the assumption of equilibration; when equilibration fails, so does much of our understanding. In isolated quantum systems, this breakdown is captured by the phenomenon known as many-body localization (MBL) [3–8, 10–23, 49–52]. Many-body localized phases conduct neither matter, charge nor heat. Moreover, they can exhibit symmetry breaking and topological order in dimensions normally forbidden by Mermin-Wagner-type arguments [16, 22]. To date, none of these phenomena has been observed in experiments, in part because of the isolation required to avoid thermalization.

In this section, we investigate dilute dipolar systems as a platform for realizing MBL phases and studying the associated localization phase transition. Our work is motivated by recent experimental advances that make it possible to produce and probe isolated, strongly interacting ensembles of disordered particles, as found in systems ranging from trapped ions [53] and Rydberg atoms [54, 55] to ultracold polar molecules [56, 57] and spin defects in solid state systems [44, 58–60]. The presence of strong interactions in these systems underlies their potential for exploring physics beyond that of single particle Anderson

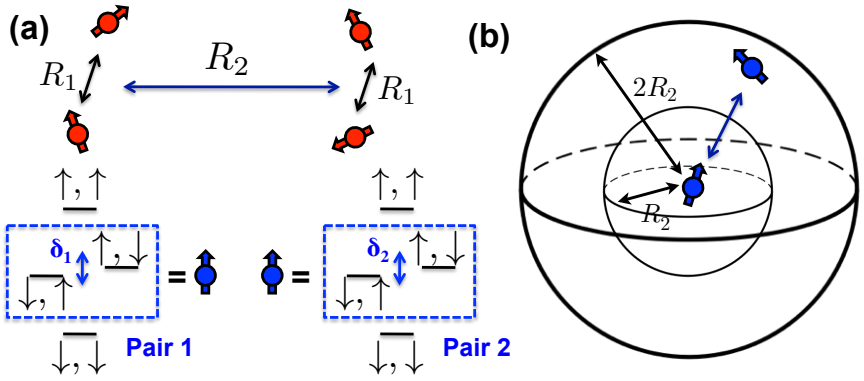

Figure 3: (a) Schematic of four spin resonance structure. Each pair of (red) spins at separation R forms a pseudospin (blue) with level structure shown below. (b) A pseudospin at the origin resonates with another pseudospin in a shell $R' < r < 2R'$.

localization [23]. However, the power law decay of those interactions immediately raises the question: can localization persist in the presence of such long-range interactions? Indeed, Anderson observed in his seminal paper that long-ranged hopping $t \sim 1/r^\alpha$ delocalizes any putatively localized single-particle states for $\alpha \leq d$, with d, the dimension of space. In what follows, we consider the generalization of Anderson's criterion to the interacting power-law regime and produce a necessary condition for localization with such interactions [51]. To support these considerations, we carry out extensive numerical analysis of power law interacting systems in $d = 1$ spatial dimension. With this criterion in hand, we analyze the feasibility of observing MBL states in two complementary ultracold polar molecule proposals, wherein the power laws, interaction scales and dimensionality may be tuned. Finally, we generalize our analysis to solid-state systems where localization can be studied in the quantum dynamics of magnetic spin impurities.

2.1.1 Conditions for localization

In localized systems, injections of energy propagate at most a finite distance even after infinite time. This is obviously inconsistent with the proliferation of long-range resonances through which energy may be transported. In the following, we identify resonant degrees of freedom and ask whether the number of such resonances diverges at large scales; such

Table 2.1.1: Critical dimensions for MBL with power laws

	Unmixed $\alpha = \beta$ [51]	Anisotropic $\beta < \alpha$	Isotropic $\beta < \alpha$
Hopping	$d < \alpha$	$d < \alpha$	$d < \alpha$
Small Pairs	$d < \beta$	$d < \beta$	$d < \beta + 2$
Extended Pairs	$d < \beta/2$	$d < \frac{\alpha\beta}{\alpha+\beta}$	$d < \frac{\alpha(\beta+2)}{\alpha+\beta+4}$
Iterated Pairs	$d < \beta/2$	$d < \beta/2$	$d < (\beta+2)/2$

divergence suggests the existence of a percolating network which conducts energy [51]. We consider a general two-body Hamiltonian of spin 1/2 particles with conserved total S^z,

$$H = \sum_i \epsilon_i S_i^z - \sum_{ij} \frac{t_{ij}}{|r_{ij}|^\alpha}(S_i^+ S_j^- + h.c.) + \sum_{ij} \frac{V_{ij}}{|r_{ij}|^\beta} S_i^z S_j^z \tag{2.1}$$

where ϵ_i is a site dependent disorder field of bandwidth W, while α and β are the exponents governing the power law decay of spin flip-flops and spin interactions, respectively; we assume $\beta \leq \alpha$ consistent with all physical realizations of which we are aware. Clearly, the analysis applies to general long-range interacting two-level systems with a conserved charge.

We identify resonant pairs of spins as those for which $|\epsilon_i - \epsilon_j| \lesssim t_{ij}/|r_{ij}|^\alpha$; the expected number of resonant spins at a distance $R_1 < |r_{ij}| < 2R_1$ from a central spin is

$$N_1(R_1) \sim (\rho R_1^d) \cdot \frac{t/R_1^\alpha}{W} \tag{2.2}$$

where ρ is the density of spins. If $N_1(R_1)$ diverges as $R_1 \to \infty$, that is, if $d > \alpha$, then any spin resonates with arbitrarily distant spins and localization is impossible; this is precisely Anderson's criterion for single-particle localization. In the critical case, $d = \alpha$, a detailed renormalization group treatment confirms subdiffusive but delocalized behavior for the non-interacting case [23, 61, 62].

As shown in Fig. 3a, the two strongly-hybridized central levels of a resonant pair define a new pseudo-spin degree of freedom (blue arrows) with local splittings $\delta \sim t/R_1^\alpha$.

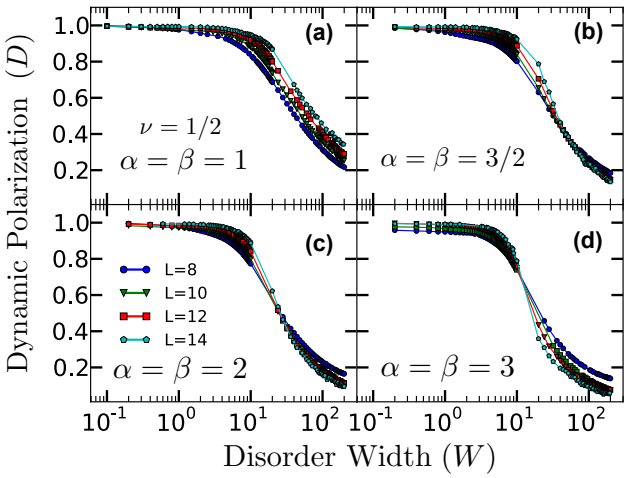

Figure 4: Finite size scaling of the long-time dynamic polarization for Eq. (A.13) in $d = 1$ (with units $t = 1, V = 2$) with a) $\alpha = \beta = 1$, b) $\alpha = \beta = 3/2$, c) $\alpha = \beta = 2$, and d) $\alpha = \beta = 3$. The lack of flow reversal in (a) suggests delocalization at all disorders. The sharpening of the crossover as a function of increasing system size in (d) suggests the existence of a phase transition at approximately $W_c \approx 10$ into an MBL phase. The flow at intermediate power-laws (b) is inconclusive.

Pseudospins can exchange energy through the interaction V since the operators S^z have spin-flip matrix elements between the two pseudospin states [51]. Two pseudo-spins separated by R_2 resonate if $\delta_1, \delta_2 > V(R_2) \gtrsim |\delta_1 - \delta_2|$. The number of such resonances available in a shell from distance R_2 to $2R_2$ around a fixed pseudospin (Fig. 3b) is

$$N_2(R_1, R_2) \sim (n_1(R_1) R_2^d) \cdot \frac{V/R_2^\beta}{t/R_1^\alpha}, \tag{2.3}$$

where $n_1 = \rho N_1$ is the density of pseudo-spins. As before, if N_2 diverges as $R_2 \to \infty$, large scale pseudo-spin resonances induce delocalization [51]. There are two limits. The simplest case occurs when one holds the pair size R_1 fixed as R_2 diverges; this "small pairs" condition yields a localization criterion $d < \beta$. The second case requires optimizing R_1 as R_2 grows in order to saturate the probability of pseudo-spin resonance. More precisely, one should replace $\frac{V/R_2^\beta}{t/R_1^\alpha} \to \min[1, \frac{V/R_2^\beta}{t/R_1^\alpha}]$ in Eq. (A.15). The optimum arises for $R_1 \sim R_2^{\beta/\alpha}$, yielding a more stringent "extended pairs" condition, $d < \frac{\alpha\beta}{\alpha+\beta}$.

It is clear that one can continue iterating the construction of pair resonances. However,

the resulting criteria for MBL saturate after the third level [63],

$$N_3(R_1, R_2, R_3) \sim (n_2(R_1, R_2)R_3^d) \cdot \frac{V/R_3^\beta}{V/R_2^\beta} \tag{2.4}$$

where $n_2 = n_1 N_2$ is the density of pseudo-pseudo-spins. There are three limits as R_3 diverges. Holding R_1, R_2 fixed reproduces the small pairs criterion. Holding R_1 fixed but optimizing $R_2 \sim R_3$ (to saturate the probability of resonance in Eq. (A.8)) yields a new, "iterated pairs" criterion $d < \beta/2$. Finally, optimizing both $R_1 \sim R_2^{\beta/\alpha}$ and $R_2 \sim R_3$ reproduces the extended pairs criterion.

The above results hold for generic anisotropic distributions of t_{ij}, V_{ij} (first two columns of Table 2.1.1). In cases where the hoppings and interactions are isotropic, the effective matrix elements that arise in the four-spin construction cancel at leading order. This can be interpreted within a multipole expansion (for $R_1 < R_2$) which amounts to replacing $V/R_2^\beta \to VR_1^2/R_2^{\beta+2}$ for N_2 and analogously for subsequent iterations (last column of Table 2.1.1).

A few comments are in order. (1) In the anisotropic and unmixed ($\alpha = \beta$) cases, the iterated pairs criterion $d < \beta/2$ is always most stringent, a result first derived in [51]. (2) In the isotropic case, for $\alpha < \beta + 4$, the extended pairs criterion is most stringent, while for $\alpha > \beta + 4$ the iterated pairs criterion dominates. (3) The case of an Anderson insulator with Coulomb interactions corresponds to the $\alpha \to \infty$ limit of the isotropic case, giving an upper critical dimension of $d_c = 1.5$. (4) The case of interacting dipoles with $\alpha = \beta = 3$ also gives $d_c = 1.5$. Interestingly, the orientation dependence of the dipolar interaction is sufficiently isotopic to enable a multipole expansion. Thus, in experiments that can realize $\alpha = 6$, $\beta = 3$ (as will be later discussed), $d_c \approx 2.3$.

Ultimately, all of the resonance arguments described above rely upon the analysis of finite subsets of spins. While providing useful insights, such arguments must be viewed as heuristic. To supplement, we have performed extensive exact diagonalization studies of

Eq. (A.13) in $d = 1$ for $\alpha = \beta = 1, 3/2, 2, 3$. We consider periodic systems up to size $L = 14$ at filling fraction $\nu = 1/2$. The random fields are drawn from a uniform distribution of width W, the interaction $V_{ij} = V = 2$ and hopping $t_{ij} = t = 1$. The presence of a many-body localized phase may be detected by the finite size flow of the dynamic polarization D, a measure of spin transport across the 1D system at infinite temperature [8]. We perturb each eigenstate with a small (long-wavelength) inhomogeneous spin modulation of the form $\hat{F} = \sum_j S^z_j e^{i2\pi j/L}$ and measure the relaxation of this inhomogeneous polarization at infinite time. For each disorder realization η and eigenstate k, the dynamic polarization is given by

$$D^k_\eta = 1 - \frac{\langle k|\hat{F}^\dagger|k\rangle\langle k|\hat{F}|k\rangle}{\langle k|\hat{F}^\dagger\hat{F}|k\rangle}. \tag{2.5}$$

We then define D as the infinite temperature disorder average of D^k_η. As $L \to \infty$, in the ergodic phase, one expects $D \to 1$ since the initial inhomogeneity relaxes away; in the MBL phase, one expects $D \to 0$ since there is no transport.

The results are shown in Fig. 4. For all exponents, we find that the finite-size flow of D is consistent with delocalization at weak disorder. At strong disorder, for $\alpha = 2, 3$ there are signs of flow reversal, consistent with a transition into an MBL phase, while for $\alpha = 1$ the flow remains toward delocalization for all disorder strengths. Owing to the small sizes accessible to exact diagonalization, flow reversal does not prove the existence of a transition; however, for $\alpha = 3$ the combination of relatively clear flow and the previous theoretical argument suggests the existence of an MBL phase. The strong disorder flow at intermediate exponents $\alpha = 3/2$ is inconclusive. Accordingly, for $d = 1$, we numerically bound the critical power-law with $1 < \alpha_c < 3$, noting that the extended pairs criterion gives $\alpha_c = 2$. The difficulty of investigating an MBL transition in small size numerics emphasizes the importance of controlled experiments.

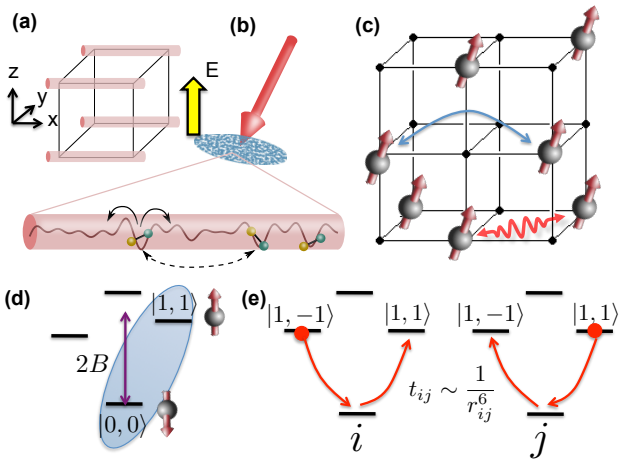

Figure 5: a) Schematic of the one-dimensional tube geometry with strong confinement in the $\hat{y}$ and $\hat{z}$ directions and hopping in the $\hat{x}$ direction. b) Dipolar molecules in each 1D tube are subject to an optical speckle pattern which generates an effective random on-site chemical potential for the hopping molecules. c) Schematic of the dipolar 'spin' hopping model. Molecules pinned with dilution in deep optical lattice may exchange rotational excitations. d) Effective rotational level structure of a polar molecule, with $|\uparrow\rangle = |1,1\rangle, |\downarrow\rangle = |0,0\rangle$ shown for the $\alpha = \beta = 3$ rotor model. e) Level structure of two polar molecules for the $\alpha = 6$ rotor model, wherein hopping is mediated by a second order dipolar process.

2.1.2 Experimental realizations

We next analyze two classes of experimentally accessible systems in which MBL phases may be realized. First, we consider an array of polar molecules confined to a one-dimensional tube geometry (via an optical lattice) as depicted in Fig. 5a,b [56]. The optical lattice is strongly confining along the $\hat{y}$ and $\hat{z}$ axes, but molecules can tunnel with nearest-neighbor hopping strength t along the tube in the $\hat{x}$ direction ($\alpha \to \infty$). The molecules are prepared in their rovibrational ground state and subject to a static electric field E perpendicular to the tube direction. The applied electric field weakly aligns the molecules along the field direction, inducing a finite dipole moment d and a long-range electric dipole-dipole interaction between the molecules $V \sim d^2/R^3$ ($\beta = 3$). By ensuring that the dipolar interaction strength is much weaker than the rotational splitting B (Fig. 5d), all molecules remain in the rovibrational ground state. Finally, an optical speckle field may be superimposed on top of the underlying lattice introducing on-site potential disorder with strength W controlled by the laser intensity (Fig. 5b) [64].

The magnitude of the electric field tunes the strength of the dipolar interaction $V \sim d^2$. In the limit $E \to 0$, the interaction strength $V \to 0$, and the resulting nearest-neighbor Hamiltonian can be fermionized. This non-interacting model is completely Anderson localized in the presence of any disorder. With the addition of local interactions, the existence of an MBL phase has been established both theoretically and numerically [3–6, 8]. According to the criterion in Table I, the MBL phase ought to also survive the introduction of long-range dipolar interactions. To confirm this expectation and further establish an experimentally relevant phase diagram, we perform exact diagonalization for molecular filling fractions $\nu = 1/2, 1/3, 1/4$ up to system sizes of $L = 16, 18, 20$ respectively (Fig. 6a). As depicted in Fig. 6b, we obtain the MBL phase diagram as a function of interaction strength, filling fraction, and speckle intensity [64].

We next consider disordered arrays of interacting molecules with fixed center of mass position and focus on the dynamics of rotational excitations (Fig. 5c). In the deep lattice limit, the orbital motion of the molecules is pinned and the residual rotational degree of freedom is governed by an effective Hamiltonian, $H_m = BJ^2 - d^z E$ [65]. A combination of electric and magnetic fields allows us to isolate an effective two-level system: $|\downarrow\rangle = |J = 0, m_j = 0\rangle$ and $|\uparrow\rangle = |J = 1, m_j = 1\rangle$ (Fig. 5d) [66]. The rotors interact via electric dipole-dipole interactions with Hamiltonian, $H_{dd} = \frac{1}{2}\sum_{i\neq j} \frac{\mathbf{d_i}(1-3\hat{r}_{ij}\hat{r}_{ij})\mathbf{d_j}}{r_{ij}^3}$, where $\mathbf{d}$ is the dipole moment operator. Projecting H_{dd} onto the two level subspace $\{|\downarrow\rangle, |\uparrow\rangle\}$ and keeping only secular terms yields the Hamiltonian of Eq. (A.13) with effective on-site fields given by $\epsilon_i = \sum_{j\neq i} \frac{d_s d_a}{r_{ij}^3}$, $\alpha = \beta = 3$, and $d_{s,a} = \frac{\langle 1|d^z|1\rangle \pm \langle 0|d^z|0\rangle}{2}$. Assuming Poissonian (uncorrelated) dilution, the fields ϵ_i become random variables with standard deviation $W \sim \frac{d_s d_a}{a_0^3}\sqrt{\nu(1-\nu)}$, where a_0 is the lattice spacing. We expect the weak correlations of the random fields to leave the previous numerical phase diagrams in $d = 1$ qualitatively unchanged (Fig. 4d).

This dipolar spin model becomes particularly intriguing as one varies the dimensionality of the system since the "extended pairs" criterion predicts $d_c = 3/2$ for $\alpha = \beta = 3$.

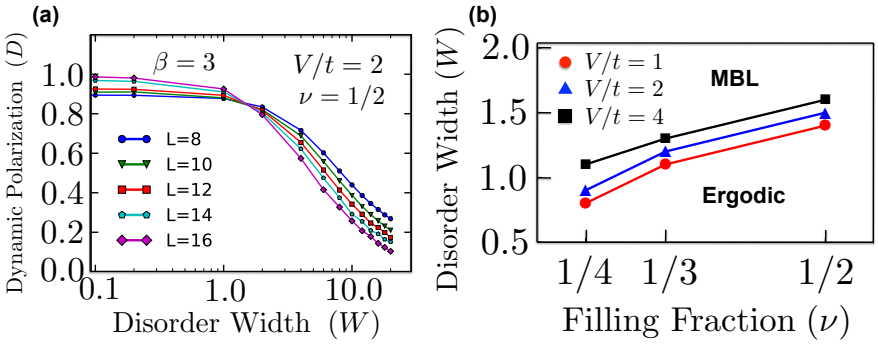

Figure 6: Exact diagonalization study of Eqn. (1) with nearest neighbor hopping ($\alpha \to \infty$) and dipolar interactions ($\beta = 3$). Random fields are drawn from a uniform distribution of width W. a) Finite size scaling of the long-time dynamic polarization. The finite size flow suggests a delocalization phase transition at approximately $W_c \approx 1.4t$. b) MBL phase boundaries determined by finite-size flow for $V/t = 1, 2, 4$. Error bars as determined by the width of the intersection region are smaller than markers.

Compared to the simple Anderson criterion, which predicts $d_c = 3$, this already allows one to investigate the validity of the resonant pair counting arguments for optical lattice pancakes where $d = 2$.

An additional feature of such systems is the ability to tune the spin-flip power-law. The large rotational constant B enables restriction to the Hilbert space spanned by $|\downarrow\rangle = |J = 1, m_j = -1\rangle$ and $|\uparrow\rangle = |J = 1, m_j = 1\rangle$. In this case, the dipolar flip-flop process is effectively eliminated at first order; the system instead hops two units of J^z via a second order process of the form (Fig. 5e), $H' = \sum \frac{t_{ij}^2}{r_{ij}^6} \left[(d_+^i)^2(d_-^j)^2 + (d_-^i)^2(d_+^j)^2\right]$, while the interaction remains formally unchanged. With the effective hopping power-law increased to $\alpha = 6$ and the interaction remaining as $\beta = 3$, one finds that (in $d = 2$) all criteria for the consistency of localization are now satisfied, including both the extended pairs criterion which predicts $d_c \approx 2.3$ and the iterated pairs criterion with $d_c = 2.5$.

Finally, solid-state implementations can be considered using spin defects in semiconductors. For example, Nitrogen-Vacancy (NV) defects in diamond [44, 58–60] are spin-1 magnetic impurities described by the Hamiltonian, $H_{NV} = D_0 S_z^2 + \mu_e B S_z$, where D_0 is a large crystal field splitting. In the presence of an applied magnetic field, one can restrict the NV dynamics to a two-level subspace and recover the Hamiltonian of Eq. (A.13).

2.1.3 Feasibility and detection

There are several probes available for detecting many-body localization in quantum optical systems: 1) observing arrested decay of a long-wavelength spin/number modulation, 2) generalized single-site spin-echo protocols that exhibit anomalously slow dephasing [10, 13–15, 20], and 3) direct measurements of real-space correlation functions. The simplest approach is to directly observe a lack of diffusion. In a typical ergodic system, an initial long-wavelength inhomogeneous number/spin polarization decays as $\sim e^{-Dk^2t}$, where D is the diffusion constant. For a many-body localized phase, $D = 0$. In any experiment, coupling to an external bath is unavoidable and produces characteristic decoherence timescales; T_1-type depolarization provides a uniform k-independent contribution to the overall decay. In the presence of weak Markovian T_2 dephasing, extrinsic energy fluctuations induce diffusion, with $D_{T_2} \sim a_0^2/T_2$ (neglecting back-action onto the bath). Since $T_2 \leq T_1$, the figure of merit in such experiments is a separation of scale between D_{T_2} and the expected ergodic diffusion, $D_e \sim a_0^2/T_{a_0}$, where T_{a_0} represents the lattice scale hopping time. Alternatively, one can also measure the decay of an initially polarized region; for a Gaussian spot of initial size ℓ (larger than any correlation length), the modulation at the origin decays as $\sim (\ell^2 + Dt)^{-d/2} e^{-t/T_1}$. Here, one hopes to extract the sub-exponential diffusive behavior, which can in principle be achieved by varying the spot size.

In the molecular case, the most direct experimental realization of our proposals would be in diatomic alkali systems [57, 67–71]. Both the orbital and rotational cases can be carried out with currently available technology; indeed the loading of ^{40}K^{87}Rb molecules into 1D [56] and 3D [67] lattices, as well as dipolar spin-exchange [66], have already been demonstrated. For a typical polar molecule with saturated dipole moment ~ 3 Debye, the interaction strength at 532nm (optical lattice spacing) corresponds to approximately 100kHz, yielding $T_{a_0} \approx 10\mu$s. Meanwhile, dephasing times of up to $T_2 \sim 100$ms [66] and ground-state lifetimes of up to $T_1 \sim 25$s have been observed [67].

In the case of NVs, recent advances in implantation and annealing have enabled dense

defect ensembles with average spacing $\sim 2-3$nm. The magnetic dipolar interaction at such distances is given by $T_{a_0} \sim 1\mu$s, significantly smaller than the typical room-temperature coherence times $T_1, T_2 \sim 10$ms of isolated NVs (working at cryogenic temperatures can lead to further improvements [72]). To observe many-body localization in such a system will require the ability to reduce the effective dimensionality; this can be achieved by fabricating quasi-1D diamond nano-pillars [73] or by controlled implantation in 2D layers [74, 75].

In summary, by constructing hierarchical spin resonances we have analyzed upper critical dimensions for many-body localization in the presence of power-laws (Table I). Our arguments suggest that MBL is accessible to AMO-type experiments involving dipolar spins in two dimensions or hopping polar molecules in three or fewer dimensions. Our work opens a number of intriguing directions: (1) generalizations to other dipolar platforms such as Rydberg atoms, trapped ions and other spin qubits, (2) working near the upper critical dimensions to probe the nature of the MBL transition.

2.2 Detecting many-body localization via double electron-electron resonance

In the previous section, we described possible experimental realizations of many-body localization. This begs the question: how does one probe a many-body localized AMO system?

In this paper, we propose and analyze a new method for studying MBL, based on coherent manipulation of individual degrees of freedom. We focus on disordered spin systems, and show that spin-echo type measurements performed on individual spins can be used as sensitive probes of localization [Fig. 7(a)-(c)]. Such measurements are standard in liquid and solid-state spin systems (see [76] and references therein), as well as in systems of cold atoms [21, 77–80]. Specifically, in order to probe MBL, we introduce a modified, non-local spin-echo protocol [Fig. 7(c)], akin to the double electron-electron resonance (DEER) technique in electron spin resonance [81–83], that allows one to probe the

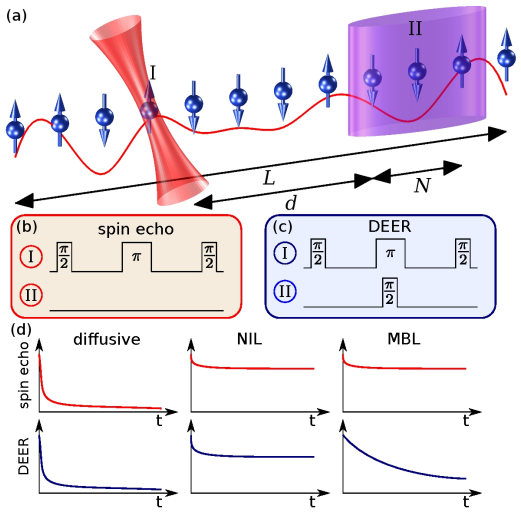

Figure 7: (Color online) Schematic illustration of the proposed protocols. (a) Spins are manipulated with lasers in two spatially separated regions I and II. (b) The protocol consists of a Hahn spin-echo sequence in region I while leaving region II untouched. (c) The DEER protocol differs by $\pi/2$ rotations in region II which are performed after half of the evolution time. (d) Schematic response of a system in the diffusive (left), non-interacting localized (center), and many-body localized (right) phases, to spin-echo and DEER protocols respectively. The combined information from both sequences allows one to distinguish the different phases.

dynamical correlations between remote regions of a many-body system. This approach can reveal interaction effects and probe quantum entanglement within the MBL phase. In particular, the slow growth of entanglement entropy associated with the MBL phase manifests itself in a power-law decay of the DEER response. Furthermore, by measuring both the spin-echo and DEER response one can distinguish the MBL phase from a non-interacting localized (NIL) phase as well as a diffusive phase [Fig. 7(d)]. We discuss specific realizations of our proposal in several cold atom and solid state systems.

2.2.1 Conceptual approach

The key idea of this work can be illustrated using a phenomenological model of the MBL phase [14, 15] that characterizes it by an infinite number of local integrals of motion, which can be chosen as effective spin-1/2 operators τ_i^z with eigenvalues ± 1. In terms of these

variables, the MBL Hamiltonian is [14, 15]

$$\hat{H} = \sum_i \tilde{h}_i \tau_i^z + \sum_{ij} \mathcal{J}_{ij} \tau_i^z \tau_j^z + \sum_{ijk} \mathcal{J}_{ijk} \tau_i^z \tau_j^z \tau_k^z + \ldots . \tag{2.6}$$

The couplings $\mathcal{J}_{ij}, \mathcal{J}_{ijk}, \ldots$ fall off exponentially with separation with a characteristic localization length ξ (expressed in units of the lattice constant). The Hamiltonian (2.6) conserves the expectation value of each τ_i^z; however, interactions between effective spins randomize relative phases of different components of the wave function. Such dephasing generates entanglement between distant parts of the system [14, 15].

We first discuss interferometric signatures of Hamiltonian (2.6) assuming that one can directly manipulate the effective spins τ_i^z (in what follows we shall refer to effective spins simply as "spins"), and later generalize these arguments to realistic cases involving manipulation of physical rather than effective spins.

Let us first consider a simple spin-echo sequence applied to an individual spin I [Fig. 7(b)]. Starting from an arbitrary eigenstate of $\hat{H}$ (i.e., a product state of the form $|\uparrow\downarrow\downarrow\uparrow\downarrow \ldots\rangle$), we initialize spin I in a superposition state $|+\rangle_{\rm I} = (|\uparrow\rangle_{\rm I} + |\downarrow\rangle_{\rm I})/\sqrt{2}$. Spin I precesses in the magnetic field $h_{\rm eff}({\rm I}) = \tilde{h}_{\rm I} + \sum_j \mathcal{J}_{{\rm I}j} \tau_j^z + \sum_{j,k} \mathcal{J}_{{\rm I}jk} \tau_j^z \tau_k^z + \ldots$, which depends on the state of the surrounding spins. The thermal average over initial states gives rise to dephasing and decay of the free precession signal. The standard spin-echo sequence, however, allows one to recover the quantum coherence of spin I, by applying a time-reversal π-pulse to it at time $t/2$. For the MBL Hamiltonian (2.6), the precession induced by $h_{\rm eff}({\rm I})$ over the initial evolution for $t/2$ is cancelled by the precession accumulated during evolution for time $t/2$ after the π-pulse, independent of the value of $h_{\rm eff}({\rm I})$. However, since spin echo is insensitive to dephasing in the MBL phase, it does not distinguish between NIL and MBL phases.

We next introduce a modified spin-echo protocol, which directly probes interaction effects in the MBL phase. The idea, inspired by the "double electron-electron resonance"

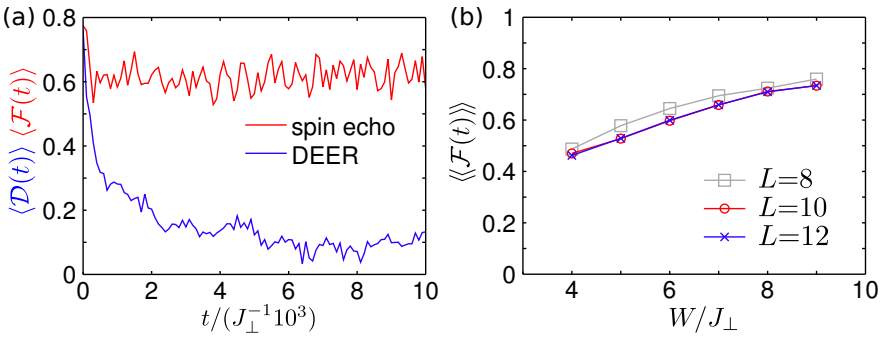

Figure 8: (a) Typical behavior of spin-echo and DEER response for the random-field XXZ model [Eq. (2.12)], averaged over 50 random eigenstates for a single disorder realization. The spin-echo response $\mathcal{F}(t)$ quickly saturates, whereas the DEER response $\mathcal{D}(t)$ slowly decays to a much smaller value. (b) Saturation values of disorder-averaged spin-echo fidelity as a function of disorder strength W and system size L for the random-field XXZ model with $J_z = J_\perp$. These results are consistent with the expectation that $\langle\langle \mathcal{F}(t) \rangle\rangle$ should saturate to a nonzero value in the thermodynamic limit (see main text).

(DEER) technique [81–83], is to perturb spins in a remote region II, situated at a distance $d \gtrsim \xi$ away from I, halfway through the spin-echo sequence. More specifically, DEER is identical to spin echo for the first $t/2$ of time evolution, but simultaneously with the π pulse to spin I, another pulse (which we shall take to be a $\pi/2$ pulse) is applied to all the spins in region II. Assuming that the remaining spins are in a state with definite τ^z, all interactions except those between spin I and region II are decoupled by this protocol; thus, the decay of the DEER response directly measures the influence of region II on spin I.

Before analyzing the DEER response, we summarize our qualitative expectations [Fig. 7(d)]. In the diffusive phase, both spin-echo and DEER responses should decay on a fast timescale set by the spin-spin interaction. In the NIL phase, both spin-echo and DEER responses should saturate at the same nonzero value in the thermodynamic limit, as dephasing is absent. Finally, in the MBL phase, the spin-echo response should saturate while the DEER response exhibits slow decay.

2.2.2 DEER response

The time-evolution of the many-body wave function under the DEER sequence is described by

$$|\psi(t)\rangle = R_{\rm I}^{\pi/2} e^{-i\hat{H}\frac{t}{2}} R_{\rm I}^{\pi} R_{\rm II}^{\pi/2} e^{-i\hat{H}\frac{t}{2}} R_{\rm I}^{\pi/2} |\psi(0)\rangle\,, \tag{2.7}$$

where $R_r^{\pi/2} = \prod_{j\in r}(\hat{1} - i\hat{\sigma}_j^y)/\sqrt{2}$, and $R_r^{\pi} = (R_r^{\pi/2})^2$.

Many features of the DEER response can be understood by keeping only two-spin interactions in Eq. (2.6), in which case the answer takes a compact form:

$$\mathcal{D}(t) \equiv \langle\psi(t)|\hat{\tau}_{\rm I}^z|\psi(t)\rangle \tag{2.8}$$

$$= \mathrm{Re}\prod_{j\in \rm II}\left(\frac{1+e^{2i\mathcal{J}_{{\rm I}j}\tau_j t}}{2}\right) \tag{2.9}$$

where the product is over the N spins of region II and τ_j is the initial configuration of spin j. The additional effects induced by three- and higher-spin interactions are considered below.

To analyze the behavior of $\mathcal{D}(t)$, we note that the couplings $\mathcal{J}_{{\rm I}j}$ decay exponentially with the separation $|j - {\rm I}|$, and therefore different terms on the r.h.s. of Eq. (2.9) oscillate at very different frequencies. This leads to a separation of scales: at a given time, there are $\sim N_{\rm fast}$ "fast" coupling constants, for which $\mathcal{J}_{{\rm I}j}t \gg 1$, and the remaining ones are "slow," $\mathcal{J}_{{\rm I}j}t \ll 1$. In the product in Eq. (2.9), the terms corresponding to slow couplings contribute factors which are close to 1 and are nearly time-independent, while the terms corresponding to fast couplings oscillate between 0 and 1. Thus, $\mathcal{D}(t)$ can be separated into a time-averaged term $\bar{\mathcal{D}}(t)$ and an oscillatory term, $\mathcal{D}_{\rm osc}(t)$:

$$\mathcal{D}(t) = \bar{\mathcal{D}}(t) + \mathcal{D}_{\rm osc}(t), \qquad \bar{\mathcal{D}}(t) = 1/2^{N_{\rm fast}(t)}, \tag{2.10}$$

where the first term is obtained by replacing rapidly oscillating terms with their average value of 1/2.

The number of "fast" couplings depends on time, and can be estimated knowing that $\mathcal{J}_{\mathrm{I}j} \propto \exp(-|j-\mathrm{I}|/\xi)$. A coupling becomes "fast" when $|j-I| \lesssim \xi \log(t)$, i.e., when entanglement has had time to propagate between the two regions [13]. Thus, the DEER response has three regimes: (i) at short times $t \lesssim t_0 \equiv \hbar/\mathcal{J}_{Ik}$ (where $k = I + d$ is the spin in region II that is most strongly coupled to I), $N_{\mathrm{fast}} = 0$ and dephasing is absent; (ii) at intermediate times $t_0 \lesssim t \lesssim t_0 e^{N/\xi}$, we find $N_{\mathrm{fast}}(t) \sim \xi \log(t/t_0)$, so that $\bar{\mathcal{D}}(t) \sim t^{-\xi \ln 2}$; and (iii) at very long times $t \gg t_0 e^{N/\xi}$, all couplings are fast, so that the DEER response saturates at $\bar{\mathcal{D}}(\infty) \approx 2^{-N}$. These three regimes can be combined using the following interpolation formula:

$$\bar{\mathcal{D}}(t) = \begin{cases} (1 + t^2/t_0^2)^{-\alpha/2} & t \lesssim t_0 e^{N/\xi} \\ 2^{-N} & t \gg t_0 e^{N/\xi} \end{cases}, \tag{2.11}$$

where $\alpha = \xi \ln 2$. Upon disorder averaging, one expects $\mathcal{D}_{\mathrm{osc}}(t)$ to be suppressed, as the oscillation frequencies vary randomly from realization to realization. Thus the full disorder-averaged DEER response is given by Eq. (2.11).

We note that, although truncating Eq. (2.6) at two-spin interactions gives the correct structure for the time- and disorder-averaged DEER response, it leads to incorrect predictions for the oscillatory term $\mathcal{D}_{\mathrm{osc}}(t)$. Three- and higher-spin terms make the oscillation frequencies dependent on the initial eigenstate, leading to the suppression of $\mathcal{D}_{\mathrm{osc}}(t)$ upon thermal averaging.

2.2.3 Numerical simulations

We now test the previous arguments against numerical simulations by studying the spin-echo fidelity and DEER response for a 1D random-field XXZ spin chain, believed to

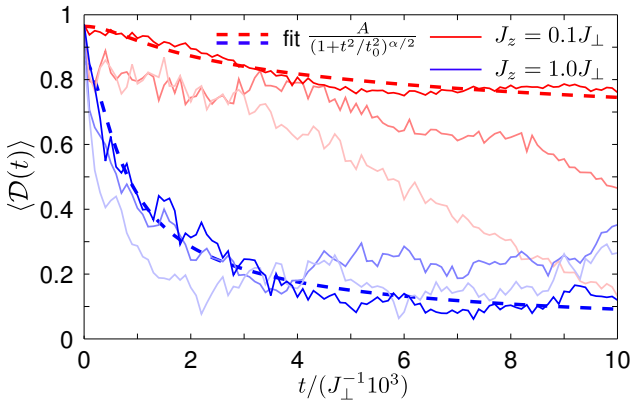

Figure 9: DEER response thermally averaged over 50 eigenstates for three particular disorder realizations of the random-field XXZ model, both at weak interactions ($J_z = 0.1J_\perp$) and moderate interactions ($J_z = J_\perp$). The general trend is consistent with that predicted by Eq. (2.11), but residual oscillations and sample-to-sample fluctuations are strong. The disorder strength is $W = 6J_\perp$; spin I is located at I = 3, and separated by $d = 3$ spins from region II with $N = 7$ spins.

exhibit an MBL phase [8]:

$$\hat{H} = \frac{J_\perp}{2} \sum_{\langle ij \rangle} (\hat{S}_i^+ \hat{S}_j^- + \hat{S}_j^+ \hat{S}_i^-) + J_z \sum_{\langle ij \rangle} \hat{S}_i^z \hat{S}_j^z + \sum_i h_i \hat{S}_i^z \tag{2.12}$$

where $\hat{S}_j^a$ with $a \in \{x, y, z\}$ are spin-1/2 operators with eigenvalues $\pm 1/2$, $\hat{S}_j^\pm = \hat{S}_j^x \pm i\hat{S}_j^y$, and the random field h_i is uniformly distributed in the interval $[-W; W]$. For open boundary conditions and $J_z = 0$, $\hat{H}$ maps onto free fermions moving in a disorder potential. In this limit, the system is in an NIL phase for any $W > 0$. When $J_z \neq 0$, the system is believed to exhibit both MBL and delocalized phases as a function of $W/J_\perp$ [8].

Although the Hamiltonian in the MBL phase can be expressed in the form of Eq. (2.6) when written in the basis of conserved quantities (effective spins), in experiments one manipulates the physical S-spins, rather than the effective τ-spins. In what follows, we calculate the response for spin-echo and DEER protocols performed on the physical spins. We show that, due to the local relation between physical and effective spin operators, the behavior of spin-echo and DEER responses discussed above remains qualitatively correct throughout the MBL phase, and becomes quantitatively correct in the limit of strong

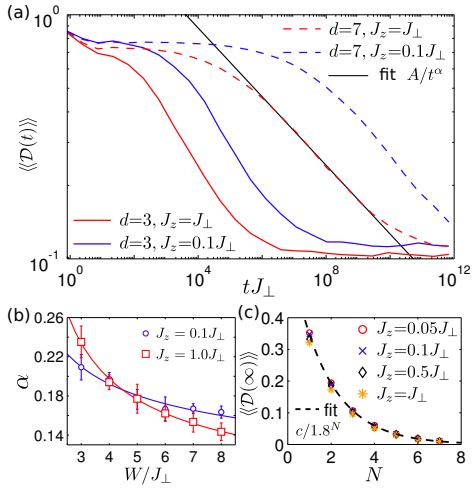

Figure 10: (a) Disorder-averaged DEER response for the random-field XXZ model for both weak ($J_z = 0.1J_\perp$) and moderate ($J_z = J_\perp$) interactions, and both small ($d = 3$) and large ($d = 7$) separations between spin I and region II. A regime of power-law decay, spanning multiple decades, can be seen in all cases. (The disorder strength is $W = 8J_\perp$, and the size of region II is $N = 3$.) (b) Dependence of the exponent α on disorder W (for $d = 7$ and $N = 3$). The fit, given by $\alpha = c_1/\ln(c_2 W)$, is consistent with the scaling of the localization length, $\xi \sim 1/\ln(W)$, at strong disorder. (c) Saturated value of DEER response, $\mathcal{D}(\infty)$, for various sizes of region II (denoted N) and various values of J_z. We find that $\mathcal{D}(\infty)$ does not depend on J_z and decreases with N as $c/1.8^N$.

disorder.

We study time evolution and response functions by exact diagonalization of the Hamiltonian (2.12). Unless otherwise specified, the chain contains $L = 12$ spins with open boundary conditions. The Hamiltonian is diagonalized for all total S^z sectors, and DEER response (2.8) is calculated numerically. The initial state $|\psi(0)\rangle$ is a randomly chosen eigenstate, such that $\mathcal{D}(0) = \langle\psi(0)|\hat{\sigma}^z_{\rm I}|\psi(0)\rangle > 0$. Thermal averaging is performed over the entire band (infinite temperature), and is denoted by single brackets, $\langle\mathcal{D}(t)\rangle$.

We first calculate thermally-averaged spin-echo and DEER response for a single disorder realization (Fig. 8). Spin echo was implemented both using the protocol of Fig. 7(b) and a modified protocol in which a $\pi/2$ pulse was applied to region II at time $t = 0$; the disorder-averaged fidelity shows the same behavior for both protocols. In the MBL phase, the spin-echo fidelity remains finite at long times, but its saturation value is smaller than

one, reflecting the difference between physical and effective spins. Each pulse affects several effective spins; therefore, the probability to come back to the initial state at the end of the sequence is reduced. At strong disorder, the spin-echo fidelity saturates to a value close to unity and is system-size independent. In contrast, the DEER response decays to values much smaller than one.

Fig. 9 demonstrates that the DEER response (thermally averaged over 50 eigenstates for a single disorder realization) fits well to the modified interpolation formula $\mathcal{D}(t) = A/(1 + t^2/t_0^2)^{\alpha/2}$, where a multiplier A has been introduced to account for the difference between effective and physical spins [cf. Eq. (2.11)]. However, the oscillations coming from $\mathcal{D}_{\rm osc}(t)$ are still significant.

Plotting the disorder-averaged DEER response (denoted by double brackets $\langle\langle \mathcal{D}(t) \rangle\rangle$) on a double logarithmic scale, Fig. 10(a), clearly reveals a power law decay spanning several decades. Comparison of $\langle\langle \mathcal{D}(t) \rangle\rangle$ for different separations d between regions I and II illustrates the sensitivity of $t_0[\sim \exp(d/\xi)]$ to d. Fig. 10(b) shows the dependence of the exponent governing the power-law decay, α, on disorder: α decreases with increasing disorder strength, and is well-described by the functional form $\alpha = c_1/\ln(c_2 W)$, consistent with the relation $\alpha = \xi \ln 2$ and scaling of the localization length $\xi \propto 1/\ln(W)$ at strong disorder. Finally, we study the dependence of the disorder-averaged saturation value of the DEER response as a function of the number of spins N in region II, Fig. 10(c). The saturation value, which is nearly independent of the interaction strength, fits to a function $f(k) = c/1.8^N$ (for effective spins, by contrast, Eq. (2.11) predicts $1/2^N$). Thus, the DEER response for physical spins has the same functional form as that for effective spins, although the coefficients are different, owing to the difference between physical and effective spin operators.

2.2.4 Experimental considerations

Promising experimental systems for studying MBL include ultracold atomic [64, 84, 85] and molecular [57, 66] gases confined in optical lattices, as well as localized spin defects in solids such as nitrogen-vacancy (NV) centers in diamond [44, 60]. Such systems can be well-isolated from their environment and feature long coherence times. Further, they can be manipulated by optical and microwave fields, thus allowing for implementation of the pulsed protocols. We now evaluate the feasibility of the present protocols in a number of experimental settings. In each case, the slow DEER decay can be observed provided that: (a) there exists a separation of scales between the couplings $J_\perp, J_z$ and the extrinsic decoherence rate T_1^{-1}, and (b) excitations are localized on a small number of sites, ensuring a reasonable spin-echo fidelity.

The most direct implementation of our protocols involves a two-component Fermi- or Bose-Hubbard model in a disordered optical lattice: in such models, random spin-spin interactions arise via superexchange, and random fields can be imposed via a state-dependent optical lattice. The typical interaction scale $J \approx 10$ Hz, whereas achievable T_1 times (limited by particle loss) are limited to about 10s [86–88]. The ratio between these scales is $\lesssim 500$; thus, the DEER protocol can detect entanglement at realistic distances $\lesssim \xi \ln(J\mathrm{T}_1) \approx 6\xi$. Even more favorable conditions exist in systems with dipolar interactions. For instance, in NV-center samples at achievable densities (e.g., spacings of 10 nm), $J \sim 100$ kHz and $\mathrm{T}_1 \sim 10$ ms, yielding $\mathrm{T}_1/J^{-1} \sim 5 \times 10^3$. For Rydberg atoms, $J \sim (1-10)$MHz (e.g. in 38s state of Rb at typical distances $\approx 5\mu$m), while $\mathrm{T}_1 \sim 100\mu$s; therefore, $\mathrm{T}_1/J^{-1} \sim (0.5-5) \times 10^3$. Finally, for polar molecules in optical lattices, $J \sim 50$Hz and $\mathrm{T}_1 \sim 25$s, and thus $\mathrm{T}_1/J^{-1} \sim 8 \times 10^3$. For all these cases, therefore, it should be feasible to probe interaction effects in the MBL phase through DEER; however, the functional form of the dephasing might differ from that considered here, as the power-law tails of the dipolar interactions modify localization (although the MBL phase is expected to survive for dipolar interactions in one dimension [51, 61, 89]).

Before concluding, we note that since the proposed protocols can distinguish various phases after disorder-averaging, they can be applied even in experiments where the disorder realization changes between individual experimental runs. This is especially important for realizations involving atoms or molecules loaded at random into a deep optical lattice; in such systems each disorder-realization is destroyed upon measurement.

In summary, we showed that coherent manipulation of spins can be used to probe many-body localization. In particular, the modified spin-echo protocol directly probes the characteristic slow entanglement growth in the MBL phase, and distinguishes it from the NIL phase and the delocalized phase. We demonstrated that the corresponding response function exhibits a power-law time decay, which reflects the broad distribution of time scales present in the MBL phase. The technique is robust with respect to thermal and disorder averaging, and can be implemented, using currently accessible experimental means, in ultracold atomic, molecular and solid-state spin systems.

2.3 Translation Invariant Many-body Localization

In the final section, we consider the possibility of many-body localization in the absence of disorder. Since its proposal in 1958 [23], Anderson localization has been observed in systems ranging from light and sound waves to electron gases and ultracold atoms. In each of these systems, disorder has been crucial to realize this single particle wave phenomenon. Extending disordered localization to the interacting many-body regime has attracted tremendous recent attention [3–8, 10–22, 49–52], in part, because it represents a fundamental breakdown of statistical mechanics. This breakdown opens the door to a number of intriguing possibilities, including: novel phase transitions in high-energy states, the protection of topological order, and quantum computing in a disordered many-body system.

Recently, a number of proposals have suggested the possibility that localization can persist even in the absence of disorder. One class of such models involves two types of

particles (light and heavy); the dynamics of the heavy particles are significantly slower than those of the light particles. At short time-scales, interactions between the heavy and light particles can induce a random quasi-static background potential for the light particles. If strong enough, this effective disorder can localize the light particles and one can argue, in perturbation theory, that transport owing to the slow dynamics of the heavy particles is insufficient to delocalize the system. Alternate models involving the motion of long-range, power-law interacting impurities or generalized Bose-Hubbard models have also been studied with similar conclusions. A central question which has emerged from these studies is whether randomness in the state of the system can be enough to cause "self-localization".

In this section, we address this question by considering a translation invariant two-leg spin ladder. We demonstrate that quasi-static many-body localization can exist for finite systems and quantify the three microscopic time scales that emerge. Despite signatures consistent with many-body localization at intermediate time-scales (e.g. a slow logarithmic growth of entanglement), we find ultimate thermalization at long times for all systems studied. We note that these results are preliminary and that there seems to emerge an extremely strong (anomalous) scaling of the decay of the fractional polarization in the heavy chain as a function of system size; this may in fact be evidence for self-induced many-body localization and is currently under study.

Consider a two-leg, spin-1/2, ladder as shown in Fig. 11, with Hamiltonian,

$$H = \sum_{\langle ij \rangle} J S_i^+ S_j^- + \sum_{\langle ij \rangle} J' \sigma_i^+ \sigma_j^- + \sum_i J_z S_i^z \sigma_i^z + h.c \tag{2.13}$$

Spins of the lower (upper) rung are labeled $S(\sigma)$ and are coupled via a nearest neighbor XY interaction of strength J (J'). The two spin species are coupled across a rung via Ising interactions of strength J_z. In the limit, $J' \to 0$, the σ spins of the upper chain can be viewed as classical variables that generate disorder for their S-spin cousins. Depending on the state of the $\{\sigma_i\}$, the lower chain sees an effective random on-site field of strength $\pm J_z$,

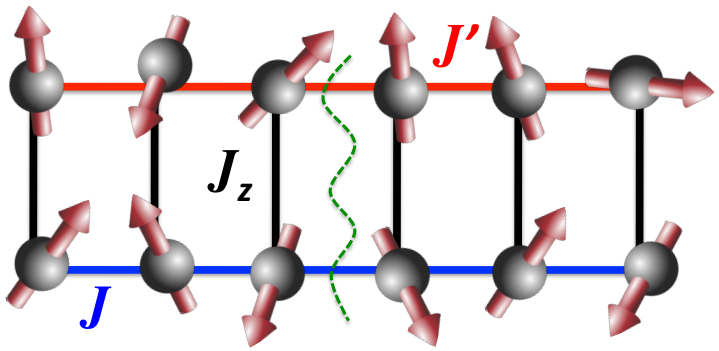

Figure 11: Schematic figure of the spin-ladder model. The upper and lower chain are governed by nearest neighbor XY models with strength J and J' respectively. For short times, the J' chain effectively creates quasi-static quench disorder for the J chain inducing localization. Once dynamics are turned on for finite J' the chains become interacting and thermalization eventually occurs. The green dotted line indicates the position of the cut used in partitioning the system for entanglement entropy calculations.

which for large J_z, induces single particle localization of the S chain.

As one turns on J' causing slow dynamics in the σ chain, the system is no longer non-interacting. Formally, this arises because strings of the Jordan-Wigner transformation no longer cancel between all pairs of sites. Thus, a perturbative J' effectively induces interactions in the system, and the question becomes: does the system transition from single-particle to many-body localized and if so, does localization persist to infinite times.

To study these questions we perform extensive exact diagonalization studies of Eq. (2.13). We consider periodic systems up to size $N = 20$ and work within the Hilbert space with $S^z_{tot} = \sigma^z_{tot} = 0$. Since we are interested in the effect of slow dynamics from the σ chain, we begin deep in the single-particle localized regime with $J = 1.0$ and $J_z 10.0$. We probe the effect of perturbative $J' \ll J$ with two measures. First, we consider the growth of entanglement entropy $S_{ent} = -\mathrm{tr}\rho_A \log \rho_A = -\mathrm{tr}\rho_B \log \rho_B$ across a central cut (parallel to a rung, Fig. 11) that divides the system in sub-regions A and B. Initial states are chosen to be random product states within the relevant Hilbert space and we average over between 30-100 states depending on system size.

Second, we explore the decay of the dynamic polarization D, a measure of spin transport

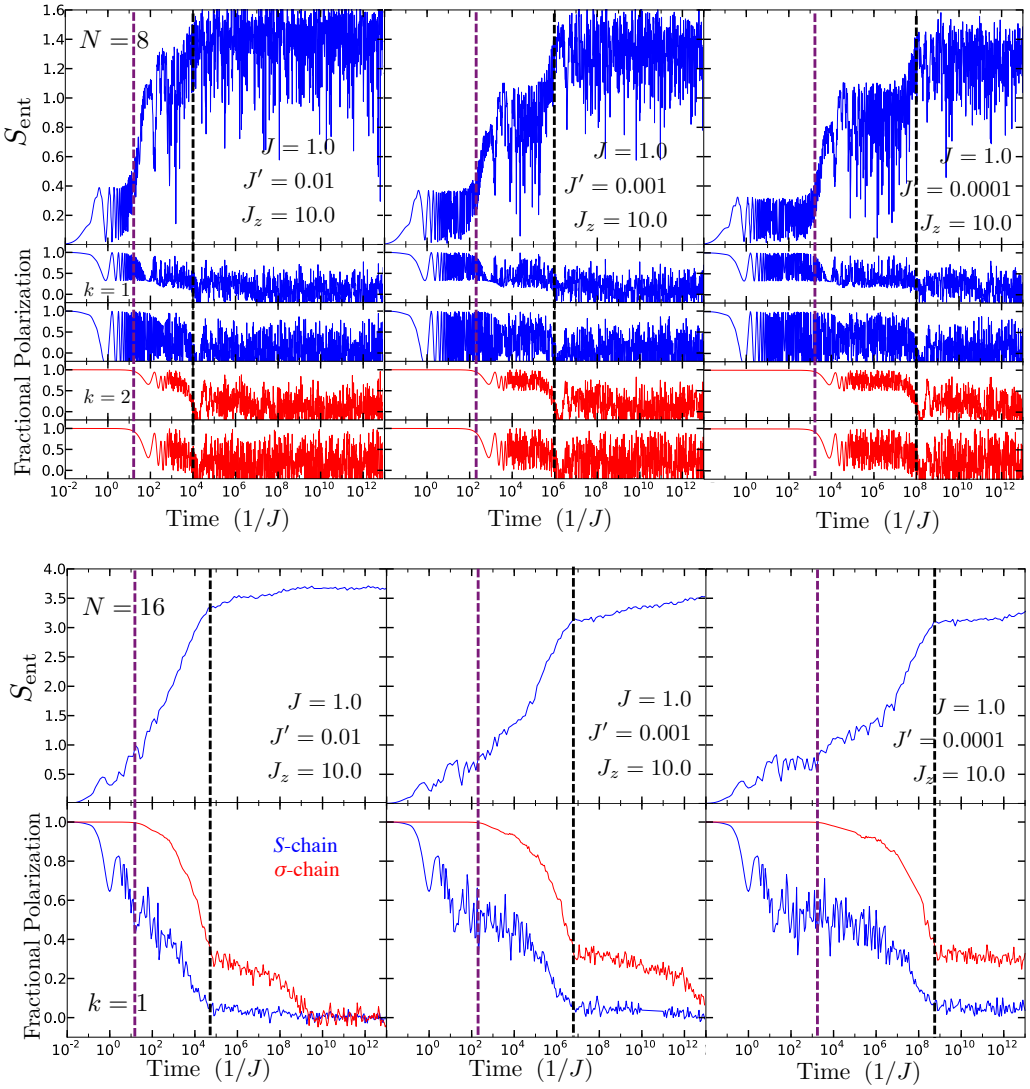

Figure 12: (a-c) Depicts the growth of entanglement entropy and the decay of fractional polarization for $N = 8$ total spins. The entanglement entropy is averaged over 30 initial product states and the fractional polarization is taken for an infinite temperature state within the $S^z_{tot} = \sigma^z_{tot} = 0$ Hilbert space. The blue polarization plots are for a $k = 1$ initial spin polarization with the upper plot depicting the S-chain response while the lower plot depicts the σ-chain response. The red plots depict the decay for a $k = 2$ initial spin polarization. t_{int} is indicated by the purple dashed line while t_d is indicated by the black dashed line. (d-f) Analogous plots for $N = 16$ total spins. Entanglement entropy is averaged over 50 initial product states and only $k = 1$ polarization decay is shown.

across the system at infinite temperature [8]. We perturb each eigenstate with a small (long-wavelength) inhomogeneous spin modulation of the form $\hat{F} = \sum_j S_j^z e^{i2\pi j/L}$ (replacing S_j^z with σ_j^z for the upper chain) and measure the time-dependent relaxation of this inhomogeneous polarization. For each eigenstate k, the dynamic polarization is given by

$$D^k = 1 - \frac{\langle k|\hat{F}^\dagger|k\rangle\langle k|\hat{F}|k\rangle}{\langle k|\hat{F}^\dagger\hat{F}|k\rangle}, \tag{2.14}$$

and we define D as the infinite temperature average of D^k.

The results for $N = 8,\ J' = 10^{-2}, 10^{-3}, 10^{-4}$ are shown in Fig. 12. Interestingly, we observe three plateaus in the growth of the entanglement entropy. For all J', we observe an initial rise of S_{ent} until time $t \sim 1/J$ corresponding to a rapid expansion of wave packets to a size of order the localization length. The entropy then saturates (albeit oscillating) for a period of time before beginning a second phase of entanglement growth. This second growth step also saturates for an extended time before a third and final spurt where the entropy reaches its thermal plateau.

The three regimes can be qualitatively understood as follows (Fig. 13a). The first entanglement plateau which arises at $t \sim 1/J$ corresponds to single-particle localization. As aforementioned, in the absence of J', the system is non-interacting. Thus for time scales $t \ll 1/J'$, the system behaves as if it were single-particle localized with interactions turning on only at some effective (J' dependent) interaction time t_{int}. The second phase of entanglement growth occurs for $t > t_{int}$ and is consistent with a slow, logarithmic rise, characteristic of many-body localization. As the system is finite, this growth ultimately saturates to a quasi-MBL plateau. Finally, at late times $t > t_d$, a third phase of entanglement growth begins, signifying thermalization of the entire system and diffusion in the upper chain.

To understand the microscopic origin of these various time-scales we consider the scaling of t_{int} and t_d as a function of J'. Comparing the growth of S_{ent} across the various

parameters yields $t_{int} \sim 1/J'$ and $t_{int} \sim 1/J'^2$; similarly, holding J, J' fixed while varying J_z yields that $t_{int} \sim J_z$ (see supplementary information). The scaling of t_{int} is consistent with a picture of J' induced departure from single-particle localization. In particular, the effective induced-interaction-strength is directly proportional to J' and arises from the delocalization of upper chain particles across a bond where a pair of S spins are aligned (inset Fig. 13a). The scaling of $t_d \sim J_z/J'^2$ suggests that the eventual diffusion in the upper chain is characterized by a diffusion constant $\sim J'^2/J_z$ consistent with a picture of off-resonant hopping across a flipped S-rung (Fig. 13b). The decay of fractional polarization confirms that the final plateau correlates with diffusion of the slow, upper chain as t_d corresponds to the location where the upper chain $D_{k=1}$ reaches its final decay step. Interestingly, it also corresponds to the location where the $k = 2$ polarization first decays to zero.

Our microscopic understanding of the triple plateau observed in the entanglement entropy suggests that the schematic picture shown in Fig. 13a may not be generic for longer chains. In particular, the slow growth of entanglement in the quasi-MBL regime owes to exponentially weak dephasing across the system; thus, the saturation of such dephasing occurs at times $t \sim e^L$. On the other hand, the eventual thermalization of the system is driven by diffusion in the upper chain. To wit, the decay of a $k = 1/L$ fractional polarization is expected to scale as $\sim e^{-Dk^2t}$, yielding $t_d \sim L^2/D$, with $D \sim J'^2/J_z$ being the effective diffusion constant from above. Thus, for longer spin ladders, one would not generically expect the logarithmic MBL entanglement growth to saturate before being cut-off by thermalization of the upper chain (Fig. 13b).

To probe this expectation, we perform analogous calculations for $N = 16$, which significantly extends the time-scale for MBL entanglement growth (factor $\sim e^8$) but which only marginally alters the expected diffusion time-scale. The results are shown in Fig. 12d-f. For all J', the intermediate quasi-MBL plateau is indeed absent. Moreover, we find that t_{int} is independent of the system size while t_d exhibits a scaling consistent with

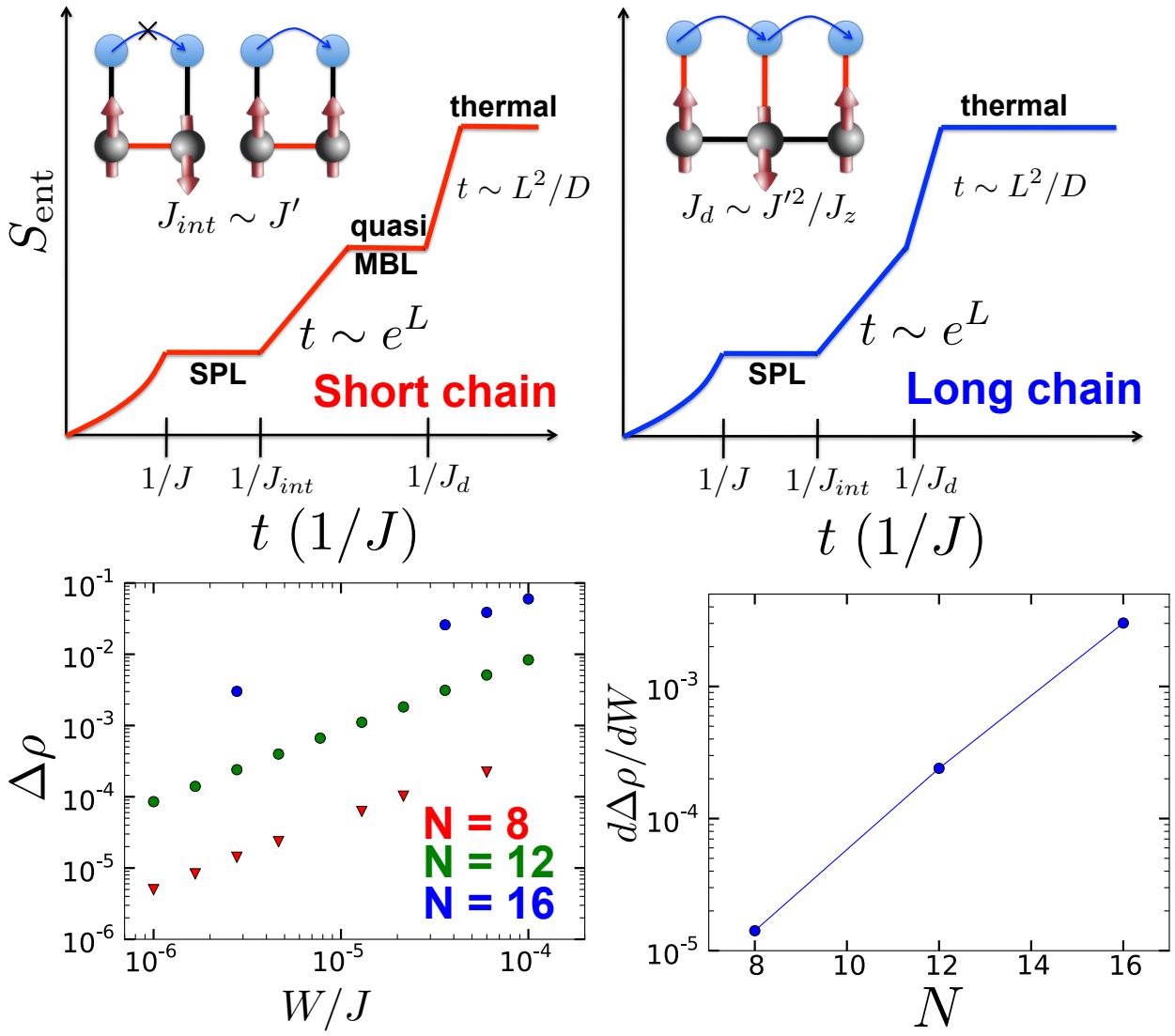

Figure 13: (a) Schematic of the entanglement entropy growth for short chains. Driven by localization length dynamics, a rapid increase in S_{ent} occurs until time scales $1/J$, wherein a single particle localization plateau occurs. Then for times $t > t_{int} = 1/J_{int}$, J' induces effective interactions in the ladder and the entanglement entropy exhibits a slow, logarithmic growth characteristic of MBL. This growth saturates for a finite system into a quasi-MBL plateau before ultimate diffusion of the upper chain takes place. For late times $t > t_d = 1/J_d$, the upper chain thermalizes with a diffusion constant $D \sim J'^2/J_z$. (b) Schematic of S_{ent} for long chains. The intermediate quasi-MBL plateau disappears since its time extent scales as e^L and becomes cut-off by diffusion which scales only as L^2. (c) Linear response of the system to translation invariance breaking perturbations. (d) Susceptibility which scales consistent with an exponential in system size.

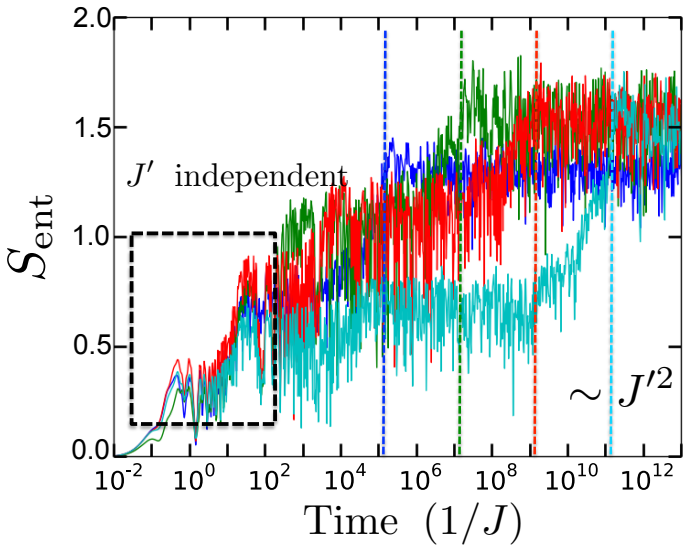

Figure 14: Entanglement entropy for a spin ladder model with Heisenberg couplings along the ladder. There no longer exists a single particle, non-interacting limit, and thus t_{int} becomes J' independent. Ultimate saturation occurs at time scales consistent with J'^2 suggesting an analogous process as the XY ladder. An intermediate plateau becomes evident for certain J' and may be associated with correlated spin-flips across a rung.

L^2. Both observations are consistent with our microscopic picture; the interaction time scale is set by resonant nearest neighbor hybridization in the upper chain while diffusion scales as $t_d \sim 1/Dk^2 \sim L^2$. For $J = 10^{-2}$, the existence of multiple regimes of entanglement growth is difficult to observe. However, since t_{int} and t_d scale differently with J', it is possible to tease apart the different phases of entropy growth by considering slower upper chain dynamics. The cut-off of slow MBL entanglement growth by thermalization is most evident for $J' = 10^{-5}$, where one observes logarithmic growth for nearly 4 decades in time before a rapid increase in S_{ent} owing to upper chain diffusion. This picture is confirmed by the time decay of fractional polarization where t_d precisely matches the location of σ-chain equilibration. Interestingly, in the fractional polarization of the σ-chain, there emerges a second long-time plateau which only decays at extremely long time-scales and which exhibits an anomalously strong scaling with J' and system size. We view this as possible evidence for self-induced many-body localization and are currently exploring these signatures in more detail.

While the spin ladder ultimately equilibrates and thermalizes at long times, it is insightful to probe the system's response to translation symmetry breaking. In particular, it has been recently proposed [52] that a system which exhibits self-induced many-body localization should also spontaneously break translational invariance, and in fact, that these notions are essentially equivalent. To probe our system's susceptibility to translation symmetry breaking, we introduce a perturbation of the form

$$H_W = \sum_i b_i^z S_i^z + \sum_i b_i'^z \sigma_i^z \tag{2.15}$$

where b, b' are independent random variables drawn from a uniform distribution of width W. To quantify the system's response to H_W, we consider an observable $\Delta\rho_\psi = \frac{1}{N}\sum_i^N |\langle\psi|S_{i+1}^z - S_i^z|\psi\rangle|$ which measures the inhomogeneity of the spin polarization in the lower chain [52]. A perturbative estimate reveals that the dynamical localization of typical quantum states should manifest as an exponential susceptibility to H_W, with

$$\frac{d\Delta\rho}{dW} \sim \left(\frac{c}{\sqrt{W/J}}\right)^N. \tag{2.16}$$

Note that this contrasts with expectations for a single particle localized state where an analogous calculation reveals $\frac{d\Delta\rho}{dW} \sim N$ (see supplementary information). We perform exact diagonalization on $H_T = H + H_W$ with $J = 1.0$, $J' = 0.01$, $J_z = 10.0$ and $10^{-6} < W < 10^{-4}$. We average over 10^3 disorder realization for $N = 8, 12$ and over 10^2 realizations for $N = 16$; we also average $\Delta\rho$ over 10 eigenstates ψ centered around energy density $J/3$. Our results are depicted in Fig. 13(c,d). As expected, for a perturbative breaking of translation invariance, we observe a linear response in $\Delta\rho$; moreover, the susceptibility is consistent with an exponential system size scaling, although the range of sizes are too small to be able to make conclusions.Interestingly, despite eventual thermalization, our system seems to exhibit an exponential susceptibility to H_W. This may manifest as a turn over from exponential to power-law scaling at larger sizes.

Finally, we consider the generalization of our ladder model to the case of Heisenberg coupled chains with

$$H_h = \sum_{\langle ij \rangle} J S_i \cdot S_j + \sum_{\langle ij \rangle} J' \sigma_i \cdot \sigma_j + \sum_i J_z S_i^z \sigma_i^z. \tag{2.17}$$

In this case, for $J' \to 0$, there is no single particle localized regime. Instead, the time scale for interactions $t_{int} \sim 1/J$ and hence, the onset of logarithmic MBL entanglement growth should be J' independent. This is indeed observed in Fig. 14. The eventual diffusion of the upper chain looks to be governed by a similar off-resonant upper-chain hop across a flipped S-rung since the final plateau scales with J'^2. Interestingly, for certain J', we observe another intermediate plateau for S_{ent} which scales with J' and is consistent with a physical process corresponding to a correlated S and σ spin-flip across a rung. The effective strength of a such a process $\sim JJ'/J_z$ and can be quantitatively compared to $1/t_d \sim J'^2/J_z$.

Chapter 3

Topology and Fractionalization in Polar Molecules

3.1 Topological Flat Bands

Single-particle flat bands, where kinetic energy is quenched relative to the scale of interactions, are being actively explored in the quest for novel strongly correlated phases of matter [24–31]. Prompted by the analogy to Landau levels, recent efforts have focused on topological flat bands (TFB) – lattice models in which the band-structure also harbors a non-trivial Chern invariant. Seminal recent work has highlighted that certain classes of highly-engineered two-dimensional tight binding models can indeed exhibit topological nearly flat bands [90–95]. However, the identification of a physical system whose microscopics naturally admit TFB remains an outstanding challenge.

In this section, we demonstrate the emergence of synthetic gauge fields for an ensemble of interacting hardcore bosons — the effective spin-flips of pinned, three-level dipoles in a two-dimensional lattice. Underlying these gauge fields are two key ingredients: spatially varying, elliptically-polarized external (microwave or optical) fields break time-reversal symmetry, while anisotropic dipolar interactions induce orientation-dependent phases onto the hopping hardcore bosons. The combination of these effects naturally produces nontrivial Chern numbers in the band structure and, when tuned appropriately, results in

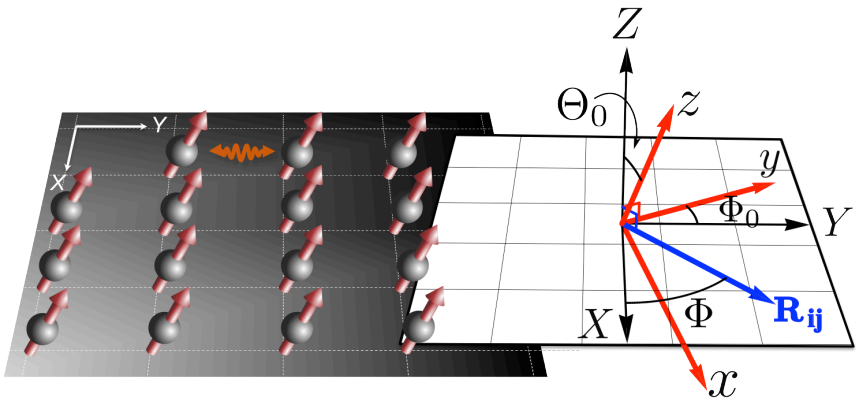

Figure 15: Schematic representation of a 2D dipolar droplet. The grey droplet represents a 2D array of interacting tilted dipoles. The dipoles are tilted by a static field in the $\hat{z}$ direction, oriented at Θ_0, Φ_0 relative to the lattice basis $\{X, Y, Z\}$. R_{ij} is a vector connecting dipoles in the XY plane.

the emergence of flat bands due to hopping interference. While we observe a variety of non-topological correlated many-body states here (ranging conventional crystals to supersolids), interacting particles living in such a flat-band-kinetic environment are also leading candidates for the realization of fractional Chern insulators [24–31]. Our proposal describes a natural framework in which ultra-cold molecules may be used to probe the exotic features of such interacting topological insulators.

Let us consider a square lattice composed of fixed, three-state magnetic or electric dipoles placed in a static external field. Such an arrangement naturally arises in experimental systems ranging from ultra-cold polar molecules [67–69, 96–99] and Rydberg atoms [100–102] to solid-state spins [44, 45] and magnetic atoms [103]. As shown in Fig. 15, the dipoles occupy the $\{X, Y\}$ plane and couple via dipole-dipole interactions,

$$H_{dd} = \frac{1}{2} \sum_{i \neq j} \frac{\kappa}{R_{ij}^3} \left[\mathbf{d}_i \cdot \mathbf{d}_j - 3(\mathbf{d}_i \cdot \hat{\mathbf{R}}_{ij})(\mathbf{d}_j \cdot \hat{\mathbf{R}}_{ij}) \right], \tag{3.1}$$

where κ is $1/4\pi\epsilon_0$ for electric dipoles or $\mu_0/4\pi$ for magnetic dipoles, and $\mathbf{R}_{ij}$ connects the dipoles $\mathbf{d}_i$ and $\mathbf{d}_j$. The three states of each dipole, which we label as $|0\rangle$, $|\pm 1\rangle$, are eigenvectors of the $\hat{z}$-component of (rotational or spin) angular momentum. We assume

that the $|\pm 1\rangle$ states are degenerate while the $|0\rangle$ state is energetically separated from them (Fig. 16a).

Each three-level dipole is driven by electromagnetic fields of Rabi frequency Ω_+ (right-circularly polarized), Ω_- (left-circularly polarized) and detuning Δ as shown schematically in Fig. 16a. With $|\Omega_+|, |\Omega_-| \ll \Delta$, the approximate eigenstates (dressed states) are: $|0\rangle$, $|B\rangle = \alpha(|-1\rangle + \beta|1\rangle)$, and $|D\rangle = \alpha^*(-\beta^*|-1\rangle + |1\rangle)$, where $\alpha = \Omega_+/\tilde{\Omega}$, $\alpha\beta = \Omega_-/\tilde{\Omega}$, and $\tilde{\Omega} = \sqrt{|\Omega_-|^2 + |\Omega_+|^2}$. The energies of these dressed states are $E_0 = -\tilde{\Omega}^2/\Delta$, $E_B = \Delta + \tilde{\Omega}^2/\Delta$, and $E_D = \Delta$ respectively. We let d represent the typical size of the dipole moment and R_0 be the nearest-neighbor spacing; by ensuring that $\kappa d^2/R_0^3 \ll \tilde{\Omega}^2/\Delta$ and so long as we initially avoid populating $|D\rangle$, the system remains within the subspace locally spanned by $|0\rangle$ and $|B\rangle$ (note that one could also choose to work in the subspace spanned by $|0\rangle$ and $|D\rangle$).

Thus, it is natural to view $|B\rangle$ as representing an effective hardcore bosonic excitation (spin-flip), while $|0\rangle$ represents the absence of such an excitation. Recasting this system in terms of operators $a_i^\dagger = |B\rangle\langle 0|_i$ ($n_i = a_i^\dagger a_i$) yields a 2D model of conserved hardcore lattice bosons,

$$H_B = -\sum_{ij} t_{ij} a_i^\dagger a_j + \frac{1}{2}\sum_{i\neq j} V_{ij} n_i n_j, \tag{3.2}$$

where we define the hopping $t_{ij} = -\langle B_i 0_j|H_{dd}|0_i B_j\rangle$, the on-site potential $t_{ii} = \sum_{j\neq i}(\langle 0_i 0_j|H_{dd}|0_i 0_j\rangle - \langle B_i 0_j|H_{dd}|B_i 0_j\rangle)$, and the interaction $V_{ij} = \langle B_i B_j|H_{dd}|B_i B_j\rangle + \langle 0_i 0_j|H_{dd}|0_i 0_j\rangle - \langle B_i 0_j|H_{dd}|B_i 0_j\rangle - \langle 0_i B_j|H_{dd}|0_i B_j\rangle$. The conservation of total boson number, $N_i = \sum_i a_i^\dagger a_i$, arises from the condition $\kappa d^2/R_0^3 \ll \Delta$, which ensures that particle-number non-conserving terms of H_{dd} are energetically disallowed. The functional form of the effective hardcore bosonic Hamiltonian Eq. (3.9) arises for any system of pinned, three-level dipoles. The parameters in H_B are given by

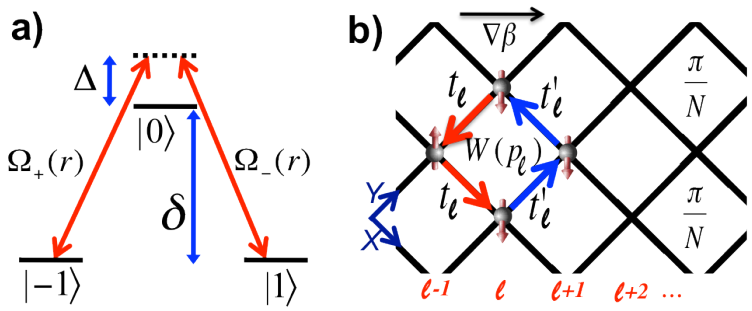

Figure 16: a) Depicts the on-site level structure and the two-photon driving scheme. These levels could, for example, be adiabatically connected to the $J = 1$ manifold of a rigid rotor as one turns on a DC electric field (see Eq. (3.6)). The resonance frequency of the dressing lasers is detuned by Δ, while their Rabi frequencies are $\Omega_-(r)$ and $\Omega_+(r)$. We consider $|\Omega_\pm| \ll \Delta$ to operate in the far-detuned limit. In the case of polar molecules, δ is the electric-field induced splitting within the $J = 1$ manifold, which we require to be larger than the typical dipolar interaction strength. b) Square lattice with a single tilted dipole per vertex. We index columns of the lattice by ℓ and plaquettes by p_ℓ. For a particle traversing the edge of a single plaquette, there are two contributions t_ℓ and t'_ℓ to $W(p_\ell)$; each contribution occurs twice as represented by the red and blue colored arrows. A simple periodic gradient of β enables uniform π/N flux per plaquette.

$(\kappa = 1, i \neq j)$:

$$
\begin{aligned}
t_{ij} &= \frac{d_{01}^2}{R^3}\left[\chi_i^\dagger(q_0 + \mathrm{Re}[q_2]\sigma^x + \mathrm{Im}[q_2]\sigma^y)\chi_j\right], \\
t_{ii} &= -\sum_{j\neq i} 2\frac{q_0}{R^3}(d^0 d_i^B - (d^0)^2), \\
V_{ij} &= 2\frac{q_0}{R^3}\left[d_i^B d_j^B - d^0 d_i^B - d^0 d_j^B + (d^0)^2\right],
\end{aligned}
\tag{3.3}
$$

where d^0 (d^B) is the permanent $\hat{z}$-dipole moment of the $|0\rangle$ ($|B\rangle$) state, d_{01} is the transition dipole moment from $|1\rangle$ to $|0\rangle$, $\chi_i = \alpha_i(1, \beta_i)^T$ is the normalized drive-spinor on site i, $q_0 = \frac{1}{2}(1 - 3\cos^2(\Phi - \Phi_0)\sin^2(\Theta_0))$, $q_2 = -\frac{3}{2}[\cos(\Phi - \Phi_0)\cos\Theta_0 - i\sin(\Phi - \Phi_0)]^2$, $\vec{\sigma}$ are the Pauli matrices, and (R, Φ) is the separation $\mathbf{R}_{ij}$ in polar coordinates (Fig. 15). We have suppressed the explicit ij dependence of R, Φ, q_0, and q_2. While the form of d_i^B, and hence of interactions, depends on the underlying implementation, the single-particle band structures that can be achieved via driving are independent of such details.

Let us first explore these topological single-particle bands and illustrate the interplay between the driven breaking of time-reversal and the anisotropic dipolar interaction. As a

simple example, we demonstrate how to achieve a synthetic background gauge field with uniform flux π/N per plaquette on a square lattice (assuming only nearest-neighbor hops). We choose the "magic" electric field tilt, $(\Theta_0, \Phi_0) = (\sin^{-1}(\sqrt{2/3}), \pi/4)$, where $q_0 = 0$ along $\hat{X}$ and $\hat{Y}$. This choice allows us to isolate the terms of H_{dd} that harbor intrinsic phases, namely, those associated with $d_i^+ d_j^+$ and $d_i^- d_j^-$, where $d_\pm = \mp(d_x \pm i d_y)/\sqrt{2}$ [99]. Moreover, it simplifies the form of nearest-neighbor hopping to

$$t_{ij}^{\hat{X}} = \frac{d_{01}^2}{R_0^3} \chi_i^\dagger \left[\frac{1}{2}\sigma^x - \frac{\sqrt{3}}{2}\sigma^y \right] \chi_j,$$
$$t_{ij}^{\hat{Y}} = \frac{d_{01}^2}{R_0^3} \chi_i^\dagger \left[\frac{1}{2}\sigma^x + \frac{\sqrt{3}}{2}\sigma^y \right] \chi_j. \tag{3.4}$$

The microscopic breaking of time-reversal arises from the asymmetry between left- and right- circularly polarized radiation and is captured by the ratio $\beta = \Omega_-/\Omega_+$. While each Rabi frequency is characterized by both an amplitude (intensity) and a phase, initially, we will consider only varying the amplitude of β; phase variations will be considered in more detail in the discussion of many-body states. Physically, it is β which defines each hardcore boson $|B\rangle$, by setting the relative admixture between the $|1\rangle$ and $|-1\rangle$ states. Keeping β real, let us now consider varying the intensities of the drive fields along the $\Phi = \pi/4$ direction in a periodic fashion.

For each plaquette, we define the Wilson loop, $W(p) = \prod_{\partial p} t_{ij}$, which is identical along columns indexed by ℓ (Fig. 16b). The flux in a plaquette is then the phase of this Wilson loop, $\Psi_\ell = \arg[W(p_\ell)] = \arg[t_\ell^2 t_\ell'^2]$, where t_ℓ are t_ℓ' are the hops depicted in Fig. 16b. Taking $\theta_\ell = \arg(t_\ell)$ and noting that $\theta_\ell' = \arg(t_\ell') = -\theta_{\ell+1}$ yields the phase of the Wilson loop as $\Psi_\ell = 2\theta_\ell - 2\theta_{\ell+1}$. To achieve a uniform π/N flux per plaquette, we can take $\theta_{\ell+1} = \eta - \ell\frac{\pi}{2N}$, where $\eta \in \mathbb{R}$ is a constant to be specified. From the definition of θ_ℓ, one finds a simple recursion relation for β,

$$\frac{\beta_{\ell+1}}{\beta_\ell} = \frac{\sin(\frac{\pi}{3} - \eta + \ell\frac{\pi}{2N})}{\sin(\frac{\pi}{3} + \eta - \ell\frac{\pi}{2N})}, \tag{3.5}$$

with maximum periodicity $4N$. Starting from any initial β_1, Eq. (3.5) yields a recursively generated drive pattern which achieves the desired uniform π/N background gauge field.

While the uniform flux per plaquette is reminiscent of the square lattice Hofstadter problem [104], we emphasize that the physics of these driven dipoles is significantly richer, owing to the additional modulation of t_{ij}. The background flux field arises, in part, from the natural phases associated with the dipolar interaction. This ensures that (as in [105]) the number of flux quanta per plaquette is not limited by the magnitude of laser intensities, contrasting with the majority of previous synthetic gauge field proposals, where the scaling to high artificial fluxes is extremely difficult [106–110].

To illustrate the symmetry breaking required for the generation of gapped Chern bands, we now turn to a detailed study of H_B restricted to a two-site unit cell (remaining at the "magic" tilt), as depicted in Fig. 17a. This restriction has the virtue of being analytically tractable and allows us to identify the anti-unitary symmetries associated with the Dirac points [111, 112]. Let us consider $\beta = \beta_1, \beta_2$ on the two sites of the unit cell and include all terms up to next-next-nearest neighbor. The topology of the bands depends on the relative ratio of β_1 and β_2. For $\beta_1 \in \mathbb{R}$, the phase diagram in Fig. 17b illustrates the Chern invariant of the bottom band as a function of the complex β_2-plane. There exist two circles of gapless (Dirac) points protected by distinct anti-unitary symmetries.

3.1.1 Implementation

An experimental realization of our proposal can be envisioned with either electric (e.g. polar molecules) or magnetic (e.g. solid-state spins) dipoles. As previously mentioned, the form of d_i^B depends on this choice, since the permanent dipole moment of the $|\pm 1\rangle$ states have either the same or opposite signs. We emphasize that the long intrinsic lifetimes of such systems make them ideal for the consideration of driven, non-equilibrium phenomena [65, 113].

To be specific, we now focus on diatomic polar molecules (trapped in a deep optical

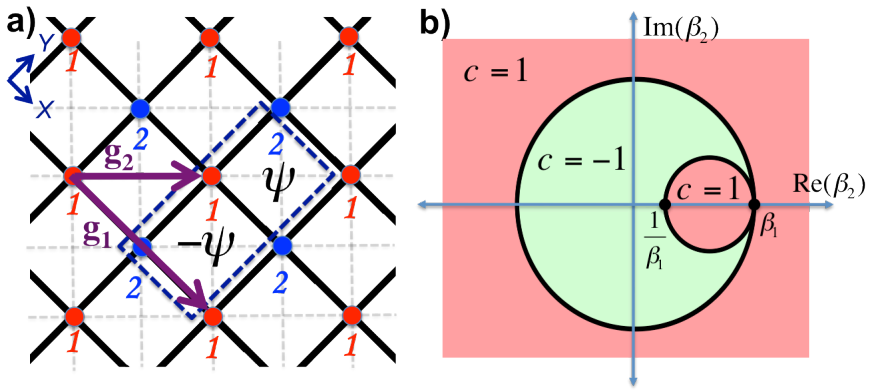

Figure 17: a) Schematic representation of the two-site unit cell lattice with $\beta = \beta_1, \beta_2$. The dotted box outlines a single unit cell. There is a flux $\Psi, -\Psi$ which alternates in neighboring square plaquettes. The direct lattice vectors g_1 and g_2 are depicted as purple arrows. While all hops are present with amplitude decaying as $1/R^3$, only nearest-neighbor (solid) and next-nearest-neighbor (dashed) hops are shown. b) The topology of bulk bands as a function of complex β_2 for $\beta_1 \in \mathbb{R}$. The Chern number is $c = \frac{1}{4\pi}\int dk_x dk_y (\partial_{k_x}\hat{d} \times \partial_{k_y}\hat{d}) \cdot \hat{d}$, where $H(k) = \vec{d}(k) \cdot \vec{\sigma} + f(k)$.

lattice) in their electronic and vibrational ground state. We utilize microwave fields to dress the molecules and partially polarize them with an applied DC electric field along $\hat{z}$ (Fig. 15); ignoring electronic and nuclear spins, this yields a single-molecule Hamiltonian,

$$H_m = BJ^2 - d_z E + H_D, \tag{3.6}$$

where B is the rotational constant, J is the rotational angular momentum operator, d_z is the $\hat{z}$ component of the dipole operator, E is the magnitude of the applied DC field, and H_D characterizes the dressing of the $J = 1$ rotational states depicted in Fig. 16a [65, 99].

In the absence of applied fields, each molecule possesses rigid rotor eigenstates $|J, M\rangle$. The applied electric field $\mathbf{E}$ mixes eigenstates with the same M, splitting the degeneracy within each J manifold and inducing a finite permanent dipole moment for each perturbed rotational state. We choose from among these states to form the effective three-level dipole; an example of one possibility for $|0\rangle$, $|\pm 1\rangle$ is shown in Fig. 16a. Since these $|\pm 1\rangle$

states have an identical induced dipole moment d^1, one finds that $d_i^B = d^1$, and hence,

$$V_{ij} \;=\; 2\frac{q_0}{R^3}(d^0 - d^1)^2. \tag{3.7}$$

The relative strength of the interaction V_{ij}/t_{ij} is thus set by $(d^0 - d^1)^2/d_{01}^2$; this is a highly tunable parameter and can easily reach ~ 100 for certain choices of rotational states and DC electric field strengths [99].

The main challenge in an experimental realization of our proposal lies in the spatial modulation of the drive fields at lattice scale. For spins in the solid-state and on-chip polar molecule experiments, one might envision using near-field techniques. A more straightforward approach, suitable for molecules, is to utilize pairs of optical Raman beams. For example, the so-called lin$\perp$lin configuration [114] automatically ensures that $\tilde{\Omega}$ and Δ are identical on all sites and moreover, generically produces gapped topological band-structures.

3.1.2 Many-body phases

To illustrate the power of the present approach, we briefly explore two examples of correlated ground state phases which arise in the Hamiltonian Eq. (3.9). As H_B conserves boson number N, we may consider its many-body physics at finite filling fractions ν (particle number per unit cell). Let us work with a two-site unit cell and truncate the dipolar interactions at next-next-nearest-neighbor order. Bosons residing in a strongly dispersing band structure generically form superfluids in order to minimize their kinetic energy. Interaction dominated phases arise when the single-particle bands disperse less than the scale of interactions. Numerical optimization of the flatness ratio (bandgap/lowest bandwidth) over the six-dimensional parameter space of microwave driving and tilt angle reveals approximately flat Chern bands in several regions of phase space. The flatness of these bands (Fig. 18a) derives from interference between the hopping in different directions

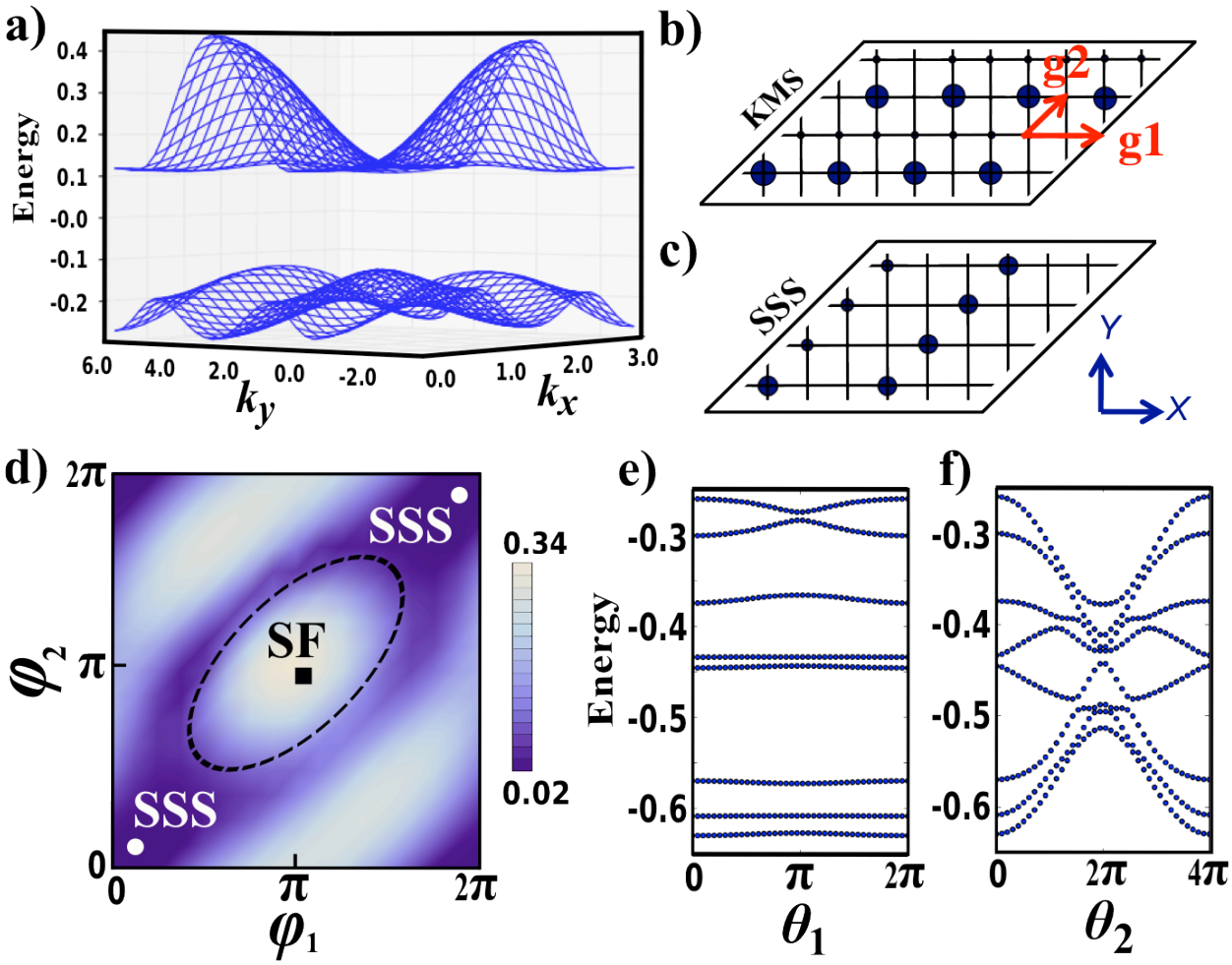

Figure 18: Phase Transitions in topological flat bands of 2D driven dipoles. a) Band structure for $(\Theta_0, \Phi_0) = (0.46, 0.42)$, $\beta_1 = 3.6e^{2.69i}$, and $\beta_2 = 5.8e^{5.63i}$. We have verified that the Chern number does not change upon adding in dipolar interactions up to order $1/27R_0$. Significantly flatter band structures with flatness ratio > 10 can be obtained for slightly generalized configurations involving a tripod level-structure and optical super-lattice [115]. b) Structure factor $S(R, 0) = \langle n(R)n(0)\rangle$ for filling $\nu = 1/2$ in KMS and c) SSS regime; size of circles indicates weight. d) Spectral gap density plot as a function of varying MW drive for parameters: $(\Theta_0, \Phi_0) = (0.66, \pi/4)$, $\beta_1 = -2.82e^{i\phi_1}$, $\beta_2 = -4.84e^{-i\phi_2}$ and $(d^0 - d^1)^2/d_{01}^2 \approx 2.8$. The transition from the SF, which has a unique finite-size ground state, to the degenerate SSS shows as a collapse of this gap. e) Spectral flow in the ground state momentum sector of the SSS under twisting of the boson boundary condition in the $\hat{g}_1$ and f) $\hat{g}_2$ directions. For the $N_s = 24$ lattice with 6 bosons, momentum sectors return to themselves after 2π in θ_1 and after 4π in θ_2.

and, microscopically, owes to an interplay between the natural anisotropy associated with dipolar interactions and the spatial variation of the drive fields.

As a first example, we consider the band structure depicted in Fig. 18a, where the lower/upper band carry Chern index, $c = \mp 1$ (parameters in caption). Exact diagonalization at filling fraction $\nu = 1/2$ and relative interaction strength $(d^0 - d^1)^2/d_{01}^2 \approx 6$ reveals a knight's move solid (KMS) phase with a 4-fold degenerate, gapped, ground state. The real-space structure factor $S(R, 0) = \langle n(R)n(0)\rangle$ (at total number of sites, $N_s = 32$) in Fig. 18b illustrates the knight's move relationship of the bosons in the ground state. Twisting the boundary condition of the KMS in the $\hat{g}_1$, $\hat{g}_2$ directions (Fig. 18b) does not significantly affect the ground state energy, as expected of an insulator.

Many other commensurate phases arise as as we tune the driving fields to other regions of phase space. Figure 18d shows a phase diagram containing both superfluid (SF) and striped supersolid (SSS) phases. We can characterize the SSS arising at $\phi_1 = \phi_2 = 0.1$ as follows: First, diagonalization reveals the existence of three degenerate ground states in the sectors: $k_2 = 0, k_1 = 0, 2\pi/3, 4\pi/3$. Consistent with striped ordering, the structure factor shows density stripes in the $\hat{g}_2$ direction (Fig. 18c). However, each of these stripes has incommensurate boson number, suggesting delocalization along the stripes. To wit, for $N_s = 24$, the 6 hardcore bosons are distributed evenly along two stripes, each containing 4 sites. Strong phase coherence along the stripes shows up in the sensitivity to twists in the $\hat{g}_2$ direction, while transverse twists produce essentially no dispersion, as shown in Fig. 18e,f.

Our proposal opens the door to a number of intriguing directions. In particular, the adiabatic preparation and detection of single-excitation states may provide an elegant approach to probing chiral dynamics, edge modes, and the Chern index [115–117]. More generally, dynamical preparation, manipulation and detection of many-body states in such driven topological systems remains an exciting open question [118]. Finally, the large

available parameter space holds the promise of more exotic phases, such as fractional Chern insulators [115]. Realizing such phases in an effective spin system may provide a deeper understanding of the stability of such states in the context of generalized long-range dipolar interactions.

3.2 Realizing Fractional Chern Insulators

In the previous section, we demonstrated that tilted dipoles can provide a versatile platform for realizing nearly flat bands and strongly correlated states. In this section, we show that such systems can be tuned to realize fractional Chern insulators - exotic phases, which arise when strongly interacting particles inhabit a flat topological bandstructure [24–31]. Particles injected into these exotic states of matter fractionalize into multiple independently propagating pieces, each of which carries a fraction of the original particle's quantum numbers. While similar effects underpin the fractional quantum Hall effect observed in continuum two dimensional electron gases [32, 33], fractional Chern insulators, by contrast, are lattice dominated. They have an extremely high density of correlated particles whose collective excitations can transform non-trivially under lattice symmetries [31, 119, 120].

In this section, we predict the existence of a fractional Chern insulator in dipolar interacting spin systems. This state exhibits fractionalization of the underlying spins into quasiparticle pairs with semionic statistics [121, 122]. The predicted FCI state may also be viewed as a gapped chiral spin liquid (CSL) [121, 123].

Several recent studies have conjectured the existence of fractionalized topological phases in idealized lattice models that require sensitively tuned long-range hopping and interactions [28–30, 90–92]. Broadly speaking, two single-particle microscopic ingredients are required. First, the dispersion of the lattice band-structure must be quenched relative to the energy scale of interactions [90–92]. Second, the flat band should possess a non-trivial Chern number, reflecting the underlying Berry phase accumulated by a particle

moving in the band-structure. To observe a fractionalized insulating state, one must partially fill the topological flat band-structure with interacting particles; since the FCI state generally competes with superfluid and crystalline orders, the resulting phase diagram naturally exhibits both conventional and topological phases (Fig. 19). Up to now, it has been unclear whether such exotic fractional Chern insulating phases can be realized in any real-world physical system.

We consider a two-dimensional array of tilted, driven, generalized spins interacting exclusively through their intrinsic dipolar interaction, as depicted in Fig. 19a. This interaction mediates the long-range hopping of spin-flip excitations. The quenching of the spin-flip band-structure owes to the anisotropy of the dipole-dipole interaction, which yields interference between different hopping directions [116]. The production of a synthetic background gauge potential is accomplished via spatially varying electromagnetic radiation [116, 124]. Together, the dipolar anisotropy and this radiation induce orientation-dependent Aharonov-Bohm phases that ultimately generate topologically nontrivial flat bands [116].

To be specific, we focus on an implementation using ultra-cold polar molecules trapped in a deep two-dimensional optical lattice. Such an implementation has many advantages, including local spatial addressing, stable long-lived spins, and strong intrinsic dipolar interactions [57, 67, 125, 126]. The molecules are subject to a static electric field $\vec{E}$ tilted with respect to the lattice plane (inset Fig. 19a). We assume that the molecular motion is pinned, and hence, restrict our attention to an effective rotational degree of freedom on each site, with associated Hamiltonian, $H_m = BJ^2 - d^z E$, where E is an applied electric field [65]. In particular, we focus on the four lowest rotational levels: $|0,0\rangle$, the rovibrational ground state and the three states within the $J = 1$ manifold ($|1,-1\rangle$, $|1,0\rangle$, $|1,1\rangle$), where J characterizes the rotational angular momentum of the molecules. Here, the quantization axis, $\hat{z}$, lies along the applied electric field and $|J,m\rangle$ denotes the state adiabatically connected (via $\vec{E}$) to the rotational eigenstates [99]. Each molecule is driven

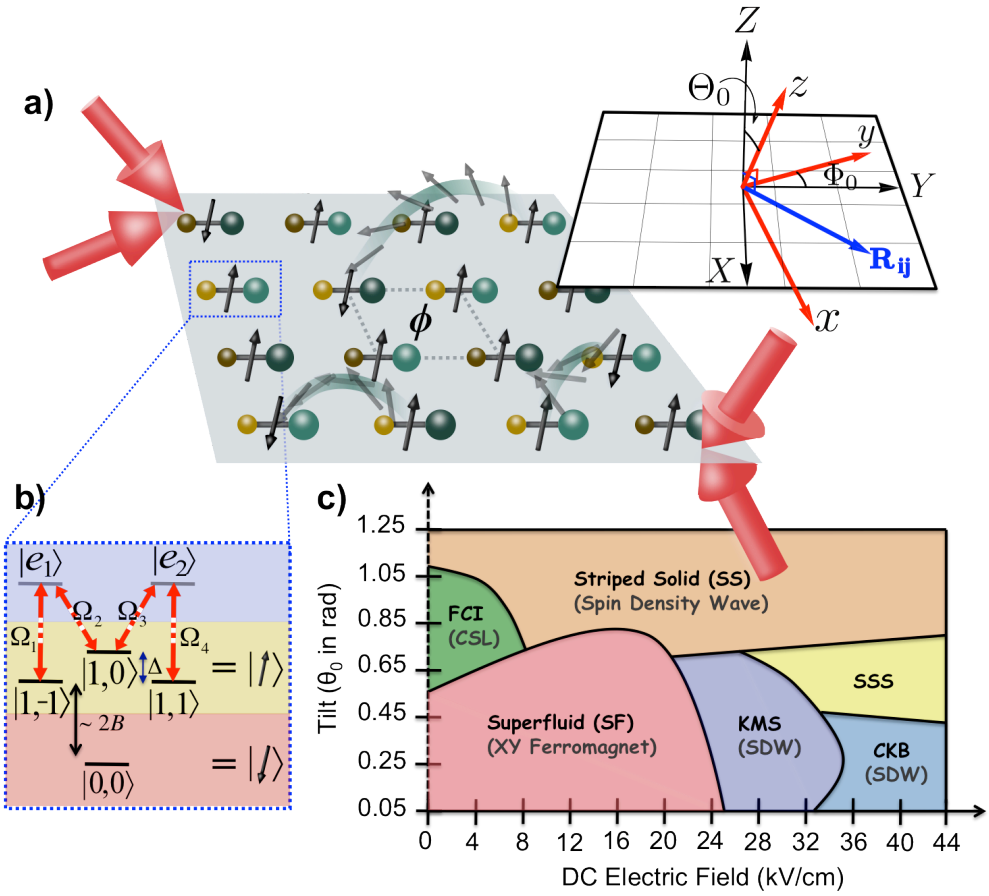

Figure 19: Realization of a fractional Chern insulator. (a) Schematic representation of the two-dimensional array of polar molecules dressed by optical beams (red arrows). Each polar molecules is characterized as an effective pseudo-spin-flip, which can hop and interact mediated by the long-range dipolar interaction; ϕ represents the Aharanov-Bohm phase which the spin-flip acquires as it traverses a plaquette. (inset) Molecules occupy the $\{X, Y\}$ plane and the rotational quantization axis is set by an applied electric field along the $\hat{z}$ direction. Θ_0 and Φ_0 define the $\{x, y, z\}$ axes with respect to the lattice coordinates $\{X, Y, Z\}$. (b) We consider the $J = 0, 1$ manifolds of each molecule with the $|0, 0\rangle$ state representing spin-down. The spin-up state is created via optical Raman dressing in the M-configuration. The optical radiation admits a single dark eigenstate, which is a linear combination of the three states in the $J = 1$ manifold. (c) Phase diagram for ^{40}K^{87}Rb molecules at half-filling with a total of $N_s = 24$ sites as a function of electric field strength and tilt Θ_0. Each phase finds a direct analogy in the language of frustrated magnetism and the equivalent nomenclature is given below. The knight's move solid (KMS), checkerboard (CKB) and striped supersolid (SSS) are named for the position of bosons in the structure factor. The dotted line at $|E| = 0$ signifies the fact that a minimal electric field is always required to split the degeneracy within the $J = 1$ manifold.

by optical radiation, which couples the three $J = 1$ states to a pair of molecular excited states $|e_1\rangle$ and $|e_2\rangle$, in the so-called M-scheme (Fig. 19b). The Hamiltonian for each molecule with the laser on has the form

$H_r = \hbar[\, |e_1\rangle(\Omega_1\langle 1,-1| + \Omega_2\langle 1,0|) + |e_2\rangle(\Omega_3\langle 1,0| + \Omega_4\langle 1,1|) + \text{h.c.}\,]$ in the rotating frame, where Ω_i are Rabi frequencies serving as the control parameters. The above Hamiltonian admits a unique "dark" eigenstate, $|\uparrow\rangle = \frac{1}{\tilde{\Omega}}(\Omega_2\Omega_4|1,-1\rangle - \Omega_1\Omega_4|1,0\rangle + \Omega_1\Omega_3|1,1\rangle)$, which is decoupled both from the excited states and from the radiation field ($\tilde{\Omega}$ is a normalization). Together with the rovibrational ground state, which we label as $|\downarrow\rangle$, this forms an effective two-state spin degree of freedom on each site [96–99, 116, 127].

Individual molecules interact with one another via electric dipole-dipole interactions,

$$H_{dd} = \frac{1}{2}\sum_{i\neq j}\frac{\kappa}{R_{ij}^3}\left[\mathbf{d}_i\cdot\mathbf{d}_j - 3(\mathbf{d}_i\cdot\hat{\mathbf{R}}_{ij})(\mathbf{d}_j\cdot\hat{\mathbf{R}}_{ij})\right], \tag{3.8}$$

where $\kappa = 1/(4\pi\epsilon_0)$ and $\mathbf{R}_{ij}$ connects molecules i and j. The dipole moment operator ($\mathbf{d}_i$ and $\mathbf{d}_j$) of each polar molecule couples its internal rotational levels and is directed along the internuclear axis. We let d be the permanent molecular dipole moment and R_0 be the nearest-neighbor lattice spacing; we note that d, although related, is not the effective dipole moment of our pseudospins. By ensuring that the characteristic dipolar interaction strength, $\kappa d^2/R_0^3$, is much weaker than the optical dressing, Ω_i, all molecules remain within the Hilbert space spanned by $\{|\uparrow\rangle, |\downarrow\rangle\}$. Moreover, this interaction is also much weaker than the bare rotational splitting $2B$ (Fig. 19b) and thus cannot cause transitions that change the total number of $|\uparrow\rangle$ excitations. This effective conservation law suggests the utility of recasting the system in terms of hardcore bosonic operators, $a_i^\dagger = |\uparrow\rangle\langle\downarrow|_i$, which create spin-flip "particles". Mediated by the dipolar interaction, these molecular spin-flips hop from site j to site i with amplitude $t_{ij} = -\langle\uparrow_i\downarrow_j| H_{dd} |\downarrow_i\uparrow_j\rangle$. As each hardcore boson harbors an electric-field induced dipole moment, there also exist long-range density-density interactions of strength

$V_{ij} = \langle\uparrow_i\uparrow_j| H_{dd} |\uparrow_i\uparrow_j\rangle + \langle\downarrow_i\downarrow_j| H_{dd} |\downarrow_i\downarrow_j\rangle - \langle\uparrow_i\downarrow_j| H_{dd} |\uparrow_i\downarrow_j\rangle - \langle\downarrow_i\uparrow_j| H_{dd} |\downarrow_i\uparrow_j\rangle$. In combination, this yields a two-dimensional model of hardcore lattice bosons,

$$H_B = -\sum_{ij} t_{ij} a_i^\dagger a_j + \frac{1}{2}\sum_{i\neq j} V_{ij} n_i n_j, \tag{3.9}$$

whose total number, $N = \sum_i a_i^\dagger a_i$, is conserved [116]. Variations in the dipolar-induced on-site potential, t_{ii}, can be regulated via tensor shifts from the optical lattice.

To ensure that our effective hardcore bosons reside in a topological flat band, we adjust the optical beams that dress the molecules to produce a square lattice with four types of sites, $\{a, b, A, B\}$, as shown in Fig. 20a. Owing to interference between the dressing lasers, the dark state on each of the sites is a different linear combination of the three $J = 1$ states, implying that the hardcore boson, $a_i^\dagger$, is site-dependent. Despite the existence of four unique lattice sites, so long as t_{ij} and V_{ij} remain invariant under translations by the direct lattice vectors $\vec{g_1}$ and $\vec{g_2}$ (Fig. 20a), the Hamiltonian retains a two-site unit cell. Thus, computing the single-particle band-structure produces two bands in momentum space, with the bottom band possessing nonzero Chern number, $C = -1$, as shown in Fig. 20b [116].

Numerical optimization of the electric-field and the optical dressing yields a variety of flat bands. The optimized band-structure depicted in Fig. 2b has a flatness ratio [90–92], $f \approx 11.5$, and is obtained at weak DC electric fields, just strong enough to split the degeneracy within the $J = 1$ manifold (relative to the dipolar interaction strength) and to set the quantization axis [67].

With topological flat bands in hand, we now consider the actual many-body phases which arise at finite lattice filling fractions ν (number of spin flips per unit cell). To this end, we perform exact diagonalization of the full many-body Hamiltonian at $\nu = 1/2$ on systems of varying sizes up to $N_s = 44$ sites with periodic boundary conditions. For weak electric fields tilted near the so-called magic angle, $\Theta_0 = \cos^{-1}(1/\sqrt{3})$ [128], diagonalization reveals the existence of a bosonic $\nu = 1/2$ fractional Chern insulator. As numerical diagnostics,

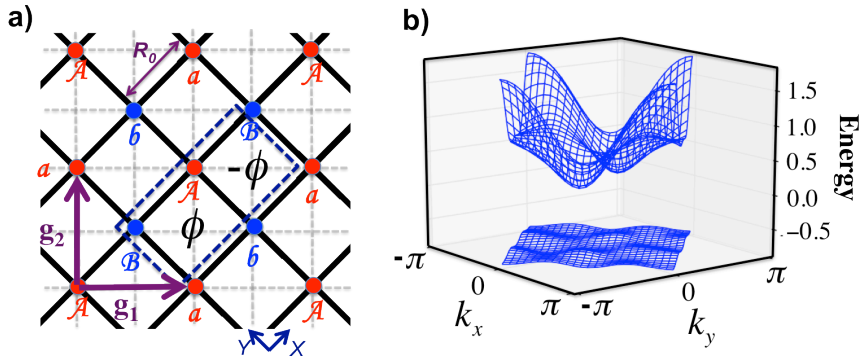

Figure 20: Topological Flat Bands. (a) Schematic representation of the 2D dipolar array. a, b, A and B sites are characterized by dark eigenstates that are different linear combinations of the three $J = 1$ states. Square plaquettes are characterized by a time-reversal breaking flux, ϕ, which is staggered throughout the lattice. The lattice harbors a two-site unit cell and is invariant under translation by direct lattice vectors $\vec{g_1}$ and $\vec{g_2}$. (b) An optimized band-structure in the reduced Brillouin zone (RBZ) depicting a flatness ratio $f \approx 11.5$. The lowest band carries Chern index $C = -1$. The electric field tilt is $\{\Theta_0, \Phi_0\} = \{0.68, 5.83\}$.

this topological state requires the presence of two-fold ground-state degeneracy on a torus (Fig. 21a) and a neutral spectral gap that is stable as the system size increases (Fig. 21b). The quantity analogous to the Hall conductance, $\sigma_{xy} = \frac{1}{2\pi}\int\int F(\theta_x, \theta_y) d\theta_x d\theta_y = -0.5$, appears unambiguously in the response of the system to boundary-condition twists $\{\theta_x, \theta_y\}$ (equivalent to flux insertion) in the form of a well-quantized many-body Berry curvature, $F(\theta_x, \theta_y) = \mathrm{Im}(\langle \frac{\partial \Psi}{\partial \theta_y} | \frac{\partial \Psi}{\partial \theta_x} \rangle - \langle \frac{\partial \Psi}{\partial \theta_x} | \frac{\partial \Psi}{\partial \theta_y} \rangle)$ [27, 28, 30].

The counting statistics of low energy quasihole states provide a direct diagnostic of the fractionalization of removed particles [27, 129]. Counting the total number of admissible quasihole arrangements on a torus (for a $\nu = 1/2$ FCI) yields, $Q_{torus} = \binom{N_{uc}+1-N_b}{N_{uc}+1-2N_b} - \binom{N_{uc}-1-N_b}{N_{uc}+1-2N_b}$, where $N_{uc} = N_s/2$ is the number of lattice unit cells and N_b is the number of hardcore bosons. As depicted in Fig. 21c for our system, numerically counting the total number of quasihole states matches the above formula precisely.

Remaining at $\nu = 1/2$, we now probe the many-body phases which arise as one varies the DC field strength and the tilt, Θ_0, while adjusting the optical parameters to keep the local dark states fixed. Changes in the tilt alter the geometry of the dipoles and introduce

Table 3.2.1: Diagnostics of Many-body Phases

Phase	Degeneracy	SF Response	Structure Factor	σ_{xy}
FCI	2	none	fluid	-0.5
SF	1	isotropic	fluid	gapless
SSS	3	uni-directional	stripes	gapless
KMS	4	none	knight's move	0
CKB	2	none	checkerboard	0
SS	4	none	stripes	0

additional dispersion into the single-particle bands. On the other hand, increasing the electric field strength enhances the long-range interactions. These qualitative differences in the microscopics yield a rich phase diagram exhibiting both conventional and topological phases, as shown in Fig. 19c. In addition to the FCI phase, there exist four distinct crystalline phases at strong DC fields and a large superfluid region at moderate fields (see Table 3.2.1 for diagnostics). While we use the language of lattice bosons above, we note that the FCI phase may also be interpreted in the language of frustrated magnetism as a chiral spin liquid while the competing superfluid and crystalline phases correspond to XY ordered magnetic and spin density wave (SDW) phases [121, 130].

3.2.1 Preparation and Detection

Next, we consider a possible route to preparing the $\nu = 1/2$ fractional Chern insulator. In current polar molecule experiments, the spin-flip "vacuum", corresponding to all sites in the $|\downarrow\rangle$ state, may be prepared with high fidelity from Feshbach molecules by two-photon stimulated Raman adiabatic passage [67–69]. If the phase boundaries surrounding the FCI state are second order, one might attempt to prepare this state by adiabatically tuning the electric field across the transition. However, the only known continuous transition between a superfluid and the $\nu = 1/2$ FCI phase is multicritical [131], which suggests that this phase boundary is generically first order, consistent with the numerics presented in the inset of Fig. 21d. On the other hand, continuous Mott insulator to FCI transitions are less

finely tuned and may constitute a promising avenue for preparation. In particular, the striped solid phase may be reduced to a simple non-translation-symmetry breaking Mott insulator in the presence of a one-dimensional superlattice potential. This observation is consistent with the existence of a weaker, finite-size, cross-over at the FCI to striped-solid phase boundary (inset Fig. 21d).

As probe light couples directly to the rotational motion of the dipoles, it is possible to measure the single spin-flip response of the system in order to detect and then characterize the FCI state. For example, the spectral function can be measured at finite energy and momentum using two-photon Bragg spectroscopy, providing direct information regarding fractionalization [132–134]. On the edge, one should observe gapless chiral Luttinger liquid behavior, while in the bulk, the response should exhibit a gap to the multi-quasiparticle continuum. Such a gap manifests as an effective "magnetization" plateau as shown in Fig. 21d [121].

3.2.2 Experimental Realization

Our proposal can be carried out in currently available ultracold polar molecules, such as ^{40}K^{87}Rb [57], ^{7}Li^{133}Cs [68], ^{41}K^{87}Rb [69] and ^{87}Rb^{133}Cs [70, 71]. The temperature scales associated with the FCI gap are set by the dipolar interaction strength. For a typical polar molecule with $d \sim 3$ Debye, the interaction at 532nm (optical lattice spacing) corresponds to $\sim 1\mu$K. With ground state molecules of both KRb and RbCs at temperatures of ~ 100nK, this suggests that current generation experiments can indeed realize stable FCI phases [67, 71, 135]. Moreover, it may be possible to work at significantly smaller optical lattice spacings (340nm for KRb and 395nm for RbCs), further enhancing the dipolar temperature scales [136].

Here, we focus on ^{40}K^{87}Rb. For the optically excited states $|e_1\rangle$ and $|e_2\rangle$, we propose the $|J', m'\rangle = |2, \pm 2\rangle$ rotational states of the $v' = 41$ vibrational level of the $(3)^1\Sigma^+$ electronic state. These states harbor a strong 640 nm transition to the ground state [67, 69]. We

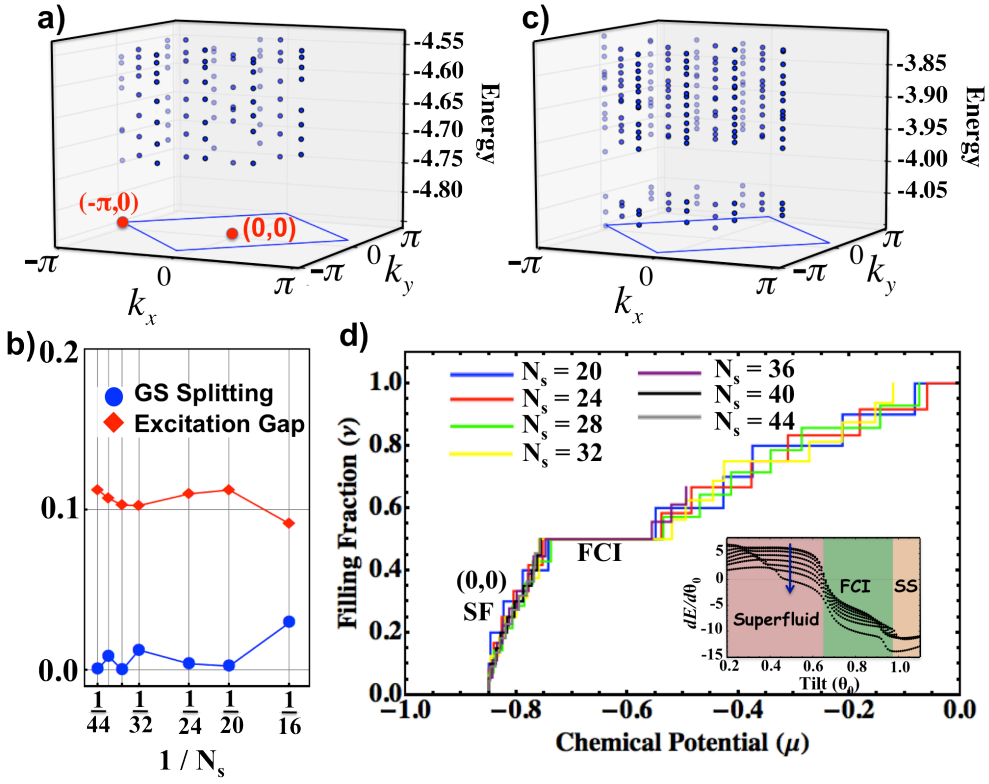

Figure 21: Evidence for $\nu = 1/2$ FCI state. (a) Exact diagonalization of the full Hamiltonian at $\nu = 1/2$ with a total of $N_s = 24$ sites and $N_b = 6$ hardcore bosons. The electric field and driving parameters are identical to those used in Fig. 2b. To avoid self-interaction, we truncate the dipolar terms at order $1/(3R_0)^3$. There exist two degenerate ground states in momentum sectors $(k_x, k_y) = (0, 0)$ and $(k_x, k_y) = (-\pi, 0)$ consistent with a $\nu = 1/2$ FCI state on a torus (k_x, k_y are crystal momenta). (b) Finite size scaling from $N_s = 16$ to $N_s = 44$ suggests a stable spectral gap in the thermodynamic limit. (c) Quasihole counting for the same parameters as in (a) with a single boson removed ($N_b = 5$). There exists a clear gap below which there are 36 low-energy quasihole states, consistent with the analytical counting formula for Q_{torus} [27]. (d) Filling fraction as a function of chemical potential, $\mu = E_{N_b+1} - E_{N_b}$ (where E_{N_b} is the ground state energy with N_b bosons). Below $\nu = 1/2$, there exists evidence of a clear compressible superfluid state, while at $\nu = 1/2$, there exists a plateau indicative of an incompressible quantum liquid. This plateau can also be interpreted as a magnetization plateau in the language of frustrated magnetism [121, 122]. (inset) Depicts $dE/d\Theta_0$ as a function of tilt Θ_0. Phase transitions between the superfluid, Chern insulator and striped solid are evidenced as jumps in $dE/d\Theta_0$; the plateaus are rounded owing to finite size effects and the kink in the superfluid region arises from a jump between a zero-momentum and finite-momentum SF ground state. Curves from top to bottom are for increasing electric field strength from $E = 0.4 - 8$ kV/cm.

require a hierarchy of energy scales corresponding to, $H_{lattice} \lesssim H_{hf} \ll \Omega_i \ll \Delta$ (Fig. 1b), where $H_{lattice}$ describes the optical lattice potential and H_{hf} characterizes the molecule's hyperfine structure [67]. For ^{40}K^{87}Rb, this hierarchy is easily realized since $H_{hf} \sim 1$ MHz, while $\Delta = 160$ MHz at a moderate DC field strength, $E = B/d \approx 0.5$kV/cm. By ensuring that the optical dressing (Ω_i) is weak relative to the splitting, $E_{1,0} - E_{1,1}$, we can employ frequency selection during the creation of the M-scheme; meanwhile, the condition $H_{lattice} \lesssim H_{hf} \ll \Omega_i$ allows us to consider hyperfine and tensor light-shift effects only after the dark state ($|\uparrow\rangle$) is already defined.

While we have focused our discussion on polar molecules, our proposal can, in fact, be realized in any system composed of electric or magnetic dipolar interacting generalized spins; such degrees of freedom are found in a diverse array of contexts ranging from magnetic atoms and Rydberg ensembles to solid-state spins [44, 101, 103]. In particular, for exchange coupled electronic spin dimers or hyperfine coupled nuclear and electronic spins, one finds an effective level-structure nearly identical to that depicted in Fig. 19b. The dipolar interaction between such coupled spins also yields topologically nontrivial, flat, spin-flip band-structures, enabling the potential realization of a solid-state Chern insulator.

Chapter 4

Yu-Shiba-Rusinov Bound States

4.1 Enhanced anti-ferromagnetic exchange from Yu-Shiba-Rusinov bound states

Understanding the interactions between magnetic impurities (localized spins) in a metallic host represents an important question at the interface of fundamental and applied science [34–36, 137, 138]. While spins always interact with one another via their intrinsic dipolar interaction, in a metal, their mutual interaction with conduction electrons can significantly enhance the effective interactions. For simple metals, this results in the so-called RKKY (Ruderman-Kittel-Kasuya-Yosida) interaction [34–36] — a coupling mechanism between magnetic moments in which one impurity partially polarizes the spin of conduction electrons; the second impurity then interacts with the spin density of the itinerant electrons, thereby inducing an effective long-range interaction. One of the crucial predictions of RKKY is the oscillatory sign of the exchange interaction, a feature which underlies giant magnetoresistance [139, 140].

More recently, significant effort has been devoted to understanding magnetic impurities on the surface of superconducting metals [138, 141–149]. This owes in part, to experimental advances in single adatom control, which have enabled the observation of locally modified

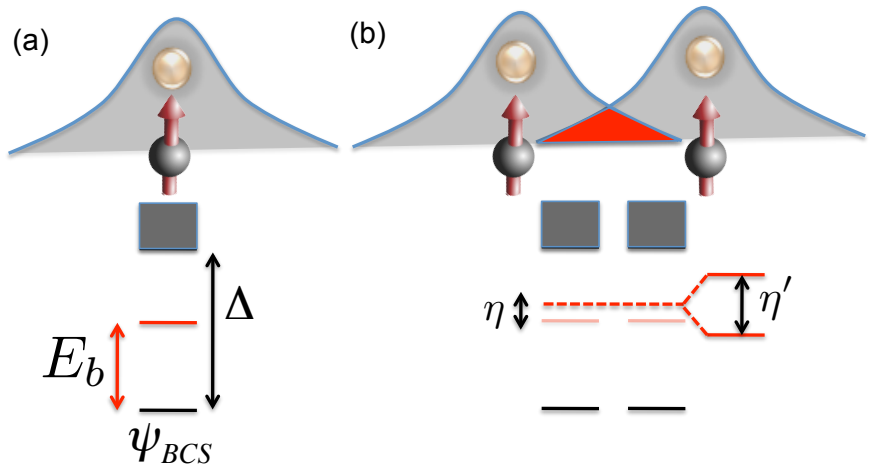

Figure 22: a) Schematic illustration of a magnetic impurity which binds a localized electronic YSR state. The associated spectrum is shown below, with the BCS ground state ψ_{BCS} separated from excited states by Δ. There exists a single mid-gap YSR state of energy E_b. b) When two impurities are separated by distances $r < \xi$, their YSR states overlap and hybridize. This hybridization causes both an overall energy shift η and a splitting η'.

electronic properties and raise the tantalizing prospect of atom-by-atom construction of magnetic nanostructures [150–152]. Moreover, interactions between such impurities may play a role in explaining low-frequency flux noise in Josephson circuits [153, 154]. The effect of superconductivity on RKKY interactions is well established at lowest-order perturbation theory (Born approximation) in the exchange interaction between the localized and itinerant spins. In particular, the suppressed spin susceptibility in the superconducting ground state modifies the inter-impurity interaction to become purely anti-ferromagnetic when the separation between the impurities exceeds the superconducting coherence length ($r \gtrsim \xi$); at such distances however, the strength of this antiferromagnetic exchange is exponentially small in the separation r. On the other hand, for impurities separated by distances $r < \xi$, conventional RKKY dominates the effective interaction and superconductivity yields only a weak antiferromagnetic correction [155–157]. Crucially, this perturbative treatment neglects the formation of so-called Yu-Shiba-Rusinov (YSR) bound states—localized electronic states that arise near a magnetic impurity.

In this section, we show that by tuning the energy of YSR states close to the middle of

the superconducting gap, one may substantially enhance the antiferromagnetic contribution stemming from the indirect spin exchange, allowing it to dominate over conventional RKKY even at distances $r \lesssim \xi$ [37–39]. When two magnetic impurities are brought near one another, their associated YSR states hybridize in a spin-dependent fashion, yielding an effective interaction. That one might expect such an interaction to dominate over RKKY results, in part, from the strong localization of the YSR state around the impurity, directly contrasting with the delocalized scattering states that mediate RKKY. This localization implies that quasiparticles bound to the YSR states are more strongly coupled to the impurity and therefore might be expected to mediate stronger exchange.

The key ideas underlying our derivation are illustrated in Fig. 71. We begin by considering a BCS superconductor with Hamiltonian,

$$H_0 = \sum_{\mathrm{k},\sigma} \epsilon_{\mathrm{k}} c^{\dagger}_{\mathrm{k},\sigma} c_{\mathrm{k},\sigma} + \Delta \sum_{\mathrm{k}} [c^{\dagger}_{\mathrm{k}\uparrow} c^{\dagger}_{-\mathrm{k}\downarrow} + c_{-\mathrm{k}\downarrow} c_{\mathrm{k}\uparrow}]. \tag{4.1}$$

The associated spectrum (Fig. 71) depicts the BCS ground state, ψ_{BCS}, separated from excited states by the superconducting gap Δ. In the presence of a spin impurity whose contact exchange interaction is of strength J, an excited-state electron can lower its energy below the superconducting gap by aligning its spin opposite the direction of the impurity. Treating the spin impurity classically yields the existence of a localized bound state (YSR state) of energy [37–39],

$$E_b = \Delta \frac{1 - (\pi J S N_0/2)^2}{1 + (\pi J S N_0/2)^2} = \Delta \frac{1 - \beta^2}{1 + \beta^2} \tag{4.2}$$

where N_0 is the normal state DOS at the Fermi energy. For pure exchange scattering, the YSR energy is conveniently re-expressed in terms of a phase shift $\tan(\delta) \equiv \beta = \pi J S N_0/2$, wherein $E_b = \Delta \cos(2\delta)$. The latter relation between E_b and δ is more general than Eq. (4.2), and valid beyond the approximation of a classical magnetic impurity [158–161]. Quantum fluctuations of the polarization of a magnetic impurity lead to the Kondo effect,

which renormalizes the exchange interaction between the impurity and itinerant electrons at low energies. The renormalized interaction is expressed in terms of the Kondo temperature, $T_K \propto \exp(-1/JN_0)$ [138]. At small Kondo temperatures, $T_K \lesssim \Delta$, the effective constant $\beta \approx 1/\ln(\Delta/T_K) \lesssim 1$. Thus, whether in the "classical" or "quantum" consideration, the YSR level can be tuned arbitrarily close to the middle of the gap by an appropriate increase of the exchange constant.

The characteristic wavefunction of the YSR state is localized around the magnetic impurity and takes the form, $\phi_{sh}(\mathrm{r}) \sim \frac{1}{\mathrm{r}} e^{-\mathrm{r}/\xi|\sin(2\delta)|}$ [138]. For two impurities separated by distances $r \gg \xi$, the overlap between their associated YSR states is exponentially suppressed. However, for distances $r < \xi$, the YSR states of the two impurities hybridize, causing both an overall energy shift η and a splitting η', as depicted in Fig. 1b. Crucially, the overall energy shift η depends on whether the impurity spins are aligned or anti-aligned; in particular, only in the anti-aligned case is it possible for a pair of YSR states to become virtually occupied by a Cooper pair from the superconducting condensate. This provides a natural intuition for our result: The effective spin-spin interaction manifests as a consequence of the spin-dependence in η.

With this intuition in mind, we now begin by considering the total energy associated with a pair of magnetic impurities (located at r_L and r_R) in a superconductor. We treat the impurities as classical spins parallel to the $\hat{z}$ axis (which defines the direction in which the impurities are either aligned or anti-aligned). The interaction Hamiltonian between the localized impurity and the itinerant electrons is then given by

$$H_{int} = J \sum_{\sigma} \int d\mathrm{r}\sigma [S_L f(\mathrm{r} - \mathrm{r}_L) c^{\dagger}_{\sigma}(\mathrm{r}) c_{\sigma}(\mathrm{r}) + S_R f(\mathrm{r} - \mathrm{r}_R) c^{\dagger}_{\sigma}(\mathrm{r}) c_{\sigma}(\mathrm{r})], \tag{4.3}$$

where $S_{L(R)}$ is the spin of the left (right) impurity and $f(\mathrm{r})$ characterizes the spatial form of the impurity potential. In momentum space,
$H_{int} = J \sum_{\sigma} \int d\mathrm{k} d\mathrm{k}' \sigma [S_L e^{i(\mathrm{k}-\mathrm{k}')r_L} \tilde{f}_{\mathrm{k},\mathrm{k}'} + S_R e^{i(\mathrm{k}-\mathrm{k}')r_R} \tilde{f}_{\mathrm{k},\mathrm{k}'}] c^{\dagger}_{\sigma,\mathrm{k}} c_{\sigma,\mathrm{k}'}$, where $\tilde{f}$ is the Fourier

transform of the potential. As is conventional [162], we now define a Nambu spinor, $\Psi_{\mathrm{k}} = (c_{\uparrow,\mathrm{k}}, c^{\dagger}_{\downarrow,-\mathrm{k}})$, wherein, $H_0 = \int d\mathrm{k}\Psi^{\dagger}_{\mathrm{k}}\left[\epsilon_{\mathrm{k}}\tau^z + \Delta\tau^x\right]\Psi_{\mathrm{k}}$ (τ are Pauli matrices acting in particle-hole space). Similarly, the interaction becomes,

$$H_{int} = J\int d\mathrm{k}d\mathrm{k}'\Psi^{\dagger}_{\mathrm{k}}[S_L e^{i(\mathrm{k}-\mathrm{k}')r_L}\tilde{f}_{\mathrm{k},\mathrm{k}'} + S_R e^{i(\mathrm{k}-\mathrm{k}')r_R}\tilde{f}_{\mathrm{k},\mathrm{k}'}]\Psi_{\mathrm{k}'} + E_0 \tag{4.4}$$

where $E_0 = -J\int d\mathrm{k}\tilde{f}_{\mathrm{k},\mathrm{k}}[S_L + S_R]$ arises from anti-commutation.

Combining the bare BCS Hamiltonian and the interactions yields, $H_T = H_0 + H_{int}$, which we diagonalize utilizing a Bogoliubov transformation, $d^{\dagger}_n = \int d\mathrm{k}(u_{n,\mathrm{k}}\psi^{\dagger}_{\uparrow,\mathrm{k}} + v_{n,\mathrm{k}}\psi^{\dagger}_{\downarrow,\mathrm{k}})$, yielding,

$$H_T = \sum_n \varepsilon_n d^{\dagger}_n d_n - \frac{1}{2}\sum_n \varepsilon_n = \sum_n \varepsilon_n(d^{\dagger}_n d_n - \frac{1}{2}). \tag{4.5}$$

The total energy of the ground state is thus given by

$$E_{tot} = -\frac{1}{2}\sum_n |\varepsilon_n| = E_V - \frac{1}{2}\int d\epsilon|\epsilon|\delta\rho(\epsilon) \tag{4.6}$$

where E_V characterizes the energy of the system in the absence of an impurity. Here, $\delta\rho(\epsilon)$ represents the change in the total density of states as a result of the impurities and includes contributions from both continuum electronic states above the gap well as the discrete YSR states. The effective exchange interaction, $I(\mathbf{r})$, between two impurities can be expressed in terms of changes to the DOS depending on whether the impurities are aligned or anti-aligned,

$$I(\mathbf{r}) = E^{\uparrow,\downarrow}_{tot} - E^{\uparrow,\uparrow}_{tot} = -\frac{1}{2}\int d\epsilon|\epsilon|\left[\delta\rho_{\uparrow,\downarrow}(\epsilon) - \delta\rho_{\uparrow,\uparrow}(\epsilon)\right]. \tag{4.7}$$

4.1.1 Shiba induced changes to the DOS

To calculate changes in the DOS, we compute $\delta\rho(\epsilon) = -\frac{1}{\pi}\mathrm{Im}\{\mathrm{Tr}[G_{\mathrm{k},\mathrm{k}'}(z) - G^{(0)}_{\mathrm{k}}(z)]\}$, where $z = \epsilon + i0^+$, $G^{(0)}_{\mathrm{k}}(z) = [z - (\epsilon_{\mathrm{k}}\tau^z + \Delta\tau^x)]^{-1}$ is the bare BCS Green's function, and $G_{\mathrm{k},\mathrm{k}'}(z)$

is the perturbed Green's function. Since translational invariance is broken by the magnetic impurities, the perturbed Green's function depends on two momenta, k and k'. Working within the T-matrix formalism [138],

$$G_{\mathrm{k,k'}}(z) = G^{(0)}_{\mathrm{k}}(z) + G^{(0)}_{\mathrm{k}}(z) T_{\mathrm{k,k'}} G^{(0)}_{\mathrm{k'}}(z), \tag{4.8}$$

where $T_{\mathrm{k,k'}}$ is the T-matrix. Applying a Dyson expansion to the T-matrix, one finds that

$$\begin{aligned} \delta\rho(\epsilon) &= -\frac{1}{\pi}\mathrm{Im}\{\mathrm{Tr}[G^{(0)}_{\mathrm{k}}(z) T_{\mathrm{k,k'}} G^{(0)}_{\mathrm{k'}}(z)]\} \\ &= -\frac{1}{\pi}\mathrm{Im}\{\mathrm{Tr}[JS\Pi(1-JSG)^{-1}]\} \end{aligned} \tag{4.9}$$

where Π, G and S are 4×4 matrices (in the tensor product space of particle-hole and left-right position) given by,

$$\Pi_{ll'}(z) = \int d\mathrm{k} G^{(0)}_{\mathrm{k}}(z) G^{(0)}_{\mathrm{k}}(z) e^{i\mathrm{k}(\mathrm{r}_l - \mathrm{r}_{l'})} \tag{4.10}$$

$$G_{ll'}(z) = \int d\mathrm{k} G^{(0)}_{\mathrm{k}}(z) e^{i\mathrm{k}(\mathrm{r}_l - \mathrm{r}_{l'})} \tag{4.11}$$

$$S_{ll'} = S_l \delta_{ll'} \otimes \tau^0. \tag{4.12}$$

Here, τ^0 represents the identity matrix in particle-hole space and l, l' run over $\{L, R\}$, indexing the left/right impurity.

We begin by considering the case of weakly bound YSR states ($J \ll 1$) and expand Eq. (4.9) to second order in the exchange coupling, $\mathrm{Tr}[JS\Pi(1-JSG)^{-1}] \approx \mathrm{Tr}[J^2 S\Pi SG]$. Evaluating this perturbative expression results in the following superconducting RKKY exchange between the magnetic impurities,

$$I(\mathrm{r}) = \frac{E_f \beta^2}{\pi (k_f r)^3} \cos(2k_f r) e^{-\frac{2r}{\xi}} F_1\left[\frac{2r}{\xi}\right] + \frac{\Delta\beta^2}{(k_f r)^2} \sin^2(k_f r) e^{-\frac{2r}{\xi}} F_2\left[\frac{2r}{\xi}\right]. \tag{4.13}$$

Here, k_f is the Fermi momentum, $r = |\mathrm{r}_L - \mathrm{r}_R|$ is the distance between the spins and

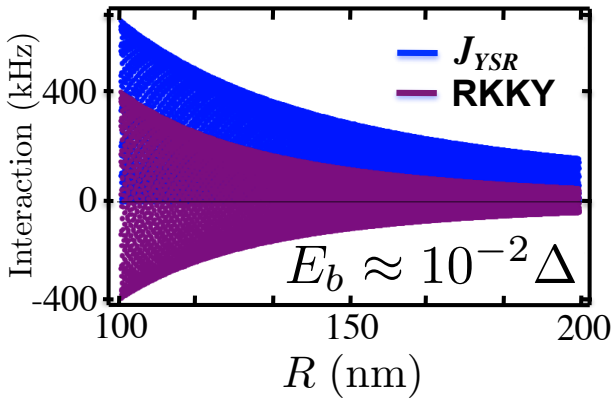

Figure 23: (color online) For concreteness, all plots are calculated using actual parameters for superconducting Aluminum, with $E_f = 11.7\text{eV}$, $k_f = 20.1\text{nm}^{-1}$, $N_0 = 35\text{eV/nm}^3$, and $\xi = 1.6\mu\text{m}$ [163]. Comparison between bare RKKY and the J_{YSR} for $E_b \sim 10^{-2}\Delta$. Resonant enhancement enables J_{YSR} to dominate at distances $r \ll \xi$.

$F_1[\alpha] = \alpha \int_0^\infty dx e^{-\alpha(\sqrt{x^2+1}-1)}$, $F_2[\alpha] = \frac{2}{\pi}\int_0^\infty dx \frac{e^{-\alpha(\sqrt{x^2+1}-1)}}{(x^2+1)}$ are dimensionless integrals. The first term represents the bare RKKY interaction, while the second represents the antiferromagnetic correction resulting from superconductivity. Although this second term scales as $1/r^2$, it is weaker by a factor of Δ/E_f and only dominates over bare RKKY at distances $r \gg E_f/(\Delta k_f) \sim \xi$, by which time the entire exchange integral $I(\text{r})$ is exponentially suppressed. The above perturbative result is consistent with previous calculations which utilize the Kubo formula to compute the exchange interaction from the magnetization response [155–157].

Returning to the interpretation of the exchange energy in terms of changes to the density of states [Eqs. (4.7,4.9)], we recall that the effective exchange contains two contributions, one from continuum electronic states and the other from discrete YSR states. One might expect that, being only weakly bound, the YSR states should induce a contribution which decays more slowly than $e^{-\frac{2r}{\xi}}$. However, we find that at $\mathcal{O}(J^2)$, the tail of the YSR contribution exactly cancels with a portion of the continuum contribution to yield the perturbative expression found in Eq. (4.13).

4.1.2 Beyond perturbation theory

Moving beyond the perturbative limit, as J increases, the energy of the YSR bound state decreases (approaching the middle of the superconducting gap) and the relative strength of the continuum and YSR contributions change. In particular, one might expect the YSR contribution to dominate for deeply bound states for two reasons: First, modifications to the bulk DOS will become weaker (since the bound state is further from the bottom of the band), and second, YSR hybridization with the superconducting condensate will become stronger as $E_b \to 0$. This second point suggests that the energy shift η has the potential to develop a singular contribution, arising from the $|\epsilon|$ in Eq. (4.6) near $\epsilon \approx 0$; thus, any singular contribution to the exchange interaction can only arise from the low energy YSR states.

To see these effects explicitly, we now compute the bound state energies as a function of impurity separation. This corresponds to a direct calculation of the discrete YSR contribution to Eq. (4.7). The YSR bound state energies can be computed from poles of $\mathrm{Tr}[G_{\mathrm{k,k'}}(z)]$. More explicitly, E_b is determined by

$$F(E_b) \equiv \mathrm{Det}[1 - SG(E_b)] = 0. \tag{4.14}$$

In the limit, $k_f r \gg 1$, one can consider the hybridization of the isolated YSR bound states to obtain perturbative corrections to the YSR energies. We derive an analytic approximation for solutions of Eq. (4.14) in the case of both parallel and anti-parallel impurities. By subtracting the bare YSR energy [Eq. (4.2)], this allows us to compute the spin-dependent total energy shift η. Our perturbative expansion is in the parameter η/E_b and remains valid so long as the energy shift is small relative to the bare YSR energy (see Eq. (4.16) and below for a discussion of validity).

We first consider the case of anti-parallel impurities where symmetry allows us to directly expand around the bare YSR energy, $F(E_b) + \eta_{\uparrow\downarrow} F'(E_b) = 0$. A straightforward

but tedious calculation then yields the leading term in $1-\beta$ as $\eta_{\uparrow\downarrow} = \Delta \frac{1}{1-\beta} \frac{\cos^2(k_f r)}{2(k_f r)^2} e^{-\frac{2r}{\xi}}$. In the case of parallel spins, the situation is slightly more complicated since one must extract the total shift by averaging the split energies (Fig. 71b). This requires expanding to third order, $F(E_b) + \eta_{\uparrow\uparrow} F'(E_b) + \frac{1}{2}\eta_{\uparrow\uparrow}^2 F''(E_b) + \frac{1}{6}\eta_{\uparrow\uparrow}^3 F'''(E_b) = 0$ and results in a non-singular shift, $\eta_{\uparrow\uparrow} = -\frac{\Delta}{2} \frac{\cos(k_f r)}{(k_f r)^2} e^{-\frac{2r}{\xi}}$, as $\beta \to 1$.

The YSR contribution to the exchange, $I(\mathbf{r})$, is given by $J_{YSR} = \eta_{\uparrow\downarrow} - \eta_{\uparrow\uparrow}$. Crucially, as the bound state energy approaches the middle of the superconducting gap ($E_b \to 0$, $\beta \to 1$), J_{YSR} is dominated by the singular contribution in $\eta_{\uparrow\downarrow}$ yielding,

$$J_{YSR} = \Delta \frac{1}{1-\beta} \frac{\cos^2(k_f r)}{2(k_f r)^2} e^{-\frac{2r}{\xi}}, \tag{4.15}$$

which exhibits a resonant enhancement of the form $\frac{1}{1-\beta}$. This resonant enhancement has an intuitive explanation. It arises from the hybridization of a pair of YSR states with the superconducting condensate; more specifically, when the impurities are anti-aligned, this hybridization occurs as a result of the conversion of a Cooper pair from the condensate into a pair of electrons in the YSR states. Heuristically, this coupling to the condensate takes the form $\Delta U(r) c_{L,\uparrow}^\dagger c_{R,\downarrow}^\dagger$, where $U(r) = \cos(k_f r)/(k_f r)$ characterizes the overlap between the bound states. While the ground state energy correction stemming from this coupling is generally suppressed by an energy denominator $2E_b$, as β approaches unity, E_b approaches zero, leading to the observed resonant enhancement.

The physical limit of the enhancement of this purely antiferromagnetic contribution is set by the condition that the YSR energies have not crossed zero, which in effect, would signify a parity changing transition. This condition also represents the regime of validity for J_{YSR} as derived from the expansion of Eq. (4.14). In combination with the constraint that J_{YSR} dominates over bare RKKY interactions, we obtain a double-sided inequality,

$$k_f r > \frac{1}{1-\beta} > \frac{\xi}{r}. \tag{4.16}$$

By stark contrast to the perturbative limit, where the superconducting correction dominates only at distances $r \gg \xi$, here, we find that the anti-ferromagnetic J_{YSR} exchange can prevail at $r \sim \sqrt{\lambda_f \xi} \ll \xi$ and reaches a maximum ($\sim \Delta/\sqrt{k_f \xi}$) at such distances.

4.1.3 Discussion of Shiba interaction

Inspection reveals that the YSR-induced interaction strength, $J_{YSR} = \eta_{\uparrow\downarrow} - \eta_{\uparrow\uparrow}$ scales as $\sim \frac{1}{r^2}$, exhibiting a weaker decay than conventional metallic RKKY interactions. We note that this power-law is in agreement with the perturbative superconducting correction in Eq. (4.13); as expected, for small β, our full non-pertubative calculation matches the perturbative results. In comparison to bare RKKY interactions, one important qualitative observation is that, while oscillatory in nature, J_{YSR} does not vary between ferromagnetic and antiferromagnetic couplings. The antiferromagnetic nature of the superconducting YSR correction results from the fact that coupling to the condensate occur most effectively for anti-aligned impurities.

For small impurity separation and weakly bound YSR states, the magnitude of the RKKY interaction dominates over J_{YSR}. However, as illustrated in Fig. 23, for bound state energies close to the middle of the gap, resonant enhancement enables $J_{YSR} > J_{RKKY}$ at distances well below the coherence length; the dominance of this anti-ferromagnetic exchange is further highlighted by the weaker power-law decay as a function of r. This effect will be especially pronounced for superconductors with relatively large coherence lengths.

To observe/utilize the resonant enhancement of J_{YSR} requires a system where the coupling strength between the impurity spin and the superconductor can be tuned continuously. In principle, any low-density system with a tunable DOS can provide a natural mechanism for controlling the exchange constant via a gate voltage. An example of such a scenario is found in graphene [164], where the exchange coupling of magnetic defects can be altered by simply changing the carrier density. In combination with demonstrations

of proximity-induced superconductivity [165], this suggests that graphene in contact with a superconductor may represent a promising system with which to realize tunable-energy YSR states. Such a system naturally possesses a large coherence length since the Fermi velocity remains substantial even at low carrier densities. Interestingly, it may also be possible to further enhance the effects of an applied gate voltage by separating the graphene from the superconductor via a layer of semiconductor such as MoS_2 [166, 167].

In summary, working beyond the Born approximation, we have derived an enhanced anti-ferromagnetic exchange between magnetic impurities on the surface of a superconductor. This interaction is intimately related to the existence of a single mid-gap bound Yu-Shiba-Rusinov (YSR) state near a magnetic impurity; indeed, it is the hybridization of these YSR states, which induces a long range antiferromagnetic interaction between spin impurities. Although our results are formulated within the treatment of classical spins, such a description is consistent for high-spin magnetic ions such as those currently used in experiments (e.g. Gd, Mn, Cr) [150, 151]. In the next section, we perform a renormalization group (NRG) study on the two-impurity Shiba molecule problem. We account for quantum fluctuations and shed light on the interplay between Kondo singlet formation and YSR-induced spin-spin interactions.

4.2 Phase Diagram and Excitations of a Shiba Molecule

In an ordinary metal, the celebrated Kondo effect describes the scattering of conduction electrons due to magnetic impurities. Below the so-called Kondo temperature (T_K), the magnetic moment of a single impurity becomes screened by the electrons [168], leading to its dissolution and hence, the formation of a Fermi liquid state [169]. This simple picture can fail when one considers a finite density of impurities. In particular, conduction-electrons mediate RKKY exchange interactions, I, between the impurities and in the limit, $I \gtrsim T_K$, such interactions can lead to the emergence of either magnetically ordered or spin glass states [170, 171]. Much of our understanding of this phase transition

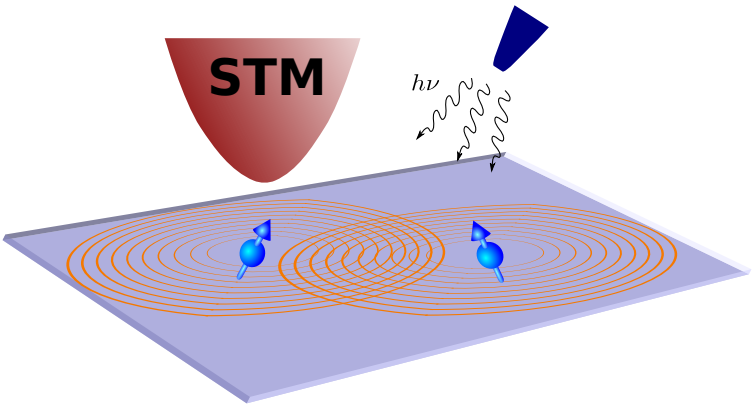

Figure 24: Two magnetic impurities placed on a superconducting surface. RF fields can be used to produce transitions between various molecular states and manipulate them.

owes to detailed studies of the two-impurity Kondo model [172, 173].

Extending the two-impurity calculations to the case of a superconducting host represents an interesting and active challenge [138, 141–149]. On the one hand, the interplay of superconductivity and magnetic moments can lead to the emergence of exotic phases and excitations. Recent results have suggested the possibility of emergent Majorana edge modes at the ends of a magnetic impurity chain situated on the surface of an s-wave superconductor; in this system, topological superconductivity arises from the formation of a spin-helix as a result of the underlying RKKY interaction [34–36]. On the other hand, the presence of magnetic impurities breaks time-reversal symmetry and gradually leads to the destruction of superconductivity. This breakdown occurs through the appearance of proliferating mid-gap states (so-called Shiba states), as first observed by Yu, Shiba and Rusinov [37–39]. In particular, within a simple classical calculation, they demonstrated that a magnetic impurity can bind an anti-aligned quasiparticle, yielding a sub-gap bound state of energy $\epsilon = \Delta - E_b$, where Δ represents the superconducting gap and E_b the binding energy [150, 151]. As the binding energy E_b increases (e.g. as a function of increasing exchange coupling), the bound state energy eventually crosses zero, signifying a parity-changing phase transition.

With certain modifications, this classical picture remains qualitatively valid even for

quantum mechanical spins [138, 174–178]. Taking into account quantum fluctuations, the aforementioned parity-changing transition occurs at a critical point, $(\Delta/T_K)_c$, when the superconducting gap becomes comparable to the Kondo temperature. [168]. For an $S = 1/2$ impurity, the spin is essentially free for $\Delta/T_K > (\Delta/T_K)_c$ and the associated mid-gap Shiba state remains unoccupied. In this 'free spin' regime, the ground state has spin $S_G = 1/2$. In the opposite limit, when $\Delta/T_K < (\Delta/T_K)_c$, the impurity spin becomes screened by a bound quasiparticle; more specifically, the mid-gap Shiba state becomes occupied and this quasiparticle spin forms a singlet with the impurity spin, leading to an $S_G = 0$ ground state. This phase transition has recently been observed in mesoscopic circuits, where the strength of the exchange interaction can be tuned by means of a pinch-off gate electrode [179].

In this section, through a combination of numerical renormalization group methods and semi-classical analytics, we derive the phase diagram of the two-impurity Kondo model for a superconducting host [1]. We consider an s-wave superconductor with Hamiltonian,

$$H_{\rm BCS} = \int \frac{d\mathbf{k}}{(2\pi)^3} \Big[\sum_\sigma \xi_{\mathbf{k}} c^\dagger_{\mathbf{k}\sigma} c_{\mathbf{k}\sigma} + \left(\Delta c^\dagger_{\mathbf{k}\uparrow} c^\dagger_{-\mathbf{k}\downarrow} + h.c. \right) \Big]$$

coupled, via exchange, to two identical spin 1/2 magnetic impurities of spin $\mathbf{S}_1$ and $\mathbf{S}_2$,

$$H_{\rm int} = \frac{J}{2}\, \mathbf{S}_1 \psi_1^\dagger \boldsymbol{\sigma}\, \psi_1 + \frac{J}{2}\, \mathbf{S}_2 \psi_2^\dagger \boldsymbol{\sigma}\, \psi_2 \,. \tag{4.17}$$

Here, ψ_1 and ψ_2 are the field operators at the impurity positions. We note that this Hamiltonian captures the essential physics of two experimental systems: (1) magnetic impurities placed on a superconducting surface (see Fig. 24) [150–152] and (2) double dot devices attached to superconductors (e.g. as recently used for Cooper pair splitting) [180, 181]. To study the ground state and excitation spectrum of $H_T = H_{\rm BCS} + H_{\rm int}$, we

[1] Some results in the limit of $\Delta \ll T_K$ are obtained in [178] and agree with the relevant cuts of our phase diagram

map the problem to a double superconducting chain, and analyze it via Wilson's numerical renormalization group (NRG) method [172].

4.2.1 Conserved currents for Shiba molecules

We observe that H_T conserves both parity, P, and total spin, S. In a superconductor, the pairing terms imply that charge is typically only conserved modulo 2. However, for $\Delta = 0$ and in the presence of particle-hole symmetry, the Wilson chain possesses a hidden $SU_c(2)$ charge symmetry [172] analogous to that of the Hubbard model [182]. For a half-filled cubic lattice, this charge symmetry is generated by the operators, $Q_x = (Q^+ + Q^-)/2$, $Q_y = (Q^+ - Q^-)/2i$, $Q^z = \frac{1}{2}\sum_\sigma \int \frac{d\mathbf{k}}{(2\pi)^3}(c^\dagger_{\mathbf{k}\sigma}c_{\mathbf{k}\sigma} - \frac{1}{2})$, where $Q^+ = \int \frac{d\mathbf{k}}{(2\pi)^3} c^\dagger_{\mathbf{k}\uparrow}c^\dagger_{\pi-\mathbf{k}\downarrow}$ and $Q^- = \left(Q^+\right)^\dagger$ [2]. Although this symmetry is strictly broken for $\Delta \neq 0$, a hidden $U_c(1)$ symmetry remains, leading to a conserved pseudo-charge, $\tilde{Q}$. Physically, this pseudo-charge can be viewed as the generator of rotations along the superconducting order parameter. For the remainder of the text, we will utilize these three quantum numbers (P, S and $\tilde{Q}$) to classify the eigenstates of the Hamiltonian.

Our NRG calculations reveal the existence of five competing subgap Shiba-molecule states, as depicted in Table 4.2.1. For large values of Δ, both of the impurity spins are essentially free. They can form a singlet state (S_0) with spin $S = 0$, parity $P = -$, and pseudocharge $\tilde{Q} = 0$, or a a triplet state (T_0) with $S = 1$, $P = +$, and $\tilde{Q} = 0$. Similar to the single impurity case, one can also create a single (antiferromagnetically) bound quasiparticle. However, in the Shiba molecule case, this quasiparticle is delocalized between the two impurities and can form either a bonding (D_+) or antibonding state (D_-) of spin $S = 1/2$, parity $P = \pm$, and pseudo-charge $\tilde{Q} = 1$. Finally, it is also possible to induce the binding of two quasiparticles, one to each of the impurities. In this case, one finds a singlet state (S_2) with pseudocharge $\tilde{Q} = 2$. The parity of this state is, rather counterintuitively, $P = -$, owing to the fermionic nature of the bound quasiparticles.

[2] Here π denotes the corner of the Brillouin zone.

State		$(S, \tilde{Q}, P)$
S_0		$(0, 0, -)$
T_0		$(1, 0, +)$
$D_\pm$		$(\frac{1}{2}, 1, \pm)$
S_2		$(0, 2, -)$

Table 4.2.1: Shiba molecular bound states and their quantum numbers. Small spins represent quasiparticles bound to the (large) impurity spins.

4.2.2 Shiba molecule phase diagram

The competition between these five states leads to a rich Shiba molecule phase diagram. A heuristic understanding of this diagram can be gained by comparing the relative strengths of superconductivity, exchange, and Kondo screening. In analogy to the single impurity case, the ratio Δ/T_K characterizes the competition between superconductivity and Kondo screening. For $\Delta/T_K \gg 1$, Kondo screening is heavily suppressed and the magnetic moments remain unscreened. The two impurities do however couple to each other via the Fermi sea of conduction electrons. For processes involving quasiparticle excitations close to the Fermi energy, this coupling is characterized by the overlap $\mathcal{S}$ of the two waves created at the impurity locations. For a three dimensional free electron system, $\mathcal{S} = \frac{\sin(k_F R)}{k_F R}$, where $R = |\mathbf{R}_1 - \mathbf{R}_2|$ is the separation between the impurities and k_F the Fermi momentum. This overlap $\mathcal{S}$ is also responsible for the hybridization of the Shiba states at sites 1 and 2, and thus for the splitting between the bonding and antibonding states ($D_\pm$).

The impurity spins also interact via RKKY exchange I, which depends on high-energy electron-hole excitations; thus, the coupling I ought be considered as an independent parameter, determined by the precise band shape and the energy dependence of the exchange coupling, J. The competition between RKKY and Kondo screening is characterized by the ratio, I/T_K [3]. The phase diagram obtained via NRG is shown in

[3] In the NRG scheme, a direct interaction between the impurities must also be introduced [172].

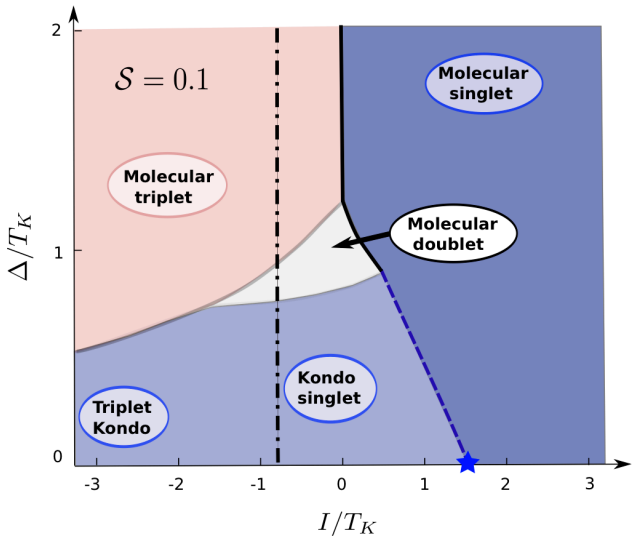

Figure 25: NRG-determined phase diagram for $\mathcal{S} = 0.1$ as function of I/T_K and Δ/T_K. The background colors indicate regions with $S = 1$ (light maroon), $S = 1/2$ (white) and $S = 0$ (blue) ground states. The blue dashed line separates the regions with S_2 (light blue) and S_0 (dark blue) ground states.

Fig. 25. We identify four distinct regions, each corresponding one of the states in Table 4.2.1: (1) For large values of Δ/T_K, the impurities are free and the ground state is a molecular triplet (T_0) for $I < 0$ and a molecular singlet (S_0) for $I > 0$. As expected, this molecular singlet phase is also observed for $I \gg T_K, \Delta$ and extends down to the $\Delta = 0$ axis. (2) In the Kondo singlet region (S_2), $|I|, \Delta \ll T_K$, one recovers strong Kondo correlations, wherein the two impurity spins are basically individually screened by quasiparticles. For perfect electron-hole symmetry this region is separated from (1) by a first order phase transition (blue dashed line in Fig. 25), corresponding to both a pseudo-charge jump from $\tilde{Q} = 0$ to $\tilde{Q} = 2$ as well as a $S_0 \to S_2$ singlet-singlet level crossing. When electron-hole symmetry is broken, the transition becomes a smooth cross-over. (3) Along the $\Delta = 0$ line, the known phase diagram of the two impurity (normal metal) Kondo model is recovered [171]. Here, a quantum critical point (blue star) separates the molecular singlet from the Kondo singlet region. For any finite Δ, the spectrum is gapped, and this critical point turns into the aforementioned first order transition line.

The nature of the Kondo singlet phase at $\Delta = 0$ gradually changes as one moves toward

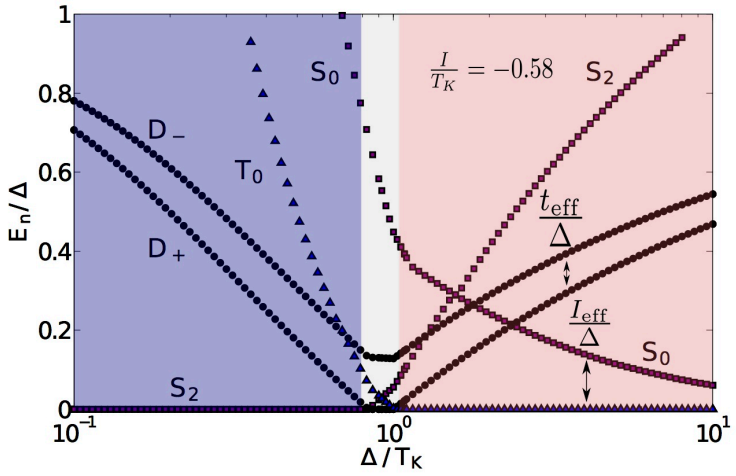

Figure 26: Evolution of the bound states as function of Δ/T_K for RKKY couplings $I/T_K = -0.58$ and an overlap parameter $\mathcal{S} = 0.1$ and corresponds to the black dashed line in Fig. 2. One observes a phase transition from the individual singlet state (S_2) into the molecular doublet phase (D_+) and then another transition to the molecular triplet phase (T_0). The effective RKKY interaction can be extracted as the splitting between the S_0 and T_0 states: $I_{\rm eff} = E_{S_0} - E_{T_0}$.

large, negative exchange interactions. In particular, for $-I \gg T_K$, the two impurity spins are first bound into a molecular triplet, which is then screened in the even and odd channels at (typically) two different Kondo temperatures. This picture survives for small but finite Δ, although strictly speaking, there is no true Kondo effect for any finite gap; nevertheless, one can still screen the impurity spins for $\Delta \ll T_K$ and a Kondo anomaly is generally observed in the tunneling spectra at intermediate energies, $\Delta \ll \omega \ll T_K$.

(4) Finally, and most strikingly, for $\mathcal{S} \neq 0$ a new $S = 1/2$ phase emerges for $\Delta \sim T_K$ and $I \approx 0$. We term this phase the molecular doublet (D_+). It can be understood as follows: For $\Delta \gg T_K$ each of the two spins can bind a single excited quasiparticle. For $\mathcal{S} = 0$ the energy of these bound states are identical; however, for $\mathcal{S} \neq 0$ these states can hybridize to form molecular bonding and antibonding states $D_\pm$. As one decreases the ratio Δ/T_K, the energy of the $D_\pm$ states moves towards zero until D_+ first crosses (zero) and becomes the ground state. This transition is accompanied by a charge-parity flip and a spin transition from $S = 1 \to 1/2$. Further decreasing Δ/T_K lowers the energy of the

two-bound-quasiparticle state until a second charge parity transition to the S_2 singlet occurs. These level crossings and the evolution of the excitation spectrum along the vertical dash-dotted line in Fig. 25 is shown in Fig. 26.

The existence of this novel molecular doublet phase can also be probed and confirmed in a semi-classical calculation where one extends the original Yu-Shiba-Rusinov calculation to the case of two classical magnetic impurities. Each magnetic impurity binds a Shiba state with wavefunction $\phi_{\rm sh}(\mathrm{r}) \sim \frac{1}{\mathrm{r}} e^{-\mathrm{r}/\zeta|\sin(2\delta)|}$ and energy $E_{\rm sh} = \Delta\frac{1-\beta^2}{1+\beta^2}$, where ζ is the coherence length, $\beta \equiv \tan(\delta) = JSN_0\pi/2$ and N_0 is the density of states at the Fermi energy.

Utilizing a two-impurity Green's function calculation [183, 184], we compute the energies of the hybridized Shiba bound states as poles of the T-matrix. Picking two values of $k_F R$ (corresponding to ferromagnetic and anti-ferromagnetic exchange) we plot the bound-state energies as a function of β (Fig. 27). In each case, hybridization causes a single bound state to first cross $E_{\rm sh} = 0$ leading to the formation of the molecular doublet phase. The second bound-state crossing then yields the transition to either the triplet Kondo phase ($I < 0$) or the Kondo singlet phase ($I > 0$).

4.2.3 Tunneling RF Spectroscopy

The most direct observation of the various molecular Shiba states can be achieved by combining RF spectroscopy with transport measurements. To this end, we determine the tunneling spectrum of the Shiba molecule by computing the spectral density of the so-called composite fermion, $F_1 \equiv \mathbf{S}_1 \cdot \boldsymbol{\sigma}\psi_1$. In the molecular triplet phase (T_0) both D_+ and D_- are visible in the tunneling spectrum and, correspondingly, a double mid-gap STM resonance is predicted (see Fig. 28). The dominant obstacle to observing such a resonance arises from thermal broadening; indeed, measurements of Mn and Gd impurities [4] on a single-crystal lead superconductor at ~ 4K are unable to resolve individual Shiba

[4] Both Mn and Gd are high spin magnetic impurities. Adding in such effects (e.g. of single-ion anisotropy) is an interesting direction [178]

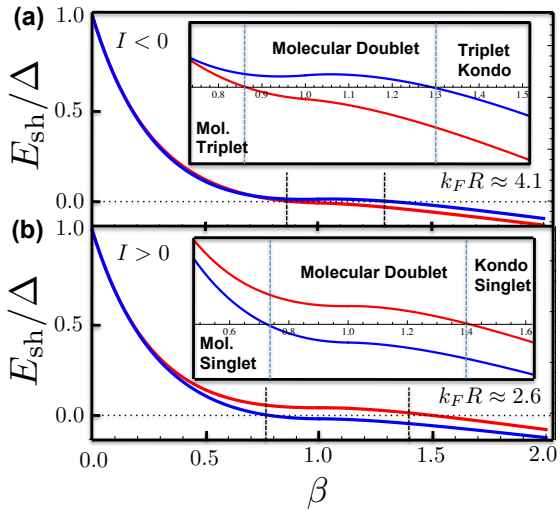

Figure 27: Semi-classical molecular doublet phase transitions. (a) For $k_F R \approx 4.1$, the RKKY exchange is negative and the bound state energies are shown as one increases $\beta = JNS\pi/2$. At $\beta \approx 0.86$, the first bound state crosses zero and a charge-parity transition from the molecular triplet phase to the doublet phase occurs. At $\beta \approx 1.3$, the second bound state crossing leads to the triplet Kondo phase. (b) Analogous semi-classical results for $k_F R \approx 2.6$ where the exchange is positive.

resonances [150]. However, operating at slightly lower temperatures (~ 500mK) should reduce the linewidth to ≈ 0.14meV, significantly smaller than the superconducting gap, $\Delta_{\rm Pb} = 1.55$meV. Such estimates are consistent with recent results which utilize a superconducting Niobium tip to explicitly resolve multiple Shiba scattering channels [151, 185]. Much lower temperatures in the range of $T \sim 20\,$mK can be attained in mesoscopic circuits, where multiple Shiba states have indeed been resolved recently [181].

Applying an additional RF field with a frequency matched to the $T_0 \to S_0$ transition ($\Delta E = h\nu$) allows one to populate the S_0 state [5]. In this case, the $S_0 \to D_\pm$ transitions also become active and visible (Fig. 5), while the tunneling gap shifts from $\Delta \to \Delta - \Delta E$. In this way, one can detect the excited state S_0 and its energy by investigating the RF-radiation-induced transport signal.

The transitions between the various phases and the corresponding STM spectra should also be observable in double-dot spin-splitter devices. In particular, the tunneling $\mathrm{d}I/\mathrm{d}V$

[5] Parity must be broken to induce a $S_0 \to T_0$ transition, e.g. by an inhomogeneous magnetic field

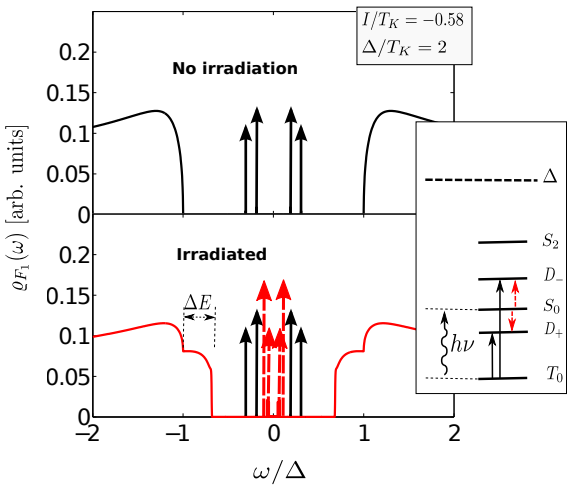

Figure 28: STM spectrum of one atom of the Shiba molecule in the molecular triplet (T_0) phase. The D_+ and the D_- states can both be observed as subgap Shiba transition lines (see top). Upon irradiation with a frequency matching the $T_0 \rightarrow S_0$ transition $h\nu = \Delta E$ (right panel), two additional subgap lines appear, and the gap shifts to lower values (bottom).

spectra can be accessed by observing the transport with normal electrodes attached. Similar to the case of a simple magnetic impurity, by approaching the phase boundaries between (D_+, S_2) or (D_+, T_0), a single midgap excitation should get 'soft' and cross zero. Interestingly, the strength of the corresponding tunneling resonance displays a universal jump at these transitions, $2 \rightarrow 1$ and $3 \rightarrow 2$, respectively; this robust jump owes to a change in ground state degeneracy [179].

As a possible application, one can consider using the singlet states S_2 and S_0 as a quantum bit. These states are protected by the superconducting gap and, being singlets, they are insensitive to magnetic noise (including the hyperfine field of nearby nuclear moments). To have a direct transition between these states, both parity and particle-hole symmetry must be broken sufficiently strongly; this can be achieved by placing a single potential scatterer near one of the magnetic impurities, as may be possible in STM-type experiments [150, 151, 185].

Chapter 5

Robust quantum wires in spin ensembles

5.1 Quantum state transfer in a thermal spin chain

This chapter moves into the portion of the thesis which focuses more on quantum information science. While still drawing from techniques and ideas in both condensed matter and AMO physics, this chapter deals specifically with quantum state transfer. In addition to diverse applications ranging from quantum key distribution to quantum teleportation [186, 187], reliable quantum state transfer between distant qubits forms an essential ingredient of any scalable quantum information processor [188]. However, most direct qubit interactions are short-range and the corresponding interaction strength decays rapidly with physical separation. For this reason, most of the feasible approaches that have been proposed for quantum computation rely upon the use of quantum channels which serve to connect remote qubits; such channels include: electrons in semiconductors [189], optical photons [41, 190–192], and the physical transport of trapped ions [193]. Coupled quantum spin chains have also been extensively studied [194–208]. A key advantage of such spin chain quantum channels is the ability to manipulate, transfer, and process quantum information utilizing the same fundamental hardware [209]; indeed, both quantum memory and quantum state transfer can be achieved in coupled spin chain arrays [210], eliminating

the requirement for an external interface between the quantum channel and the quantum register. Prior work on spin chain quantum channels has focused on three distinct regimes, in which the spin chain is either initialized [194, 201, 203, 204, 208], engineered [196, 211, 212] or dynamically controlled [198, 213–216].

An important application of spin-chain mediated coherent coupling is in the context of realizing a room temperature quantum information processor based upon localized spins in the solid-state [217]. In this case, it is difficult to envision mechanical qubit transport, while other coupling mechanisms are often not available or impose additional prohibitive requirements such as cryogenic cooling [192]. At the same time, long spin chains are generally difficult to polarize, impossible to control with single-spin resolution, and suffer from imperfect spin-positioning [205, 206]; such imperfections can cause both on-site and coupling disorder, resulting in localization [218]. For these reasons, a detailed understanding of quantum coherence and state transfer in random spin chains with a limited degree of external control is of both fundamental and practical importance.

In this section, we propose and analyze a novel method for quantum state transfer (QST) in an unpolarized, infinite temperature spin chain. In contrast to prior work, the method requires neither external modulation of the Hamiltonian evolution nor spin chain engineering and initialization. Furthermore, it is robust to specific, practically important types of disorder. The key idea of our approach is illustrated in Fig. 29(a). The two spin qubits at the ends of the spin chain can be initialized and fully controlled, while the coupling between these remote qubits is mediated by a set of intermediate spins, which can not be initialized, individually controlled, or optically detected. We assume that the qubit-chain coupling g, which can be variably adjusted, and the intrachain coupling κ, which is fixed, are characterized by short-range XX interactions. The essence of the state transfer is the long-range coherent interaction between the spin qubits, mediated by a specific collective eigenmode of the intermediate spin chain. This mode is best understood via Jordan-Wigner (JW) fermionization, which allows for the states of an XX spin chain to

be mapped into the states of a set of non-interacting spinless fermions. In this representation, the state transfer is achieved by free fermion tunneling, as shown in Fig. 29(b). In what follows, we show that the initial state of the intermediate chain does not affect the tunneling rate associated with free fermion state transfer (FFST), allowing for the implementation of a SWAP operation between the end qubits after a period of unitary evolution.

5.1.1 Thermal State Transfer

To be specific, we consider an XX Hamiltonian governing two distant qubits connected by a quantum channel consisting of a spin-1/2 chain

$$H = H_0 + H' \tag{5.1}$$

with $H_0 = \sum_{i=1}^{N-1} \kappa(S_i^+ S_{i+1}^- + S_i^- S_{i+1}^+)$ and $H' = g(S_0^+ S_1^- + S_{N+1}^+ S_N^- + \text{ h.c.})$, as shown in Fig. 29(a). Here, $S^{\pm} = S^x \pm iS^y$, where $\vec{S} = \vec{\sigma}/2$ and $\vec{\sigma}$ are Pauli spin operators ($\hbar = 1$). We consider the limit $g \ll \kappa$, and work perturbatively in H'. Upon introducing fermi operators $c_i = e^{i\pi \sum_0^{i-1} S_j^+ S_j^-} S_i^-$, H_0 is transformed to $H_0 = \sum_{i=1}^{N-1} \kappa(c_i^\dagger c_{i+1} + c_i c_{i+1}^\dagger)$, wherein conservation of total spin z-projection becomes conservation of fermion number [219]. The subsequent diagonalization of this tight-binding Hamiltonian occurs through an orthogonal transformation $f_k^\dagger = \frac{1}{A} \sum_{j=1}^{N} \sin \frac{jk\pi}{N+1} c_j^\dagger$ with $k = 1, \cdots, N$ and $A = (\frac{N+1}{2})^{1/2}$, yielding $H_0 = \sum_{k=1}^{N} E_k f_k^\dagger f_k$, where $E_k = 2\kappa \cos \frac{k\pi}{N+1}$ [219]. The perturbation Hamiltonian is likewise transformed to

$$H' = \sum_{k=1}^{N} t_k (c_0^\dagger f_k + (-1)^{k-1} c_{N+1}^\dagger f_k + \text{ h.c.}), \tag{5.2}$$

where $t_k = \frac{g}{A} \sin \frac{k\pi}{N+1}$. We begin by restricting our discussion to odd N, where there exists a single zero energy fermionic mode in the intermediate chain corresponding to $k = z \equiv (N+1)/2$. Thus, the two end spins are resonantly coupled to the zero energy fermion by H', and under the assumption that the tunneling rate $t_z \sim g/A$ is much smaller

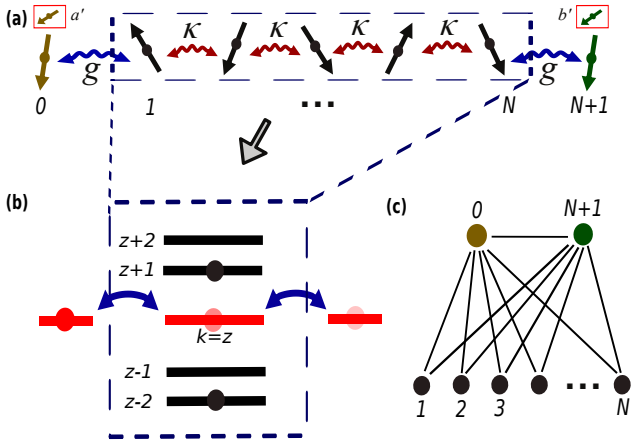

Figure 29: (color online). (a) Distant spin qubits coupled by an unpolarized spin-chain quantum channel with g, the coupling between qubits (yellow, green) and the spin chain and κ, the coupling between intra-chain elements. The spin chain can be re-expressed in terms of free fermions via the Jordan-Wigner transformation, wherein the hopping strength is characterized by κ. Boxed spins, labeled a' and b', represent additional spin qubits that can correspond to the memory of a quantum register or ancillary qubits associated with quantum information encoding. (b) By ensuring that the end spins are resonant with a single fermion mode ($k = z$), unpolarized spin-chain state transfer becomes analogous to fermionic tunneling. Maintaining $g \ll \kappa/\sqrt{N}$ ensures that off-resonant coupling to other fermionic modes can be neglected and enables state transfer independent of the intermediate spin-chain state. (c) Graph-like state generated by FFST, between the qubits and the intermediate spin chain [202]. Each line represents a controlled-phase gate.

than the fermion detuning, $|E_z - E_{z\pm1}| \sim \kappa/N$, off-resonant coupling to other fermionic modes can be neglected. Upon absorbing a phase factor of $(-1)^{z-1}$ into $c^\dagger_{N+1}$, evolution is governed by the effective Hamiltonian, $H_{eff} = t_z(c^\dagger_0 f_z + c^\dagger_{N+1} f_z + \text{ h.c.})$, which describes resonant fermionic tunneling, as shown in Fig. 29(b).

Unitary evolution under H_{eff} for a time $\tau = \frac{\pi}{\sqrt{2}t_z}$ results in $U_{eff} = e^{-i\tau H_{eff}} = (-1)^{f^\dagger_z f_z}(1 - (c^\dagger_0 + c^\dagger_{N+1})(c_0 + c_{N+1}))$. Upon projection to the subspace spanned by $\{(1, c^\dagger_0, c^\dagger_{N+1}, c^\dagger_0 c^\dagger_{N+1})|00\rangle_{0,N+1}\}$, the effective evolution can be expressed as

$$U^{fermi}_{eff} = (-1)^{n_0+n_{N+1}+n_z}(-1)^{n_0 n_{N+1}}\text{SWAP}_{0,N+1}, \tag{5.3}$$

where $n_\theta = f^\dagger_\theta f_\theta$ is the fermion number operator. Hence, as desired, time evolution under H_{eff} swaps the quantum state of the two end fermions. However, in addition to the SWAP

gate and single fermion rotations, the end fermions are entangled through a controlled phase gate $\mathrm{CP}_{0,N+1} = (-1)^{n_0 n_{N+1}}$, which arises from fermionic anticommutation relations [198, 202, 220]. Before discussing this entanglement, let us first consider the analogous prescription in the spin basis.

We consider a generic initial state $\Phi_i = (\alpha|\downarrow\rangle + \beta|\uparrow\rangle)_0 \otimes (\alpha'|\downarrow\rangle + \beta'|\uparrow\rangle)_{N+1} \otimes \Psi_{M,n_z}$ where Ψ represents the intermediate spin chain state, characterized as the co-eigenstate of commuting operators $M = \sum_{j=1}^{N} S_j^+ S_j^-$ and n_z. After fermionization, evolution and inversion back to the spin basis, the final spin chain state becomes

$$\Phi_f = (\prod_{j=1}^{N} \mathrm{CP}_{0,j}\mathrm{CP}_{N+1,j})\mathrm{CP}_{0,N+1}\mathrm{SWAP}_{0,N+1}\Phi_i \tag{5.4}$$

up to single qubit rotations. In this basis, the Wigner-strings become controlled-phase gates and generate a graph-like entangled state between the two end spins and the intermediate spins, as shown in Fig. 29(c) [202].

Despite this entanglement, the use of a simple two-qubit encoding can achieve coherent quantum state transfer [221]. The quantum information is encoded in two spins, a and a', with logical basis $|\downarrow\rangle = |\downarrow\rangle_a|\downarrow\rangle_{a'}$, $|\uparrow\rangle = |\uparrow\rangle_a|\uparrow\rangle_{a'}$. After encoding, one first performs FFST between spins a and b via the unpolarized spin chain, and then, repeats the operation between spins a' and b', as shown in Fig. 29(a). Finally, the quantum information is decoded by applying a CNOT gate between spins b and b', after which, the information has been coherently mapped to spin b. Thus, we have demonstrated the ability to perform QST between spatially separated spin qubits. Furthermore, as detailed in the subsequent section on experimental realizations utilizing Nitrogen-Vacancy registers, we offer an alternative solution which achieves remote coupling of spatially separated quantum registers through a dual-transfer protocol.

To confirm perfect quantum state transfer, we perform numerics, as shown in Fig. 30. Specifically, we calculate the average fidelity, $F = \frac{1}{2} + \frac{1}{12}\sum_{i=1,2,3} \mathrm{Tr}\left[\sigma^i \mathcal{E}(\sigma^i)\right]$, of two-qubit

encoded state transfer, where $\mathcal{E}$ represents the quantum channel consisting of encoding, state transfer and decoding [222]. This average fidelity can be expressed in terms of elements of the matrix $e^{-iK\tau}$, where K is the $N\times N$ coupling matrix of the full Hamiltonian found in Eq. (5.1), $H = \sum_{i,j} K_{i,j} S_i^+ S_j^-$; crucially, this allows for simulations of channel fidelity in extremely long spin chains, since diagonlization of the full Hilbert space is no longer necessary. In finite chains of fixed length, the infidelity, $\epsilon = 1 - F$, varies as a function of g/κ, as shown in Fig. 30(a). This infidelity results from the leakage of quantum information into the off-resonant modes of the intermediate spin chain, and can be analytically expressed, in the limit $g \ll \kappa$, as $\epsilon \approx \sum_{k\neq z} \frac{5}{3} \left(\frac{t_k}{E_k}\right)^2 [1 + (-1)^{k+z} \cos(E_k \tau)]$, where $z = \frac{N+1}{2}$. In this limit, the analytic expression is in exact agreement with the numerics, and is upper-bounded by the theoretical estimate, $\sum_{k\neq z} \frac{10}{3} \left(\frac{t_k}{E_k}\right)^2$, as shown in Fig. 30(a).

Utilizing the analytic upper bound for a given chain length N, a given intrachain coupling κ, and a given tolerable infidelity ϵ_0, we can compute the maximum allowed g and hence the minimum state transfer time τ. By contrast to direct dipole-dipole interactions, which would depict a cubic scaling of τ with N, the time required for FFST scales linearly with chain length, as shown in Fig. 30(b) [223]. Intuitively, this results from the fact that the condition on t_z allowing for off-resonant coupling to be neglected is $t_z \ll \kappa/N$, implying that $\tau \sim 1/t_z \sim N/\kappa$.

5.1.2 Extensions of the protocol

While we have chosen to focus on the case of odd N length intermediate chains, the extension to even N is directly analogous. In even N chains, since the fermion eigenspectrum is symmetric about $E = 0$, no fermionic eigenmode is initially resonant with the end spin qubits. However, by introducing a controllable detuning to the end spins, $H_\Delta = \Delta(S_0^z + S_{N+1}^z)$, it is possible to choose an N-dependent Δ such that the end spins are resonant with any single fermion eigenmode in both even and odd N cases [210]. In

particular, for $\Delta = E_k$, resonant tunneling will occur at the rate t_k, allowing for control over the speed of FFST.

We now generalize our analysis and consider optimizing the FFST protocol in the context of realistic imperfections including disorder and decoherence. On-site and coupling disorder cause localization, asymmetry of the eigenmodes, and changes in the statistics of the eigenenergies [205, 206, 218]. In the thermodynamic limit in 1D, localization occurs for any amount of disorder; thus, it will be necessary to utilize eigenmodes whose localization length is sufficiently large relative to the chain length, thereby rendering such modes effectively extended and viable for QST. Crucially, in the case of particle-hole (PH) symmetric disorder (e.g. coupling-strength disorder), there exists an extended critical state at $E = 0$ with a diverging localization length; this ensures the existence of an extended eigenmode with a known eigenenergy, suggesting that FFST is intrinsically robust against coupling-strength disorder [218]. In the case of on-site disorder, random modulation of the on-site potential may be able to restore PH symmetry [224]; in cases where this is insufficient, it is possible to characterize the energy spectrum and coupling strengths of the intermediate spin chain solely through tomography of a single end spin [225]. This characterization will help allow for the identification of a suitable, extended eigenmode.

However, the existence of an extended mode is not sufficient to ensure state transfer as disorder also enhances off-resonant tunneling rates and causes the eigenmode wavefunction amplitude to become asymmetric at the two ends of the chain. Despite such imperfections, by individually tuning the qubit-chain couplings, g_L (left) and g_R (right), it is possible to compensate for eigenmode asymmetry; furthermore, sufficiently decreasing the magnitude of the qubit-chain coupling ensures that off-resonant tunneling can safely be neglected, even in the presence of disorder.

In addition to disorder, decoherence of the spin qubits and the intermediate spin chain places a stringent lower bound on the values of g_L and g_R, since $\tau \sim \sqrt{N}/g$ [210]. Thus, an interplay of disorder and decoherence will ultimately limit the experimental realization of

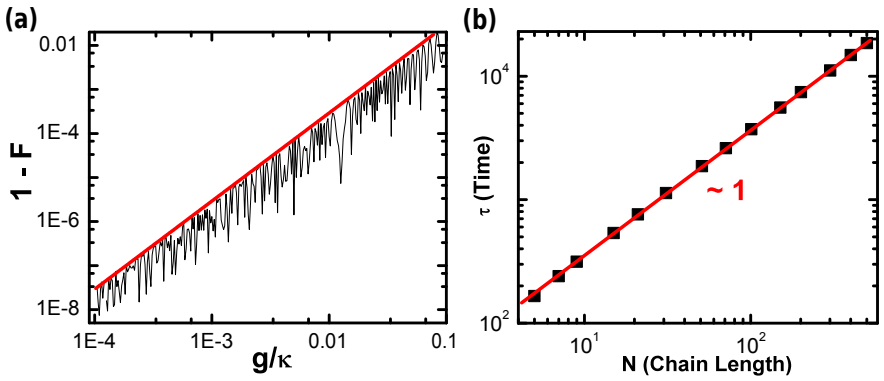

Figure 30: (color online). (a) Numerical simulation of the infidelity of QST for $N = 7$ as a function of g/κ depicting fluctuations in the infidelity. The numerical infidelity is bounded by the theoretical estimate (bold line). (b) For a chosen tolerable infidelity $\epsilon_0 = 10^{-3}$, the minimum time τ (in units of $1/\kappa$), required for state transfer scales linearly with chain length.

FFST; further numerical exploration of such an interplay will provide insight into the relevant constraints [210].

5.1.3 Experimental Realization

Both the necessity and realization of FFST can be evinced by considering Nitrogen-Vacancy (NV) registers in diamond, which have extremely long room-temperature coherence times [210]. In particular, the imperfect conversion of NV centers from single Nitrogen impurities results in substantial spatial separation between individual registers. However, the unconverted spin-1/2 Nitrogen impurities form a natural spin chain connecting remote registers. At ambient temperatures, the Nitrogen impurity spin chain, which is optically unaddressable, would be unpolarized and hence, the proposed scheme would be essential to enable distant NV register coupling.

Thus, we envision an array of two-qubit NV registers connected by a quantum channel consisting of spin-1/2 implanted Nitrogen impurities [210]. Recent experiments have demonstrated the ability to fully manipulate the two-qubit NV register corresponding to the NV nuclear spin, which serves as the memory qubit, and the NV electronic spin, which is used to initialize, readout, and mediate coupling to the intermediate spin

chain [44, 45, 226, 227]. The effective Hamiltonian described in Eq. (5.1) can be achieved in such a mixed spin system via dynamic decoupling [210], and the qubit-chain coupling g can be fully tuned by utilizing the structure of the NV center ground-state manifold [210]. To apply arbitrary two qubit gates between the nuclear memory of distant NV registers: 1) SWAP the state of the nuclear and electronic spin of the first register 2) apply FFST between the electronic spins of the two registers 3) apply a CP-gate between the electronic and nuclear spin of the second register 4) repeat (2) and (1) to return the nuclear memory of the first register and disentangle from the intermediary chain. Together with single qubit rotations, such an implementation of FFST achieves a universal set of gates and hence computation in an array of NV registers connected by Nitrogen impurity spin chains.

In summary, we have proposed a robust method to coherently couple spatially separated quantum registers by means of an unpolarized spin chain. The proposed method is examined in the context of NV diamond centers, where its direct application can potentially allow for the realization of a scalable room-temperature quantum information processor [210]. While we have focused on the specific case of an XX chain, the conceptual framework can be used in a wide range of systems to achieve QST through effective eigenmode tunneling. For example, QST in an unpolarized chain can also be achieved in the transverse field Ising model, where in contrast to the XX chain, the JW transformation yields a fermionic Hamiltonian which no longer conserves fermion number. In fact, all Hamiltonians that are quadratic in bose and fermi operators can be exactly diagonalized and thus provide a natural starting point to further explore eigenmode-mediated QST. Finally, the proposed approach may also provide insight into entanglement generation in a many-body system and the dynamics of the disorder-driven localization transition.

5.2 Fidelity of thermal quantum wires: dipolar interactions and decoherence

In the previous section, we described the method of thermal state transfer in a spin chain. In this section, we analyze various decoherence mechanisms and quantify the fidelity of

such state transfer. In the solid-state, our thermal state transfer method will naturally suffer from localization effects associated with lattice imperfections and disorder [218]. Exploration of the interplay between such localization effects and intrinsic constraints set by finite coherence times, is important to assess the feasibility of proposed architectures.

This section is organized as follows. In subsection II, we extend the previously proposed notion of eigenmode-mediated quantum state transfer [116] to the transverse field Ising model. In addition to being closely related to the actual achievable Hamiltonian of certain driven spin systems, this simple model enables an analytic description of the state transfer protocol. In subsection III, we build upon these protocols and derive analytic expressions characterizing the channel fidelity for state transfer between remote quantum registers. Next, we generalize our method to bosonic systems (e.g. coupled cavities and pendulum arrays) in subsection IV. In particular, we demonstrate that chains of coupled oscillators can faithfully transport quantum information even at high oscillator temperature.

Having described eigenmode-mediated QST in both the fermionic and bosonic context, we then turn to a specific implementation within a solid-state quantum computing architecture. In subsection V, we analyze eigenmode-mediated quantum state transfer between remote spin-quantum-registers [44, 45, 226]. To be specific, we consider Nitrogen-Vacancy (NV) defect center registers and examine the optimization of state transfer fidelities in the presence of both disorder and a finite depolarization (T_1) time. The interplay between disorder-induced localization and decoherence yields a natural optimal channel fidelity, which we calculate. Ultimately, this optimization demonstrates the feasibility of scalable architectures whose remote logic gates can harbor infidelities below the threshold for error correcting codes [228, 229]. While eigenmode-mediated QST fundamentally requires the register-chain coupling to be weaker than the intra-chain coupling, in subsection VI we consider generalizations to the strong coupling regime. In particular, motivated by several recent studies [208, 230–232], we provide numerical simulations in parallel with the analytic channel fidelities derived in subsection III.

In subsection VII, we perform exact diagonalization for spin systems, which includes the full long-range dipolar interaction. We find remarkably high fidelities for our proposed QST protocols in chains of length up to $L = 12$. Finally, in subsection VIII, we describe and analyze an alternate architecture, which utilizes globally controlled pulses for state transfer [216, 233]. In this case, we demonstrate that all spins in the system (e.g. even dark intermediate chain spins) can be viewed as potential qubits. However, while this dramatically increases the number of qubits available, the composite operations required to manipulate such intermediary spin qubits significantly raise the error threshold for robust operation.

5.2.1 Eigenmode-mediated QST

In this subsection, we begin with an idealized system in which to understand eigenmode-mediated QST, namely, the transverse field Ising model,

$$H = -\sum_{i=1}^{N-1} \kappa \sigma_i^x \sigma_{i+1}^x + \sum_{i=1}^{N} B\sigma_i^z \tag{5.5}$$

where κ is the nearest-neighbor coupling strength and B represents a uniform transverse field on each site. In addition to being realizable in a variety of experimental systems, ranging from NVs and trapped ions to electrons floating on helium [116, 234, 235], this model also has the virtue of being exactly solvable; this will allow us to clearly illustrate the essence of eigenmode-mediated state transfer and to understand the many-body entanglement which arises.

Expanding σ_i^x as a function of spin flip operators, $\sigma_i^{\pm} = (\sigma_i^x \pm i\sigma_i^y)/2$, and utilizing the Jordan-Wigner transformation [236], $c_i^\dagger = \sigma_i^+ e^{-i\pi \sum_{j=1}^{i-1} \sigma_j^+ \sigma_j^-}$, yields the fermionized Hamiltonian,

$$H_{JW} = -\sum_{i=1}^{N-1} \kappa (c_i^\dagger c_{i+1} + c_i^\dagger c_{i+1}^\dagger - c_i c_{i+1}^\dagger - c_i c_{i+1}) \sum_{i=1}^{N} B(c_i^\dagger c_i - c_i c_i^\dagger) \tag{5.6}$$

which is quadratic and conserves fermionic parity without conserving particle number. To solve H_{JW}, we re-express it as $\vec{\phi}^{\dagger} A \vec{\phi}$, where we define $\vec{\phi} = (c_1, c_2, ..., c_N, c_1^{\dagger}, c_2^{\dagger}, ..., c_N^{\dagger})^T$. The matrix A is real, symmetric and is diagonalized to

$$\Lambda = \begin{pmatrix} \epsilon_1 & 0 & 0 & 0 & \cdots \\ 0 & -\epsilon_1 & 0 & 0 & \cdots \\ 0 & 0 & \epsilon_2 & 0 & \cdots \\ 0 & 0 & 0 & -\epsilon_2 & \cdots \\ \vdots & \vdots & \vdots & \vdots & \ddots \end{pmatrix} \tag{5.7}$$

via an orthogonal matrix, ψ, such that $\psi A \psi^T = \Lambda$. The eigenmodes come in pairs with energy $\pm\epsilon_k$, corresponding to eigenvectors $d_k = \psi_{2k-1,j}\phi_j$ and $d_k^{\dagger} = \psi_{2k,j}\phi_j$, where $k = 1, \cdots, N$. This transformation yields

$$H_{JW} = \sum_{k=1}^{N} \epsilon_k (d_k^{\dagger} d_k - d_k d_k^{\dagger}), \tag{5.8}$$

where the d-modes satisfy standard Dirac anticommutation relations. For a uniform chain the spectrum is, $\epsilon_k \approx \sqrt{\kappa^2 + B^2 - 2B\kappa \cos q_k}$, where $q_k = k\pi/(N+1)$.

We now consider the addition of quantum registers, labeled 0 and $N+1$, at the ends of the data bus (Fig. 31). The registers couple perturbatively with strength g to the ends of the Ising spin chain [116, 201] and we apply a local Zeeman field B',

$$H' = -g(\sigma_0^x \sigma_1^x + \sigma_N^x \sigma_{N+1}^x) + B'(\sigma_0^z + \sigma_{N+1}^z). \tag{5.9}$$

Upon fermionizing,

$$\begin{aligned} H'_{JW} &= -g(c_0^\dagger c_1 + c_0^\dagger c_1^\dagger + c_1^\dagger c_0 - c_0 c_1) \\ &- g(c_N^\dagger c_{N+1} + c_N^\dagger c_{N+1}^\dagger + c_{N+1}^\dagger c_N - c_N c_{N+1}) \\ &+ B'(c_0^\dagger c_0 - c_0 c_0^\dagger + c_{N+1}^\dagger c_{N+1} - c_{N+1} c_{N+1}^\dagger). \end{aligned} \tag{5.10}$$

By tuning $B' = \epsilon_z$, we ensure that the external registers are coupled resonantly to a single finite-energy eigenmode $d_z^\dagger$ of the intermediate chain. Quantum state transfer proceeds via resonant tunneling through this mode. Noting that $c_i = \sum_{k=1}^{N} (\psi^T)_{i,2k-1} d_k + \sum_{k=1}^{N} (\psi^T)_{i,2k} d_k^\dagger$ allows us to re-express c_1 and c_N in terms of the d-modes. By choosing $g\psi_{2z-1,1} = g\psi_{2z-1,N} \ll B', |\epsilon_z - \epsilon_{z\pm1}|$ we ensure that off-resonant eigenmodes are only weakly coupled to the quantum registers, leaving an effective three-mode picture,

$$\begin{aligned} H_{eff} &\approx \epsilon_z(d_z^\dagger d_z - d_z d_z^\dagger) + \epsilon_z(c_0^\dagger c_0 - c_0 c_0^\dagger) + \epsilon_z(c_{N+1}^\dagger c_{N+1} - c_{N+1} c_{N+1}^\dagger) \\ &- g\psi_{2z-1,1}(c_0^\dagger d_z + d_z^\dagger c_0) - g\psi_{2z-1,N}(c_{N+1}^\dagger d_z + d_z^\dagger c_{N+1}). \end{aligned} \tag{5.11}$$

It is interesting to note that for $B < \kappa$, the Hamiltonian in Eq. (5.6) represents a spin-less p-wave superconductor in its topological phase [237]. The zero energy boundary modes of this system have received a great deal of attention recently. As these Majorana zero modes are exponentially localized [238], they cannot be employed for state transfer. In our analysis, this follows from the failure of the secular approximation to remove fermion number non-conserving terms. A straight-forward calculation shows that the pairing terms precisely cancel the hopping terms in the effective evolution.

Equation (5.11) represents the key result of the above manipulations. State transfer is

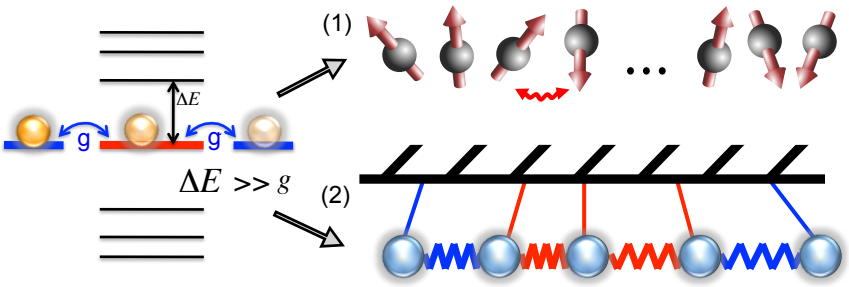

Figure 31: (color online). Quantum state transfer is achieved by tuning the left and right quantum registers (blue) to a particular eigenmode (red) of the intermediate data bus. By ensuring that the coupling, g between the registers and the chain is sufficiently weak relative to the spacing of adjacent eigenmodes, it is possible to consider evolution in an effective three-mode picture. Such eigenmode-mediated QST is applicable in a variety of contexts, ranging from solid-state spin chains to coupled bosonic degrees of freedom (e.g. pendulums or cavity arrays).

achieved by time-evolving for $\tau = \frac{\pi}{\sqrt{2}g\psi_{2z-1,1}}$, leading to unitary evolution,

$$\begin{aligned} U_{eff} &= e^{-i\tau H_{eff}} = (-1)^{n_z}(-1)^{(c_0^\dagger + c_{N+1}^\dagger)(c_0+c_{N+1})/2} \\ &= (-1)^{n_z}(1-(c_0^\dagger + c_{N+1}^\dagger)(c_0+c_{N+1})), \end{aligned} \tag{5.12}$$

where $n_z = d_z^\dagger d_z$. It is instructive to write the explicit action of U_{eff} on the subspace spanned by $\Psi = \{|\Omega\rangle, c_0^\dagger|\Omega\rangle, c_{N+1}^\dagger|\Omega\rangle, c_0^\dagger c_{N+1}^\dagger|\Omega\rangle\}$, where $|\Omega\rangle$ is the vacuum associated with c_0, c_{N+1},

$$U_{eff}\Psi = (-1)^{n_z}\begin{pmatrix} 1 & 0 & 0 & 0 \\ 0 & 0 & -1 & 0 \\ 0 & -1 & 0 & 0 \\ 0 & 0 & 0 & -1 \end{pmatrix}\Psi. \tag{5.13}$$

Up to signs, the effective evolution in the register subspace is a swap gate. In the spin representation, owing to Wigner strings ($e^{-i\pi\sum_{j=1}^{i-1}\sigma_j^+\sigma_j^-}$), there exists an additional set of controlled phase (CP) gates, as shown in Fig. 32. Since $\mathrm{CP}^2 = \mathbb{I}$, this entanglement can be easily cancelled and logic gates between the remote registers can be successfully accomplished [221, 239]. We detail two possible such protocols below.

One protocol, herein termed "there-and-back", is particularly applicable to the case of

multi-qubit quantum registers. For a two-qubit register, we can label one qubit as the memory qubit while the other represents the "coupling" qubit. Once an eigenmode-mediated swap between the coupling qubits is accomplished, an intra-register CP-gate is then performed between the two qubits of the remote register. The return swap then cancels the unwanted entanglement illustrated in Fig. 32, leaving only a controlled-phase gate between the two memory qubits. Since CP gates are themselves universal, such a procedure enables universal logic between remote registers.

An alternate method, which we call the "paired protocol" utilizes a two-qubit encoding to cancel the Wigner strings. In this approach, the quantum information is encoded in two spins, a and b, with logical basis $|\downarrow\rangle = |\downarrow\rangle_a|\downarrow\rangle_b$, $|\uparrow\rangle = |\uparrow\rangle_a|\uparrow\rangle_b$ [116, 221, 239]; the intuition behind this encoding is that it produces an effective bosonic excitation, thereby mitigating the effect of the fermionic Wigner strings. State transfer proceeds by successively transferring a and b through the intermediary chain.

5.2.2 Analytic Channel Fidelity

We now derive the channel fidelity associated with the paired protocol. To set up the analytic framework, we begin by calculating the fidelity of a simplified protocol, termed the "double-swap". In this double-swap, we consider the left register (indexed 0) undergoing two successive eigenmode-mediated swap gates. Ideally, this simplified protocol swaps the quantum information twice, thereby disentangling it from the intermediate chain and also returning it to its initial position at the left register. We then consider a second protocol, termed the "single-swap", in which the quantum information undergoes only one eigenmode-mediated swap-gate. Analyzing this protocol will illustrate the effect of the residual entanglement on the channel fidelity. Finally, we turn to the paired-protocol and demonstrate that the proposed two-qubit encoding can eliminate this entanglement, thereby enabling quantum state transfer.

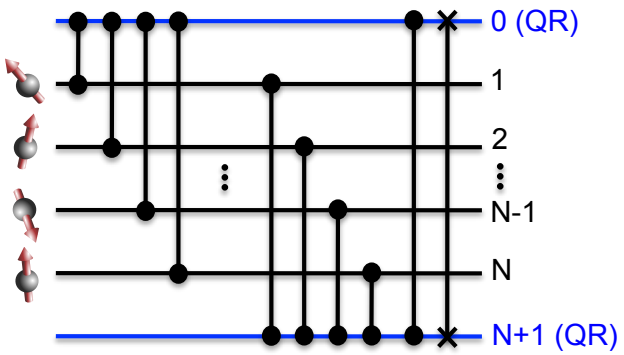

Figure 32: (color online). Schematic circuit diagram depicting eigenmode-mediated state transfer between the quantum registers (QR) 0 and $N+1$. Controlled phase gates are represented as circle-ending dumbbells while X-ending dumbbells depict a swap gate. In addition to the desired state transfer, each register is CP-entangled with all intermediate spins owing to the Wigner strings associated with fermionization. This additional entanglement can be cancelled by utilizing a simple two-qubit encoding.

Double-swap

The average channel fidelity for a quantum dynamical operation is given by

$$F = \frac{1}{2} + \frac{1}{12} \sum_{i=x,y,z} \mathrm{Tr}\left[\sigma^i \mathcal{E}(\sigma^i)\right], \tag{5.14}$$

where $\mathcal{E}$ characterizes the quantum channel [222]. For simplicity of notation, we will restrict ourselves to the XX-model, $H = g(\sigma_0^+\sigma_1^- + \sigma_N^+\sigma_{N+1}^- + \text{h.c.}) + \sum_{i=1}^{N-1} \kappa(\sigma_i^+\sigma_{i+1}^- + \text{h.c.})$, although analogous results hold for the previously considered transverse field Ising model. For the double-swap (DS), we let U represent evolution under H for a time, $t = 2\tau$, equivalent to twice the state-transfer time. Let us suppose that the left register is initially disentangled from the remainder of the chain, which is in a thermal mixed state ρ_{ch}^{DS}; the

average double-swap channel fidelity is then given by,

$$\begin{aligned} F_{DS} &= \frac{1}{2} + \frac{1}{12} \sum_{i=x,y,z} \mathrm{Tr}\left[\sigma_0^i U(\sigma_0^i \otimes \rho_{ch}^{DS})U^\dagger\right] \\ &= \frac{1}{2} + \frac{1}{12} \sum_{i=x,y,z} \mathrm{Tr}\left[U^\dagger \sigma_0^i U(\sigma_0^i \otimes \rho_{ch}^{DS})\right] \\ &= \frac{1}{2} + \frac{1}{12} \sum_{i=x,y,z} \mathrm{Tr}\left[\sigma_0^i(t)(\sigma_0^i \otimes \rho_{ch}^{DS})\right], \end{aligned} \tag{5.15}$$

where $\sigma_0^i(t)$ is the Heisenberg evolution of the left register. By fermionization, this evolution can be re-expressed with respect to elements of the matrix $M = e^{-iKt}$ where K is the $(N+2) \times (N+2)$ coupling matrix of the full Hamiltonian (including registers), $H = \sum_{i,j=0}^{N+1} K_{ij} c_i^\dagger c_j$. Evolution of the fermi operators is governed by $\dot{c_m} = -i \sum_n K_{mn} c_n$, implying that $c_m(t) = \sum_n M_{mn} c_n$ and further, that

$$\sigma_0^+(t) = U^\dagger \sigma_0^+ U = U^\dagger c_0^\dagger U = \sum_i M_{0i}^* c_i^\dagger = \sum_i M_{0i}^* \sigma_i^+ \prod_{l<i} e^{i\pi \sigma_l^+ \sigma_l^-}, \tag{5.16}$$

$$\begin{aligned} \sigma_0^z(t) &= 2c_0^\dagger(t)c_0(t) - 1 = -1 + 2\sum_{ij} M_{0i}^* M_{0j} c_i^\dagger c_j \\ &= -1 + 2\sum_{ij} M_{0i}^* M_{0j} \sigma_i^+ \sigma_j^- \prod_{i<l<j} e^{i\pi \sigma_l^+ \sigma_l^-}, \end{aligned} \tag{5.17}$$

where we have used the fact that $c_0^\dagger$ carries no Wigner string. To evaluate F_{DS}, we note that $\sigma^\pm = (\sigma^x \pm i\sigma^y)/2$, and hence, $\mathrm{Tr}\left[\sigma_0^x(t)(\sigma_0^x \otimes \rho_{ch})\right] = \mathrm{Tr}\left[(\sigma_0^+(t) + \sigma_0^-(t))((\sigma_0^+ + \sigma_0^-) \otimes \rho_{ch})\right]$. Contributions are only obtained from the cross-terms, $\sigma_0^+(t)(\sigma_0^- \otimes \rho_{ch})$ and $\sigma_0^-(t)(\sigma_0^+ \otimes \rho_{ch})$, since the number of excitations in $i = 0$ must be preserved to generate a non-zero trace.

For example, using Eq. (5.16),

$$\begin{aligned} \mathrm{Tr} \quad & \left[\sigma_0^+(t)(\sigma_0^- \otimes \rho_{ch})\right] \\ = \quad & \mathrm{Tr}\left[(\sum_i M_{0i}^* \sigma_i^+ \prod_{l<i} e^{i\pi\sigma_l^+\sigma_l^-})(\sigma_0^- \otimes \rho_{ch})\right] \\ = \quad & \mathrm{Tr}\left[M_{00}^* \sigma_0^+\sigma_0^- \otimes \rho_{ch}\right] = M_{00}^*. \end{aligned} \tag{5.18}$$

An analogous calculation yields $\mathrm{Tr}\left[\sigma_0^-(t)(\sigma_0^+ \otimes \rho_{ch})\right] = M_{00}$. Finally, for the σ^z terms, one finds, using Eq. (5.17),

$$\begin{aligned} \mathrm{Tr} \quad & [\sigma_0^z(t)(\sigma_0^z \otimes \rho_{ch})] = \mathrm{Tr}\left[-\sigma_0^z \otimes \rho_{ch}\right] \\ + \quad & \mathrm{Tr}\left[(2\sum_{ij} M_{0i}^* M_{0j} \sigma_i^+ \sigma_j^- \prod_{i<l<j} e^{i\pi\sigma_l^+\sigma_l^-})(\sigma_0^z \otimes \rho_{ch})\right] \\ = \quad & \mathrm{Tr}\left[2M_{00}^* M_{00} \sigma_0^+\sigma_0^-\sigma_0^z \otimes \rho_{ch}\right] = 2|M_{00}|^2, \end{aligned} \tag{5.19}$$

where we've noted that $i = j$ to ensure that the number of excitations in each mode is conserved. Moreover, we must also have that $i = j = 0$, since $\mathrm{Tr}[\sigma_0^z] = 0$. Combining the above terms yields the double-swap channel fidelity as,

$$F_{DS} = \frac{1}{2} + \frac{1}{6}(M_{00} + M_{00}^* + |M_{00}|^2). \tag{5.20}$$

Interestingly, we need to compute only a single matrix element to obtain the relevant channel fidelity.

Single-swap

We now consider the single-swap (SS) channel fidelity associated with the transfer of quantum information from the right register (indexed $N+1$) to the left register (indexed 0),

$$F_{SS} = \frac{1}{2} + \frac{1}{12} \sum_{i=x,y,z} \mathrm{Tr}\left[\sigma_0^i(t)(\rho_{ch}^{SS} \otimes \sigma_{N+1}^i)\right], \tag{5.21}$$

where ρ_{ch}^{SS} now characterizes the initial state for spins $\{0, \cdots, N\}$. Note that F_{SS} will be independent of the direction of state transfer, and we have chosen right to left for notational simplicity. From Eq. (5.16), one finds,

$$\begin{aligned} \sigma_0^x(t) &= c_0^\dagger(t) + c_0(t) = \sum_i M_{0i}^* c_i^\dagger + M_{0i} c_i \\ &= \sum_i [\{\mathrm{Re}(M_{0i})\sigma_i^x + \mathrm{Im}(M_{0i})\sigma_i^y\} \prod_{l=0}^{i-1}(-\sigma_l^z)]. \end{aligned} \tag{5.22}$$

In analogy to the DS case, $i \neq N+1$ terms do not contribute to the trace,

$$\mathrm{Tr}[\sigma_0^x(t)(\rho_{ch} \otimes \sigma_{N+1}^x)] = 2\mathrm{Re}(M_{0,N+1})\mathrm{Tr}[\rho_{ch}^{SS} \prod_{l=0}^{N}(-\sigma_l^z)]. \tag{5.23}$$

The σ^y term yields an identical contribution while the σ^z term yields, $\mathrm{Tr}[\sigma_0^z(t)(\rho_{ch}^{SS} \otimes \sigma_{N+1}^z)] = 2|M_{0,N+1}|^2$. Therefore,

$$F_{SS} = \frac{1}{2} + \frac{1}{6}[2\mathrm{Re}(M_{0,N+1})\mathrm{Tr}[\rho_{ch}^{SS} \prod_{l=0}^{N}(-\sigma_l^z)] + |M_{0,N+1}|^2). \tag{5.24}$$

For perfect transfer with $F_{SS} = 1$, we would require both $|M_{0,N+1}| = 1$ and $|\mathrm{Tr}[\rho_{ch}^{SS} \prod_{l=0}^{N}(-\sigma_l^z)]| = 1$. In the case of an unpolarized chain, the second condition is unsatisfied since the expectation value of the chain parity operator $P = \prod_{l=0}^{N}(-\sigma_l^z)$ is zero. The dependence of the single-swap fidelity on the intermediate chain's parity demonstrates the entanglement illustrated in Fig. 32, and presents an obvious problem for QST.

Paired-Protocol

To overcome this problem, we now turn to the two-qubit encoding proposed in Sec. II., e.g. $|\downarrow\rangle = |\downarrow\rangle_a|\downarrow\rangle_b$, $|\uparrow\rangle = |\uparrow\rangle_a|\uparrow\rangle_b$. Let us index the full chain as $\{0_a, 0_b, 1, \cdots, N, (N+1)_b, (N+1)_a\}$ and define U_b as the transfer process through the sub-chain $\{0_b, 1, \cdots, N, (N+1)_b\}$, while U_a represents the transfer process through the

sub-chain $\{0_a, 1, \cdots, N, (N+1)_a\}$. The composite $U = U_b U_a$ then represents the unitary characterizing the encoded state transfer, with average channel fidelity given by

$$F_{enc} = \frac{1}{2} + \frac{1}{12} \sum_{i=x,y,z} \mathrm{Tr}\left[\sigma^i_{N+1}(t)(\sigma^i_0 \otimes \rho^{PP}_{ch} \otimes \rho_{N+1})\right]. \tag{5.25}$$

Here, ρ^{PP}_{ch} is the mixed initial state of the intermediate chain ($\{1, \cdots, N\}$), σ^i_0 acts on the encoded logical subspace of the 0-register, and ρ_{N+1} is the mixed state of the encoded $(N+1)$ register within the logical subspace. Working within this logical subspace is crucial to ensure that $\mathrm{CP}_{0_a,N+1_a}\mathrm{CP}_{0_b,N+1_b} = \mathbb{I}$. Inspection reveals that the paired-protocol includes two contributions from the chain parity operator, and since $P^2 = \mathbb{I}$, we have effectively disentangled from the intermediate chain. Since a consistent ordering of the spin-chain is required to implement the Jordan-Wigner transformation, the Hamiltonian, H_{U_a} governing the U_a transfer evolution will contain uncanceled Wigner strings. For example, the piece of H_{U_a} containing the coupling between the registers and the ends of the spin-chain takes the form, $H_{U_a} = g(c^\dagger_{0_a} e^{i\pi n_{0_b}} c_1 + c^\dagger_N e^{i\pi n_{(N+1)_b}} c_{(N+1)_a} + \mathrm{h.c.})$. While one must take care to correctly evaluate such strings, an otherwise straightforward computation yields,

$$\begin{aligned} F_{enc} &= \frac{1}{6}(2|M_{0,N+1}|^2 \mathrm{Re}\left[M^2_{0,N+1} - M_{0,0}M_{N+1,N+1}\right] \\ &+ |M_{0,N+1}|^2 + |\sum_i M_{N+1,i}M_{i,0}|^2) + \frac{1}{2}. \end{aligned} \tag{5.26}$$

Again, one only needs to compute certain matrix elements of M and in fact, an analytic form for all such elements can be obtained [201].

5.2.3 Generalization to Oscillator Systems

Motivated by the fact that quadratic bosonic systems can also be exactly solved and by the tremendous experimental progress in realizing coupled-oscillator arrays, in this section, we analyze the generalization of eigenmode-mediated state transfer to systems of bosonic

oscillators. By contrast to our previous discussions of dipolar spin chains, where we made an explicit nearest neighbor assumption, which truncates the otherwise $1/r^3$ interaction, many bosonic oscillator systems are often naturally nearest neighbor. For example, the realization of such coupled-oscillators is currently being explored in systems such as, cavity arrays [240–242], nano-mechanical oscillators [243, 244], Josephson junctions [43, 245, 246], and optomechanical crystals [247].

Consider a chain of coupled harmonic oscillators with Hamiltonian

$$H_B = \sum_{i=1}^{N} \omega a_i^\dagger a_i + \sum_{i=1}^{N-1} \kappa (a_i^\dagger a_{i+1} + a_{i+1}^\dagger a_i). \tag{5.27}$$

As before, we begin by diagonalizing the Hamiltonian. Let us define $b_k = \frac{1}{A}\sum_j \sin\frac{jk\pi}{N+1} a_j$, with $A = \sqrt{(N+1)/2}$ and $k = 1, \cdots, N$, yielding $H = \sum_k (\omega + \epsilon_k) b_k^\dagger b_k$, where $\epsilon_k = 2\kappa\cos(\frac{k\pi}{N+1})$. The perturbative coupling of the two additional quantum registers at the ends of the oscillator chain is given by,
$H'_B = g(a_0^\dagger a_1 + a_N^\dagger a_{N+1} + \text{h.c.}) + \omega'(a_0^\dagger a_0 + a_{N+1}^\dagger a_{N+1})$, where g characterizes the register-oscillator-chain coupling strength and ω' is the register frequency. Upon re-expressing a_1 and a_N as a function of the eigenmodes b_k, we arrive at the full Hamiltonian,

$$\begin{aligned} H_B \;+\; H'_B &= \sum_{k=1}^{N} t_k (a_0^\dagger b_k + (-1)^{k-1} a_{N+1}^\dagger b_k + \text{h.c.}) \\ &+ \quad \omega'(a_0^\dagger a_0 + a_{N+1}^\dagger a_{N+1}) + \sum_{k=1}^{N} (\omega + \epsilon_k) b_k^\dagger b_k, \end{aligned} \tag{5.28}$$

where we let $t_k = (g/A)\sin[k\pi/(N+1)]$. In analogy to subsection. II, we consider resonant tunneling through a particular mode b_z, by tuning $\omega' = \omega + \epsilon_z$ and ensuring that $t_z \ll |\epsilon_z - \epsilon_{z\pm1}|$. The resulting effective Hamiltonian is $H_{eff}^B = \sqrt{2} t_z (\eta_0^\dagger b_z + b_z^\dagger \eta_0)$, where $\eta_0 = 1/\sqrt{2}(a_0 + a_{N+1})$. To demonstrate state transfer, we introduce operators

$\xi_\pm = 1/\sqrt{2}(\eta_0 \pm b_z)$, yielding

$$H^B_{eff} = \sqrt{2}t_z(\xi^\dagger_+\xi_+ + \xi^\dagger_-\xi_-). \tag{5.29}$$

Let us now consider unitary evolution under H^B_{eff} for a time $\tau_B = \pi/(\sqrt{2}t_z)$, wherein $U^B_{eff} = e^{-iH^B_{eff}\tau_B} = (-1)^{\xi^\dagger_+\xi_+}(-1)^{\xi^\dagger_-\xi_-}$, so that $(U^B_{eff})^\dagger\xi_\pm(U^B_{eff}) = -\xi_\pm$. Returning to the original basis and evaluating the time evolution of a_0 and a_{N+1} yields

$$\begin{aligned} a_0(\tau) &\to (U^B_{eff})^\dagger a_0(U^B_{eff}) = -a_{N+1}, \\ a_{N+1}(\tau) &\to (U^B_{eff})^\dagger a_{N+1}(U^B_{eff}) = -a_0, \end{aligned} \tag{5.30}$$

demonstrating a swap gate between the oscillator-registers at the ends of the chain. As before, this state transfer is achieved independent of the state of the intermediate chain. Moreover, there exists no additional entanglement between the registers and the intermediary oscillators; this is a direct consequence of the bosonic nature of the modes, which, unlike their Wigner-fermionic counterparts in subsection. II, carry no strings.

One crucial difference with the spin-chain case is that the occupation of the bosonic eigenmodes is not limited to 0 or 1. In a highly excited system, this induces a "bosonic enhancement" of off-resonant errors and will limit the achievable state transfer fidelity as a function of temperature. In particular, the state transfer unitary evolution gives $a_{N+1}(\tau) = M_{N+1,0}a_0 + \sqrt{\epsilon}a_\epsilon$, where $\epsilon = 1 - |M_{N+1,0}|^2 \propto g^2$ is a small error and a_ϵ is a normalized linear combination of the a_i modes ($i = 1, \ldots, N+1$). The total number of excitations in mode $N+1$ after the state transfer is $\langle n_{N+1}(\tau)\rangle = (1-\epsilon)\langle n_0\rangle + \epsilon\langle n_\epsilon\rangle$, where $n_i = a^\dagger_i a_i$. Therefore, if the chain is thermally occupied with $\langle n_\epsilon\rangle \approx kT/\omega > 1$, the coupling strength g must be reduced to $g\sqrt{\omega/(kT)}$ in order to keep errors comparable with the zero-temperature bosonic case. In realistic experimental systems, this implies an interplay between temperature, which sets the bose-enhancement of off-resonant errors and

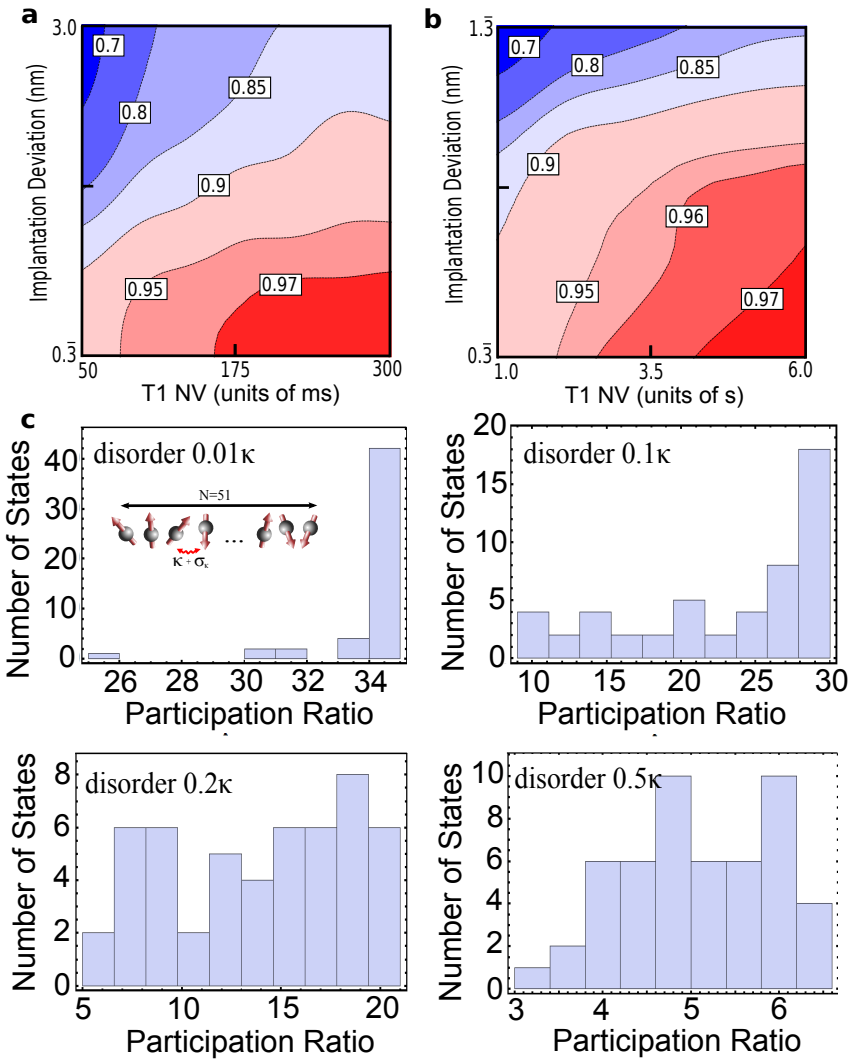

Figure 33: (color online). (a) Contour plots for $N = 11$ characterizing the average achievable fidelity as a function of the NV depolarization time (T_1) and the coupling strength disorder induced by imperfect implantation. Numerics utilize an average intrachain spin spacing of $d = 10$nm corresponding to a $\kappa = 50$kHz dipole-dipole interaction strength. This intrachain spacing is assumed to be independent Gaussian distributed and the implantation deviation represents the standard deviation, σ_d. For each σ_d, 1000 realizations were averaged to obtain the plotted fidelity and a smooth contour plot is generated via a third-order spline interpolation. The register-chain coupling strengths g_L, g_R, Eq. (5.33), are assumed to be fully tunable via control of the 3-level NV ground state manifold [116]. (b) Analogous contour plots for $N = 51$. In this case, the NV registers are separated by order optical wavelength enabling individual laser manipulation without the need for subwavelength techniques. (c) Participation ratio for eigenmodes ($N = 51$). Each eigenmode is indexed by its PR and the number of states within a certain PR bin is shown. For each disorder (which are represented as fractions of the bare coupling strength $\kappa = 50$kHz), 1000 realizations are averaged.

decoherence rates, which limit the minimal speed of state transfer.

5.2.4 Disorder and Decoherence

Eigenmode-mediated state transfer naturally finds use in a variety of quantum computing architectures where data buses are required to connect high-fidelity remote registers [116, 239, 248]. Within such architectures, it is crucial to consider an interplay between naturally occurring disorder and finite decoherence rates. While disorder in 1D systems generically localizes all eigenmodes [218, 230, 249, 250], leading to an exponentially long state-transfer time, in finite-size systems with weak disorder, the localization lengths can be large relative to the inter-register separation. In these cases, one must still reduce the register-chain coupling strength g to compensate disorder effects, but so long as the register decay time is sufficiently long, it remains possible to achieve high-fidelity QST. In this section, we will discuss the impact of coupling-strength disorder on spin chains and will analyze the optimization of g as a function of disorder strength and qubit depolarization time.

In particular, we will consider two sources of error: 1) off-resonant coupling to alternate eigenmodes (which becomes enhanced as disorder increases) and 2) a finite register depolarization time T_1,

$$\epsilon = \sum_{k \neq z} \left(g_L^2 \frac{|\psi_{k,L}|^2}{\Delta_k^2} + g_R^2 \frac{|\psi_{k,R}|^2}{\Delta_k^2} \right) + N \frac{t}{T_1}, \tag{5.31}$$

where $g_{L(R)}$ is left (right) register-chain coupling, $\psi_{k,L(R)}$ is the eigenmode amplitude at the left (right) register, Δ_k is the energy difference from mode z to mode k, N is the chain length, t is the state transfer time and T_1 is the depolarization time of the register. The additional factor of N in the final term results from the entanglement discussed in subsection II; indeed, since each register is CP-entangled with all intermediate spins, any spin-flip of the intermediate chain immediately dephases the quantum information.

To ensure that the tunneling rates at each end of the intermediate chain are equivalent, we envision tuning g_L and g_R independently, such that $t_z = g_L|\psi_{z,L}| = g_R|\psi_{z,R}|$. Plugging in for the state transfer time, $t = \pi/\sqrt{2}t_z$ yields,

$$\epsilon = \sum_{k\neq z} g_L^2 \left(\frac{|\psi_{k,L}|^2}{\Delta_k^2} + \frac{|\psi_{z,L}|^2}{|\psi_{z,R}|^2}\frac{|\psi_{k,R}|^2}{\Delta_k^2} \right) + \frac{N\pi}{\sqrt{2}T_1 g_L |\psi_{z,L}|}, \tag{5.32}$$

which enables us to derive the optimal coupling strength,

$$g_L = \sqrt[3]{\frac{N\pi}{2\sqrt{2}T_1|\psi_{z,L}|}\left(\sum_{k\neq z} \frac{|\psi_{k,L}|^2}{\Delta_k^2} + \frac{|\psi_{z,L}|^2}{|\psi_{z,R}|^2}\frac{|\psi_{k,R}|^2}{\Delta_k^2} \right)^{-1}}. \tag{5.33}$$

Disorder Numerics for a Specific NV-based Architecture

We now consider an example implementation of eigenmode-mediated state transfer in the context of a quantum computing architecture based upon Nitrogen-Vacancy (NV) registers in diamond [44, 45, 226]. Each fully controllable NV register consists of a coupled electronic and nuclear spin. The nuclear spin, with extremely long multi-second room-temperature coherence times is often thought of as the memory qubit [113], while the electronic spin, which can be optically initialized and read out, mediates interactions with other NVs [116, 239]. Our analysis of disorder effects will be based upon the specific architecture proposed in [116]; there, NV registers are connected by a dark-spin-chain data bus composed of spin-1/2 electronic spins associated with Nitrogen impurities. One of the crucial advantages of utilizing spin chains to connect remote NVs is that this enables optical addressing of individual registers in parallel, a necessary requirement for the implementation of many error-correcting codes.

We consider realistic experimental parameters, with an average spin spacing of about 10nm, corresponding to a dipole coupling strength $\approx$ 50kHz. At room-temperature, NV centers are characterized by $T_1 \sim$ 10ms [113], owing to an Orbach spin-lattice relaxation

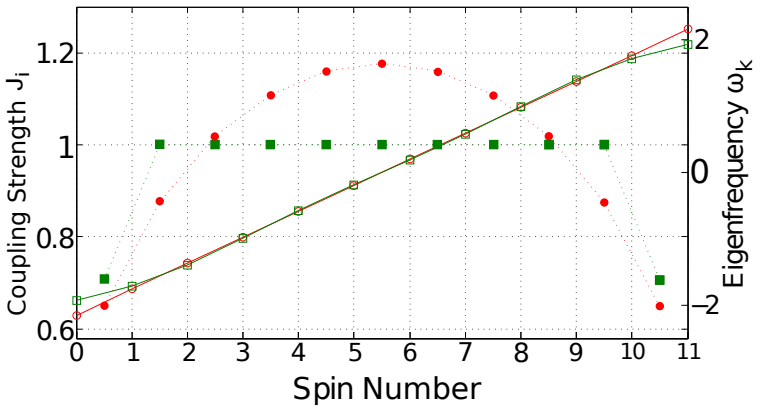

Figure 34: (color online). Coupling pattern $\{J_i\}$ between spins for two differing cases: 1) engineered couplings (circles) as in [196] and 2) strong coupling regime (squares). The left y-axis characterizes the coupling strength for each case and is associated with solid symbols; the couplings are plotted between spin numbers (e.g. J_0 is plotted between spin number 0 and 1). The right y-axis characterizes the fermionic spectrum (in this case, the x-axis is simply an index) and is associated with the open symbols. The open red circles depict the exactly linear spectrum of engineered chain, while the open green squares depict the quasi-linear spectrum of the strong coupling case with uniform interchain couplings $\kappa = 1$ and optimized $g \approx 0.7$.

process; the exponential dependence of the Orbach process on temperature suggests that slight cooling can significantly extend T_1, with many seconds already demonstrated at liquid Nitrogen temperatures [116, 251]. We now perform disorder-averaged numerics for two separate chain lengths: 1) sub-wavelength addressable ($N = 11$) and 2) optical-wavelength addressable ($N = 51$) [227]. We characterize the amount of disorder by the standard deviation associated with imperfect spin positioning; in the case of NVs, the origin of this imperfection is straggle during the ion-implantation process [74, 75]. We average over 1000 disorder realizations and calculate the fidelity, $1 - \epsilon$, according to Eq. (5.32); in particular, for each realization, we calculate the error for each eigenmode of the spin-chain and choose the maximum achievable fidelity. As shown in Fig. 33a, high-fidelity quantum gates can be achieved for few nanometer straggle provided that the NV depolarization time is ~ 200ms; similarly, for the longer chain case (Fig. 33b) with $N = 51$, high-fidelity gates are also possible, but require significantly longer T_1 of a few seconds.

Next, we analyze the participation ratio (PR) [230, 250],

$$N_{PR} = \frac{1}{\sum_{i=1}^{N} |\psi_i|^4} \tag{5.34}$$

which provides a characterization of the number of sites which participate in a given eigenmode; modes are typically said to be extended if $N_{PR} \sim \mathcal{O}(N)$ and localized if $N_{PR} \ll N$. In the case where the participation ratio is much shorter than the overall chain length, it becomes extremely difficult to perform quantum state transfer within the coherence window set by the quantum register. This allows us to quantitatively determine the regime over which high fidelity state transfer can be achieved despite the interplay between disorder and decoherence. As shown in the histograms of Fig. 33c, for increasing disorder, N_{PR} drops sharply as a function of σ_κ. By $\sigma_\kappa \approx 0.5\kappa$, on average, all eigenmodes exhibit a state transfer fidelity $< 2/3$ even for extremely long $T_1 \sim 5$s.

5.2.5 Strong Register Coupling

The eigenmode-mediated QST discussed above operates in the weak coupling regime, $g\psi \ll \kappa/N$. Numerical simulations reveal that by optimally tuning $g = g_M(N) \sim \kappa$, high-fidelity QST can also be achieved (see Fig. 35). This "strong-coupling" regime enables faster state transfer and has been analyzed in several recent studies [208, 230–232]. Here, our contribution is to show that this strong coupling regime still enables high fidelity state transfer in the case of unpolarized channels. We demonstrate this by performing numerical simulations and by deriving analytic channel fidelities valid for an arbitrary coupling pattern (analogous to subsection III). We emphasize that our results are consistent with and motivated by those in [208, 230–232].

To provide intuition for this strong-coupling regime [208, 230–232], we will begin by considering the engineered spin-chain described in [196], where we have $N + 2$ spin-1/2 atoms with nearest-neighbor XX-interactions. The intra-chain coupling is non-uniform and

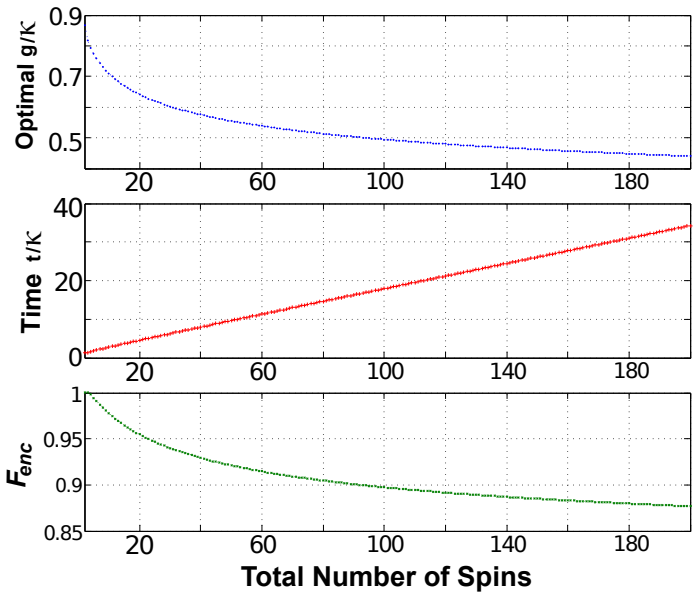

Figure 35: (color online). Strong coupling regime: By tuning $g/\kappa \sim N^{-1/6}$, we obtain high-fidelity QST utilizing an unpolarized chain with two-qubit encoding (paired-protocol). The transfer time scales linearly with N (Lieb-Robinson bound) [223] and high fidelities $> 90\%$ can be maintained for chain lengths up to $N = 100$.

is given by, $J_i = \frac{1}{2}\sqrt{(i+1)(N+1-i)}$, yielding a Hamiltonian

$$H = \sum_{i=0}^{N} J_i(\sigma_i^+\sigma_{i+1}^- + h.c.) + \sum_{i=0}^{N+1} \frac{h}{2}\sigma_i^z, \tag{5.35}$$

where h is a uniform background magnetic field. Upon employing the Jordan Wigner transformation, we once again return to a simple tight-binding form, with $H = \sum_{ij} K_{ij} c_i^\dagger c_j$ where $K_{ij} = J_i\delta_{j,i+1} + J_j\delta_{i,j+1} + h\delta_{i,j}$ up to a constant. Diagonalizing reveals $H = \sum_{k=0}^{N+1} \omega_k f_k^\dagger f_k$ with a linear spectrum given by $\omega_k = k + h - \frac{N+1}{2}$.

As described in subsection. III., the system's evolution is governed by $c_i(t) = \sum_j M_{ij}(t)c_i(0)$. Upon setting $h = \frac{N+1}{2}$, one finds that at time $t = 2\pi$, $M(2\pi) = \mathbb{Id}$ and therefore $c_i(2\pi) = c_i(0)$, returning the system to its initial state. As the coupling pattern $\{J_i\}$ harbors mirror symmetry with $J_i = J_{N-i}$, the orthogonal transformation, ψ, which diagonalizes H can also be chosen mirror symmetric, $\psi_{ik} = (-1)^{N+1+k}\psi_{N+1-i,k}$.

Setting $h = \frac{3}{2}(N+1)$ and $t = \pi$ yields,

$$M_{ij} = \sum_k \psi_{N+1-i,k}\psi_{jk} = \delta_{N+1-i,j}. \tag{5.36}$$

To demonstrate state transfer, let us recall the analytic single-swap fidelity given by Eq. (5.24). For the moment, let us assume that the spins $\{0, 1, \ldots N\}$ are all polarized, so that $\mathrm{Tr}[\rho_{ch}^{SS} P] = 1$. Combined with Eq. (5.36), which ensures $M_{0,N+1} = 1$, we find $F_{SS} = 1$, enabling perfect QST. We note that in lieu of applying a uniform magnetic field $h = \frac{3}{2}(N+1)$, one can also just apply a simple phase gate $U_P = \begin{pmatrix} 1 & 0 \\ 0 & (-i)^{N+1} \end{pmatrix}$ on spin 0 following transfer.

Turning now to the case of an unpolarized spin chain, we again employ the two-qubit encoding previously described. In this case, one will need to apply the phase gate, $U_P^2 = \begin{pmatrix} 1 & 0 \\ 0 & (-1)^{N+1} \end{pmatrix}$ to the logical qubit after state transfer.

The state transfer fidelities for these two strong coupling methods are given analogously by,

$$F_{SS} = \frac{1}{2} + \frac{1}{6}[2|M_{0,N+1}| + |M_{0,N+1}|^2), \tag{5.37}$$

$$F_{enc} = \frac{1}{2} + \frac{1}{6}[2|M_{0,N+1}|^2|M_{0,N+1}^2 - M_{0,0}M_{N+1,N+1}| + |M_{0,N+1}|^2 + |\sum_i M_{N+1,i}M_{i,0}|^2]. \tag{5.38}$$

While these expressions are valid for an arbitrary coupling pattern (so long as the resultant fermionic Hamiltonian is quadratic), to ensure high-fidelity QST, we require $|M_{0,N+1}| \approx 1$. As depicted in Eq. (5.36), satisfying this constraint is intimately related to the linear spectrum resulting from the choice of $J_i = \frac{1}{2}\sqrt{(i+1)(N+1-i)}$.

Let us now consider the strong coupling regime ($g \sim \kappa$) where $J_0 = J_N = g$ and $J_1 = J_2 = ... = J_{N-1} = \kappa$. Surprisingly, tuning only g/κ enables one to obtain a

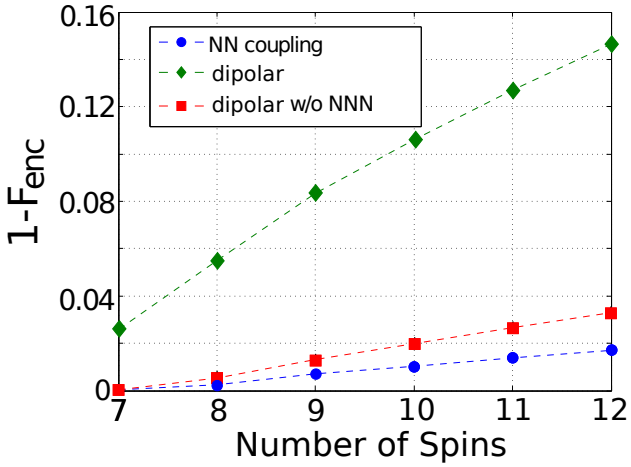

Figure 36: (color online). Infidelity of QST for a strongly coupled chain with long range interactions ($1/T_1$ is assumed negligible). Encoded state transfer (paired protocol) fidelities are shown for dipolar (diamonds), NNN-canceled-dipolar (squares) and NN interaction (circles) models.

quasi-linear spectrum [231]; such a spectrum will then ensure that $|M_{0,N+1}| \approx 1$, as desired. Of course, for $N = 2, 3$, $J_i = \frac{1}{2}\sqrt{(i+1)(N+1-i)}$ can be satisfied exactly. Although for $N > 3$, an exactly linear spectrum cannot be obtained, it is possible to optimally tune $g = g_M(N)$, so that ω_k looks nearly identical to the previous linear spectrum, $k - \frac{N+1}{2}$ $(h = 0)$, as shown in Fig. 34. In particular, by optimizing F_{enc}, we obtain $g_M \sim N^{-1/6}$, with a transfer time $\tau \sim N$ (Fig. 35), consistent with [231].

5.2.6 Long-range Interactions

Finally, we now consider the effect of longer range interactions. The majority of proposals for spin-chain state transfer focus on approximate nearest-neighbor models; however, the microscopic magnetic dipolar interaction is naturally long-range and decays as $1/r^3$, inducing an important infidelity in quantum state transfer. The origin of this infidelity becomes especially evident as we examine the Jordan-Wigner fermionization of the spin chain. Each Wigner fermion carries a string of the form $e^{-i\pi \sum_{j=1}^{i-1} \sigma_j^+ \sigma_j^-}$. In the nearest-neighbor case, all such strings cancel pairwise leaving a simple quadratic model. However, with longer-range interactions, uncanceled strings remain and generically

introduce perturbative quartic terms into the Hamiltonian. These quartic terms imply that the model, unlike the transverse field Ising model, is no longer diagonalizable in terms of free fermions. In the previous free fermion case, the energy of each eigenmode is independent of the occupation of all other eigenmodes; this enables state transfer even when the spin-temperature of the chain is effectively infinite. By contrast, the quartic terms associated with the long-range dipolar coupling introduce interactions between fermionic eigenmodes; the energy fluctuations of each eigenmode, caused by changing occupations of other modes, naturally dephases quantum information, limiting the operational spin temperature of the chain.

Certain proposals have suggested the possibility of using dynamical decoupling to effectively cancel next-to-neareast neighbor (NNN) interactions [116], but the complete canceling of all long-range interactions requires a level of quantum control that is currently beyond the realm of experimental accessibility. Since any long-range XX coupling destroys the quadratic nature of the fermionic Hamiltonian, an analytic solution for state transfer fidelities in the presence of full dipolar interactions is not available. Thus, we perform exact diagonalization for chains of length up to $N = 12$ (total number of spins), as shown in Fig. 36. We obtain the encoded state transfer fidelities for dipolar, NNN-canceled-dipolar and NN interaction models. Remarkably, even with full dipolar interactions, fidelities $\sim 90\%$ can be obtained for a total of $N = 10$ spins; in the case where NNN interactions are dynamically decoupled, the fidelities can be further improved to $\sim 98\%$ at similar lengths.

5.2.7 Quantum Mirror Architecture

In this subsection, we present an alternate quantum computing architecture based upon pulsed quantum mirrors [216, 233]. By contrast to eigenmode-mediated state transfer, remote quantum logic will be achieved by global rotations and NN Ising interactions. To remain consistent, we choose to discuss the advantages and disadvantages of such an architecture within the context of NV registers. In particular, analogous to Sec. V, we

consider NV registers connected by spin 1/2 chains of implanted Nitrogen impurities.

Let us begin with a detailed discussion of the mixed spin system composed of NV centers and Nitrogen impurities [116]. The full Hamiltonian of a single Nitrogen impurity is,

$$H_N = -\gamma_e \vec{B} \cdot \vec{S} - \gamma_N \vec{B} \cdot \vec{I} + A_\parallel S^z I^z + A_\perp (S^x I^x + S^y I^y), \tag{5.39}$$

where $\vec{S}$ is the spin-1/2 electronic spin operator, $\vec{I}$ is the nuclear spin operator, and $A_\parallel = -159.7$MHz, $A_\perp = -113.8$MHz are the hyperfine constants associated with the Jahn-Teller axis.

We envision the application of a magnetic field and field gradient, which, within a secular approximation, reduces the Hamiltonian of a nearest neighbor Nitrogen-impurity chain to Ising form [116],

$$H_N = \kappa \sum_{i=1}^{N-1} S_i^z S_{i+1}^z + \sum_{i=1}^{N} (\omega_0 + \delta_i) S_i^z, \tag{5.40}$$

where κ is the relevant component of the dipole tensor, ω_0 captures the electronic Zeeman energy, and δ_i characterizes the hyperfine term, which is nuclear-spin-dependent, for each impurity. Taking into account the magnetic dipole coupling between the electronic spin of the NV register and the surrounding Nitrogen impurities allows us to consider the mixed spin system,

$$H_{eff} = \sum_{i=1}^{a-1} \kappa S_i^z S_{i+1}^z + J S_{NV}^z (S_a^z + S_b^z) + \sum_{i=b}^{N-1} \kappa S_i^z S_{i+1}^z, \tag{5.41}$$

where J is the strength of register-impurity interaction, the Zeeman term in Eq. (5.40) is assumed to be echoed out, and superscripts a, b represent the pair of nearest-neighbor impurities next to a given register (assuming for simplicity a 1D geometry as shown in Fig. 37). The selective individual addressing of the NV registers is accomplished via a combination of optical beams and microwave driving; this enables an isolation of the coupling between the NV register and the two neighboring impurities. In particular, it is

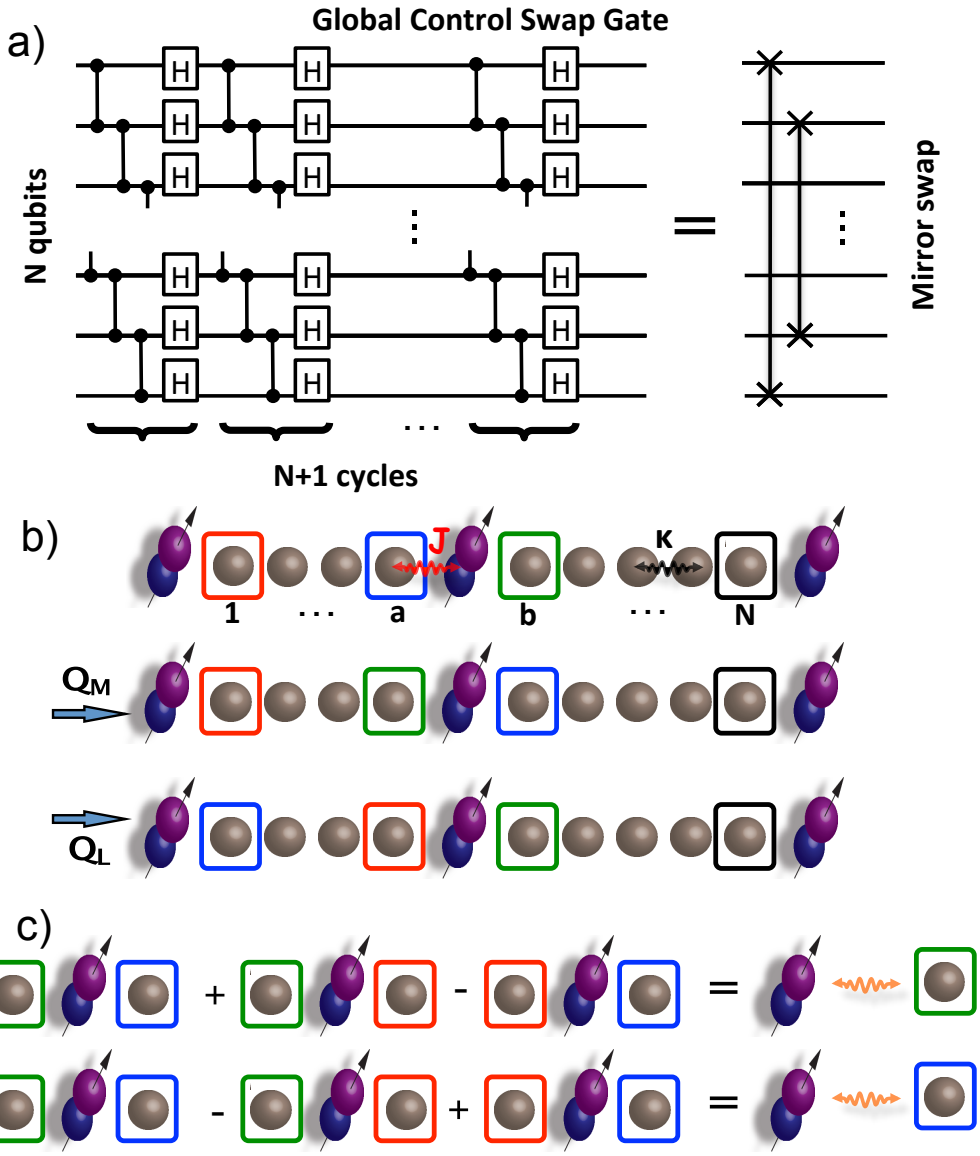

Figure 37: (color online). (a) In a qubit chain of length N, a mirror swap operation is defined as the pairwise swap between the $(1, N)$, $(2, N-1)$, $\cdots$ qubits. This can be achieved via global control in the form of single qubit gates (Hadamards) and controlled phase gates. Regardless of the initial state, a mirror swap occurs after a $N+1$ cycles of $Q = \tilde{H} \cdot \tilde{CP}$ [216], where $\tilde{H}$ represents a global Hadamard operation and $\tilde{CP}$ denotes a global controlled phase operation. (b) Coupling the central NV register to the NV on the left (right) requires the ability to perform a directed swap to a neighboring Nitrogen spin (grey). These directed swap operations are made possible by using combinations of the mirror sequences Q_M (swapS a pair of impurities directly surrounding an NV) and Q_L (mirror swaps an individual impurity chain). (c) Utilizing a fast echo-pulse on the NV register (in combination with Q_M and Q_L) allows one to generate selective interactions between the NV and any outlined Nitrogen.

possible to perform unitary evolution of the form
$U_{eff} = e^{-iH_{eff}T'/2}S^x_{NV}e^{-iH_{eff}T'/2}S^x_{NV} = e^{-i\kappa\sum S^z_i S^z_{i+1}T'}$ and hence,

$$U_{local} = e^{-iH_{eff}T}e^{-i\kappa\sum S^z_i S^z_{i+1}T'} = e^{-iJS^z_{NV}(S^z_a+S^z_b)T} \tag{5.42}$$

by choosing $\kappa(T+T') = 2\pi m$ for integer m. We note that this condition implies that the fidelity of U_{local} is extremely sensitive to both coupling-strength disorder as well as the general long-range nature of the dipolar interaction.

Globally Controlled Mirror swap

Considering only global addressing of the Nitrogen spin-chain and unitary evolution as described above, we demonstrate a universal set of operations between remote NV registers. Coherent register coupling is achieved by means of global pulses which mirror the quantum state of the impurity chain [216]; the pulses take the form of Hadamard gates and controlled phase gates, which can be generated by evolution under an Ising Hamiltonian. In an impurity spin-chain of length N, the global pulses swap the state of the first and N^{th} spin, the state of the second and $(N-1)^{st}$ spin etc, as shown in Fig. 37a. The total mirror swap results from $N+1$ cycles of Hadamard and controlled phase gates on all impurities, $Q_{n+1} = (\prod H_i \cdot \prod CP_i)^{n+1}$. This globally controlled impurity mirror will ultimately enable the directed and coherent interaction between remote NV registers.

Let us now consider a specific NV register, separated from neighboring registers by impurity spin-chains on both sides, as shown in Fig. 37b. Since the Ising Hamiltonian generates a controlled phase gate, it is possible to achieve a mirror swap between any set of qubits connected by Ising interactions. In particular, the impurity Ising interaction allows for a mirror operation within any impurity chain, while the Ising interaction corresponding to U_{local} allows for a three qubit mirror centered around any NV register. This local unitary enables an operation, Q_M, which swaps the state of the Nitrogen neighbors of the

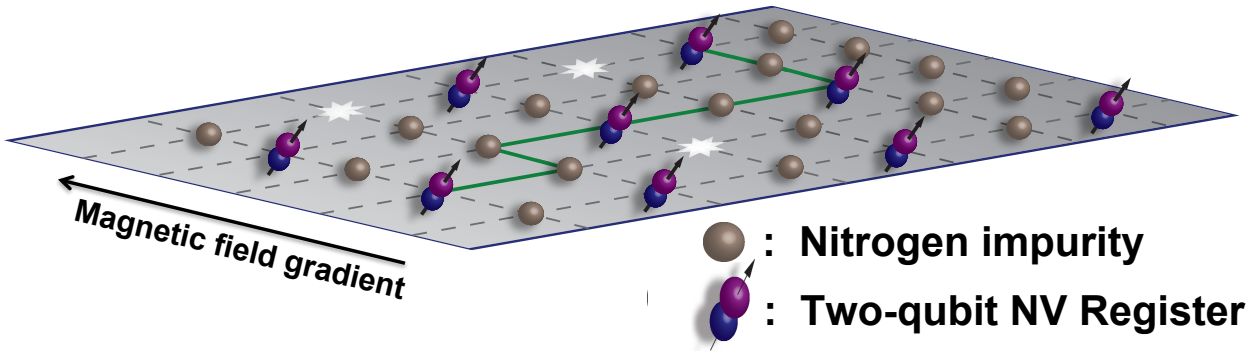

Figure 38: (color online). Schematic diagram of the 2D computational lattice showing limitations imposed by missing Nitrogen implantations (stars) and imperfect Nitrogen-to-NV conversions. Coherent coupling of distant NV registers in a faulty 2D array can be achieved via global pulsed control of a spin-chain quantum data bus. A combination of optical beams and a magnetic field gradient allows for individual control of NV registers; combined with global single qubit operations on Nitrogen impurities in any given row (orthogonal to the field gradient) [116], directed swap operations (e.g. dark green path) can be achieved, which allow for quantum information transfer along arbitrary paths. This field gradient enables a swap gate to be performed between two NV registers in adjacent rows, which occupy the same column. Moreover, it in fact also enables any pair of rows to be swapped, provided that the intrarow interactions refocus.

central NV register as shown in Fig. 37b.

To couple the central NV register to a specific side register, it will be necessary to break the left-right symmetry of the Ising interaction; this is achieved by exploiting the length asymmetry between Nitrogen chains to the left and right of the NV register. Indeed, it is often possible to refocus the mirror operation in one impurity chain while causing the edge impurity pair to swap in the other chain; we will denote this operation as Q_L, as shown in Fig. 37b. Combinations of Q_M and Q_L successfully manipulate and permute the impurities such that the nearest neighbors of the central NV register can be any pair of the three impurities (blue, red, green), as depicted in Fig. 37c. In combination with local rotations of the central register, this enables the application of "directed" unitary evolution, e.g. $U_{directed} = e^{-iJS^z_{NV}S^z_{N_b}T}$, allowing for the NV register to selectively couple to either side. This enables an interaction between any pair of neighboring NV registers effectively mediated by a single Nitrogen impurity,

$$H_{med} = J(S^z_{NV_1} + S^z_{NV_2})S^z_{N_b}, \tag{5.43}$$

where NV_1 and NV_2 denote the neighboring registers to be coupled and N_b represents the mediating impurity. The form of this Ising interaction implies that an application of Q_M on this effective three qubit system will swap the quantum information of the two electronic spins of the remote NV registers. Since each NV center harbors a nuclear-spin qubit in addition to its electronic spin [44], the "there-and-back" protocol described in subsection. II enables universal logic between remote registers.

Having achieved the ability to coherently couple distant NV registers within a row, assisted by Nitrogen impurities, we now turn to the coupling between adjacent rows in a two-dimensional lattice (Fig. 38). The simplest approach involves applying a magnetic field gradient along the columns. This would enable a swap gate to be performed between two NV registers in adjacent rows, which occupy the same column, provided all other interactions are echoed out. The limited occurrence of vertically adjacent NVs is a significant source of overhead; however, this limitation can be overcome if we achieve the ability to swap any pair of nearest neighbor qubits in the two-dimensional array, essentially allowing for the construction of arbitrary paths (Fig. 38). Moreover, the ability to swap along arbitrary paths also provides an elegant solution to the experimental limitation imposed by implantation holes, where a Nitrogen impurity may be missing from the ideal 2D lattice. Finally, it also enables the use of nominally dark Nitrogen impurities as computational resources, thereby significantly increasing the number of effectively usable qubits.

While arbitrary individual control of impurities would trivially enable such a scheme, realistic constraints limit us to individual control of NV registers and only global control of the impurity chains. Thus, it is necessary to utilize the permutation operation inherent to individual cycles $(\prod H_i \cdot \prod CP_i)^{n+1}$ of the mirror operation. These gate cycles correspond to an effective propagation of local gates via a relabelling of qubits within a given chain. In the simplest scenario, it is possible to apply a swap gate between the second and third qubit by only utilizing local rotations on the first qubit and global operations elsewhere, as

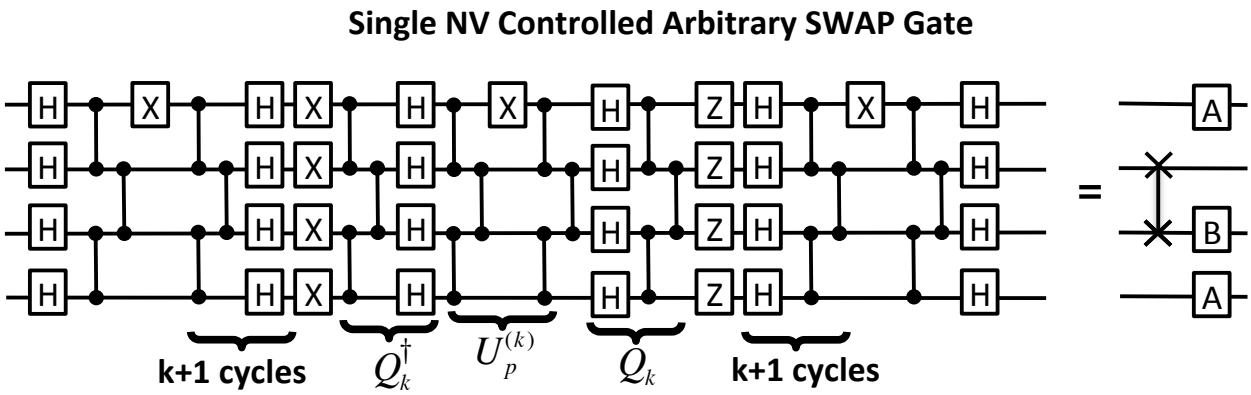

Figure 39: (color online). Individual control of any given NV register (row 1) enables a swap operation between any two neighboring qubits along the same row. We illustrate the specific example of a four qubit chain. The depicted gate sequence achieves a swap gate (up to individual qubit rotations A, B) between the second and third qubit by only applying a local gate X on the first qubit (NV register) and global operations elsewhere.

shown in Fig. 39. The fundamental operation to be propagated is $U_p = \tilde{CP} \cdot X_1 \cdot \tilde{CP}$ where X_1 is an x rotation (by π) on the first qubit and $\tilde{CP}$ represents a global controlled phase gate; propagation takes the form of conjugation by mirror cycles where $Q_k = (\tilde{H} \cdot \tilde{CP})^k$ and $U_p^{(k)} = Q_k^\dagger U_p Q_k$. To apply a swap operation on the n and $n+1$ qubit, we let $k = n-1$ and apply

$$U_{swap} = \tilde{H} U_p^{(k)} \tilde{H} \tilde{X} U_p^{(k)} \tilde{Z} \tilde{H} U_p^{(k)} \tilde{H}, \tag{5.44}$$

where $\tilde{X}$ is a global x rotation and $\tilde{Z}$ is a global z rotation (by π). This protocol requires the ability to produce a boundary at the location of the first qubit and allows for swaps between arbitrary spins in a given row; moving quantum information between rows can be achieved provided intrarow interactions refocus (e.g. if vertical and horizontal nearest-neighbor distances differ).

In summary, we have extended the analysis of eigenmode-mediated state transfer to a variety of imperfections ranging from disorder-driven localization to uncompensated long-range interactions. By calculating the analytic channel fidelity associated with eigenmode-mediated state transfer, we clarify the effects of entanglement arising from the protocol and illustrate the method in which the two-qubit encoding overcomes this

challenge. We analyze our protocol in the context of proposed solid-state quantum computing architectures; numerical simulations with realistic experimental parameters reveal that QST errors can be kept below certain surface-code error-correcting thresholds. Furthermore, we have generalized our protocol to the case of bosonic oscillator systems. This approach may enable the routing of a "ground-state-cooled" mode through a relatively "hot" intermediate oscillator chain, thereby significantly reducing the resources associated with system-wide cooling.

Moreover, our work may also provide insight into generalized infinite-temperature state transfer. In particular, by introducing a time-dependent control of the register-chain coupling, one may be able to compensate for off-resonant errors. This approach finds analogy to the continuum wave-packet limit, where dispersion limits transfer fidelities; in this case, pre-shaping of the packet can overcome nonlinearities of the dispersion.

Finally, we describe an alternate architecture based upon global control pulses which also enables remote quantum logic; in particular, we demonstrate that even intermediate chain spins can be used as registers, despite the fact that they are unable to be individually addressed. This may provide the blueprint for a novel quantum computing architecture which utilizes dark spins as quantum memory resources.

5.3 Long-range quantum gates using dipolar crystals

In this section, we explore an alternate method to realize long-range quantum gates by utilizing a finite-size phase transition through a dipolar crystal. We demonstrate that adiabatic driving of a dipolar spin system across a quantum phase transition can be used to implement a controlled phase gate between distant qubits in a robust manner.

Our approach is especially applicable to solid state systems that are strongly affected by natural imperfections leading to disorder, which can render the solid state system unable to act as a reliable quantum bus any longer. If one assumes perfect control over the quantum bus these imperfections can be characterized and corrected dynamically, but such a level of

control is currently out of reach for most realistic applications.

Thus motivated, we therefore take a different route to create a quantum bus within a disordered system. The key element is the phenomenon discussed in the context of Rydberg atoms as the blockade effect: due to the strong repulsive interactions, there cannot be two Rydberg excitations on distances shorter than an intrinsic length scale known as the blockade radius. Within this radius, the underlying spatial distribution of the particles is largely irrelevant. Thus, the arising many-body ground state washes out the disorder effects, up to the point where the Rydberg excitations form a crystalline phase [252]. However, we would like to stress that our proposal is not limited to Rydberg atoms. The same setup can be realized with nitrogen-vacancy (NV) defect centers in diamond, opening a route to many-body physics within these systems. Furthermore, we show using general scaling arguments that the fidelity of the proposed gate is equivalent to a microscopic $1/r^2$ interaction between the qubits and finally we discuss the required experimental parameters.

Our protocol for the controlled phase gate is based on the dynamical crystal formation in these dipolar systems [252–255], see Fig. 40. We consider two qubits A and B that are coupled to a quantum bus, which is initially prepared in the ground state that contains no Rydberg excitations. Then, the quantum bus is driven adiabatically across the phase transition. Depending on the boundary condition set by the state of the qubits, the resulting many-body state has a different energy. One can readily understand this effect as a compression of the crystal, by which the distance between two Rydberg excitatons a_R is decreased. Under free evolution, the energy difference is translated into a phase difference, which entangles the qubits. After reversing the adiabatic step, the quantum bus returns to its initial state while the qubits remain entangled.

5.3.1 Rydberg dipolar crystal

For the quantum bus we consider are an ultracold gas of atoms that can be excited to a Rydberg state, or an array of NV centers in diamond. Here, we are interested in the

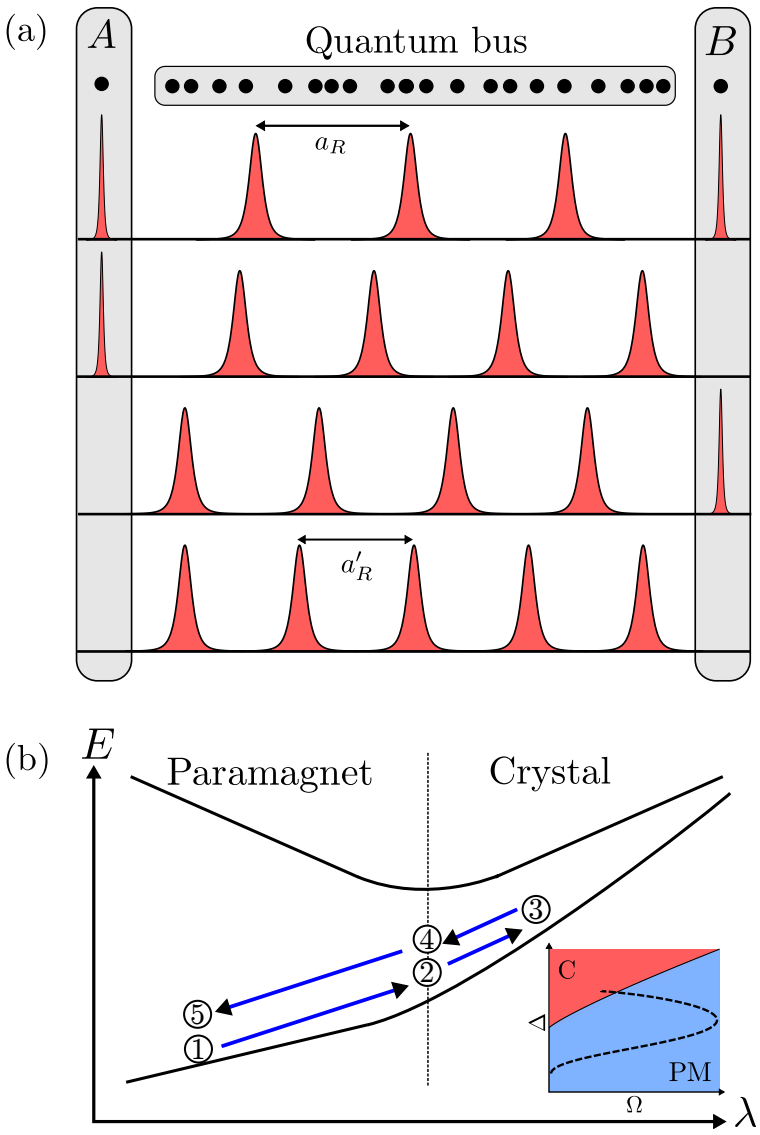

Figure 40: Setup for the proposed gate.(a) Depending on the state of the qubits A and B, the quantum bus prepared in a crystalline phase possesses a different ground state, where the distance between two Rydberg excitations a_R is changed, corresponsing to a compression of the crystal. (b) Ground state and first excited state during the control sequence. Initially, the quantum bus is prepared in the paramagnet (1). Then, control parameter λ is increased adiabatically (2), driving the system across the phase transition. Once in the crystal the system evolves freely and picks up a phase shift depending on the qubit states (3). After the adiabatic process is reversed (4), the quantum bus is disentangled from the qubits (5). The inset contains the phase diagram of the system, with the dashed line showing the control path depending on the Rabi frequency Ω and the detuning Δ.

strongly interacting regime, where the dipolar interaction between the particles is dominant. Within Rydberg atoms, the strongly interacting regime can also be reached for van der Waals interactions decaying like $1/r^6$. Both for Rydberg atoms and NV centers the quantum bus can be described in terms of an interacting spin 1/2 model, whose Hamiltonian is given by

$$H = -\frac{\hbar\Delta}{2}\sum_i \sigma_i^z + \frac{\hbar\Omega}{2}\sum_i \sigma_i^x + \sum_{i<j} \frac{C_p}{|\mathbf{r}_i - \mathbf{r}_j|^p} P_i^{\uparrow} P_j^{\uparrow}. \tag{5.45}$$

In the case of Rydberg atoms Δ and Ω are external laser parameters accounting for the detuning from the atomic resonance and the Rabi frequency driving the transition, respectively. Strong interactions with long-range character are described by a generalized C_p coefficient and involve the projectors onto the Rydberg state $P_i^{\uparrow} = |\uparrow\rangle\langle\uparrow| = (1+\sigma_i^z)/2$. For NV centers, the $m_s = 0$ state, which can be efficiently prepared by optical pumping, corresponds to the atomic ground state, while the $m_s = 1$ state possessing a magnetic dipole moment corresponds to the excited Rydberg state. Strong magnetic dipole interactions between different NV centers can be obtained if the separation is sufficiently small [256]. In the following, we will refer to the $|\uparrow\rangle$ state as the "Rydberg state", independent of the underlying physical implementation. The interaction between the quantum bus and qubits is governed by a similar interaction, i.e.,

$$H_{AB} = \sum_i \frac{C_p}{|\mathbf{r}_A - \mathbf{r}_i|^p} P_A^{\uparrow} P_i^{\uparrow} + \frac{C_p}{|\mathbf{r}_B - \mathbf{r}_i|^p} P_B^{\uparrow} P_i^{\uparrow}. \tag{5.46}$$

Note that this interaction conserves σ_A^z and σ_B^z, therefore the only possible entangling operation between the qubits is a controlled phase gate.

For one-dimensional (1D) systems it has been shown that the crystal spacing $a_R = [\zeta(p)(p+1)C_p/\Delta]^{1/p}$ is essentially independent of the spacing between individual spins, which suggests that the crystalline phase is stable against disorder [257]. Therefore, the effects of disorder can be analyzed in the classical limit with $\Omega = 0$. The crystalline

phase will break down when fluctuations in the positions of neighboring spins result in an additional interaction energy that overcomes the cost Δ to remove one Rydberg excitation. From this, we can see that the relevant quantity for this process is given by the maximum separation of two neighbors in the spin chain $R_{\max}$. For a uniform distribution of spins, this quantity can be calculated from the pairwise distance distribution $p_r(r)$, which is given by $p_r(r) = n \exp(-nr)$ with n being the density. Using extreme value statistics we find $\langle R_{\max} \rangle = n^{-1} \log N$, where N is the number of particles. Then, the creation of an additional Rydberg excitation is energetically favorable for

$$\hbar\Delta = \frac{C_p}{(a_R - R_{\max})^p}, \tag{5.47}$$

from which the critical detuning at which the crystal melts due to disorder can be calculated.

Let us now focus on the general properties of the proposed scheme that are largely independent of the microscopic detail. In particular, we are interested in the scaling behavior of a 1D setup with the system size L. There are three different factors that influence the asymptotic scaling with L: (i) the scaling of the effective interaction strength with the size of the system, (ii) the scaling properties of the energy gap protecting the adiabatic evolution, and (iii) the effects of decoherence. The effective interaction strength between the qubits A and B that eventually creates the entanglement between them can be computed as

$$E_{\text{int}} = E_{\uparrow\uparrow} - E_{\uparrow\downarrow} - E_{\downarrow\uparrow} + E_{\downarrow\downarrow}, \tag{5.48}$$

where $E_{\alpha\beta}$ refers to the energy of the many-body state with the qubits in state $|\alpha\rangle_A |\beta\rangle_B$, see Fig. 40. A straightforward calculation within the continuum limit of a classical crystal yields $E_{\text{int}} \sim b^2/L$, where b is the distance between the qubits and the ends of the quantum bus. Note that the classical crystal cannot be the true ground state of the system due to quantum fluctuations, instead the system has to be described in terms of a Luttinger liquid

[257, 258]. However, these corrections leading to an algebraic decay of the correlation functions only occur for very large system sizes [257].

5.3.2 Vanishing gap and decoherence

For analyzing the influences of both the gap and decoherence, we first note that we can write the gate error ε for nearly perfect gates as $\varepsilon \approx \varepsilon_1 + \varepsilon_2$, where ε_1 and ε_2 are the individual errors due to the gap and decoherence, respectively. To understand the scaling behavior of the gap, we first need to discuss some aspects of the underlying phase transition. While in the thermodynamic limit the gap vanishes at the phase transition, there is still a finite gap for finite size systems. For gapless phases, as in the Rydberg crystal, it is possible that the gap decreases even more the further one enters into the ordered phase. The qualitative behavior of the process can be described with a Landau-Zener model. There, the error of the process due to nonadiabatic transitions, i.e., the probability to stay in the ground state, is given by $\varepsilon_1 = \exp[-\Delta_G^2 t_g/(\hbar\lambda)]$, where Δ_G is the minimum value of the gap, t_g is the gate time, and λ is a microscopic coupling constant. It is possible to improve this scaling by adding a nonlinearity to the Landau-Zener sweep, resulting in a scaling of the form $\varepsilon_1 = \exp(-c\Delta_G t_g/\hbar)$, with c being a numerical constant that depends on the details of the model and the variation of the coupling constant [259, 260]. For the Rydberg crystal we have $\Delta_G \sim 1/L$ due to the phononic nature of excitations [257, 258], which is the theoretical optimum according to the Lieb-Robinson bound for information transfer [223]. In the following we separate off the system size dependence as $\alpha = c\Delta_G/\hbar = \alpha_0/L$.

The scaling properties of decoherence processes can be analyzed in a similar manner. Ignoring errors related to the non-adiabadicity of the process, the error $\varepsilon_2 = \varepsilon_2(\gamma t_g)$ is a monotonously increasing function depending only on the product of a decoherence rate γ and the gate time t_g. Here, we assume the form $\varepsilon_2 = 1 - \exp[-(\gamma t_g)^\delta] \approx (\gamma t_g)^\delta$, where the exponent δ depends of the physical details of the decoherence process. Since a

superposition of the different many-body states depicted in Fig. 40 is a highly entangled state, the decoherence rate $\gamma \sim L$ has to be proportional to the system size. We express this scaling again as $\gamma = \gamma_0 L/L_0$, where γ_0 is the single spin decoherence and L_0 is a length scale depending on the details of the many-body state. For the Rydberg crystal, we have L_0 to be given by the average distance between two Rydberg excitations a_R, since decoherence processes are only relevant at sites where there is an actual excitation.

Combining these results, we obtain for the error

$$\varepsilon = \exp(-\alpha_0/Lt_g) + (\gamma_0 L/L_0 t_g)^\delta. \tag{5.49}$$

Consequently, there exists an optimal time t_{opt}, at which the error is minimal. For high fidelity gates with $\alpha \gg \gamma$ the optimal time is given by $t_{\text{opt}} = \delta L \log[L_0\alpha_0/(L^2\gamma_0)]/\alpha_0$, which yields for the minimum error

$$\varepsilon = \left(\delta \frac{L^2\gamma_0}{L_0\alpha_0} \log \frac{L_0\alpha_0}{L^2\gamma_0}\right)^\delta. \tag{5.50}$$

Consequently, we find the same scaling as a microscopic interaction between the qubits decaying as $1/L^2$.

In the following we present numerical simulation results demonstrating that superior fidelities compared to the microscopic interaction can be obtained using the proposed setup. We consider a chain of N equidistant or disordered spins with interparticle distance a with the qubits being located at a distance b away from the ends of the chain. The details of the numerical simulation method are described in [252]. Initially, the qubits are prepared in the state $|\psi\rangle_{A,B} = (|\uparrow\rangle_{A,B} + |\downarrow\rangle_{A,B})/\sqrt{2}$, as this state is most affected by decoherence and consequently allows us to compute the fidelity of the gate. The spin chain is fully

polarized, i.e., $|\psi\rangle_{SC} = \prod_i |\downarrow\rangle_i$. Then, the external control fields are varied according to

$$\Omega(t) = \Omega_0 \sin^2\left(\frac{8t/t_0}{1+16t^2/t_0^2}\right) \quad (5.51)$$

$$\Delta(t) = \Delta_0[1 - 5\exp(-4t/t_0)], \quad (5.52)$$

where t_0 is the duration of the adiabatic step. Note that this protocol features the nonlinearity needed to improve the scaling properties of the gate fidelity. However, the protocol has not been optimized in great detail, therefore it might be possible to achieve even higher fidelities with improved protocols. At $t = t_0$ the system is held for a time $t_\pi = \pi\hbar/E_{\rm int}$, in order to have the system pick up a phase shift of π. Following this free evolution, the adiabatic step is reversed. Note that there are two ways how this reversal can be performed. One can either adiabatically follow the ground state or completely reverse the dynamics of the adiabatic step by flipping H to $-H$. The possibility to change the sign of the interaction depends on the physical implementations, for Rydberg atoms this can be achieved by transferring the population from a repuslsive to an attractive state. However, we find that both cases give very similar results and focus on the latter, as it simplifies the numerical analysis. The entire protocol will take the time $t_g = 2t_0 + t_\pi$. Then, the fidelity of the proposed gate is given by the residual entanglement between the qubits and the rest of the chain, which can be expressed as the disentanglement fidelity $F = \sqrt{\mathrm{tr}\,\rho_{AB}^2}$, where ρ_{AB} is the reduced density matrix of the qubits A and B. The data collapse in Fig. 41 shows that the fidelity depends only on the product $\Delta_G t_0$ according to $F = 1 - c\exp(-d\Delta_G t_0)$, where c and d are fit parameters. We have checked numerically that the resulting density matrix ρ_{AB} does indeed implement a controlled phase gate up to local phases.

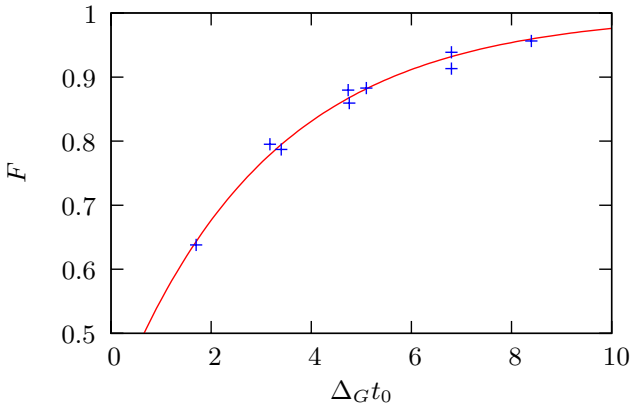

Figure 41: Numerical simulation results for the gate fidelity in the absence of decoherence depending on the product of the gap Δ_G and duration of the adiabatic step t_0 for up to $N = 34$ particles for equidistant (diamonds) and disordered (crosses) configurations. The gap has been varied independently from t_0 by changing Ω_0. The solid line is an exponential fit to the data. ($p = 3$, $C_3 = 100\Omega_0 a^3$, $\Delta_0 = 2.3\Omega_0$, $b = 3a$).

5.3.3 Fidelity of dipolar crystal gate

As discussed previously, there exists an optimum value for t_0 with respect to decoherence processes and nonadiabatic transitions. Here, the decoherence rate of the many-body state is enhanced by the factor $L/\langle a_R \rangle$. The fidelity for the quantum gate, including both nonadiabatic processes and decoherence, is given by

$$F = \frac{1}{2}[1 - c\exp(-d\Delta_G t_0)]\left\{1 + \exp\left[-\left(\gamma_0 L/\langle a_R\rangle t_g\right)^3\right]\right\} \tag{5.53}$$

for a spin echo type decoupling from the environment with $\delta = 3$. Note that up to the numerical constant β, this expression is equivalent to Eq. (5.49). Determining the optimum value for t_0 leading to the maximum fidelity is then straightforward. We now investigate in detail the consequence of disorder based on the previous analysis. Therefore, we numerically determine the gap Δ_G and the interaction energy E_{int} for 100 different uniformly distributed random configurations. We calculate the fidelity according to Eq. (5.53) and determine the optimum value of t_0. Figure 42 demonstrates that the fidelity is significantly higher than when directly using the microscopic interaction between the qubits A and B, even in the presence of disorder.

Using Rydberg atoms the proposed scheme can be either realized using the van der Waals interaction between S states ($p = 6$) or using the dipolar interaction between states within the Stark fan in an external electric field ($p = 3$). Focussing on the latter case with for a Rydberg state with a principle quantum number of $n' = 43$ and a decoherence rate $\gamma_0 = 10\,\mathrm{KHz}$, the laser parameters corresponding to a gate fidelity $F = 0.95$ are given by $\Omega_0 = 2\pi \times 3.2\,\mathrm{MHz}$ and $\Delta_0 = 2\pi \times 7\,\mathrm{MHz}$. Then, the corresponding interaction strength is found to be $C_3 n^3 = 2\pi \times 320\,\mathrm{MHz}$, which can be obtained in an atom cloud with an interparticle distance of $a = 1\mu\mathrm{m}$. Note that these parameters are compatible with present experimental techniques [261]. For van der Waals interactions the requirements to observe an improvement of the gate fidelity are even more relaxed.

As discussed above, it is also possible to implement the Hamiltonian required for the proposed gate using NV centers. There, coherence times of several milliseconds have been reached in isotopically pure diamond samples [45]. Using $\gamma_0 = 100\,\mathrm{Hz}$, this translates to a requirement for the microwave frequency of $\Omega_0 = 2\pi \times 80\,\mathrm{KHz}$ and $\Delta_0 = 2\pi \times 170\,\mathrm{KHz}$, and an average spacing of the NV centers of $a = 2\,\mathrm{nm}$. Note that fluctuation in the magnetic field giving rise to T_2^* dephasing processes can be canceled by stroboscopically switching the system between the $m_s = +1$ and $m_s = -1$ states, and adjusting the driving fields accordingly. In the resulting dynamics the election spin is then dynamically decoupled and coherence times up to the spin relaxation time T_1 can in principle be reached [262].

Finally, we would like to remark that the proposed long-range quantum gate is not limited to the dipolar crystal case. In fact, one can implement this setup using any continuous phase transition from a disordered to an ordered phase, provided that the couplings between the qubits and the quantum bus obey similar conservation laws and the ground state in the disordered phase is a product state. However, the robustness against disorder appears to be a characteristic feature of the dipolar crystals and opens up a common perspective for Rydberg atoms and NV centers.

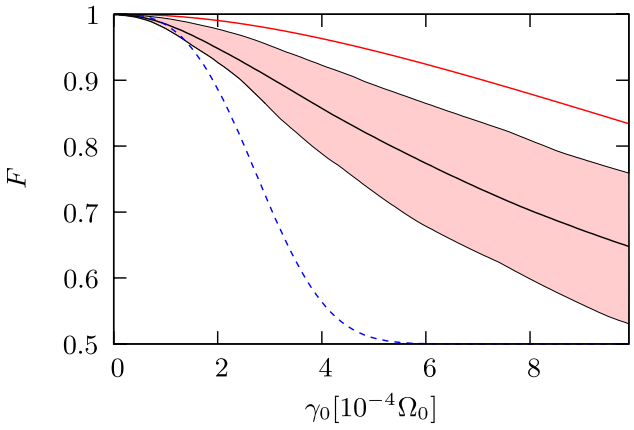

Figure 42: Dependence of the maximum fidelity of the proposed quantum gate on the decoherence rate γ_0 with parameters taken from the numerical simulation. The solid red line is the fidelity in the equdistant case, while the shaded areas correspond to 90% confidence intervals for a disordered situation. The dashed line indicates the fidelity that can be achieved using the dipolar interaction between the qubits.

5.4 Collectively enhanced quantum gates

Harnessing collective phenomena by utilizing ensembles of identical particles is a powerful tool, which has been exploited in effects ranging from superradiance to scattering suppression [263]. The coherent dynamics resulting from interactions with individual constituents of an ensemble are often too weak to be observed directly; however, as evidenced by experiments in systems such as Rydberg atoms [264–266], cavity QED [267, 268], atomic ensembles [269, 270] and solid state qubits [271], collective enhancement provides a natural route to overcoming this challenge. In this section, we demonstrate that, for electronic spin quantum registers, such collective effects enable an extended coherent coupling over large distances — an essential prerequisite for quantum information processing.

Owing to favorable coherence properties, electronic spins associated with point-like defects in solid-state systems have garnered significant recent interest as candidates for room-temperature quantum registers. Quantum control of such spins can be achieved using a combination of optical, magnetic and electric fields. While our considerations apply to a variety of electronic spin qubits [272–274], here, we focus on the Nitrogen-Vacancy (NV)

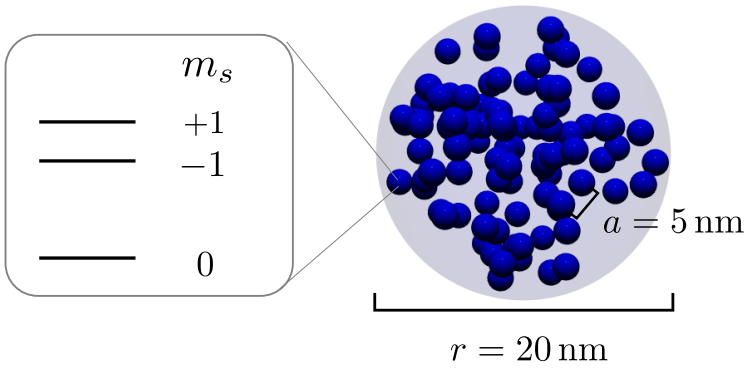

Figure 43: High-density NV spin ensemble distributed randomly within a sphere of diameter r, with an average distance a. The NV centers have three internal spin states that are split by a zero-field splitting and a Zeeman field.

center in diamond. The NV center harbors an electronic spin ($S = 1$), which can be optically initialized, coherently manipulated and read out on sub-wavelength scales [44, 59, 275]. These results have sparked several recent proposals which utilize networks of NV registers as the platform for a scalable quantum information processor [116, 210, 276, 277]. However, for any spin qubit candidate, two crucial challenges remain to be addressed: 1) the weakness of the magnetic dipolar interactions on distances compatible with individual optical addressing and 2) the disorder in spin positioning due to inherent imperfections during defect creation.

We present a novel approach to remote quantum logic which harnesses collectively enhanced interactions to overcome both of the above challenges. The key idea underlying our proposal is to associate a single, robust qubit with a collective, generally disordered spin-ensemble (Fig. 43). If the spins behave in an aggregate fashion, such a qubit can produce a large state-dependent magnetic field, leading to enhanced long-range coupling between ensembles; this is reminiscent of tailored light-matter interactions achieved via atomic ensembles [278]. However, we note that quenched disorder naturally leads to localization in solid-state spin systems, implying that each eigenmode of the ensemble is composed of only a few spins. Here, we demonstrate the use of a uniform transverse magnetic field to overcome this issue. The applied field causes the symmetric W-state

[279, 280] to become an approximate eigenstate of the Hamiltonian, thereby enabling us to harness it as a collective qubit. Moreover, we show that this particular state is largely insensitive to the underlying spin distribution and hence robust to effects of disorder.

5.4.1 Collective W State

To be specific, we now describe our proposal in the context of NV diamond color centers. The largest energy scale in this system (Δ) is set by a combination of the zero field splitting (2.87GHz) and a Zeeman field along the NV axis. We assume that this Zeeman field is sufficiently strong to ensure that the $m_s = -1$ spin state is sufficiently far detuned and hence does not contribute to the effective dynamics. Thus, the number of $m_s = 1$ spins, m, is an approximately good quantum number and a perturbative description is justified. The second-largest energy scale arises due to the perturbation created by the transverse field Ω. To gain a qualitative understanding, let us restrict ourselves to the analytically tractable case where m is either 0 or 1. The effective Hamiltonian is, $H_r = -\Delta|0\rangle\langle 0| + \sqrt{N}\Omega(|0\rangle\langle W| + \text{h.c.})$, where the state $|0\rangle$ has all ensemble spins polarized into $m_s = 0$, and the collective $|W\rangle$ state is fully symmetric with all spins sharing a single excitation,

$$|W\rangle = \frac{1}{\sqrt{N}} \sum_i |0 \ldots 1_i \ldots\rangle \,. \tag{5.54}$$

Second order perturbation theory in $\sqrt{N}\Omega/\Delta$ yields $H_r' = -\Delta|0\rangle\langle 0| + J|W\rangle\langle W|$, with $J = N\Omega^2/\Delta$. Including higher m manifolds merely leads to a renormalization of J, without changing this qualitative picture (so long as we are in the perturbative limit). This is equally true in the presence of dipolar interactions, provided that the energy scale J is larger than the characteristic strength of the dipolar interaction V_{dd}. Thus, even with these additional terms, the new eigenstates will still have substantial overlap with the collective $|W\rangle$ state. This is in stark contrast to the situation without a transverse field, where strongly quenched disorder owing to random spin positions localizes all such eigenstates, even in three dimensions. Furthermore, the dipolar interaction naturally ensures that

collective states with different m values will have different energies, leading to a "blockade"-type scenario, where manifolds with $m > 1$ are energetically inaccessible [279, 280]. This allows us to selectively drive the transition between $|0\rangle$ and $|W\rangle$ without populating any other collective states, provided that the external driving Ω_{ext} is weaker than V_{dd}. This hierarchy of energy scales can be summarized as: $\Delta \gg J \gg V_{dd} \gg \Omega_{\text{ext}}$.

Let us consider a three dimensional ensemble of $N = 100$ NV centers randomly distributed within a diameter $r = 20\,\text{nm}$, as depicted in Fig. 43. Such high density NV ensembles have been recently realized using long-time annealing of repeat-electron-irradiated diamond samples [74, 75, 281, 282]. We will characterize our effective two-level system ($m_s = 0, 1$) using Pauli spin operators σ_α. Being magnetic dipoles, NV centers interact with one another via long-range magnetic dipolar interactions (ignoring energy non-conserving terms which are suppressed by the NV center's zero field splitting),

$$V_{ij} = \left(1 - 3\cos^2\vartheta_{ij}\right) \frac{\mu^2}{|\mathbf{r}_i - \mathbf{r}_j|^3} \times \left\{ \frac{1}{4}\left[1 + \sigma_z^{(i)}\right]\left[1 + \sigma_z^{(j)}\right] - \sigma_+^{(i)}\sigma_-^{(j)} - \sigma_-^{(i)}\sigma_+^{(j)} \right\}, \quad (5.55)$$

where $\mathbf{r}_i$ denotes the position, μ characterizes the magnetic dipole moment, and ϑ_{ij} is the angle between the NV axis and the vector connecting sites $\mathbf{r}_i$ and $\mathbf{r}_j$. The total Hamiltonian including both on-site and interaction terms is then given by $H = \Delta/2 \sum_i \sigma_z^{(i)} + \Omega \sum_i \sigma_x^{(i)} + \sum_{i<j} V_{ij}$.

Let us now consider the enhanced coupling between an isolated NV defect (hereon termed "qubit") and the collective ensemble. We envision the ensemble to be initialized into the $|0\rangle$ state, while the NV qubit is initialized to the $m_s = 1$ state. By ensuring that the qubit splitting is tuned resonant with only the $|W\rangle$ state, one finds that the effective dynamics are restricted to the single-excitation manifold of the combined qubit-ensemble system; to lowest order, these dynamics are governed by,

$$H_{\text{eff}} = \sqrt{N_c}\frac{\mu^2}{R^3}(|1_q, 0\rangle\langle 0_q, W| + \text{h.c.}), \quad (5.56)$$

where N_c characterizes the approximate number of spins participating in the $|W\rangle$ state and the notation $|1_q, 0\rangle$ refers to the combined state with the NV qubit being in $m_s = 1$ and with the ensemble spins being in $|0\rangle$. Consistent with sub-wavelength techniques such as STED ($R = 100\,\text{nm}$), we will assume that the NV qubit can be manipulated and read out independently of the ensemble [227].

To support the qualitative picture presented above, we now perform exact diagonalization of the full Hamiltonian. In the majority of the numerics, we restrict ourselves to $m \leq 2$ excitations; however, we check the validity of our results by including the $m = 3$ manifold for slightly smaller system sizes. For each eigenstate $|\phi\rangle$, we calculate the collective enhancement factor, defined as

$$N_c = \left(\sum_i^N \langle 0_1 \dots 1_i \dots 0_N | \phi \rangle \right)^2, \tag{5.57}$$

which essentially characterizes the number of ensemble spins participating in the eigenmode. As expected, in the absence of a transverse field, disorder localizes all eigenstates and as depicted in Fig. 44 (blue circles), $N_c \ll N$ for all eigenstates. On the other hand, In the case of a moderate transverse field, $\Omega \approx h \times 100\,\text{MHz}$, one finds the existence of a single eigenstate with $N_c \approx 70 \sim N$. While the specific details of this state depend on the microscopic details (e.g., spin distribution within the ensemble and magnitude of the applied transverse field), its collective nature is rather robust. In particular, as one varies the strength of the transverse field Ω, there exists a large parameter regime where $N_c > 50$ (Fig. 44). The dips in N_c are associated with resonance effects, which arise when other eigenstates become near-degenerate with the collective state. Finally, the decrease of N_c for large values of Ω signals the breakdown of perturbation theory as $\sqrt{N}\Omega/\Delta$ approaches unity.

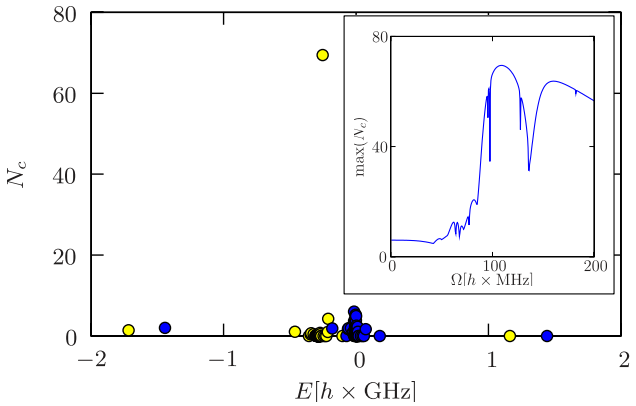

Figure 44: Comparison of the collective enhancement N_c for $\Omega = 0$ (blue) and $\Omega = h \times 110\,\mathrm{MHz}$ (yellow) within the single excitation manifold. In the latter case there is a collectively enhanced state with $N_c \approx 70$, corresponding to an increase by more than one order of magnitude ($\Delta = h \times 4\,\mathrm{GHz}$). The inset shows the maximum value of N_c depending on the transverse field strength Ω.

5.4.2 Numerical simulations

We now perform simulations of the combined qubit-ensemble system. As previously discussed, the system is initialized to $|1_q, 0\rangle$ and the qubit splitting is tuned resonant with the energy of the collective mode; the resulting dynamics is evinced in Fig. 45. Interestingly, the probability of finding the qubit in the $m_s = 1$ state, p_q, exhibits collectively enhanced Rabi oscillations. The frequency of these oscillations is enhanced by nearly an order of magnitude relative to that expected for bare dipolar interactions between two individual NV qubits at a similar distance. The numerics also allow us to obtain the time required for an interaction-induced π pulse, t_π and from this, one can derive the effective distance R associated with H_{eff}. Surprisingly, in all cases, we observe that this distance corresponds not to $R - r$, but instead to the distance between the NV qubit and the center of the ensemble. We study the effects of putting the qubit closer to the ensemble by calculating the collectively enhanced coupling strength V_c (as extracted from the numerically obtained t_π). As shown in Fig. 45, we find that only for distances very close to the ensemble does the collective enhancement deviates from the asymptotic $1/R^3$ scaling, e.g., the qubit is coupled to individual spins rather than to the entire ensemble.

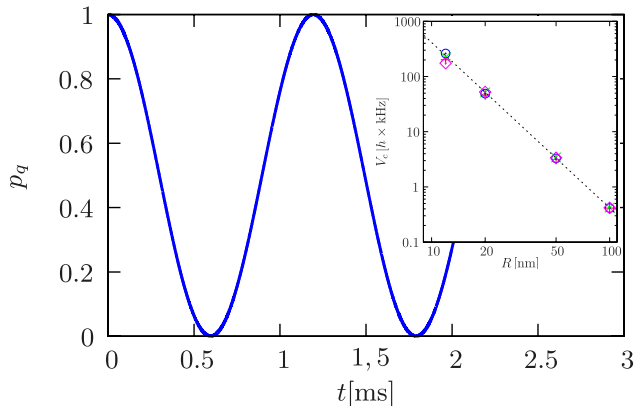

Figure 45: Collectively enhanced Rabi oscillations between an isolated NV qubit and a NV ensemble. The probability to find the qubit in the $m_s = 1$ state, p_q, goes to zero within a time $t_\pi \approx 600\,\mu$s. The inset shows the collectively enhanced coupling strength V_c between the qubit and the ensemble for four different realizations. The dashed line shows the asymptotic $1/R^3$ dependence.

5.4.3 Experimental Realization and Decoherence

Thus far, our discussion has assumed that both the NV qubit and the ensemble spins are perfectly decoupled from the environment. In any experimentally realistic scenario, however, there are two natural decoherence effects which will be present: spin dephasing and spin depolarization. We are particularly interested in the scaling of the decoherence rates with N, as this may adversely affect the scaling fidelity of our proposed long-range gates [210]. As the decoherence processes act locally on individual spins, we first calculate the decoherence rate for a single spin and multiply the result by N to obtain the rate for the collective state. For simplicity, we assume that the collective state is the previously described $|W\rangle$ state in which a single excitation is shared among all N spins.

First, let us consider the effects of spin dephasing. The worst-case scenario for such dephasing is given by the leaking out into non-symmetric states. Consequently, the error probability after a single T_2 dephasing event on spin i is given by the probability to leave the $|W\rangle$ state,

$$p_{\bar{W}} = p_{T_2}\left[1 - |\langle W|\,\sigma_z^{(i)}\,|W\rangle|^2\right] = \frac{4}{N} p_{T_2}\left(1 - \frac{1}{N}\right), \tag{5.58}$$

where p_{T_2} is the single spin dephasing rate. For large N, this result is essentially

independent of N (after weighing with the number of spins); therefore, the effect of T_2 processes on such a collective $|W\rangle$ state does not get enhanced by system size and in fact, is only slightly worse than for a single spin, i.e., it can be expressed in terms of an effective dephasing time T_2^{eff}.

Second, we consider the decoherence arising from phonon-induced spin depolarization processes (T_1). Here, we must distinguish between processes which flip an ensemble spin from $m_s = 1$ to $m_s = 0$, and the reverse. This asymmetry can easily be seen by noting that the $|W\rangle$ state has only one spin in $m_s = 1$, while all other spins are in $m_s = 0$. We denote the error probability associated with these two events as $p_{T_1}^{1\to0}$ and $p_{T_1}^{0\to1}$, respectively. For $p_{T_1}^{1\to0}$, the state $|0\rangle$ with all ensemble spins in $m_s = 0$ is not affected at all, while the probability to flip from the $|W\rangle$ state into $|0\rangle$ is given by

$$p_{W\to0} = p_{T_1^{1\to0}} |\langle 0| \sigma_-^{(i)} |W\rangle|^2 = \frac{p_{T_1^{1\to0}}}{N}, \tag{5.59}$$

which is again independent of the size of the ensemble after rescaling with N.

However, this is not the case for $T_1^{0\to1}$ processes. Both the $|0\rangle$ and the $|W\rangle$ state are strongly affected by such processes, since the existence of any additional spin in the $m_s = 1$ state corresponds to an effective magnetic impurity; this impurity modifies the energy of the collective state, thus tuning it out of resonance with the NV qubit. Additionally, this new state is also no longer an eigenstate of the Hamiltonian; numerical simulations demonstrate that this state dephases very quickly due to dipolar interactions within the ensemble. Thus, since any single spin $T_1^{0\to1}$ error will immediately dephase the collective state, the effective decoherence rate owing to $p_{T_1}^{0\to1}$ is enhanced by N and scales with the size of the ensemble.

While the system size scaling of $p_{T_1}^{0\to1}$ errors might seem unfortunate, in solid-state spin systems, it is often the case that $T_1 \gg T_2$. Our proposed protocol is particularly useful in cases where T_1/N remains longer than T_2, implying that the ensemble's decoherence is

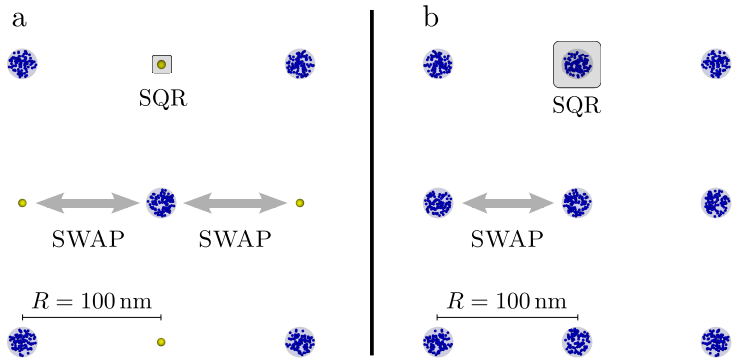

Figure 46: Scalable architectures with collectively enhanced interactions, corresponding to a lattice spacing of $R = 100\,\mathrm{nm}$, compatible with sub-wavelength optical addressing. (a) Individually addressable NV qubits (yellow) are used for single qubit operations (SQR), whereas the collectively enhanced interaction with an ensemble is used to mediate two-qubit gates via SWAP operations. (b) NV ensembles are used as collective qubits, where also single qubit operations are performed using the collective $|W\rangle$ state.

dominated by dephasing as opposed to the enhanced depolarization. The specific example of NV centers highlights this crucial point. The dephasing of the NV originates from fluctuating magnetic fields as neighboring pairs of dipoles flip-flop [45, 72]. Even at low temperatures it is impossible to freeze out such magnetic fluctuations and T_2 remains on the order of milliseconds [45, 113]. On the other hand, the depolarization of the NV is thought to originate from an Orbach spin-phonon process; such a process has an exponential dependence on temperature and implies that even moderate cooling can yield exceedingly long T_1 times ($\gg$ 1s at cryogenic temperatures) [283–285]. By liquid nitrogen temperatures, the errors introduced by the enhanced T_1 processes are already sub-percent, enabling us to focus on the effects of dephasing. An alternate approach to combat the enhanced depolarization of the collective state is to utilize conventional dynamical decoupling techniques (e.g. WAHUHA) [286] to suppress dipolar interactions within the individual ensembles.

5.4.4 Collective quantum gates

We now turn to a possible application where isolated NV qubits are interspersed with high-density NV ensembles, forming a regular structure, as depicted Fig. 46a. The qubits are used for initialization, single-qubit rotations, and readout. Two-qubit gates between remote spin qubits are mediated by the ensemble between them and thus benefit from collectively enhanced interactions. The gate time t_g is limited by the SWAP time t_π required to to transfer the information from one of the qubits to the ensemble (required four times per gate operation) [116]. The resulting error (assuming $T_1/N \gg T_2$) of the gate is given by $\varepsilon = 1 - \exp[-(4t_\pi/T_2^{\text{eff}})^3]$ in the presence of spin echo decoupling [287]. For an error of $\varepsilon = 10^{-2}$, this translates to a required dephasing time of $T_2^{\text{eff}} = 11\,\text{ms}$, which can be readily realized in isotopically pure diamond samples [45, 113] or by using dynamical decoupling pulses [72, 262]. The requirements on the coherence time can be further relaxed by increasing the number of spins in the ensemble or by reducing the qubit-ensemble separation.

An architecture featuring even better gate fidelities can be realized using a collective encoding scheme for the qubits (see Fig. 46b). There, the logical $|0\rangle$ state corresponds to all nuclear spins being polarized, while the logical $|1\rangle$ state is a collective nuclear spin $|W\rangle$ state. This state can be prepared by applying a microwave pulse to map the electronic $|W\rangle$ state onto a nuclear spin $|W\rangle$ state [280]. The timescale for such a single qubit operation is limited to approximately 100 kHz by the hyperfine splitting of the NV centers in the $m_s = 1$ state ($A_\parallel \approx -2.14\,\text{MHz}$ for ^{14}N) [288]. In this collective qubit architecture, two-qubit gates between ensembles are enhanced by a factor of N instead of $\sqrt{N}$, thus leading to a SWAP time of $t_\pi = 70\,\mu\text{s}$. Thus, we find that a gate error of $\varepsilon = 10^{-2}$ requires a dephasing time of $T_2^{\text{eff}} = 700\,\mu\text{s}$, while for $\varepsilon = 10^{-4}$, a coherence time of $T_2^{\text{eff}} = 3\,\text{ms}$ is needed [45, 113].

In summary, we have shown that collectively enhanced interactions can be realized between an NV qubit and a mesoscopic NV ensemble. Our proposed approach relies upon a transverse magnetic field to inhibit the localization of symmetric W-eigenstate. Our work

enables the realization of collectively enhanced quantum gates with high fidelity and provides an important step towards the realization of scalable quantum information architectures involving solid-state electronic spins.

Chapter 6

Architecture for a Nitrogen-Vacancy based Quantum Information Processor

In this previous chapter, we described various mechanisms to implement robust quantum logic between distant quantum registers. In this chapter, we take advantage of those mechanisms and propose a scalable architecture for a room-temperature quantum computer using thermal state transfer. The realization of a scalable quantum information processor has emerged over the past decade as one of the central challenges at the interface of fundamental science and engineering. Much progress has been made towards this goal. Indeed, quantum operations have been demonstrated on several trapped ion qubits, and other solid-state systems are approaching similar levels of control. Extending these techniques to achieve fault-tolerant operations in larger systems with more qubits remains an extremely challenging goal, in part, due to the substantial technical complexity of current implementations. Here, we propose and analyze an architecture for a scalable, solid-state quantum information processor capable of operating at or near room temperature. The architecture is applicable to realistic conditions, which include disorder and relevant decoherence mechanisms, and includes a hierarchy of control at successive length scales. Our approach is based upon recent experimental advances involving

Nitrogen-Vacancy color centers in diamond and will provide fundamental insights into the physics of non-equilibrium many-body quantum systems. Additionally, the proposed architecture may greatly alleviate the stringent constraints, currently limiting the realization of scalable quantum processors.

Nitrogen-Vacancy (NV) color centers in diamond stand out among other promising qubit implementations [40–43, 289–291] in that their electronic spins can be individually polarized, manipulated and optically detected under room-temperature conditions. Recent advances involving the quantum manipulation of such crystal defects have allowed researchers to achieve sub-diffraction limited resolution and dipole-coupling mediated entanglement between neighboring NV electronic spins [44–47, 58, 192, 226, 256, 292–295]. Despite such substantial developments in this and other experimental systems, it remains unclear whether these pieces can be combined into a scalable quantum information processor (QIP) capable of operating under ambient, room temperature conditions.

In what follows, we describe and analyze a feasible architecture for a diamond-based quantum information processor. Our approach makes use of an array of single NV centers, created through implantation of ions and subsequent annealing [45, 296]. Each NV center constitutes an individual quantum register containing a nuclear spin and a localized electronic spin. The nuclear spin, which has a long coherence time, serves as the memory qubit, storing quantum information, while the electronic spin will be used to initialize, read out, and mediate coupling between nuclear spins of adjacent registers. Magnetic dipole interactions allow for coherent coupling between NV centers spatially separated by tens of nanometers. While in principle, a perfect array of NV centers would enable scalable quantum information processing, in practice, the finite creation efficiency of such centers, along with the requirements for parallelism, necessitate the coupling of registers separated by significantly larger distances. To overcome this challenge, we show that the coupling between NV centers can be mediated by an optically un-addressable "dark" spin chain data bus (DSCB). For concreteness, within our architecture, we will consider the specific

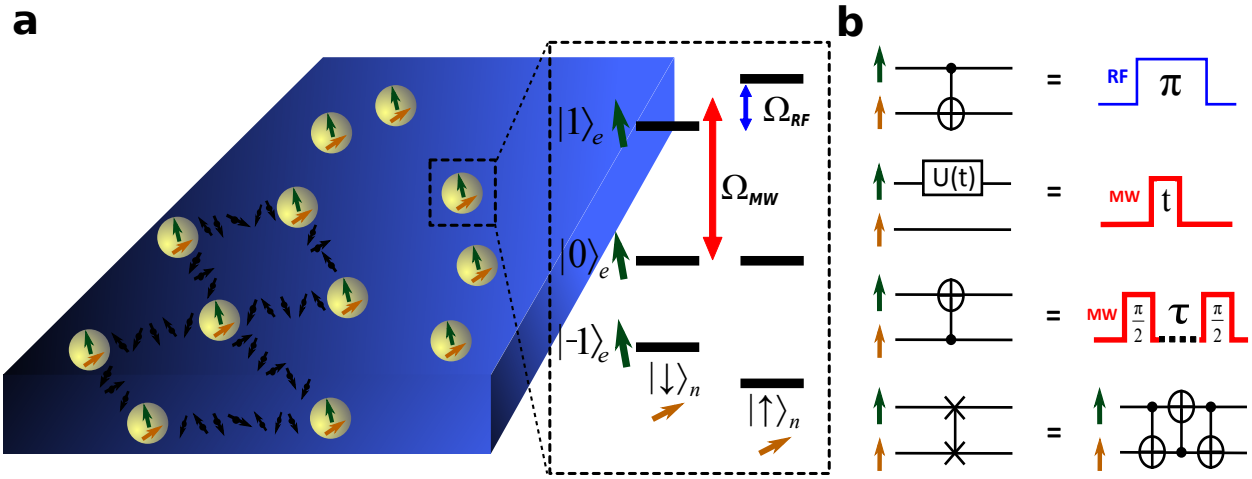

Figure 47: Schematic representation of individual NV registers within bulk diamond. (a) Each NV register contains a nuclear spin $I = 1/2$ (yellow), providing quantum memory, and an electronic spin $S = 1$ (green). Dark spins (black) represent elements of an optically un-addressable spin chain which coherently couples spatially separated NV registers. The NV level structure (in a high B field) is shown. A resonant microwave (Ω_{MW}) pulse coherently transfers the electronic spin of the register from $|0\rangle_e$ to $|1\rangle_e$; subsequent manipulation of the nuclear spin is accomplished through an RF pulse (Ω_{RF}). The far detuned $|-1\rangle_e$ state can be neglected to create an effective two-qubit register. However, the full three level NV structure will be utilized in horizontal DSCB mediated coherent coupling of NV registers. (b) A universal set of two-qubit gates can easily be achieved with only MW and RF controls [48]. Electronic spin manipulation can be accomplished with a MW field, where t represents the duration of the MW pulse. By exploiting the hyperfine coupling between the electronic and nuclear spin, one can achieve controlled-NOT operations conditioned on either spin. In particular, a $C_e NOT_n$ gate can be accomplished by utilizing a RF π-pulse, which flips the nuclear spin conditioned on the electronic spin being in $|1\rangle_e$. Similarly, a $C_n NOT_e$ gate can be accomplished by utilizing the hyperfine interaction to generate a controlled-phase (CP) gate, where τ represents the duration of the wait time required to achieve such a hyperfine-driven CP gate. Performed between two single-qubit Hadamard gates ($\pi/2$-pulses) on the electronic spin, such a CP gate generates the desired $C_n NOT_e$ gate. Finally, combining the $C_e NOT_n$ and $C_n NOT_e$ gates allows for the execution of a SWAP gate.

implementation of such a DSCB by utilizing implanted Nitrogen impurities (P3 centers) with spin 1/2, as shown in Fig. 47a. [292, 297].

6.0.5 The NV Qubit Register

Single NV registers contain a spin triplet electronic ground state ($S = 1$) and can be optically pumped and initialized to the $|0\rangle_e$ spin state, which has no magnetic dipole coupling with other NV registers or impurities. After optical initialization, the electronic

spin of each register remains in the $|0\rangle_e$ state, unless coherently transferred to the $|1\rangle_e$ state by a resonant microwave (MW) pulse, as depicted in Fig. 47a [44–47]. The nuclear spin associated with Nitrogen atoms ($I = 1/2$ for ^{15}N) possesses an extremely long coherence time and will serve as the memory qubit in our system [59]; manipulation of the nuclear spin is accomplished with RF pulses [48]. The Hamiltonian governing the electronic and nuclear spin of the NV register is

$$H_{e,n} = \Delta_0 S_z^2 + \mu_e B S_z + \mu_n B I_z + A S_z I_z, \tag{6.1}$$

with zero-field splitting $\Delta_0 = 2.87$GHz, electronic spin gyromagnetic ratio $\mu_e = -2.8$MHz/Gauss, nuclear spin gyromagnetic ratio $\mu_n = -0.43$ kHz/Gauss, and hyperfine coupling $A = 3.0$ MHz [44]. The application of a magnetic field along the NV-axis ($\hat{z}$) ensures full addressability of the two-qubit system, resulting in the energy levels shown in Fig. 47a. A universal set of two qubit quantum operations can easily be achieved with only MW and RF controls, as shown in Fig. 47b [48].

Furthermore, it is possible to selectively readout the state of the NV register; for example, to readout the nuclear qubit of a register, we apply a $C_n NOT_e$ gate to couple the electronic and nuclear spins, thereby allowing for readout of the electronic spin based on fluorescence detection. In the case where NV registers are separated by sub-optical-wavelength distances, the readout of registers will be complicated by the strong fluorescence background from neighboring NV centers. To suppress this background fluorescence, a red donut beam can be used, with its minimum located at the particular NV center being read out [226]. Thus, while the fluorescence signal from the NV register located at the minimum persists, the remaining illuminated registers will be dominated by the stimulated emission induced by the red donut beam. In addition to suppressing the background noise, the red donut beam can also suppress the nuclear decoherence of the remaining NV registers, by reducing the amount of time these registers spend in the

excited electronic state. After each round of fluorescence detection, the electronic spin is polarized to the $|0\rangle_e$ state, while the I_z component of the nuclear spin, a quantum non-demolition observable, remains unchanged [298]. Therefore, it is possible to repeat this readout procedure multiple times in order to improve the readout fidelity [256, 295]. A strong magnetic field $B_{z,0} \sim 1$ Tesla along the NV axis should be used to decouple the electronic and nuclear spins in order to achieve high fidelity single shot readout of NV registers [256]. In addition to sub-wavelength readout, optical donut beams also introduce the possibility of selectively manipulating individual NV registers with subwavelength resolution. While un-illuminated NV centers may respond to a resonant MW pulse, illuminated registers undergo a strong optical cycling transition which suppresses their response to microwave pulses due to the quantum Zeno effect [227, 299].

6.0.6 Approach to Scalable Architecture

One of the key requirements for fault-tolerant quantum computation is the ability to perform parallel gate operations. In our approach, this is achieved by considering a hierarchy of controllability. The lowest level of the hierarchy consists of an individual optically addressable plaquette with horizontal and vertical spatial dimensions $\sim 100 - 500$nm, containing a single computational NV register, as shown in Fig. 48a. The plaquette dimensions are chosen such that register control and readout can be achieved using conventional far-field or sub-wavelength optical techniques [44, 59, 226, 227, 293]. The second level, termed a super-plaquette ($\sim 10\mu$m $\times 10\mu$m), consists of a lattice of plaquettes whose computational registers are coupled through DSCBs. At the highest level of the hierarchy, we consider an array of super-plaquettes, where individual super-plaquettes are controlled by confined microwave fields [300]. In particular, micro-solenoids can confine fields to within super-plaquettes, allowing for parallel operations at the super-plaquette level. For example, as depicted in Fig. 48, independent microwave pulses can allow for simultaneous operations on the electronic spins of all

computational NV registers within all super-plaquettes. In order to control registers at the super-plaquette boundaries, we define a dual super-plaquette lattice (Fig. 48a). Localized microwave fields within such a dual lattice can provide a smooth transition between the boundaries of neighboring super-plaquettes.

Taking advantage of the separation of length scales inherent to optical control and microwave confinement provides a mechanism to achieve parallelism; indeed, the hierarchical control of plaquettes, super-plaquettes, and super-plaquette arrays allows for simultaneous single- and two-qubit gate operations, which are fundamental to fault-tolerant computation. One of the key difference in the currently proposed architecture as compared to previous proposals [42, 290] is that the design here does not rely on optically resolved transitions, which are only accessible at cryogenic temperatures.

The required 2D array of NV centers can be created via a two-step implantation process and the selective manipulation of individual registers within such an array is enabled by the application of a spatially dependent external magnetic field $B_z(y) = \frac{dB_z}{dy} y + B_{z,0}$. The 1D magnetic field gradient is sufficiently strong to allow for spectroscopic microwave addressing of individual NV registers, each of which occupies a unique row in the super-plaquette, as shown in Fig. 48b.

6.0.7 Results and Discussion

Dark Spin Chain Data Bus

To coherently couple two spatially separated NV centers, we consider two distinct approaches. First, we consider an approach, which is appropriate for spin-state transfer along the direction of the magnetic field gradient, in which individual addressing of spins is possible. This allows for an adiabatic sequential SWAP between neighboring qubits and, consequently, between the ends of the chain. Alternatively, in the situation where individual addressing of spins is not possible (i.e. direction transverse to the field gradient),

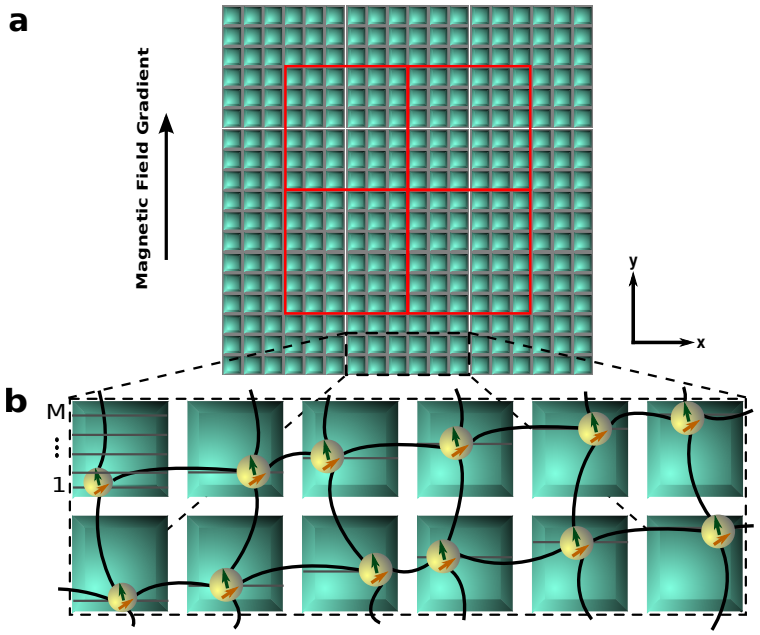

Figure 48: The architecture for a room-temperature solid-state quantum computer. (a) A two-dimensional hierarchical lattice allowing for length-scale based control, which enables fully parallel operations. At the lowest level, individual plaquettes are outlined in grey and each contains a single computational NV register. At the second level of hierarchy, a super-plaquette, outlined in white, encompasses a lattice of plaquettes; each super-plaquette is separately manipulated by micro-solenoid confined microwave fields. In order to allow for quantum information transfer across boundaries of super-plaquettes, there exists a dual super-plaquette lattice outlined in red. (b) The schematic NV register implantation within a super-plaquette. Two rows of individual plaquettes within a super-plaquette are shown. NV registers, consisting of an electronic (green) and nuclear (yellow) spin are depicted within a staggered up-sloping array which is row-repetitive. Individual rows within a single plaquette are specified by an integer n with $n = 1$ being the bottom row and $n = M$ being the top row. To achieve a staggered structure, we specify a unique implantation row within each plaquette wherein single impurities are implanted and subsequently annealed. For a given row of plaquettes, the implantation row corresponding to the left-most plaquette is n = 1, while the plaquette to the immediate right has implantation row n = 2; this pattern continues until the final plaquette in a given row, which by construction, has the highest implantation row number. The implantation process is repeated for each row of plaquettes within the super-plaquette and creates an array of NV registers, which each occupy a unique row in the super-plaquette. Since each NV register occupies a unique row within the super-plaquette, the magnetic field gradient in the $\hat{y}$ direction allows for individual spectroscopic addressing of single registers. Coherent coupling of spatially separated NV registers in adjacent plaquettes is mediated by a dark spin chain data bus (DSCB) and is schematically represented by the curved line connecting individual registers. The second implantation step corresponds to the creation of these horizontal and vertical dark spin chains.

we show that global control pulses achieve effective Hamiltonian evolution, which enables quantum state transfer through the spin chain. In both cases, we show that perfect state transfer and remote coupling gates are possible even when the intermediate spin chain is completely unpolarized (infinite spin temperature).

We begin by analyzing the adiabatic sequential SWAP in a spin-1/2 chain. This approach is suitable to couple registers in plaquettes that are vertically adjacent, relying upon the individual addressability of qubits and utilizing the magnetic dipole coupling between spin-chain elements. Under the secular approximation, the magnetic dipole coupling between a pair of neighboring spins can be reduced to Ising form

$$H_{int} = 4\kappa S_z^1 S_z^2 + \sum_{i=1,2} (\omega_0 + \delta_i) S_z^i, \tag{6.2}$$

where κ is the relevant component of the dipole tensor, ω_0 captures the electronic Zeeman energy, and δ_i characterizes both the hyperfine term (nuclear spin dependent) and the magnetic field gradient. From the Ising Hamiltonian, an XX interaction between qubits can be distilled by driving with $H_{drive} = \sum_{i=1,2} 2\Omega_i S_x^i \cos[(\omega_0 + \delta_i)t]$, leading to (under the rotating wave approximation, in the rotating frame, and in a rotated basis with $(x, y, z) \to (z, -y, x)$)

$$H_{int} = \kappa(S_1^+ S_2^- + S_1^- S_2^+) + \Omega_1 S_z^1 + \Omega_2 S_z^2. \tag{6.3}$$

The spin-flip process in H_{int} is highly suppressed in the limit of $|\Omega_1 - \Omega_2| \gg \kappa$, while the same process is dominant in the case of $|\Omega_1 - \Omega_2| \ll \kappa$. Hence, by slowly ramping the Rabi frequencies Ω_1 and Ω_2 through one another, adiabatic SWAP of the quantum states of the two impurities can be achieved through rapid adiabatic passage, as shown in Fig. 49a. Generalizing to arbitrary length spin chains yields $H_{int} = \sum_i \kappa(S_i^+ S_{i+1}^- + S_i^- S_{i+1}^+) + \sum_i \Omega_i S_z^i$, whereby the sequential adiabatic SWAP of quantum states along the spin chain can be achieved by successively tuning individual Rabi

frequencies across one another. During the adiabatic SWAP of a single pair of spins, higher order interactions, such as those resulting from next-to-nearest neighbors, will be suppressed due to the differences in Rabi frequencies. By including the magnetic dipole coupling between the electronic spin of the NV register and the spin chain quantum channel, we arrive at an effective mixed spin chain with the DSCB connecting the two electronic spins of the vertically separated NV registers. The specific procedure resulting in adiabatic sequential SWAP mediated coupling between NV registers is depicted in Fig. 3c.

Crucially, such an adiabatic sequential SWAP is robust against variations in the coupling strength κ, which can be induced by the imprecise implantation of impurities that form the spin-1/2 chain; in particular, even for the case of varying $\kappa_{i,i+1}$, perfect adiabatic SWAP occurs so long as the rate at which Ω_i and Ω_{i+1} are ramped through one another is sufficiently small. Within the proposed architecture, the impurities forming the horizontal spin chain will not induce operational errors during the vertical adiabatic sequential SWAP since the design principle allows for selective spin echoing.

Next, we consider a second method, termed free fermion state transfer (FFST) developed in [116], to coherently couple NV registers. In contrast to the adiabatic sequential SWAP, the method utilizes only global control over impurities and effective Hamiltonian evolution. The relaxation of the requirement of individual control over elements of the dark spin chain renders this second method applicable for coherent coupling between NV registers in horizontally adjacent plaquettes, transverse to the direction of the field gradient. In particular, the protocol achieves coherent coupling through an unpolarized, infinite temperature spin chain, employing purely Hamiltonian evolution under

$$H_{FFST} = g(S^+_{NV_1}S^-_1 + S^+_{NV_2}S^-_N + \text{ h.c.}) + \sum_{i=1}^{N-1} \kappa(S^+_i S^-_{i+1} + S^-_i S^+_{i+1}) \tag{6.4}$$

as shown in Fig. 49b. This Hamiltonian, obtained in analogy to Eq. (6.3), results in coherent interactions between NV centers, which is best understood via an analogy to

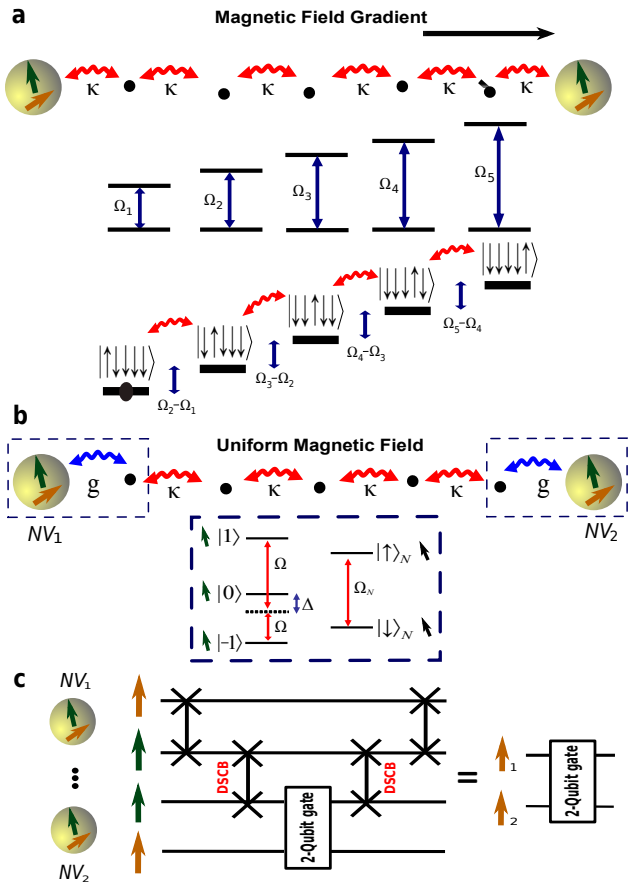

Figure 49: Dark spin chain data bus (DSCB) mediated coherent coupling of spatially separated NV registers, which does not require spin chain initialization. (a) Adiabatic sequential SWAP along the vertical direction, parallel to the magnetic field gradient. Individual addressing of impurities, enabled by the field gradient, allows for a slow ramping of the Rabi frequencies Ω_i and Ω_j through one another; this achieves adiabatic SWAP of the quantum states of the two impurities through rapid adiabatic passage. Thus, sequential adiabatic SWAP of quantum states along the spin chain can be achieved by successively tuning individual Rabi frequencies across one another. (b) Free fermion state transfer in the horizontal direction, transverse to the magnetic field gradient. The coupling strength between the end qubits and the spin chain is g, while the interchain coupling strength is κ. Schematic representation of the level structure of the NV electronic spin and a dark impurity spin. Controlling the NV-impurity coupling g is an essential component of FFST and occurs by driving the NV in two-photon resonance, with Rabi frequency Ω and detuning Δ. (c) Schematic circuit diagram outlining the protocol to achieve coherent coupling between the nuclear memory qubits of spatially separated NV registers. First, the nuclear and electronic qubits of a single register are swapped. Next, the electronic qubits of the two NV centers to be coupled are swapped via the DSCB. Finally, a two-qubit gate between the electronic and nuclear spin of the second register is performed before the memory qubit is returned to the nuclear spin of the original NV center.

eigenmode tunneling in a many-body system. Specifically, the spin chain described by H_{FFST} can viewed as a system of non-interacting fermions. As described in [116], by tuning the NV centers into resonance with a single fermionic eigenmode, an effective three-state system can be realized. Mediated by this fermionic eigenmode, the electronic states of two remote NV centers can be coherently swapped, leading to an analogous protocol for remote register coupling as shown in Fig. 49c. Crucially, such a SWAP gate is insensitive to the polarization of the intermediate dark spins and high-fidelity quantum state transfer can be achieved, provided that the fermionic mode is delocalized and that the coupling, g, of the NV qubit to the spin chain is controllable. As detailed in the Materials and Methods, by utilizing the three-level NV ground-state structure (Fig. 49b), it is possible to fully control the NV-chain coupling. This tunability also ensures that FFST is fundamentally robust to experimentally relevant coupling-strength disorder, which could be induced by implantation imprecision. Indeed, by separately tuning the NV-chain coupling on either side of the DSCB, it is possible to compensate for both disorder-induced asymmetry in the fermionic eigenmode as well as altered statistics of the eigenenergies [116, 218, 301].

Implementation, Operational Errors and Gate Fidelities

The specific implementation of the DSCB can be achieved with implanted Nitrogen impurity ions. Dipole coupling between neighboring Nitrogen electronic spins forms the DSCB, while dipole coupling between the NV and Nitrogen electronic spins forms the qubit-DSCB interaction; non-secular terms of this magnetic dipole coupling are highly suppressed due to the spatially dependent external magnetic field $B_z(y)$, resulting in the effective interaction found in Eq. (6.2). In addition, the Nitrogen impurities possess a strong hyperfine coupling, the principal axis of which can take on four possible orientations due to tetrahedral symmetry [285, 302, 303]. Dynamic Jahn-Teller (JT) reorientation of the Nitrogen impurity's hyperfine principal axis results in two particular considerations: 1) the addressing of additional JT frequencies yielding a denser super-plaquette frequency

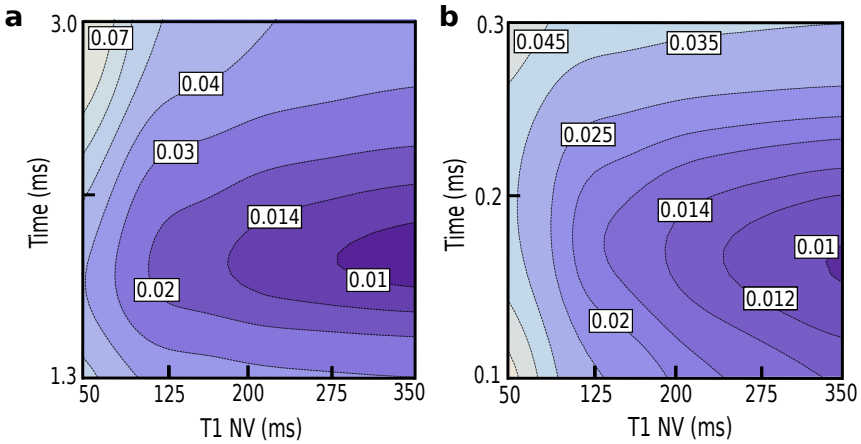

Figure 50: Numerical simulation of the DSCB fidelity. (a) The operational infidelity associated with the adiabatic sequential SWAP for $N = 18$. The simulations account for the Jahn-Teller orientation of Nitrogen impurities and utilize the optimized adiabatic ramp profile [259]. Simulations utilize an optimized coupling strength of 8.71kHz (18.1nm spacing). Full numerical integration of the time dependent Schrödinger equation produces infidelity contour plots as a function of total SWAP time and T_1^{NV}. (b) Numerical simulations of the operational infidelity associated with FFST for $N = 7$. Non-nearest neighbor interactions are assumed to be refocused through dynamic decoupling. Simulations, which utilize an optimized coupling strength of 12.6kHz (16nm spacing), are based upon a full diagonalization and also account for the Jahn-Teller orientation of Nitrogen impurities. Infidelity contour plots are again shown as a function of total SWAP time and T_1^{NV}.

spectrum and 2) the JT-governed spin-lattice relaxation (SLR) time T_1^N. Since T_1^N is characterized by an Arrhenius rate equation [302] at ambient temperatures, a combination of a static electric field and slight cooling by ≈ 50K allows for a substantial extension of the relaxation time to ~ 1s; hence, in the following consideration of operational errors, we will assume that we are limited by T_1^{NV}, the spin-lattice relaxation time of the NV center.

We now consider various imperfections, which may introduce operational errors. In particular, we consider the errors associated with: 1) sequential SWAP mediated coupling between vertically adjacent registers and 2) FFST between horizontally adjacent registers. We begin by discussing the analytic error estimate associated with each method, after which, we summarize the results of full numerical simulations.

First, we consider the accumulated infidelity associated with the adiabatic sequential

SWAP,

$$p_{err}^{SS} \approx N(p_{off}^{SS} + p_{adia} + p_{dip} + p_{T1}^{SS} + p_{T2}^{SS}). \tag{6.5}$$

The first term, $p_{off}^{SS} \sim \left(\frac{\Omega_i}{\Delta_g}\right)^2$, represents off-resonant excitations induced by microwave manipulations with Rabi frequency Ω_i. Here, Δ_g characterizes the gradient-induced splitting achieved within the super-plaquette frequency spectrum. The second term, p_{adia}, corresponds to the non-adiabatic correction resulting from an optimized adiabatic ramp profile [259, 304, 305]. The third term, $p_{dip} \sim \left(\frac{\kappa}{\Omega_i}\right)^2$, is directly obtained from Eq. (6.3) and corresponds to additional off-resonant errors. The fourth error term, p_{T1}^{SS} corresponds to the depolarization error induced by the finite NV T_1 time, while the final error term, p_{T2}^{SS} corresponds to the infidelity induced by dephasing. Since each error term is considered within the context of a single adiabatic SWAP, the total error contains an additional factor of N, representing the chain length, which is plaquette size dependent (e.g. $N \approx 5$ for 100nm and $N \approx 20$ for 500nm).

We can similarly consider the accumulated infidelity associated with FFST,

$$p_{err}^{FFST} \approx p_{off}^{FFST} + p_{fermi} + p_g + p_{T1}^{FFST} + p_{T2}^{FFST}. \tag{6.6}$$

In direct analogy to p_{err}^{SS}, the first term in p_{err}^{FFST} corresponds to the excitation of an NV register by off-resonant microwave fields. The second term, p_{fermi}, corresponds to the undesired coupling with off-resonant fermionic modes. Since the coupling strength is characterized by $g/\sqrt{N}$ [116], while the splitting of the eigenenergy spectrum $\sim \kappa/N$, such an off-resonant error induces an infidelity $\sim (\frac{g/\sqrt{N}}{\kappa/N})^2$. The third error term, p_g, results from the protocol designed to control, g, the NV-chain coupling (see Materials and Methods for details). Finally, directly analogous to p_{err}^{SS}, the fourth and fifth terms correspond to errors induced by the operational time, t_{FFST}, which causes both depolarization and dephasing.

Finally, we perform numerical simulations, taking into account the Nitrogen JT frequencies, to characterize the infidelity of both the adiabatic sequential SWAP and FFST

within the NV architecture, as depicted in Fig. 50. The results of these calculations are in excellent agreement with the above theoretical predictions. In particular, these simulations reveal that, for sufficiently long $T_1^{NV} \sim 100$ms, operational infidelities in both DSCB methods can be kept below 10^{-2}.

These simulations clearly show that the T_1 time of the NV electronic spin is of critical importance in obtaining high-fidelity quantum operations. While at room temperature T_1 appears to vary depending on the particular sample and on the specific properties of the local NV environment, such as strain, values on the order of 10ms are generally obtained [59, 285]. However, the spin-lattice relaxation mechanism governing T_1 is most likely related to an Orbach process [283], which is strongly temperature dependent. In such a case, modest cooling of the sample by $\approx$ 50K, is likely to extend T1 by more than an order of magnitude, thereby making high fidelity gates possible.

Given that such numerical estimations suggest the possibility of achieving high fidelity two-qubit operations between remote NV registers, the proposed architecture seems well suited to the implementation of topological quantum error correction [228, 229, 289, 306]. Recent progress in optimizing the 2D nearest-neighbor surface code has yielded an error threshold of $\epsilon \approx 1.4\%$ [229], which is above the estimated infidelity corresponding to both the adiabatic sequential SWAP and FFST; thus, in principle, implementation of the 2D surface code can allow for successful topological quantum error correction, and hence, fault tolerant quantum computation [307].

6.0.8 Outlook

The above considerations indicate the feasibility of experimentally realizing a solid-state quantum computer capable of operating under ambient conditions at or near room temperature. We emphasize that a majority of the elements required for the realization of individual qubits in our architecture have already been recently demonstrated. In our approach, these techniques are supplemented by both a new mechanism for remote register

coupling between NV centers as well as a hierarchical design principle, which facilitates scalability. The remote coupling mechanisms discussed can naturally be implemented via Nitrogen ion implantation in ultra-pure diamond crystals and are robust to realistic imperfections and disorder [116].

While the implementation and integration of the various proposed elements still require substantial advances in areas ranging from quantum control to materials science, a feasible approach to room temperature quantum information processing can greatly alleviate the stringent requirements associated with cryogenic temperatures, thereby making the realization of a scalable quantum computer significantly more practical.

The present work opens a number of new directions which can subsequently be explored. In particular, while we have considered the direct errors associated with DSCB mediated coupling, it is instructive to note that the fidelity of such quantum gates can often be significantly improved using techniques from optimal control theory [308, 309]. For example, such methods of optimal control, while negating the detrimental effects of decoherence, can also simultaneously allow for the implementation of high-fidelity gates despite both frequency and coupling disorder as induced by ion implantation errors. Indeed, the ability to precisely guide the quantum evolution via optimal control, even when the system complexity is exacerbated by environmental coupling, provides an alternative solution to improve single and two-qubit gate fidelities [310]. In addition, it is well known that the local strain field surrounding each NV center can significantly alter the register's properties; hence, through a detailed understanding of electric field induced strain, it may be possible to improve the coherence properties of the qubit. Beyond these specific applications, a number of scientific avenues can be explored, including for example, understanding and controlling the non-equilibrium dynamics of disordered spin systems.

6.0.9 Theoretical Methods

Controlling Qubit-Chain Coupling in the NV Architecture

To achieve an effective Hamiltonian of the form given by Eq. 6.4, it is essential to control the coupling strength between the NV register and the neighboring impurity. Here, we utilize the three levels of the NV electronic spin [311] to effectively control g, as shown in Fig. 49b, whereby the Hamiltonian (under microwave driving) can be written as

$$H = -\Delta(|1\rangle\langle 1| + |-1\rangle\langle -1|) - \Omega(|0\rangle\langle 1| + |0\rangle\langle -1| + \text{h.c.}) - \Omega_N S_x^N + 4\kappa S_z^{NV} S_z^N, \tag{6.7}$$

where Ω represents the Rabi frequency on the NV register, Δ represents the associated detuning, and Ω_N represents the Rabi frequency on the Nitrogen impurity. In this case, since the NV two-photon detuning is zero, it is convenient to define bright and dark states, $|B\rangle = \frac{|1\rangle+|-1\rangle}{\sqrt{2}}$ and $|D\rangle = \frac{|1\rangle-|-1\rangle}{\sqrt{2}}$; further, in the resulting two-level picture, the associated dressed states are $|+\rangle \approx |B\rangle + \frac{\sqrt{2}\Omega}{\Delta}|0\rangle$ and $|-\rangle \approx |0\rangle - \frac{\sqrt{2}\Omega}{\Delta}|B\rangle$, in the limit $\Omega \ll \Delta$. Hence, rewriting the Hamiltonian in this limit yields

$$\begin{aligned} H = & -\Delta|D\rangle\langle D| - (\Delta + \frac{2\Omega^2}{\Delta})|+\rangle\langle +| \\ & + \frac{2\Omega^2}{\Delta}|-\rangle\langle -| - \frac{1}{2}\Omega_N(|+\rangle_N\langle +| - |-\rangle_N\langle -|) \\ & + 2\kappa(|B\rangle\langle D| + |D\rangle\langle B|)(|+\rangle_N\langle -| + |-\rangle_N\langle +|), \end{aligned} \tag{6.8}$$

where $|\pm\rangle_N = \frac{|\uparrow\rangle_N \pm |\downarrow\rangle_N}{\sqrt{2}}$ correspond to the two S_x^N-eigenstates of the Nitrogen impurity. The coupling term can be further re-expressed as

$$2\kappa\left\{(|+\rangle\langle D| + |D\rangle\langle +|) - \frac{\sqrt{2}\Omega}{\Delta}(|-\rangle\langle D| + |D\rangle\langle -|)\right\}(|+_N\rangle\langle -_N| + |-_N\rangle\langle +_N|). \tag{6.9}$$

Thus, by working within the NV subspace $\{|D\rangle, |-\rangle\}$, it is possible to completely control the coupling between the NV register and Nitrogen impurity, $g \sim \kappa\frac{\Omega}{\Delta}$, by tuning the Rabi

frequency and detuning. It is possible to work in the required two-state subspace by ensuring that $\kappa \ll \Delta$ and hence, that the $|+\rangle$ state remains unpopulated, with corresponding off-resonant error κ^2/Δ^2.

Furthermore, we evince a possible scheme to coherently map the quantum information that is stored in the nuclear memory into the desired electronic subspace. For example, consider mapping $|0\rangle \otimes (\alpha|\uparrow\rangle + \beta|\downarrow\rangle)$ to $(\alpha|-\rangle + \beta|D\rangle) \otimes |\uparrow\rangle$, where the first (tensor) factor corresponds to the electronic state and the second corresponds to the nuclear state of a single NV. The proposed mapping can be achieved in a two-step process. First, by simultaneously performing a $\pi-$pulse on the transitions $|0\rangle \otimes |\downarrow\rangle \rightarrow |-1\rangle \otimes |\downarrow\rangle$ and $|0\rangle \otimes |\downarrow\rangle \rightarrow |1\rangle \otimes |\downarrow\rangle$ with oppositely signed Rabi frequencies, one can map $|0\rangle \otimes |\downarrow\rangle$ to $|D\rangle \otimes |\downarrow\rangle$. Next, one utilizes an RF pulse to flip the nuclear spin, which yields $|D\rangle \otimes |\downarrow\rangle \rightarrow |D\rangle \otimes |\uparrow\rangle$. Finally, turning Ω on in an adiabatic fashion ensures that the state preparation populates only $|D\rangle$ and $|-\rangle$, thereby mapping the quantum information into the desired electronic subspace.

Chapter 7

Topologically protected quantum state transfer

At the end of the previous chapter, we mentioned that one crucial challenge facing the implementation of an NV-based room-temperature quantum computer is the issue of disorder. In particular, disorder tends to localize modes of the spin chain, limiting the fidelity of quantum state transfer. In this chapter, we address this challenge by describing a possible topological spin data bus which can overcome effects of disorder. Topology plays a central role in ensuring the robustness of a wide variety of physical phenomena. Notable examples range from the robust current carrying edge states associated with the quantum Hall and the quantum spin Hall effects to proposals involving topologically protected quantum memory and quantum logic operations. Here, we propose and analyze a topologically protected channel for the transfer of quantum states between remote quantum nodes. In our approach, state transfer is mediated by the edge mode of a chiral spin liquid. We demonstrate that the proposed method is intrinsically robust to realistic imperfections associated with disorder and decoherence. Possible experimental implementations and applications to the detection and characterization of spin liquid phases are discussed.

The decoherence of both quantum states and quantum channels represents a major hurdle in the quest for the realization of scalable quantum devices [312, 313]. Several avenues are currently being explored to address these important challenges. For example,

quantum repeater protocols are expected to improve the fidelity of quantum state transfer – the fundamental building block of quantum communication [314, 315]. Similarly, quantum error correction can significantly extend the lifetime of quantum memories and suppress the errors associated with quantum logic operations [316, 317]. The practical realization of these technologies, however, requires a high level of quantum control that is as yet, not experimentally accessible. An alternative paradigm to achieving protected quantum states is provided by topology; indeed, if such states can be stored in the topological degrees of freedom of certain exotic states of matter, they become intrinsically robust against local noise [237, 238, 318–321].

The implementation of robust long-lived quantum memories can also be achieved by encoding quantum bits in appropriately chosen physical degrees of freedom. For example, the natural isolation of nuclear spins immunizes them from the environment and makes them an exceptional candidate for the storage of quantum information [44, 45, 59, 256, 322, 323]. Such solid-state spin qubits can be locally coupled with high fidelities, enabling the realization of few-bit quantum registers [59, 256]. However, spatially remote registers interact extremely weakly; thus, in this context, the challenge of scalability is shifted to the development of quantum channels capable of connecting remote registers in a robust and noise-free fashion [116, 241, 324].

This chapter describes a novel approach to the realization of intrinsically robust quantum channels and exploits topological protection to enable high-fidelity quantum information transport. We envision quantum state transfer between remote spin registers to be mediated by a 2D system composed of interacting spins. Specifically, the spin system is tuned into a gapped chiral spin liquid phase, which harbors a fermionic edge mode. The prototype of this specific chiral spin liquid is the gapped B phase (CSLB) of the Kitaev honeycomb model [325]. Although such a phase is best known for its non-Abelian vortex excitations, here, by operating at finite temperatures below the gap, we make use of its Majorana fermionic edge mode as a topologically protected quantum channel. Moreover,

we discuss possible applications of our protocol for the spectroscopic characterization of spin liquid states [326].

7.0.10 Approach to Topologically Protected State Transfer

Our approach to quantum state transfer is schematically illustrated in Fig. 51. Quantum information is encoded in a two-qubit spin register, with each qubit capable of being individually manipulated. The register is coupled to the edge of a two-dimensional spin droplet, whose elements we assume cannot be individually addressed but can be globally "engineered" to create a spin liquid state in the CSLB phase. The transfer protocol proceeds by mapping the quantum information stored in the left-hand spin-register onto the chiral edge mode of the droplet. The resulting wavepacket traverses the edge before retrieval at the remote register.

A distinct feature of our protocol, as compared with previous approaches [116, 196, 202, 216, 241], is the fundamental robustness of the quantum channel. The chiral nature of the fermionic edge mode ensures that destructive backscattering during state transfer is highly suppressed; moreover, the characteristic (linear) dispersion of the edge-mode ensures that wave packet distortion is minimized. Finally, we demonstrate that our approach is remarkably insensitive to disorder and decoherence affecting both the bulk and edge of the droplet. Although any spin system with a stable CSLB-like phase can potentially mediate topologically protected state transfer (TPST), to illustrate the microscopic mechanism responsible for such state transfer, we turn initially to a particular model and will later generalize our analysis to include the effects of disorder, additional interactions, and decoherence.

7.0.11 TPST on the Decorated Honeycomb

We now consider a specific exactly solvable spin-1/2 model which supports robust TPST [327]. Within this Yao-Kivelson model, the spins are situated on a triangular-decorated

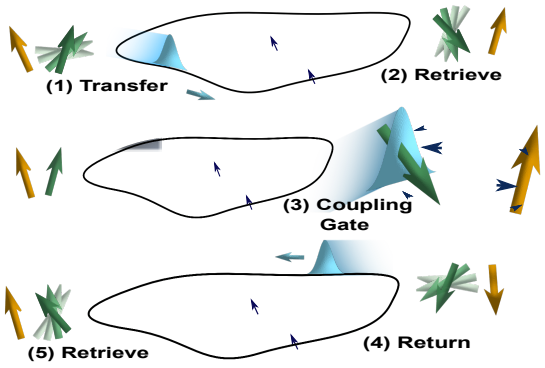

Figure 51: Schematic representation of topologically protected state transfer | The grey droplet represents a 2D array of interacting spins tuned into the CSLB phase. Quantum spin-registers composed of a transfer qubit (green) and a memory qubit (gold) are arranged around the edge of the 2D droplet and coupling between them occurs through the chiral edge mode. (1) By mapping the quantum information onto a fermionic wave-packet (blue) traveling along the edge, the quantum state can be transferred to a remote register. The wavepacket travels only in the direction of the blue arrow; this chirality prevents mode localization and destructive backscattering. At a specified time at the remote register location, the coupling is turned on and the wavepacket is captured (2). Given an ancillary memory qubit and local register manipulations, a two-qubit gate (3) can be performed before the quantum state is transferred back to the original register and stored (4-5). This allows for universal computation between the memory qubits of spatially separated registers.

honeycomb lattice as depicted in Fig. 52 [327]. The associated Hamiltonian naturally generalizes the Kitaev model [319] and features a chiral spin liquid ground state (CSLB phase),

$$H_0 = \frac{1}{2}\sum_{\substack{x,x'\\ links}} \kappa\sigma_i^x\sigma_j^x + \frac{1}{2}\sum_{\substack{y,y'\\ links}} \kappa\sigma_i^y\sigma_j^y + \frac{1}{2}\sum_{\substack{z,z'\\ links}} \kappa\sigma_i^z\sigma_j^z, \tag{7.1}$$

where $\vec{\sigma}$ are Pauli spin operators ($\hbar = 1$). The model may be solved by introducing four Majorana operators, $\{\gamma^0, \gamma^1, \gamma^2, \gamma^3\}$ for each spin, as shown schematically in Fig. 52a and by representing the spin algebra as: $\sigma^x = i\gamma^1\gamma^0$, $\sigma^y = i\gamma^2\gamma^0$, $\sigma^z = i\gamma^3\gamma^0$ [325, 327]. The Majorana operators are Hermitian and satisfy the standard anticommutation relation $\{\gamma^l, \gamma^m\} = 2\delta_{lm}$. The Hilbert space associated with the physical spin is a two-dimensional subspace of the extended four-dimensional Majorana Hilbert space; thus, we must impose the gauge projection, $P = \frac{1+D}{2}$, where $D = \gamma^1\gamma^2\gamma^3\gamma^0$ [325].

Transforming to Majorana operators results in the extended Hamiltonian

$$H^{\gamma} = \frac{i}{4}\kappa \sum_{i,j} \hat{U}_{i,j}\gamma_i^0\gamma_j^0, \tag{7.2}$$

where $\hat{U}_{i,j} = i\gamma_i^{\alpha}\gamma_j^{\alpha}$ (α depends on the type of ij-link) for ij connected and zero otherwise; these $\hat{U}_{i,j}$ correspond to the boxed Majorana pairs illustrated in Fig. 52a. Remarkably each $\hat{U}_{i,j}$ commutes with the Hamiltonian and with all other $\hat{U}_{l,m}$, implying that the extended Hilbert space can be divided into sectors corresponding to static choices of $\{U_{i,j} = \pm 1\}$ [325, 327].

The choice of $\{U_{i,j}\}$ yields a Hamiltonian which is quadratic in the γ^0 Majorana operators; from the perspective of these Majoranas, $U_{i,j}$ is a static background $\mathbb{Z}_2$ gauge field. The physical states are sensitive only to the flux of the gauge field, $w(p) = \prod_{ij\in\partial p} U_{i,j}$, where p represents a plaquette, ∂p is its boundary and ij is oriented according to the arrows in Fig. 52b [327]. For any link with $U_{i,j} = +1$, this orientation can also be interpreted as the direction in which a γ^0 Majorana hops in order to accumulate a $\pi/2$ phase. The ground state flux sector of the model has $w(p) = +1$ for all plaquettes, corresponding to π phase around the dodecagonal plaquettes and $\pi/2$ phase around the triangular plaquettes, as shown in Fig. 52b. The $\pi/2$ phase around the triangular plaquettes indicates the breaking of time-reversal symmetry necessary for a chiral ground state. Alternate flux sectors contain plaquettes with vortex excitations defined by $w(p) = -1$. In general, such vortices are energetically gapped by Δ_v, but the energy and dynamics of vortices near the edge are controlled by the details of the boundary.

In each flux sector, the associated Majorana Hamiltonian can be diagonalized through a unitary transformation Q such that $\kappa \sum_{i,j} Q_{k,i}(iU_{i,j})Q^*_{k',j} = \delta_{kk'}\epsilon_k$, yielding $H^{\gamma} = \frac{1}{2}\sum_{k=-N/2}^{N/2} \epsilon_k c_k^{\dagger}c_k$, where $c_k = \frac{1}{\sqrt{2}}\sum_j Q_{k,j}\gamma_j^0$, N is the number of spins on the lattice, and the index k is ordered according to energy. Owing to particle-hole symmetry,

$\epsilon_k = -\epsilon_{-k}$ and $c_k^\dagger = c_{-k}$; thus, by restricting to $k > 0$,

$$H^\gamma = \sum_{k>0} \epsilon_k (c_k^\dagger c_k - \frac{1}{2}), \tag{7.3}$$

where c_k and $c_k^\dagger$ satisfy Dirac anticommutation relations. Diagonalization of the ground state flux sector on a cylinder yields three bulk fermion bands, energetically gapped by Δ_b, as shown in Fig. 53 [327]. At the edge, the fermionic quasiparticles form gapless chiral modes which are guaranteed by the nontrivial Chern number of the bulk fermion bands.

7.0.12 Spin-Register Coupling to a Chiral Edge

We now consider the addition of spin qubits, which can be individually manipulated and read out, to the edge of the exactly solved model with open boundary conditions [59, 256]. Each edge spin with coordination two has an uncoupled Majorana operator, which we term dangling as depicted in Fig. 52a. We can extend the definition of vortices to include the dangling plaquettes defined by the $U_{i,j}$ links between dangling Majoranas, as shown by the red rectangle in Fig. 52a. These dangling vortices are completely decoupled from the fermions and lead to a large degeneracy of the model. However, generic perturbations will lift this degeneracy by gapping out these dangling vortex states; in this situation, as we later describe, the control of dangling vortices at the injection point will become important.

To illustrate TPST, we consider the full Hamiltonian $H_T = H_0 + H_{int}$ where H_{int} characterizes the coupling between the two spin-registers (termed L and R) and dangling spins at the edge of the droplet (Fig. 52b),

$$H_{int} = -\frac{\Delta_S}{2}(\sigma_L^z + \sigma_R^z) + g_L \sigma_L^\beta \sigma_a^\beta + g_R \sigma_R^\eta \sigma_b^\eta. \tag{7.4}$$

Here, Δ_S is the splitting of the register states (e.g. by an applied field), β, η are chosen to respect the interaction symmetry at the injection points, and g_L, g_R represent the

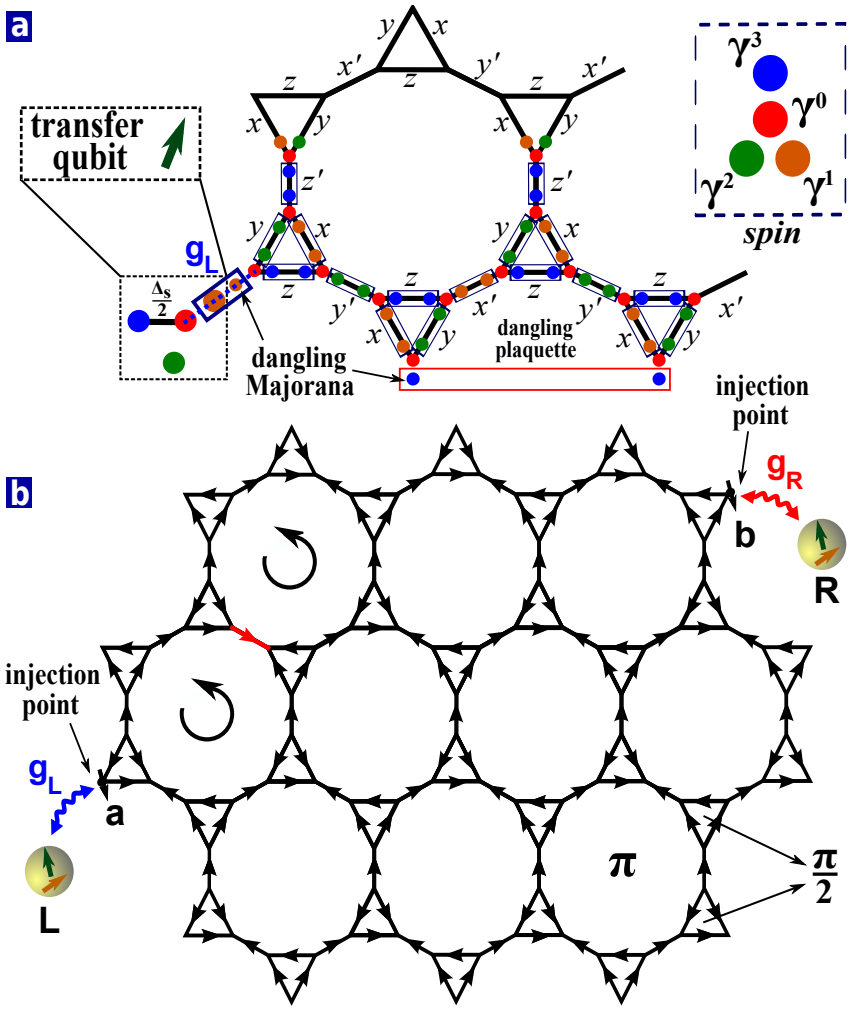

Figure 52: Coupling between spin-register and the droplet edge | (a) Schematic representation of the generalized Kitaev Hamiltonian on the decorated honeycomb lattice. Spins are represented by four Majorana operators; spin-spin interactions become products of the four Majoranas living on each link. Boxed spins correspond to the $\hat{U}_{i,j}$ operators which determine the effective hopping associated with the γ_0 Majoranas. Coupling (dashed line) between the quantum register and the 2D droplet can occur at any edge vertex with an unpaired Majorana; the Majorana flavor determines the form of the spin-spin interaction that introduces the desired additional hopping. (b) Schematic representation of the ground state flux configuration. Each arrow represents a Majorana hopping of i, yielding π phase (oriented CCW) around the dodecagonal plaquettes and $\pi/2$ phase around the triangular plaquettes. Vortex excitations (circular arrows) correspond to the flipping of a U_{ij} link (red arrow and link), which yields $w(p) = -1$ in the two adjacent plaquettes. Quantum registers corresponding to a transfer qubit (green) and a memory qubit (gold) are shown coupled into the droplet (injection points) at two different dangling edge spins.

interaction strength between the registers and the injection spins (a and b) as shown in Fig. 52. Transforming to Majorana operators yields
$H_{int} = -\frac{\Delta_S}{2}(i\gamma_L^3\gamma_L^0 + i\gamma_R^3\gamma_R^0) + g_L\gamma_L^1\gamma_a^1\gamma_L^0\gamma_a^0 + g_R\gamma_R^1\gamma_b^1\gamma_R^0\gamma_b^0$, where, without loss of generality, we have chosen a $\sigma^x\sigma^x$ register-edge interaction.

The existence of a dangling Majorana at the droplet edge is critical to enable spin-edge coupling. At the injection points (Fig. 52b), the register-edge coupling of equation (7.4), not only creates a fermionic excitation, but also introduces a dangling vortex (by flipping the $U_{i,j}$ corresponding to the adjacent dangling plaquette). Thus, in order to exploit the chiral fermion mode to transport spin-based quantum information, we will need to control the injection point. Imperfections in such control will result in the spin-register coupling to additional nearby spins. However, since the nearest spins surrounding the injection point will not contain dangling Majoranas, these additional interactions will naturally gap out.

Even in the presence of the additional interactions prescribed in equation (7.4), since $U_{L,a}$ and $U_{R,b}$ are conserved, the model remains exactly solvable. Expressed in terms of the eigenmodes of the unperturbed Hamiltonian in the ground state flux sector,

$$\begin{aligned} H_T = H + H_{int} &= \sum_{k>0} \epsilon_k (c_k^\dagger c_k - \frac{1}{2}) \\ &+ \Delta_S (c_L^\dagger c_L - \frac{1}{2}) + \Delta_S (c_R^\dagger c_R - \frac{1}{2}) \\ &- g_L U_{L,a} (c_L + c_L^\dagger) \frac{i}{\sqrt{2}} (\sum_k Q_{k,a}^* c_k + \sum_k Q_{k,a} c_k^\dagger) \\ &- g_R U_{R,b} (c_R + c_R^\dagger) \frac{i}{\sqrt{2}} (\sum_k Q_{k,b}^* c_k + \sum_k Q_{k,b} c_k^\dagger), \end{aligned} \tag{7.5}$$

where we have defined $c_{L,R}^\dagger = 1/2(\gamma_0^{L,R} - i\gamma_3^{L,R})$ and $c_{L,R} = 1/2(\gamma_0^{L,R} + i\gamma_3^{L,R})$; in this language, the σ^z spin state of the L(R) qubit is encoded in the occupation of the L(R) fermion mode. The first term of the Hamiltonian characterizes the modes of the 2D droplet, the second and third term characterize the splitting associated with the spin-registers, while the final two terms capture the coupling between the registers and the

dangling edge spins. This Hamiltonian acts in the extended fermionic Hilbert space and returning to physical spin states requires gauge projection.

7.0.13 Topologically Protected State Transfer in the Dot and Droplet Regime

The coupling between the register and the chiral edge mode can be analyzed in two distinct regimes: 1) the mesoscopic dot regime and 2) the macroscopic droplet regime. The distinction between these two regimes is best understood from a perspective of resolvability; in the dot regime, we consider the coupling to a small finite-size system, enabling energy resolution of the individual chiral edge modes. Thus, TPST is mediated by a single fermionic eigenmode of the system [116]. Meanwhile, in the droplet regime, we consider the coupling to a larger system, in which energy resolution at the single mode level would be extremely difficult. In this regime, we encode the spin register's quantum information in a traveling fermionic wave-packet.

In both the dot and droplet regimes, TPST relies on the coherent transfer of fermionic occupation from register L to R. In order for this to be well-defined, we choose $\Delta_S > 0$ and $g_L, g_R < \Delta_S$ so that the effective Dirac fermions, $c_k^\dagger$, are conserved. In the dot regime, TPST can be understood by tuning Δ_S to be resonant with a single edge mode, $\tilde{k}$, with energy $\epsilon_{\tilde{k}}$; so long as the coupling strength is weak enough to energetically resolve this mode, evolution is governed by the effective Hamiltonian,

$$H_{eff} = -\frac{i}{\sqrt{2}} g_L Q^*_{\tilde{k},a} c_L^\dagger c_{\tilde{k}} - \frac{i}{\sqrt{2}} g_R Q^*_{\tilde{k},b} c_R^\dagger c_{\tilde{k}} + h.c. \tag{7.6}$$

and hence, state transfer proceeds via resonant fermion tunneling, as depicted in Fig. 54a [116]. The timescale, τ, required to achieve high fidelity state transfer depends only on the energy spacing between adjacent modes, $\Delta\epsilon \sim \kappa/\ell$, where ℓ is the system's linear dimension; to prevent the leakage of quantum information into off-resonant fermionic modes, $\tau \gtrsim \ell/\kappa$ [116].

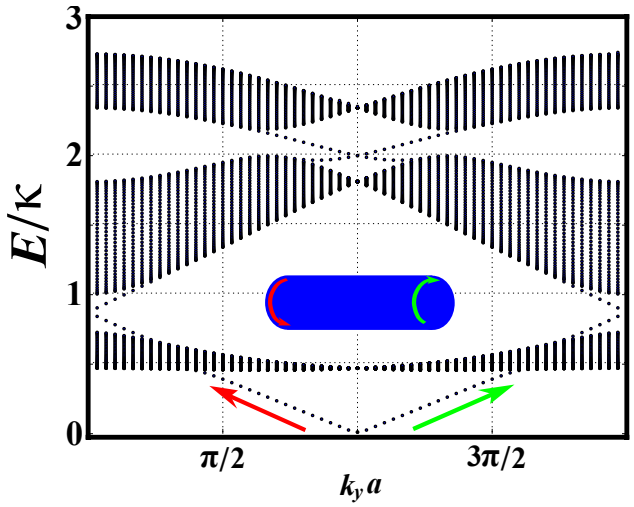

Figure 53: Fermionic spectrum of the ground state flux sector | The model is placed on a cylinder of circumference 61 and width 40 unit cells, with a zigzag edge oriented such that the y direction is periodic [328]. The chiral edge modes are clearly visible near $k_y a = \pi$ at energies below the bulk fermion gap $\Delta_b = 0.46\kappa$. Numerical simulations also indicate the following values of the two vortex gaps: 0.14κ (dodecagonal vortex) and 0.17κ (triangular vortex).

In the droplet regime, we encode the fermionic occupation into the presence/absence of a wavepacket traveling along the chiral edge, as illustrated in Fig. 54b [329]. Upon tuning both spin-registers to an energy Δ_S, the encoding can be performed by choosing $g_L(t)$ with the following time-dependence,

$$g_L(t) = \frac{\sqrt{v} f(t)}{\sqrt{\int_t^\infty dt' |f(t')|^2}}, \tag{7.7}$$

where $f(t)$ characterizes the shape of the desired wave-packet and v is the group velocity of the chiral mode. Subsequent retrieval can be similarly achieved by employing time-reversal symmetry to appropriate choose the shaping of $g_R(t)$. We note that such wavepacket encoding is in direct analogy to the storage and retrieval of photonic wavepackets [278, 330, 331]. In contrast to the dot regime, the magnitude of the coupling strengths may be of order Δ_S, which is independent of ℓ. However, the time scale of TPST includes the wavepacket's propagation time, which depends on both the physical separation of the registers and the wavepacket group velocity.

7.0.14 Effects of Imperfections, Disorder and Decoherence

Having explicitly demonstrated TPST in an exactly solvable model, we now consider additional imperfections, disorder, temperature and decoherence. As the CSLB phase has a bulk gap and a topological invariant protecting its chiral edge mode, we expect the effective low energy fermion dynamics to be insensitive to small perturbations [325]. Furthermore, the chirality of the edge mode prevents localization and the Majorana nature of the edge fermions strongly suppresses the phase space for scattering, thereby limiting nonlinear corrections to the dispersion [116, 196, 202, 216, 241]. In the following, we consider various classes of imperfections arising from local spin perturbations and coupling to a finite temperature bath; these result in: 1) vortex excitations, 2) finite Majorana lifetime and 3) dynamical decoherence.

Vortex Excitations

At low temperatures T, there will be a dilute gas of bulk vortices, $N_v \sim n_p e^{-\Delta_v/T}$, where n_p represents the total number of bulk plaquettes. Since a vortex excitation corresponds to a π flux relative to the ground state, a circumambulating fermion acquires an additional phase of $N_v\pi$. Thus, the presence of vortices can have two relevant effects: 1) vortices within a localization length, $\xi \sim a$ (where a is the lattice spacing), of the edge can scatter a traveling fermion and 2) an odd number of vortices induces a π-shift of the net phase [332].

In addition to introducing bulk vortices, perturbations also generically lift the aforementioned degeneracy associated with dangling edge vortices. However, this will only affect the fidelity of TPST at the injection point, where one must ensure the existence of a single dangling edge Majorana. Away from the injection point, three possibilities arise: First, zero energy dangling vortices are completely decoupled from the fermions and hence will be irrelevant for TPST. Second, low energy dangling vortices will scatter only minimally, since the interaction strength between the dangling Majoranas, and hence the hopping strength across the dangling link, will be extremely weak. Finally, much as in the

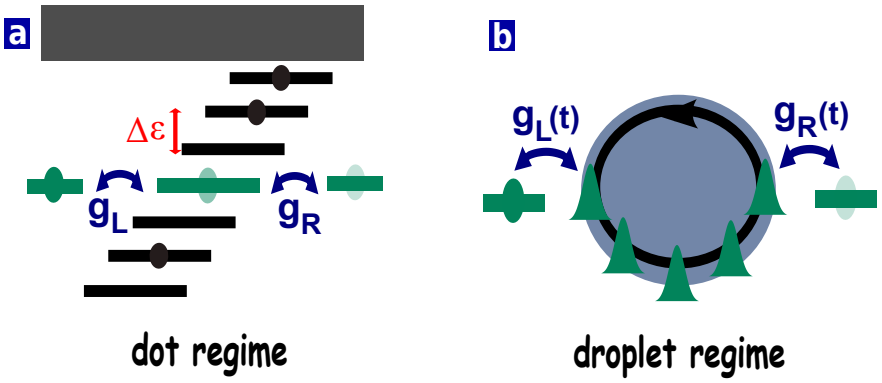

Figure 54: Regimes of TPST | (a) Schematic representation of the dot regime wherein TPST becomes analogous to tunneling. In this mesoscopic dot regime, the coupling strength is kept weak enough to enable resolution of single edge modes. (b) Schematic representation of the droplet regime wherein TPST is achieved by mapping the quantum information from a spin-register onto a traveling fermionic wave-packet. The wave-packet is caught at the remote register, after which a two-qubit gate is performed before the information is returned (via a wave-packet) to the initial register.

bulk, the effect of high energy dangling vortices will be suppressed by their gap.

As static effects, all of the aforementioned error contributions can be abrogated by the use of tomography; hence, it is crucial to effectively freeze out vortex fluctuations on the time scale of TPST, and this is most easily accomplished at temperatures which are small compared to Δ_v.

Finite Majorana Lifetime

Next. we consider the addition of generic perturbative local spin interactions, H_p, to the full Hamiltonian, H_T. Certain classes of perturbations leave the model exactly solvable; more generally however, if H_p is longer ranged or does not respect the model's interaction symmetry, the gauge field acquires dynamics and the effective fermionic theory is no longer free. In order to understand these effects, we turn to a low-energy continuum theory of the Majorana edge (assuming that dangling vortex excitations are either decoupled or gapped out),

$$H_e = v \int \frac{dp}{2\pi} p c_p^\dagger c_p = v \int dx\, \gamma(x)(i\partial)\gamma(x), \tag{7.8}$$

where $c_p^\dagger = c_{-p}$ is the subset of $\{c_k^\dagger\}$ in equation (7.3) which creates an edge excitation at momentum p and where we have switched to a continuum normalization of the Majorana field, $\{\gamma(x), \gamma(y)\} = \delta(x-y)$ [332].

The introduction of interactions induces decay of the quasiparticle excitations $c_p^\dagger$. This quasiparticle lifetime limits the size of the droplet around which coherent excitations may be sent. The leading order symmetry-allowed interaction is of the form [333]

$$H_e' = \lambda \int dx\, \gamma(x)(i\partial)\gamma(x)(i\partial)^2\gamma(x)(i\partial)^3\gamma(x), \tag{7.9}$$

where λ characterizes the strength of the interaction. We estimate the decay rate Γ_p^{int} of a single quasiparticle excitation using Fermi's golden rule. In the low temperature limit ($\epsilon_p \gg k_B T$),

$$\Gamma_p^{int} \sim \frac{\lambda^2 p^{13}}{v} + \frac{\lambda^2 p^{11} T^2}{v} + \mathcal{O}(T^4). \tag{7.10}$$

To relate Γ_p^{int} to the microscopic model parameters, we consider generic vortex-inducing local spin perturbations of strength κ', which yield $\lambda \sim \kappa(\frac{\kappa'}{\kappa})^2 a^7$ in second order perturbation theory. Substituting into equation (10) allows us to re-express the zero temperature decay rate as $\Gamma_p^{int} \sim \frac{\kappa^2}{\Delta_S}(\frac{\kappa'}{\kappa})^4 (ap)^{14}$, where $\Delta_S = vp$ is the energy of the injected TPST fermion. The surprisingly strong dependence on momenta suggests that quasiparticle decay can safely be neglected so long as $p < 1/a$.

Dynamical Decoherence

Finally, we consider dynamical decoherence due to weak coupling with a low temperature phonon bath, which induces additional decay Γ_p^{dec} of the fermion involved in TPST. We assume that the bath couples to local spin operators σ_i^α and that its effect is characterized by its noise spectral density, $\Gamma_p^{dec} \sim S(\omega)$ [334]. In the bulk, each such operator creates a pair of vortices (Fig. 52b) in addition to creating or destroying a Majorana quasiparticle. As the fermionic edge modes are exponentially localized, the contribution of this process to

the decay rate is suppressed by $e^{-d/\xi}$, where d is the distance from site i to the edge. Moreover, there is an additional energy suppression from $S(\omega_0) \sim e^{-\omega_0/k_B T}$ where $\omega_0 = 2\Delta_v$ is the energy cost of creating a pair of vortices.

This brings us to the primary decoherence effect: edge noise. There are two types of spin operators acting on the lattice edge: 1) those which only create or destroy an edge fermion (type I) and 2) those which also introduce vortices (type II-IV), as shown in Fig. 55. Type I spin operators can only induce decay if they directly annihilate the injected TPST edge fermion, a process costing energy Δ_S. By contrast, once a vortex is created at any edge plaquette it can scatter the traveling TPST fermion, implying that the associated decoherence is enhanced by a factor of ℓ, as depicted in Fig. 55. Thus, the total TPST decay rate induced by edge noise is,

$$\Gamma_p^{dec} \sim e^{-\Delta_S/k_B T} + \ell e^{-\Delta_V/k_B T}. \tag{7.11}$$

Strikingly, the sources of decoherence in TPST are exponentially suppressed in temperature and thus can be controlled [116].

The above analysis generalizes to other types of noise sources. Of particular relevance in the context of solid-state spin systems are nuclear spin baths, in which $S(\omega) \sim \frac{1}{\omega^2 + 1/t_c^2}$, where t_c is the bath's correlation time. In this model, the Arrhenius-type energy suppressions of equation (11) becomes $\Gamma_p^{dec} \sim 1/\Delta_v^2$ if $\Delta_v \gg 1/t_c$ [334].

7.0.15 Experimental Realizations and Outlook

The search for novel topological phases represents one of the most exciting challenges in many-body physics; indeed, this challenge has led to a widespread effort to experimentally identify or engineer systems exhibiting exotic topological order. One of the prototypes of such order is provided by the CSLB phase of the Kitaev honeycomb model; while such chiral spin liquid phases have yet to be experimentally implemented, several realistic

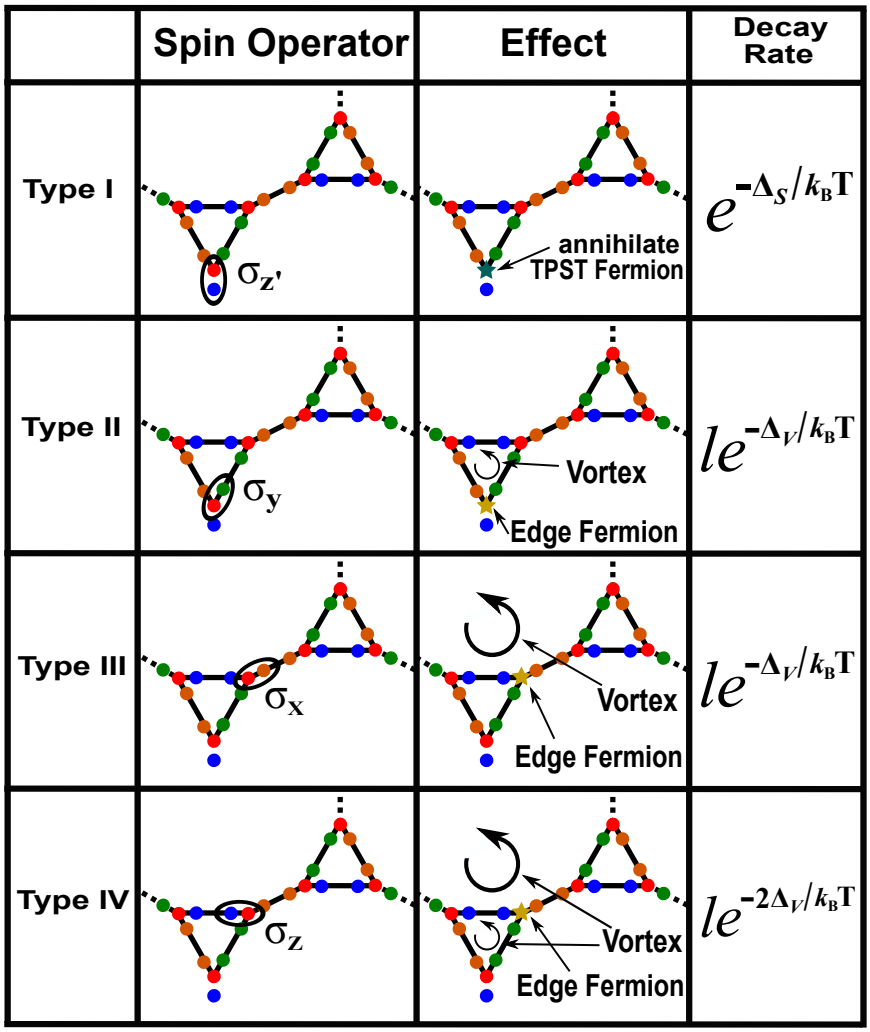

Figure 55: Schematic representation of the various forms of edge decoherence | Type I spin operators correspond to non-vortex inducing decoherence and can affect TPST only by annihilating the TPST fermion (teal star), a process suppressed by $e^{-\Delta_S/k_BT}$, where Δ_S represents the detuning of the spin registers and hence also the energy of the injected quasiparticle. Type II-IV spin operators create vortices (circular arrow) in edge plaquettes. Once a vortex is created at any edge site, it can scatter the traveling TPST fermion, leading to the decoherence being enhanced by ℓ (the droplet's linear dimension). In addition to creating vortices, Type II-IV spin operators also create un-gapped edge fermions (gold star), which we assume does not affect TPST since quasiparticle interactions have been shown to be extremely weak.

approaches toward their realization have been envisioned.

The realization of a honeycomb lattice, an essential component of implementing the Kitaev gapped B phase, is currently being considered in systems ranging from ultra-cold atoms [335–337] and polar molecules [96, 338] to superconducting lattices [339, 340] and dipolar-coupled electronic spin arrays [74, 210]. While engineering a macroscopic honeycomb droplet remains a daunting challenge, recent experiments have demonstrated the ability to control mesoscopic ensembles containing tens of qubits [341–345]. Despite these remarkable advances, such mesoscopic systems are insufficient in size to support the existence of several well-separated quasiparticles, a crucial prerequisite to demonstrate the non-abelian braiding essential for topological quantum computing [238, 321, 325]. However, these smaller systems represent ideal candidates to demonstrate topologically protected state transfer and hence, the existence of a chiral fermion edge - another hallmark of the CSLB phase.

Moreover, our proposed technique can also be used to directly characterize spin liquid states via passive spectroscopy of the droplet edge. By observing the splitting-dependent relaxation of the spin-qubit probe, one could map the energy spacing between the chiral edge-modes. In addition, asymmetries in correlation measurements provide a direct indication of chirality. In this case, by gradually altering the physical distance separating two spin-qubit probes, one could characterize the timescale of incoherent interactions between the remote registers. Asymmetry in this timescale, dependent on the direction in which the qubits are separated provides a strong indication of the existence of a chiral edge and would enable direct evaluation of the velocity associated with the edge dispersion. Alternatively, one could also imagine holding the spin qubits fixed and characterizing asymmetries associated with L-to-R versus R-to-L TPST. These considerations imply that solid-state magnetic spin probes can provide a potential tool for exploring the properties of natural spin liquid candidates in both organic and inorganic insulators [326, 346–348].

Finally, our technique suggests a new avenue for a hybrid solid-state quantum computing

architecture. In particular, while solid-state spin systems enable the realization of long-coherence-time quantum memories and high-fidelity quantum registers, scaling these individual components up to a local area quantum network remains a critical challenge [45, 46, 59, 116, 210, 256]. Thus, we envision a hybrid architecture in which conventional solid-state spin qubits are connected by topologically protected channels. In this scenario, dynamical decoupling of spins within an engineered CSLB droplet generates a lattice of mesoscopic CSLB islands around which individual qubits reside [262]. The edge-modes of these island regions act as quantum routers, ferrying quantum information between remote spin registers. Since spin-qubits are naturally well-separated in such a hybrid architecture, the individual addressing and direct control of single qubits is greatly simplified [227]. Furthermore, such an architecture suggests a perspective in which control fields can reshape CSLB islands and thereby dynamically reconfigure network connectivities.

Chapter 8

Quantum primitives enabled by Nitrogen-Vacancy centers

8.1 Quantum credit cards

In the chapter, we describe a variety of quantum primitives enabled by the Nitrogen-Vacancy center. The realization of devices which harness the laws of quantum mechanics represents an exciting challenge at the interface of modern technology and fundamental science[187, 313]. An exemplary paragon of the power of such quantum primitives is the concept of "quantum money" [349]. A dishonest holder of a quantum bank-note will invariably fail in any forging attempts; indeed, under assumptions of ideal measurements and decoherence-free memories such security is guaranteed by the no-cloning theorem [350]. In any practical situation, however, noise, decoherence and operational imperfections abound. Thus, the development of secure "quantum money"-type primitives capable of tolerating realistic infidelities is of both practical and fundamental importance. Here, we propose a novel class of such protocols and demonstrate their tolerance to noise; moreover, we prove their rigorous security by determining tight fidelity thresholds. Our proposed protocols require only the ability to prepare, store and measure single qubit

quantum memories, making their experimental realization accessible with current technologies [113, 351, 352].

Recent extensions to Wiesner's original "quantum money" protocol [349] have garnered significant interest [353–356]. One particular extension enables the authentication of quantum tokens via classical public communication with a trusted verifier [357]. However, to tolerate noise, the verification process must condone a certain finite fraction of qubit failures; naturally, such a relaxation of the verification process enhances the ability for a dishonest user to forge quantum tokens. It is exactly this interplay which we, here, seek to address, by focusing on a class of "quantum token"-protocols which involve either direct physical or classical communication verification of qubit memories.

8.1.1 Quantum tickets

Our approach to quantum tokens extends the original quantum money primitive[349] by ensuring tolerance to finite errors associated with encoding, storage and decoding of individual qubits. We denote the tokens within our first primitive as quantum tickets (qtickets); each qticket is issued by the mint and consists of a unique serial number and N component quantum states, $\rho = \bigotimes_i \rho_i$, where each ρ_i is drawn uniformly at random from the set, $\tilde{Q} = \{|+\rangle, |-\rangle, |+i\rangle, |-i\rangle, |0\rangle, |1\rangle\}$, of polarization eigenstates of the Pauli spin operators. The mint secretly stores a classical description of ρ, distributed only among trusted verifiers. In order to redeem a qticket, the holder physically deposits it with a trusted verifier, who measures the qubits in the relevant basis. This verifier then requires a minimum fraction, F_{tol}, of correct outcomes in order to authenticate the qticket; following validation, the only information returned by the verifier is whether the qticket has been accepted or rejected.

The soundness of a qticket, e.g. the probability that an honest user is successfully verified, depends crucially on the experimental fidelities associated with single qubit encoding, storage and decoding. Thus, for a given qubit ρ_i, we define the map, M_i, which

characterizes the overall fidelity, beginning with the mint's encoding and ending with the verifier's validation; the average channel fidelity[222] is then given by, $F_i = 1/|\tilde{Q}| \sum_{\rho_i} \mathrm{Tr}[\rho_i M_i(\rho_i)]$. With this definition, the verification probability of an honest user is,

$$p_{\mathrm{h}} = \frac{1}{|Q|} \sum_{\rho \in Q} \mathrm{Tr}[P_{\mathrm{acc}} M(\rho)] \geq 1 - e^{-ND(F_{\mathrm{exp}} \| F_{\mathrm{tol}})}, \tag{8.1}$$

where $Q = \tilde{Q}^{\otimes N}$, P_{acc} represents the projector onto the subspace of valid qtickets, $M = \bigotimes_i M_i$, $F_{\mathrm{exp}} = 1/N \sum_i F_i$ is the average experimental fidelity, and D, the relative entropy, characterizes the distinguishability of two distributions (see Methods for details). Crucially, so long as the average experimental fidelity associated with single qubit processes is greater than the tolerance fidelity, an honest user is exponentially likely to be verified.

To determine a tight security threshold, we consider the counterfeiting of a single qticket. For a given tolerance fidelity (F_{tol}) set by the verifiers, a qticket is only accepted if at least $F_{\mathrm{tol}}N$ qubits are validated. In the event that a dishonest user attempts to generate two qtickets from a single valid original, each must contain a minimum of $F_{\mathrm{tol}}N$ valid qubits to be authenticated. As depicted in Fig. 56a., in order for each counterfeit qticket to contain $F_{\mathrm{tol}}N$ valid qubits, a minimum of $(2F_{\mathrm{tol}} - 1)N$ qubits must have been perfectly cloned. Thus, for a set tolerance fidelity, in order for a dishonest user to succeed, he or she must be able to emulate a qubit cloning fidelity of at least $2F_{\mathrm{tol}} - 1$. Crucially, so long as this fidelity is above that achievable for optimal qubit cloning (2/3) [358], a dishonest user is exponentially unlikely to succeed,

$$p_{\mathrm{d}} = \frac{1}{|Q|} \sum_{\rho \in Q} \mathrm{Tr}\left[P_{\mathrm{acc}}^{\otimes 2} T(\rho)\right] \leq e^{-ND(2F_{\mathrm{tol}} - 1 \| 2/3)}, \tag{8.2}$$

where T represents any completely positive trace preserving qticket counterfeiting map. To ensure $2F_{\mathrm{tol}} - 1 > 2/3$, the tolerance fidelity must be greater than 5/6, which is precisely the average fidelity of copies produced by an optimal qubit cloning map [358]. In certain cases, an adversary may be able to sequentially engage in multiple verification rounds;

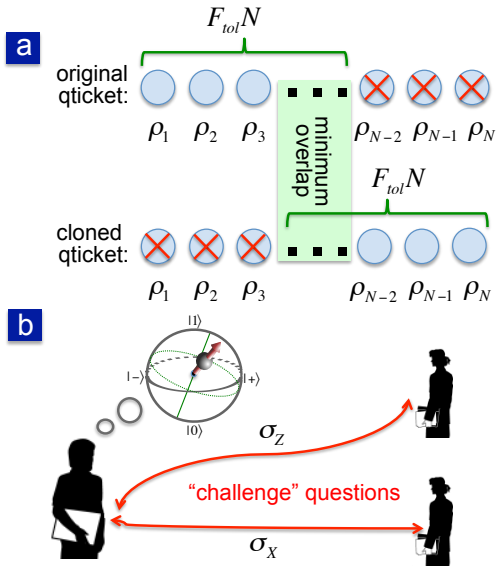

Figure 56: a) Depicts the pigeonhole type argument which is utilized in the proof of qticket soundness. For a tolerance fidelity F_{tol}, a qticket is only successfully authenticated if it contains at least $F_{\text{tol}}N$ valid qubits. However, for two counterfeit qtickets, not all valid qubits must coincide. The minimum number of perfectly cloned qubits enabling both qtickets to be accepted is, $(2F_{\text{tol}} - 1)N$. b) Depicts the quantum retrieval type situation envisioned for cv-qtickets. For two verifiers asking complementary "challenge" questions, the optimal strategy is for the user to measure in an intermediate basis. Such a strategy saturates the tolerance threshold, $F_{\text{tol}}^{\text{cv}} = \frac{1+1/\sqrt{2}}{2}$.

however, the probability of successfully validating counterfeited qtickets grows at most quadratically in the number of such rounds, and hence, the likelihood of successful counterfeiting can remain exponentially small even for polynomially large numbers of verifications.

Our previous discussion of qtickets assumed that such tokens are physically transferable to trusted verifiers (e.g. concert tickets); however, in many situations, this assumption of physical deposition, may either be impossible or undesirable. Recently, it has been shown [357] that it remains possible, even remotely, for a holder to prove the validity of a token by responding to a set of "challenge" questions; these questions can only be successfully answered by measuring an authentic token. The core behind this approach is to ensure that the "challenge" questions reveal no additional information about the quantum state of the token.

8.1.2 Classical verification quantum ticket

We now discuss a specific realization of such an approach, the classical verification quantum ticket (cv-qticket), and demonstrate its robustness against noise and operational imperfections. In contrast to the case of bare qtickets, a cv-qticket holder will be expected to answer "challenge" questions and hence to measure qubits himself. One might imagine that the ability to participate in multiple remote verifications simultaneously could offer a dishonest user an additional advantage over the bare qticket case; in particular, certain measurement strategies may yield an increased likelihood for multiple successful authentications.

One example of a cv-qticket framework, is to utilize a set of eight possible two-qubit product states with each qubit prepared along either X or Z (note that a single qubit framework is also possible):

$$\{|0,+\rangle, |0,-\rangle, |1,+\rangle, |1,-\rangle, |+,0\rangle, |-,0\rangle, |+,1\rangle, |-,1\rangle\}.$$

We then envision each cv-qticket to consist of n blocks, each containing r qubit pairs, and thus, a total of $n \times r \times 2$ qubits; as before, each of the qubit pairs is chosen uniformly at random from the allowed set above. A "challenge" question consists of randomly asking the holder to measure each block (of qubits) along either the X or Z basis; naturally, as depicted in Table 8.1.1, a valid qubit pair (within a block) is one in which the holder correctly answers the state for the particular qubit (within the pair) which was prepared along the questioned basis. For a given tolerance threshold, an overall answer will only be deemed correct if at least $F_{\text{tol}}^{\text{cv}} r$ qubits within each of the n blocks are found valid. By analogy to the qticket case, honest users are exponentially likely to be verified so long as $F_{\text{exp}} > F_{\text{tol}}^{\text{cv}}$; in particular, since there now exist n blocks of qubits, each of which can be

thought of as an individual qticket (with r qubits),

$$p_{\mathrm{h}}^{\mathrm{cv}} \geq \left(1 - e^{-rD(F_{\mathrm{exp}} \| F_{\mathrm{tol}}^{\mathrm{cv}})}\right)^n . \tag{8.3}$$

The proof of cv-qticket security is based upon a generalized formalism of quantum retrieval games [357, 359], in combination with a generalized Chernoff-Hoeffding bound [360]. So long as $F_{\mathrm{tol}}^{\mathrm{cv}} > \frac{1+1/\sqrt{2}}{2}$, a dishonest user is exponentially unlikely to be authenticated by two independent verifiers. For two complementary "challenge" questions, one finds that on average, no more than $1 + 1/\sqrt{2} \approx 1.707$ can be answered correctly. Interestingly, the threshold $F_{\mathrm{tol}}^{\mathrm{cv}}$ corresponds exactly to that achievable by either covariant qubit cloning[361] or by measurement in an intermediate basis (Fig. 56b), suggesting that both such strategies may be optimal [187]. Similar to the qticket case, one finds that a dishonest user is exponentially likely to fail,

$$p_{\mathrm{d}}^{\mathrm{cv}} \leq \binom{v}{2}^2 \left(1/2 + e^{-rD(F_{\mathrm{tol}} \| \frac{1+1/\sqrt{2}}{2})}\right)^n , \tag{8.4}$$

where v represents the number of repeated verification attempts. Moreover, so long as two verifiers agree to ask complementary "challenge" questions, participation in simultaneous verifications is unable to improve a dishonest user's emulated fidelity. Thus, in the case of both qtickets and cv-qtickets, so long as the hierarchy of fidelities is such that: $F_{\mathrm{dishonest}} < F_{\mathrm{tol}} < F_{\mathrm{exp}}$, it is possible to prove both soundness and security of each protocol.

8.1.3 Quantum credit card primitive

Next, we consider applications of the above primitives to practically relevant protocols. For instance, one might imagine a composite cv-qticket which allows for multiple verification rounds while also ensuring that the token cannot be split into two independently valid subparts [357]. Such a construction may be used to create a quantum-protected credit

Prepare	$\|-,0\rangle$	$\|0,+\rangle$	$\|1,+\rangle$	$\|0,+\rangle$	$\|0,+\rangle$	$\|+,1\rangle$	$\|-,0\rangle$	$\|1,+\rangle$
B:Ask	Z				X			
H:Ans.	$0,0$	$0,1$	$1,1$	$0,1$	$-,+$	$+,-$	$-,+$	$+,-$
Correct	✓	✓	✓	✓	✓	✓	✓	×
Block			✓				✓	
B:Res.	Verified							

Table 8.1.1: Verification of a single cv-qticket. Here, we consider a cv-qticket with $n = 4$ and $r = 2$, totaling 8 qubit pairs and $F_{\text{tol}} = 3/4$ (for illustrative purposes only). The prepared qubit-pairs are chosen at random, as are the bank's requested measurement bases (for each block). The holder's answer has at most, a single error per block, which according to, $F_{\text{tol}} = 3/4$, is allowed. Secure cv-qtickets require $F_{\text{tol}} > 1/2 + 1/\sqrt{8}$ and a larger number of constituent qubits.

card. Indeed, the classical communication which takes place with the issuer (bank) to verify the cv-qticket (via "challenge" questions) may be intentionally publicized to a merchant who needs to be convinced of the card's validity. By contrast to modern credit card implementations, such a quantum credit card would be unforgeable and hence immune to fraudulent charges (Fig. 57a).

An alternate advantage offered by the qticket framework is evinced in the case where verifiers may not possess a secure communication channel with each other. Consider for example, a dishonest user who seeks to copy multiple concert tickets, enabling his friends to enter at different checkpoint gates. A classical solution would involve gate verifiers communicating amongst one another to ensure that each ticket serial number is only allowed entry a single time; however, as shown in Fig. 57b., such a safeguard can be overcome in the event that communication has been severed. By contrast, a concert ticket based upon the proposed qticket primitive would be automatically secure against such a scenario; indeed, the security of qtickets is guaranteed even when verifiers are assumed to be isolated. Such isolation may be especially useful for applications involving quantum identification tokens, where multiple verifiers may exist who are either unable or unwilling to communicate with one another.

While quantum primitives have been the subject of tremendous theoretical interest, their practical realization demands robustness in the face of realistic imperfections. Our above

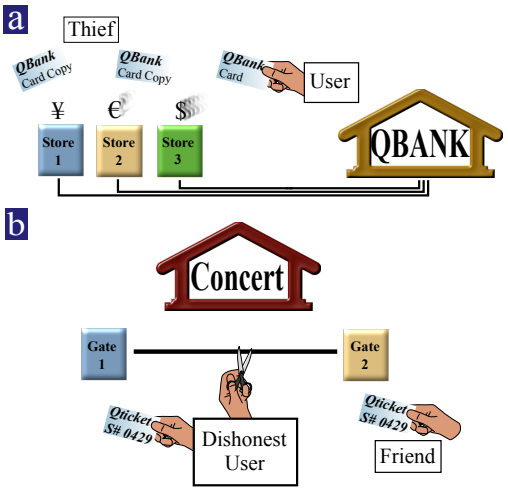

Figure 57: a) Depicts the possibility of using the cv-qticket framework to implement a quantum-protected credit card. Unlike its classical counterpart, the quantum credit card would naturally be unforgeable; this prevents thieves from being able to simply copy credit card information and perform remote purchases. b) Depicts a dishonest user who attempts to copy a concert qticket (e.g. same serial number), enabling his friend to enter at an alternate checkpoint gate. Naively, each verifier can communicate with one another to prevent such abusive ticket cloning. However, such a safeguard can be overcome in the event that the communication among verifiers is either unsecured, unavailable or severed (possibly by the dishonest user himself). The qticket is exempt from this type of attack since security is guaranteed even in the case of isolated verifiers.

analysis demonstrates that such noise tolerance can be achieved for certain classes of unforgeable quantum tokens. Moreover, the derived tolerance thresholds are remarkably mild and suggest that proof of principle experiments are currently accessible in systems ranging from trapped ions [351, 362] and superconducting devices [339, 352] to solid-state spins [45, 59, 113, 322]. In particular, recent advances on single nuclear spins situated in a compact room-temperature solid, have demonstrated that ultra-long storage times can be attained in combination with high fidelity initialization and readout [113]; such advances suggest that quantum devices based upon single qubit quantum memories may be both practical and realistically feasible.

While our analysis has focused on describing a primitive based upon single tokens, natural extensions to the case of multiple identical quantum tokens open up the possibility of even more novel applications. In particular, it is possible to extend our threshold results to the case where c identical copies of the quantum token are issued. In this case, to ensure

that the production of $c+1$ valid tokens is exponentially improbable, the required threshold fidelity must be greater than $1-\frac{1}{(c+1)(c+2)}$. The existence of such multiple identical tokens can provide a certain degree of anonymity for users and could be employed in primitives such as quantum voting. A crucial question that remains is whether a rigorous proof of anonymity can be obtained in a noisy environment. Furthermore, our proposed quantum tokens can also be seen as a basic noise tolerant building block for implementing more advanced application schemes; such schemes can range from novel implementations of quantum key distribution [187, 363–365] based upon physical qubit transport to complex one-time-entry identification cards. Beyond these specific applications, a number of scientific avenues can be explored, including for example, understanding whether an interplay between computational assumptions and quantum memories can yield fundamentally new approaches to encryption.

8.1.4 Proof of Quantum Ticket Soundness

To demonstrate the soundness and security of qtickets, we employ the framework of a Chernoff Bound, which characterizes the central limiting behavior of a set of independent random variables; in particular, it provides exponentially decreasing bounds on tail distributions of their sums. Here, we state a generalization of this bound [360],

Theorem: Generalized Chernoff-Hoeffding bound Let $X_1, \ldots, X_n$ be Boolean $\{0,1\}$ random variables, such that for some δ_i and every $S \subseteq \{1, \ldots, n\}$, it holds that $\mathbf{Pr}\left[\bigwedge_{i\in S} X_i\right] \leq \prod_{i\in S} \delta_i$. Then

$$\mathbf{Pr}[\sum_{i=1}^{n} X_i \geq \gamma n] \leq e^{-nD(\gamma\|\delta)}$$

with $\delta := n^{-1}\sum_{i=1}^{N} \delta_i$ and for any γ s.t. $\delta \leq \gamma \leq 1$.

$D(p\|q) = p\ln\frac{p}{q} + (1-p)\ln\frac{1-p}{1-q}$ characterizes the distinguishability of two binary probability distributions, where $\Pr(X=1) = p$ for the first distribution and $\Pr(X=1) = q$

for the second. To establish the soundness of qtickets, we now define the "acceptor", P^{ρ}_{acc}, which projects a pure N qubit product state onto the subspace of valid qtickets. As expected, the size of this subspace will depend on the verifiers tolerance fidelity, F_{tol}.

Definition: Acceptance Projector

Given $\rho = \bigotimes_{i=1}^{N} \rho_i$ and a security parameter $0 \leq F_{\text{tol}} \leq 1$, the acceptance projector is given by

$$P^{\rho}_{\text{acc}} = \sum_{\vec{b}:|\vec{b}|_1 \geq F_{\text{tol}} N} \bigotimes_{i=1}^{N} \left(b_i \rho_i + \bar{b_i} \rho_i^{\perp} \right).$$

$\vec{b} \in \{0,1\}^N$ is a length N, boolean string with $|\vec{b}|_1 = \sum_{i=1}^{N} b_i$, $\bar{b_i} = 1 - b_i$, and $\rho_i^{\perp} = \mathbb{1} - \rho_i$. Intuitively, $|\vec{b}|_1$ can be thought of as a Hamming weight since it characterizes the number of non-zero entries of the string. The sum is over all strings which have at least $F_{\text{tol}} N$ entries which are 1; thus, the definition of $\vec{b}$ naturally enforces the projection onto the set of valid qticket states. We now recall the qubit map M_i which characterizes the overall fidelity, F_i, of encoding, storage and decoding. We define $F_{\text{exp}} = 1/N \sum_i F_i$ to be the average achievable experimental fidelity. This brings us to the statement of qticket soundness.

Theorem: Soundness of a Quantum Ticket

For $F_{\text{exp}} > F_{\text{tol}}$, an honest holder successfully redeem a qticket with probability

$$p_{\text{v}} \geq 1 - e^{-ND(F_{\text{tol}} \| F_{\text{exp}})}.$$

Proof. Consider a vector composed of boolean random variables, $\vec{X} = (X_1, \ldots, X_N)$, with a joint probability distribution given by

$$\begin{aligned} \mathbf{Pr}[\vec{X} = \vec{b}] &= \frac{1}{|Q|} \sum_{\rho \in Q} \text{Tr} \left[M(\rho) \bigotimes_{i=1}^{N} \left(b_i \rho_i + \bar{b}_i \rho_i^{\perp} \right) \right] \\ &= \prod_{i=1}^{N} \frac{1}{6} \sum_{\rho_i \in \tilde{Q}} \text{Tr} \left[M_i(\rho_i) (b_i \rho_i + \bar{b}_i \rho_i^{\perp}) \right] \end{aligned}$$

As evidenced, we can consider X_i to be independent boolean random variables with probability $\mathbf{Pr}[X_i] = F_i$. Moreover, a simple calculation reveals that Eq. 8.1 of the main text can be recast as, $\frac{1}{|Q|}\sum_{\rho\in Q}\mathrm{Tr}[P^{\rho}_{\mathrm{acc}}M(\rho)] = \mathbf{Pr}[\sum_{i=1}^{N} X_i \geq F_{\mathrm{tol}}N]$. Application of the Chernoff bound yields the desired result. ■

The security proof for qtickets follows in a similar fashion; it requires the generalized Chernoff-Hoeffding bound to rigorously deal with arbitrary counterfeiting attacks, which may in principle generate correlations between qticket components.

8.2 Spin squeezing

Electronic spins associated with nitrogen-vacancy (NV) centers in diamond exhibit long coherence times and optical addressability, motivating extensive research on NV-based quantum information and sensing applications. Recent experiments have demonstrated coupling of NV electronic spins to nuclear spins [44, 275], entanglement with photons [192], as well as single spin [287, 293] and ensemble [366, 367] magnetometry. An outstanding challenge is the realization of controlled interactions between several NV centers, required for quantum gates or to generate entangled spin states for quantum-enhanced sensing. One approach toward this goal is to couple NV centers to a resonant optical [368, 369] or mechanical [370–372] mode; this is particularly appealing in light of rapid progress in the fabrication of diamond nanostructures with improved optical and mechanical properties [373–377].

In this section, we describe a new approach for effective spin-spin interactions between NV centers based on strain-induced coupling to a vibrational mode of a diamond resonator. We consider an ensemble of NV centers embedded in a single crystal diamond nanobeam, as depicted in Fig. 58a. When the beam flexes, it strains the diamond lattice which in turn couples directly to the spin triplet states in the NV electronic ground state [378, 379]. For a thin beam of length $L \sim 1$ μm, this strain-induced spin-phonon coupling can allow for

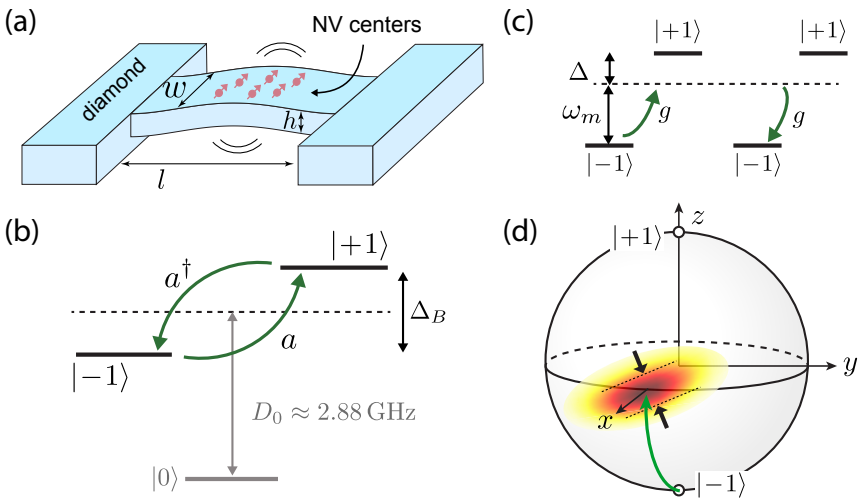

Figure 58: (a) All-diamond doubly clamped mechanical resonator with an ensemble of embedded NV centers. (b) Spin triplet states of the NV electronic ground state. Local perpendicular strain induced by beam bending mixes the $|\pm 1\rangle$ states. (c) A collection spins in the two-level subspace $\{|+1\rangle, |-1\rangle\}$ is off-resonantly coupled to a common mechanical mode giving rise to effective spin-spin interactions. (d) Squeezing of the spin uncertainty distribution of an NV ensemble.

coherent effective spin-spin interactions mediated by virtual phonons. Based on these effective interactions, we explore the possibility to generate spin squeezing of an NV ensemble embedded in the nanobeam. We account for spin dephasing and mechanical dissipation, and describe how spin echo techniques and mechanical driving can be used to suppress the dominant decoherence processes while preserving the coherent spin-spin interactions. Using these techniques we find that significant spin squeezing can be achieved with realistic experimental parameters. Our results have implications for NV ensemble magnetometry, and provide a new route toward controlled long-range spin-spin interactions.

8.2.1 Model for NV spin squeezing

The electronic ground state of the negatively charged NV center is a spin $S = 1$ triplet with spin states labeled by $|m_s = 0, \pm 1\rangle$ as shown in Fig. 58b. In the presence of external electric and magnetic fields $\vec{E}$ and $\vec{B}$, the Hamiltonian for a single NV is ($\hbar = 1$) [379]

$$H_{\rm NV} = (D_0 + d_{\parallel} E_z) S_z^2 + \mu_B g_s \vec{S} \cdot \vec{B} - d_{\perp} \left[E_x (S_x S_y + S_y S_x) + E_y (S_x^2 - S_y^2) \right], \tag{8.5}$$

where $D_0/2\pi \simeq 2.88$ GHz is the zero field splitting, $g_s \simeq 2$, μ_B is the Bohr magneton, and $d_\parallel$ ($d_\perp$) is the ground state electric dipole moment in the direction parallel (perpendicular) to the NV axis [380, 381].

Motion of the diamond nanoresonator changes the local strain at the position of the NV center, which results in an effective, strain-induced electric field [379]. We are interested in the near-resonant coupling of a single resonant mode of the nanobeam to the $|\pm1\rangle$ transition of the NV, with Zeeman splitting $\Delta_B = g_s\mu_B B_z/\hbar$, as shown in Fig. 58b,c. The perpendicular component of strain $E_\perp$ mixes the $|\pm1\rangle$ states. For small beam displacements, the strain is linear in its position and we write $E_\perp = E_0(a + a^\dagger)$, where a is the destruction operator of the resonant mechanical mode of frequency ω_m, and E_0 is the perpendicular strain resulting from the zero point motion of the beam. We note that the parallel component of strain shifts both states $|\pm1\rangle$ relative to $|0\rangle$ [382]; however, with near-resonant coupling $\Delta = \Delta_B - \omega_m \ll D_0$ and preparation in the $|\pm1\rangle$ subspace, the state $|0\rangle$ remains unpopulated and parallel strain plays no role in what follows. Within this two-level subspace, the interaction of each NV is $H_i = g\left(\sigma_i^+ a + a^\dagger \sigma_i^-\right)$, where $\sigma_i^\pm = |\pm1\rangle_i \langle\mp1|$ is the Pauli operator of the ith NV center and g is the single phonon coupling strength. For many NV centers we introduce collective spin operators, $J_z = \frac{1}{2}\sum_i |1\rangle_i \langle 1| - |-1\rangle_i \langle -1|$ and $J_\pm = J_x \pm iJ_y = \sum_i \sigma_i^\pm$, which satisfy the usual angular momentum commutation relations. The total system Hamiltonian can then be written as

$$H = \omega_m a^\dagger a + \Delta_B J_z + g\left(a^\dagger J_- + a J_+\right), \tag{8.6}$$

which describes a Tavis-Cummings type interaction between an ensemble of spins and a single mechanical mode. In Eq. (8.6) we have assumed uniform coupling of each spin to the mechanical mode for simplicity. In general the coupling may be nonuniform and we discuss this further below.

To estimate the coupling strength g, we calculate the strain for a given mechanical mode

and use the experimentally obtained stress coupling of 0.03 Hz Pa^{-1} in the NV ground state [192]. We take a doubly clamped diamond beam (see Fig. 58a) with dimensions $L \gg w, h$ such that Euler-Bernoulli thin beam elasticity theory is valid [383]. For NV centers located near the surface of the beam we obtain

$$\frac{g}{2\pi} \approx 180 \left(\frac{\hbar}{L^3 w \sqrt{\rho E}} \right)^{1/2} \text{GHz}, \tag{8.7}$$

where ρ is the mass density and E is the Young's modulus of diamond. For a beam of dimensions $(L, w, h) = (1, 0.1, 0.1)\,\mu$m we obtain a vibrational frequency $\omega_m/2\pi \sim 1$ GHz and coupling $g/2\pi \sim 1$ kHz. While this is smaller than the strain coupling $g_e/2\pi \approx 10$ MHz expected for electronic excited states of defect centers [384, 385] or quantum dots [386], we benefit from the much longer spin coherence time T_2 in the ground state. An important figure of merit is the single spin cooperativity $\eta = \frac{g^2 T_2}{\gamma \bar{n}_{\text{th}}}$, where $\gamma = \omega_m/Q$ is the mechanical damping rate and $\bar{n}_{\text{th}} = (e^{\hbar\omega_m/k_B T} - 1)^{-1}$ is the equilibrium phonon occupation number at temperature T. Assuming $Q = 10^6$, $T_2 = 10$ ms and $T = 4$ K, we obtain a single spin cooperativity of $\eta \sim 0.8$. This can be further increased by reducing the dimensions of the nanobeam and operating at lower temperatures.

8.2.2 Figure of merit for spin squeezing

In the dispersive regime, $g \ll \Delta = \Delta_B - \omega_m$, virtual excitations of the mechanical mode result in effective interactions between the otherwise decoupled spins. In this limit, H can be approximately diagonalized by the transformation $e^R H e^{-R}$ with $R = \frac{g}{\Delta}\left(a^\dagger J_- - a J_+\right)$. To order $(g/\Delta)^2$ this yields an effective Hamiltonian,

$$H_{\text{eff}} = \omega_m a^\dagger a + \left(\Delta_B + \lambda a^\dagger a\right) J_z + \frac{\lambda}{2} J_+ J_-, \tag{8.8}$$

where $\lambda = 2g^2/\Delta$ is the phonon-mediated spin-spin coupling strength. Rewriting $J_+ J_- = \mathbf{J}^2 - J_z^2 + J_z$, and provided the total angular momentum J is conserved, we obtain

a term $\propto J_z^2$ corresponding to the one-axis twisting Hamiltonian [387].

To generate a spin squeezed state, we initialize the ensemble in a coherent spin state (CSS) $|\psi_0\rangle$ along the x axis of the collective Bloch sphere. The CSS satisfies $J_x |\psi_0\rangle = J |\psi_0\rangle$ and has equal transverse variances, $\langle J_y^2 \rangle = \langle J_z^2 \rangle = J/2$. This can be achieved using optical pumping and global rotations of the spins with microwave fields [388]. The squeezing term $\propto J_z^2$ describes a precession of the collective spin about the z axis at a rate proportional to J_z, resulting in a shearing of the uncertainty distribution and a reduced spin variance in one direction as shown in Fig. 58d. This is quantified by the squeezing parameter [389, 390],

$$\xi^2 = \frac{2J \langle \Delta J_{\text{min}}^2 \rangle}{\langle J_x \rangle^2}, \tag{8.9}$$

where $\langle \Delta J_{\text{min}}^2 \rangle = \frac{1}{2}\left(V_+ - \sqrt{V_-^2 + V_{yz}^2}\right)$ is the minimum spin uncertainty with $V_\pm = \langle J_y^2 \pm J_z^2 \rangle$ and $V_{yz} = \langle J_y J_z + J_z J_y \rangle / 2$. The preparation of a spin squeezed state, characterized by $\xi^2 < 1$, has direct implications for NV ensemble magnetometry applications, since it would enable magnetic field sensing with a precision below the projection noise limit [389].

We now consider spin squeezing in the presence of realistic decoherence. In addition to the coherent dynamics described by H_{eff}, we account for mechanical dissipation and spin dephasing using a master equation

$$\begin{aligned}\dot{\rho} = &- i\left[-\frac{\lambda}{2} J_z^2 + \left(\Delta_B + \lambda a^\dagger a\right) J_z, \rho\right] + \frac{1}{2T_2} \sum_i \mathcal{D}[\sigma_z^i]\rho \\ &+ \Gamma_\gamma(\bar{n}_{\text{th}} + 1)\mathcal{D}[J_-] + \Gamma_\gamma \bar{n}_{\text{th}} \mathcal{D}[J_+],\end{aligned} \tag{8.10}$$

where $\mathcal{D}[c]\rho = c\rho c^\dagger - \frac{1}{2}\left(c^\dagger c \rho + \rho c^\dagger c\right)$ and the single spin dephasing T_2^{-1} is assumed to be Markovian for simplicity (see below). Note that we absorbed a shift of $\lambda/2$ into Δ_B, and ignored single spin relaxation as T_1 can be several minutes at low temperatures [251]. The second line describes collective spin relaxation induced by mechanical dissipation, with

$\Gamma_\gamma = \gamma g^2/\Delta^2$. Finally, the phonon number $n = a^\dagger a$ shifts the spin frequency, acting as an effective fluctuating magnetic field which leads to additional dephasing.

Let us for the moment ignore fluctuations of the phonon number n; we address these in detail below. Starting from the CSS $|\psi_0\rangle$, we plot the squeezing parameter in Fig. 59a for an ensemble of $N = 100$ spins and several values of $\bar{n}_{\rm th}$, in the presence of dephasing T_2^{-1} and collective relaxation Γ_γ. Here we calculated ξ^2 by solving Eq. (8.10) using an approximate numerical approach treating Γ_γ and T_2 separately, and verified that the approximation agrees with exact results for small N. To estimate the minimum squeezing, we linearize the equations of motion for the averages and variances of the collective spin operators (see dashed lines in Fig. 59a). From these linearized equations, in the limits of interest, $J \gg 1$, $\bar{n}_{\rm th} \gg 1$ and to leading order in both sources of decoherence, we obtain approximately

$$\xi^2 \simeq \frac{4\Gamma_\gamma \bar{n}_{\rm th}}{J\lambda^2 t} + \frac{t}{T_2}. \tag{8.11}$$

Optimizing t and the detuning Δ, we obtain the optimal squeezing parameter,

$$\xi^2_{\rm opt} \simeq \frac{2}{\sqrt{J\eta}}, \tag{8.12}$$

at time $t_{\rm opt} = T_2/\sqrt{J\eta}$, similar to results for atomic systems [391–393]. Note that for non-Markovian dephasing, the scaling is even more favorable [394]. In Fig. 59b we plot the scaling of the squeezing parameter with J for small but finite decoherence, and find agreement with Eq. (8.12). For comparison we also plot the unitary result in the absence of decoherence, scaling as $\xi^2_{\rm opt} \sim J^{-2/3}$ and limited by the Bloch sphere curvature [387].

8.2.3 Phonon number fluctuations

In Eq. (8.8) we see that the phonon number $n = a^\dagger a$ couples to J_z, leading to additional dephasing due to thermal number fluctuations. On the other hand, this same coupling can

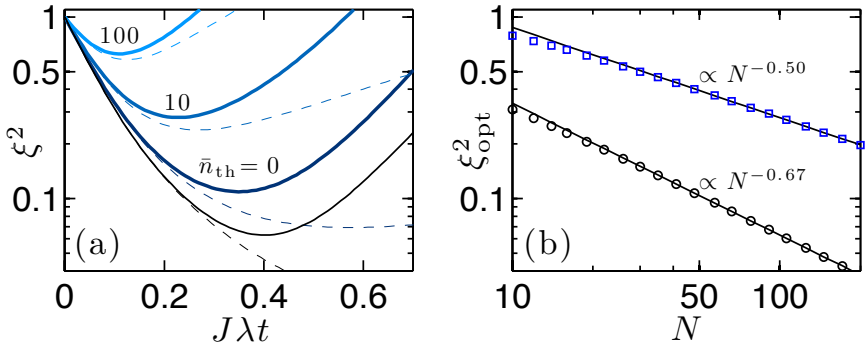

Figure 59: (a) Spin squeezing parameter versus scaled precession time with $N = 100$ spins. Solid blue lines show the calculated squeezing parameter for $T_2 = 10$ ms and values of $\bar{n}_{\rm th}$ as shown. For each curve, we optimized the detuning Δ to obtain the optimal squeezing. Blue dashed lines are calculated from the linearized equations for the spin operator averages. Black solid (dashed) line shows exact (linearized) unitary squeezing. (b) Optimal squeezing versus number of spins. Lower (upper) red line shows power law fit for $\bar{n}_{\rm th} = 1$ (10) and $T_2 = 1$ (0.01) s. The detuning Δ is optimized for each point. Other parameters in both plots are $\omega_m/2\pi = 1$ GHz, $g/2\pi = 1$ kHz, $Q = 10^6$.

also lead to additional spin squeezing from cavity feedback, by driving the mechanical mode [391–393]. In the following, we consider a twofold approach to mitigate thermal spin dephasing while preserving the optimal squeezing. First, we apply a sequence of global spin echo control pulses to suppress dephasing from low-frequency thermal fluctuations. This also extends the effective coherence time T_2 of single NV spins [388]. Second, we consider driving the mechanical mode, and identify conditions when this results in a net improvement of the squeezing.

To simultaneously account for thermal dephasing, driven feedback squeezing, and spin control pulse sequences, we write the interaction term in Eq. (8.8) in the so-called "toggling frame" [395],

$$H_{\rm int}(t) = \lambda J_z f(t) \delta n(t). \tag{8.13}$$

The function $f(t)$ periodically inverts the sign of the interaction as shown in the inset of Fig. 60a, describing the inversion of the collective spin $J_z \to -J_z$ with each π pulse of the spin echo sequence. Phonon number fluctuations are described by $\delta n(t) = n(t) - \bar{n}$, where $\bar{n}$ is the mean phonon number and we have omitted an average frequency shift proportional

to $\bar{n}$ in Eq. (8.13). The number fluctuation spectrum $S_n(\omega) = \int dt e^{i\omega t} \langle \delta n(t) \delta n(0) \rangle$ is plotted in Fig. 60a for a driven oscillator coupled to a thermal bath.

We calculate the required spin moments within the Gaussian approximation for phonon number fluctuations, and obtain

$$\langle J_+(t) \rangle = e^{-\chi} \left\langle e^{-i\mu(J_z - 1/2)} J_+(0) \right\rangle, \tag{8.14}$$

and similar results for $\left\langle J_+^2(t) \right\rangle$ and $\langle J_+(t) J_z(t) \rangle$. In Eq. (8.14) the dephasing parameter χ and effective squeezing via μ are given by

$$\chi = \lambda^2 \int \frac{d\omega}{2\pi} \frac{F(\omega\tau)}{\omega^2} \bar{S}_n(\omega), \tag{8.15}$$

$$\mu = \lambda^2 \int \frac{d\omega}{2\pi} \frac{K(\omega\tau)}{\omega^2} A_n(\omega), \tag{8.16}$$

where $\bar{S}_n(\omega) = \left(S_n(\omega) + S_n(-\omega)\right)/2$ and $A_n(\omega) = \left(S_n(\omega) - S_n(-\omega)\right)/2$. The filter function $F(\omega\tau) = \frac{\omega^2}{2} \left| \int dt e^{i\omega t} f(t) \right|^2$ describes the effect of the spin echo pulse sequence with time τ between π pulses [396–398]. The function $K(\omega\tau)$ plays the analogous role for the effective squeezing described by μ, and is related to F by a Kramers-Kronig relation. We plot K and F for a sequence of $M = 4$ pulses in Fig. 60a.

8.2.4 Impact of thermal fluctuations

We now consider the impact of thermal fluctuations on the achievable squeezing. The noise spectrum $S_n(\omega) = 2\gamma\bar{n}_{\rm th}(\bar{n}_{\rm th} + 1)/(\omega^2 + \gamma^2)$ is symmetric around $\omega = 0$. Without spin echo control pulses, this low frequency noise results in nonexponential decay of the spin coherence, $\chi_0(t) = \frac{1}{2}\lambda^2 \bar{n}_{\rm th}^2 t^2$ (with $\bar{n}_{\rm th} \gg 1$), familiar from single qubit decoherence [388, 399]. The inhomogeneous thermal dephasing time is $T_2^* \simeq \sqrt{2}/\lambda\bar{n}_{\rm th}$, severely limiting the possibility of spin squeezing. In particular, at time $t = t_{\rm opt}$ we find that squeezing is prohibited when $\bar{n}_{\rm th} > \sqrt{J}$. However, one can overcome this low frequency thermal noise using spin echo. By applying a sequence of M equally spaced global π-pulses to the spins

during precession of total time t, we obtain $\chi_{\rm th} \sim \lambda^2 \gamma \bar{n}_{\rm th}^2 t^3/M^2$, suggesting that thermal dephasing can be made negligible relative to both Γ_γ and T_2^{-1}. For a sufficiently large number of pulses, $M \gg \bar{n}_{\rm th}\sqrt{\gamma T_2}$, we recover the optimal squeezing in Eqs. (8.11) and (8.12).

Adding a mechanical drive can further enhance squeezing via feedback; however, it also increases phonon number fluctuations, contributing to additional dephasing. We consider a detuned external drive of frequency $\omega_{\rm dr} = \omega_m + \delta$, leading to two additional peaks in $S_n(\omega)$ at $\omega = \pm\delta$, as shown in Fig. 60a. The area under the left [right] peak scales as $\bar{n}_{\rm dr}\bar{n}_{\rm th}$ $[\bar{n}_{\rm dr}(\bar{n}_{\rm th}+1)]$, where $\bar{n}_{\rm dr}$ is the mean phonon number due to the drive at zero temperature. The symmetric and antisymmetric parts of this noise contribute to dephasing and squeezing as described by Eqs. (8.15) and (8.16). Choosing the interval $t/M = 2\pi/\delta$ between π pulses, we obtain additional dephasing $\chi_{\rm dr} \simeq \left(\frac{\lambda}{\delta}\right)^2 \bar{n}_{\rm dr}\bar{n}_{\rm th}\gamma t$ and effective squeezing with $\mu \simeq \frac{\lambda^2}{\delta}\bar{n}_{\rm dr} t$. In the limit $\bar{n}_{\rm dr} \gg \bar{n}_{\rm th}$, the effects of the drive dominate over $\chi_{\rm th}$ and Γ_γ and we recover the ideal scaling given in Eq. (8.12), even with a small number of echo pulses. This is shown in Fig. 60b,c where we see that the optimal squeezing improves with increasing $\bar{n}_{\rm dr}$ for a fixed number of pulses $M = 4$.

Finally, we discuss our assumption of uniform coupling strength g in Eq. (8.6). This is an important practical issue, as we expect the coupling to individual spins to be inhomogeneous in experiment due to the spatial variation of strain in the beam. Nonetheless, even with nonuniform coupling, we still obtain squeezing of a collective spin with a reduced effective total spin $J_{\rm eff} < J$, provided $J \gg 1$. First, we note that inhomogeneous magnetic fields resulting in nonuniform detuning are compensated by spin echo. Second, for a distribution of coupling strengths g_i, the effective length of the collective spin is $\sum_i g_i/\sqrt{\sum_i g_i^2}$ for the direct squeezing term, and $\sum_i g_i^2/\sqrt{\sum_i g_i^4}$ for feedback squeezing with a mechanical drive. Similar conclusions were reached in atomic and nuclear systems [391–393, 400]. In the case of direct squeezing, it is important that the sign of the g_i's is the same to avoid cancellation; this is automatically achieved by using

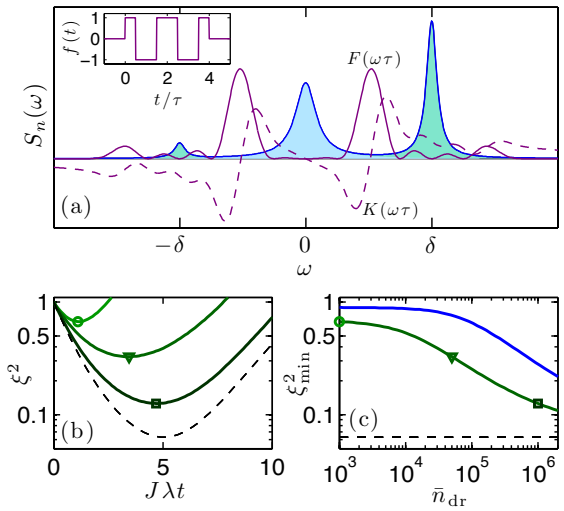

Figure 60: (a) Number fluctuation spectrum of thermal driven oscillator. Center (blue) peak is purely thermal while side (green) peaks are due to detuned drive. Solid (dashed) purple line shows filter function F (K) for $M = 4$ pulses. Inset: corresponding function $f(t)$ for $M = 4$. (b) Solid green curves show squeezing parameter versus precession time for $\bar{n}_{\rm th} = 10$ and $\bar{n}_{\rm dr} = 10^3, 5\times10^4, 10^6$ (top to bottom). Dashed black line shows unitary squeezing. (c) Minimum squeezing versus drive strength for $\bar{n}_{\rm th} = 50, 10$ (top to bottom). Symbols mark corresponding points with (b). Dashed black line shows unitary squeezing. Parameters in (b) and (c) are $M = 4$, $g/2\pi = 1$ kHz, $T_2 = 10$ ms, $N = 100$, $\omega_m/2\pi = 1$ GHz, $Q = 10^6$.

NV centers implanted on the top of the beam. For beam dimensions $(1, 0.1, 0.1)\,\mu$m analyzed above, we estimate that $N \sim 200$ NV centers can be embedded without being perturbed by direct magnetic dipole-dipole interactions. A reduction of the effective spin length by factor ~ 2 still leaves $N_{\rm eff} \sim 100$, sufficient to observe spin squeezing.

We have shown that direct spin-phonon coupling in diamond can be used to prepare spin squeezed states of an NV ensemble embedded in a nanoresonator, even in the presence of dephasing and mechanical dissipation. With further reductions in temperature, beam dimensions, and spin decoherence rates, the regime of large single spin cooperativity $\eta \gg 1$ could be achieved. This would allow for coherent phonon-mediated interactions and quantum gates between two spins embedded in the same resonator via $H_{\rm int} = \lambda\left(\sigma_1^+\sigma_2^- + \text{h.c.}\right)$, and coupling over larger distances by phononic channels [384].

8.3 Nitrogen-Vacancy atomic clock

Atomic clocks are the most accurate systems for measuring time and frequency. They are used in a broad array of applications, ranging from communication and computation to navigation (e.g. global positioning system (GPS)). Modern frequency standards derive their stability from the precisely measured internal hyperfine level splittings of atoms of Cs, Rb, or H. When an oscillating magnetic field is resonant with the energy difference of these internal states, a change in population between levels changes the radiofrequency or optical absorption. Standard lock-in techniques modulate the driving frequency and monitor the absorption as a correction for a tunable active reference oscillator, e.g. a quartz crystal, thus stabilizing it to the atomic line [401]. Recent experiments on single trapped ions [402] and on ensembles of atoms trapped in optical lattices [403, 404] have far exceeded the international cesium standard, enabling the observation of general relativity corrections at distances of a few meters [405]. Such precision, however, comes at the expense of mobility, as the infrastructure for these standards encompass several tens of cubic meters of space. At the other extreme, portable standards based on rubidium vapor cells provide excellent stability for time scales ranging from 1 s to 10^4 s and find usage in satellites, laboratory equipment, and cellular communications [406]. Mobile devices, which typically do not contain their own precision standards, can share GPS time signals for maintaining communication standards, but when the external lock signal is obstructed, a precise local frequency standard with minimal drift is necessary to maintain synchronization.

To address this need, several groups have miniaturized these atomic standards on-chip through the aid of modern microfabrication techniques applied to detectors and lasers [407–409]. Here, we propose a solid-state alternative based upon electronic spin states in the negatively charged nitrogen vacancy center (NVC) in diamond. This diamond system offers a host of advantages and some unique challenges. First, single crystal diamond can be grown into a micron-scale, radiation hard chip, which makes it portable and well-suited

for integration in a semiconductor fabrication process [75]. Second, this solid-state system derives its performance as a clock from exceptional spin lifetimes of the NVC [45] and resembles atomic and molecular systems. The optical detection of the NVC also increases the signal-to-noise of solid-state standards based on inductive detection [410]. Compared to vapor cells, this standard does not suffer from doppler or collisional broadening. However, owing to a complex mesoscopic environment, both single and ensembles of NVCs exhibit an increased homogeneous linewidth compared to atomic standards [44]. The higher density of defects in solids allows for a comparable frequency stability in smaller sensor volumes when ensemble effects can be mitigated. Similar to atomic clocks, temperature fluctuations can degrade the clock stability. For the NVC, these temperature changes induce a shift in the resonance frequency of the entire ensemble. To this end, we will discuss temperature stabilization methods based upon certain unique properties of the NVC strain and defect symmetry.

We estimate a stability, expressed as an Allan deviation, of $\sigma_y \approx 2 \times 10^{-12}$ at 1s of averaging for a 0.1 mm^3 diamond sample with an ensemble of NVCs. Paired with potentially modest operational power requirements, this NV clock could result in a new generation of portable solid-state frequency standards. A proposed device is shown in Figure 61 and contains: a diamond chip grown with a dielectric cavity for lowering the optical pumping power requirements, photoluminescence (PL) collection with on-chip Si photodiodes, and planar microwave waveguides for addressing the NV transitions, all of which can be integrated within modern device fabrication.

8.3.1 The NV zero-field splitting as a frequency standard

An atomic clock derives its stability from the large quality factor, $Q = \nu/\Delta\nu$, of the probed resonance, with narrow linewidth, $\Delta\nu$, being much smaller than the resonant frequency ν. In the solid-state, we desire: (i) a microwave transition ($\nu \sim$ GHz) that also exhibits a large Q; (ii) a resonance that does not vary due to material or fabrication processes; and

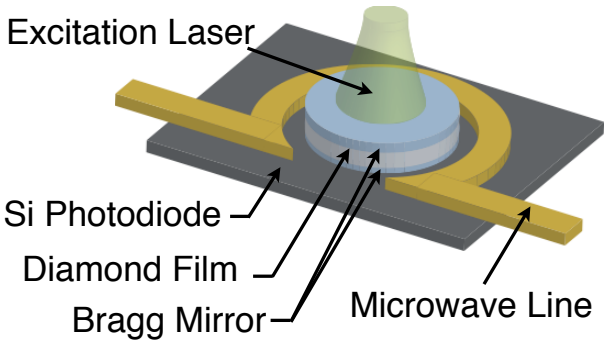

Figure 61: Schematic of the diamond frequency standard. A thin (100 μm) diamond chip is surrounded by dielectric stacks (Bragg Reflectors) on both sides to create a resonant cavity for 532nm excitation in order to reduce the power requirements. On-chip 532nm excitation comes from a doubled 1064nm surface emitting laser (not shown). Silicon photodetectors underneath the diamond serves to collect emission. Microwaves, which address the NV magnetic sublevels, are applied to the entire sample by a planar stripline.

(iii) a precise method of measuring population changes. The NVC in diamond satisfies these criteria by having: a ground state spin triplet characterized by long (>1ms) coherence times, a ground state crystal field splitting with an intrinsic resonance frequency near 2.870 GHz, which is independent, to lowest order, of applied magnetic field, and spin states that are optically polarizable and detectable on single site length scales.

The magneto-optical description of the NVC is well-documented in the literature, thus we give only a brief phenomenological summary. Figure 62A shows the relevant spin sublevels (0,1,2,3 and S) for the NVC. Optical absorption of green laser light causes broadband PL of the NVC from 637-800 nm. A spin-dependent intersystem crossing between the excited state triplet (3) and the metastable, dark singlet level (S) changes the integrated PL for the spin states $|0\rangle$ and $|\pm1\rangle$. The deshelving from this singlet occurs primarily to the $|0\rangle$ spin state, providing a means to polarize the NVC. Microwave fields resonant between levels $|0\rangle$ and $|1\rangle$, perturb the spin populations, and thus the PL response. This can, in principle be characterized in two ways: 1) by measuring a continuous wave response to simultaneous optical and microwave fields (e.g. Figure 62B) or 2) in a pulsed manner, by preparing a state using only microwaves, and observing the

transient PL response.

In order to compare these two methods quantitatively, we construct a simple model for the relevant spin dynamics described by Hamiltonians for the lowest and first excited triplet state and two metastable singlet states. For the purposes of a frequency standard, we monitor the response of only the ground state triplet sublevels to resonant excitation, yielding the ground state Hamiltonian[381]:

$$\mathbf{H}_{gs} = (D_{gs} + d_{\parallel}\sigma_z)S_z^2 + g\mu_b\vec{S}\cdot\vec{B} + d_{\perp}\sigma_x(S_xS_y + S_yS_x) + d_{\perp}\sigma_y(S_x^2 - S_y^2) \tag{8.17}$$

Here, $d_{\parallel,\perp}$ are the ground state electric dipole moment components along and perpendicular to the C_{3v} symmetry axis of the defect. D_{gs} is the ground state crystal field splitting (2.870 GHz), μ_b is the Bohr magneton, and g is the Lande factor. S_k are spin-1 operators in the $k = \{x, y, z\}$ directions. The local electric field vector, induced by crystal strain, is $\vec{\sigma}$. We assume there is no applied external electric field. In the limit of static magnetic and electric fields much smaller than D_{gs}, the eigenfunctions are those of the S_z operator, as show in Fig. 62.

A driving field at frequency ω induces electron spin resonance (ESR) transitions between $|0\rangle$ and $|\pm1\rangle$. On resonance ($\omega \approx D_{gs}$), the PL decreases and provides a feedback signal with which to lock ω to D_{gs}. The dynamics are best viewed as a response to a time-varying magnetic field $B_1 = 2b_1\cos(2\pi\omega t)\hat{x}$; transforming H_{gs} into the interaction frame defined by the operator $V = e^{2\pi i\omega t S_z^2}$ and performing the rotating wave approximation yields,

$$\mathbf{H}'_{gs} = (D_{gs} + d_{\parallel}\sigma_z - \omega)S_z^2 + g\mu_b B_z S_z + g\mu_b b_1 S_x \tag{8.18}$$

The relaxation rates of the excited triplet and singlet states, shown in Fig. 62A, play an important role in the optical pumping and spin measurement [411]. We model the total

magneto-optical response using a master equation approach:

$$\dot{\rho} = \frac{1}{i\hbar}[H'_{gs}, \rho] + \sum_k L_k \rho L_k^\dagger - \frac{1}{2} L_k^\dagger L_k \rho - \frac{1}{2} \rho L_k^\dagger L_k \tag{8.19}$$

where ρ is the density operator for the NVC ground, excited triplet, and effective singlet states. The jump operators, L_k, have magnitudes corresponding to relaxation rates $\sqrt{r_k}$. The solution to the equation yields the total magneto-optical response for both continuous and pulsed excitation, allowing for a numerical assessment of the clock sensitivity with respect to changes in the electromagnetic fields.

8.3.2 CW Approach

Under continuous excitation of optical and microwave fields the NVC frequency standard closely resembles a two-isotope Rb standard. Spin-dependent PL of the NVC occurs under non-resonant absorption of green light of intensity I. Application of a microwave field of intensity $\Omega = g\mu_b b_1$, detuned from resonance by an amount $\Delta = D_{gs} - \omega$, causes a broad, phonon-assisted PL: $F(I, \Omega, \Delta) = \gamma \rho_{22}^{ss} + \frac{\gamma^2}{\kappa+\gamma} \rho_{33}^{ss}$. Here ρ_{22}^{ss} and ρ_{33}^{ss} represent the populations of the first excited state spin sublevels in the steady-state, as analytically derived from a master equation. Figure 62B shows the typical response of F for varied detunings, which displays a Lorentzian lineshape. The stability of the clock can be derived from the resonance curve by considering the Allan variance:

$$\sigma_y(\tau) = \frac{1}{2\pi Q} \frac{1}{(S/N)} \frac{1}{\sqrt{\tau}} \tag{8.20}$$

where τ is the averaging time and S/N is the signal-to-noise ratio, which depends on both the photon shot noise as well as the imperfect modulation of the resonance (i.e. $C \neq 1$). The intrinsic linewidth is limited by the paramagnetic and nuclear spin environments which fluctuate during the measurement. This linewidth broadens if the microwave and optical transitions are driven near saturation ('power broadening'); however, higher pump powers

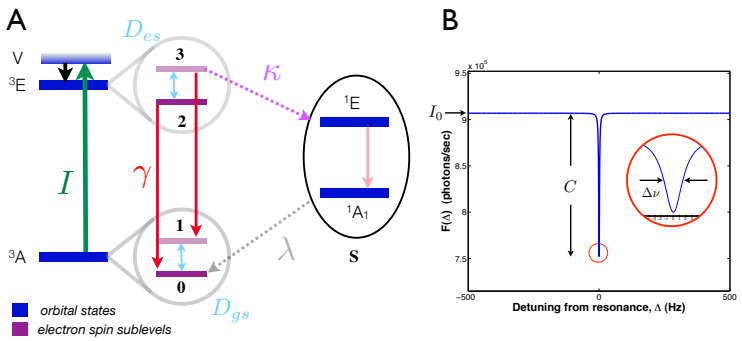

Figure 62: Nitrogen-vacancy center energy levels and resonant response. (A) The lowest lying triplet (^3E, ^3A) and singlet (^1E, ^1A) orbital states of the NV$^-$ center. I, γ, κ, and λ represent the absorption, PL, intersystem crossing, and deshelving rates, respectively. Sublevels 0 and 2 are S_z eigenstates $|0\rangle$, whereas 1 and 3 are $|\pm 1\rangle$, with the degeneracy lifted by small crystal strain or applied magnetic field. The model is simplified by approximating both singlet states as a single metastable level. (B) The steady-state fluorescence emission of the NVC under continuous optical and microwave irradiation, detuned from resonance by Δ [412].

also increase the the depth of the dip ($C \to 1$). Indeed, far below optical saturation, the PL rate is sufficiently small, and the modulation depth (C) reduced, so as to cause a decrease in the stability per averaging time. As Q is the most important factor for stability, there exists an optimal condition, which balances line broadening with the reduced signal. Under these conditions we estimate a linewidth of 3.6 MHz ($T_2^* = 88$ns), an off-resonance fluorescence rate of ∼9400 photon/s (accounting for a finite detector efficiency), and a 17% modulation depth. With these parameters, $\sigma_y(\tau) = 8.124 \times 10^{-5}\ \tau^{-1/2}$ for a single NVC. In short, the NVC lacks sufficient stability when monitoring the PL response continuously. This results from the fact that the laser excitation must be reduced far below saturation so that optical power broadening reaches the homogeneous linewidth. At such low pump powers, the fluorescent photon flux is so small that the gains in Q are offset by losses in S/N. As seen in magnetometry studies of the NVC [287], a pulsed microwave excitation scheme, which monitors transient fluorescence behavior can drastically improve the performance beyond the naive continuous excitation/detection method.

8.3.3 Pulsed Approach

Thus, we now consider monitoring the NVC crystal field splitting (D_{gs}) in a pulsed fashion, akin to the Ramsey spectroscopy used in atomic clocks. The standard two-pulse Ramsey sequence, with time separation T, imprints a phase proportional to the frequency drift, $\delta\omega$, between two t hyperfine states of the atomic system. The PL response varies sinusoidally with $\delta\omega T$ and can be linearized to provide a passive standard with frequency uncertainty set by T^{-1}. However, if the system does not remain coherent for times $T \gg T_c$ (coherence time), the modulation of the PL response does not persist. In atomic vapor cells, trapped ions, or atomic fountains, T_c can be greater than a second due to a complex infrastructure involving magnetic shielding and the minimization of atomic collisions. In the NV system, a spin-bath environment limits T_c to tens of microseconds in a typical sample. Quantum memories and AC magnetometers often employ a Hahn echo sequence to extend this coherence time to T_2 by removing slowly varying magnetic fields; however, for frequency standards based on $m_f = 0$ "clock" states, the additional π-pulse of the Hahn echo would completely remove the phase accumulation associated with frequency drift, making it useless for time-keeping. Luckily, the S=1 nature of the NVC allows for a modified echo sequence, which yields a PL signal proportional to the drift for $T \sim T_2$.

In particular, let us begin with the usual spin echo sequence:

$$\frac{\pi}{2}\Big)_x \xrightarrow{\tau} \pi\Big)_{-x} \xrightarrow{\tau} \frac{\pi}{2}\Big)_x$$

where the notation $\theta\big)_\phi$ indicates a pulse with a flip angle θ and phase ϕ. The pulse durations, t_p are set to the flip angles $\theta = g\mu_b b_1 t_p$ and for $\Omega_1 \equiv g\mu_b b_1 \gg (D_{gs} - \Omega), g\mu_b B_z$, off-resonant excitations are suppressed. To simplify the analysis, we will directly calculate the propagator for the echo sequence:

$U_{echo} = e^{-i\frac{\pi}{2}S_x}e^{-i(\delta\Omega S_z^2+bS_z)\tau}e^{i\frac{\pi}{2}S_x}e^{i\frac{\pi}{2}S_x}e^{-i\frac{\pi}{2}S_x}e^{-i(\delta\Omega S_z^2+bS_z)\tau}e^{-i\frac{\pi}{2}S_x} = WW'$, where W is

$$W = e^{-i\frac{\pi}{2}S_x}e^{-i(\delta\Omega S_z^2+bS_z)\tau}e^{i\frac{\pi}{2}S_x} \quad (8.21)$$

$$= e^{-i(\delta\Omega\hat{X}-bS_y)\tau}, \quad (8.22)$$

W' is

$$W' = e^{i\frac{\pi}{2}S_x}e^{-i(\delta\Omega S_z^2+bS_z)\tau}e^{-i\frac{\pi}{2}S_x} \quad (8.23)$$

$$= e^{-i(\delta\Omega\hat{X}+bS_y)\tau}, \quad (8.24)$$

and $\hat{X}$ is

$$\hat{X} = \begin{bmatrix} \frac{1}{2} & 0 & -\frac{1}{2} \\ 0 & 1 & 0 \\ -\frac{1}{2} & 0 & \frac{1}{2} \end{bmatrix}. \quad (8.25)$$

Since $[\hat{X}, S_y] = 0$, we can write the product of W and W' as the sum of exponential arguments such that $U_{echo} = e^{-2i(D_{gs}-\Omega)\tau\hat{X}}$. To take advantage of this propagator we must first apply a pulse that creates a superposition of $\hat{X}$ eigenstates with differing eigenvalues; starting from the optically pumped $|0\rangle$ state, we accomplish this by applying a $\frac{\pi}{4}$ pulse about the $\hat{x}$ axis: $U_{45} = e^{-i\frac{\pi}{4}S_y}$, such that $U_{45}|0\rangle = \frac{1}{\sqrt{2}}(|0\rangle - i|+\rangle)$, where $|+\rangle$ is the symmetric superposition of the ±1 eigenstates of S_z. This yields the state prior to clock measurement:

$$U_{echo}U_{45}|0\rangle = \frac{1}{\sqrt{2}}\Big(-ie^{i\delta\Omega\tau}|+\rangle + e^{-i\delta\Omega\tau}|0\rangle\Big). \quad (8.26)$$

As seen in Eq. (8.18), the term proportional to S_z^2 is sensitive to the frequency drift ($\delta\nu$), whereas the term proportional to S_z vary with $\vec{B}$. In addition, hyperfine interactions with nearby nuclear spins have a secular correction term to the Hamiltonian $\propto A_\parallel S_z I_z$. By modifying the flip-angle of the first and last pulses of the echo sequence from $\pi/2$ to $\pi/4$, as shown in Fig. 63, the phase accumulation due to the S_z term cancels while that from

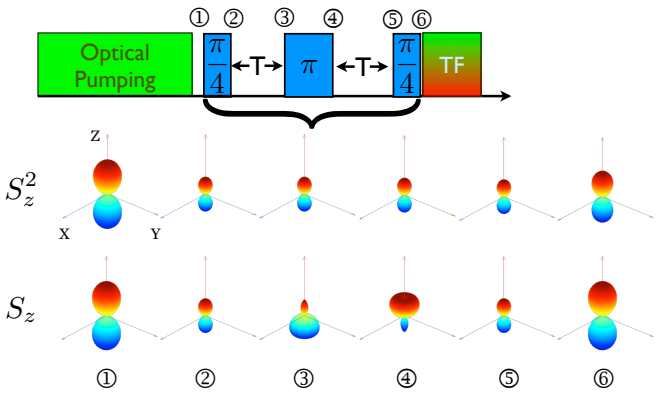

Figure 63: The spin-1 ground state $|0\rangle$ state is prepared by optical pumping. 45° rotations ensure that the S_z term evolution averages within the echo sequence, while the S_z^2 does not, as illustrated in the Euler projections of the state (inset). Note that the S_z term is completely refocused by the echo sequence, while the S_z^2 operator evolves, resulting in a different magnitude between the first and sixth states. A transient fluorescence (TF) measurement records the photocurrent for about 300ns timed with a pulse of green light.

the S_z^2 terms add over the duration $2T$. For simplicity, we monitor the eigenkets of S_z to describe the clock, assuming perfect microwave pulses and no optical illumination. First, optical pumping of the NV prepares the initial state $|\psi_0\rangle = |m_s = 0\rangle$. Evolution under our drift echo sequence, U_{echo}, gives:

$$|\psi_f\rangle = U_{echo}U_{45}\,|\psi_0\rangle = \frac{1}{\sqrt{2}}\sin(\phi)\,|0\rangle - \frac{1}{2}\cos(\phi)\big(\,|+1\rangle + |-1\rangle\,\big) \tag{8.27}$$

where $\phi = (D_{gs} - \omega)T = \delta\omega T$.

Unlike the steady-state case, the NVC is prepared in a state used for time keeping, then measured optically, without simultaneous microwave excitation. The transient PL response of the NV center can be modeled using projective measurements. The operator $\hat{M}$ describes the spin expectation value for a PL measurement [413],
$\hat{M} = a\,|0\rangle\langle 0| + b\big(\,|+1\rangle\langle +1| + |-1\rangle\langle -1|\,\big)$, where a and b are independent Poisson random variables. The fractional frequency deviation varies as the quantum observable, $\hat{M}$ for our

state $|\psi_f\rangle$ according to:

$$\frac{\delta\omega}{\omega_0} = \frac{1}{\omega_0}\frac{\langle\Delta\hat{M}\rangle}{|\partial\langle\hat{M}\rangle/\partial\omega|} \tag{8.28}$$

where $\langle\Delta\hat{M}^2\rangle = \langle\hat{M}^2\rangle - \langle\hat{M}\rangle^2$ is the variance of the operator. For room temperature spin readout of the NVC, $2a \approx 3b$ [295]. By calculating the moments of $\hat{M}$ and by assuming we accumulate M' independent measurements (e.g. total sampling time $\tau = M'T$), we arrive at:

$$\left\langle\frac{\delta\omega}{\omega_0}\right\rangle_{M'} = \frac{\xi}{D_{gs}\sqrt{T\tau}} \tag{8.29}$$

with $\xi \approx 5$ due to a combination of imperfect spin readout (i.e. $b \neq 0$), imperfect collection efficiency ($a \approx 0.031$), and a small ratio, λ/γ, of the metastable deshelving rate to the radiative lifetime. Taking $T = T_2 \approx 1$ms and $D_{gs} = 2870$ MHz, gives a deviation of $\delta\omega/\omega_0 = 8.8 \times 10^{-9}/\sqrt{\tau}$ for a single NVC. Thus, the pulsed NV frequency standard dramatically outperforms the CW scheme. A comparison of the two schemes for different defect concentrations, along with established standards, is shown in Figure 66. Note that all optical collection efficiencies (assumed to be $\sim 0.2\%$ of the total radiated photons) do not yet include cavity or resonant enhancements; this is, in fact, an area of current research [414] and will likely lead to further improvements.

The stability for a single NV center can be scaled by collecting the fluorescence from an ensemble of N non-interacting NV centers, yielding a $1/\sqrt{N}$ enhancement. To make a reasonable estimate of N, we start with the density of pure diamond: 1.74×10^{23} C atoms/cm^3. At an NV$^-$ defect fraction of 10^{-11} (0.01 part per billion), the density of defects is 1.74 / μm^3, consistent with commercially available samples. For a 1 mm^3 sample, the proposed $1/\sqrt{N}$ enhancement would yield a fractional frequency deviation of $2 \times 10^{-13}/\sqrt{\tau}$ for the pulsed scheme and $2 \times 10^{-9}/\sqrt{\tau}$ for the CW scheme; thus, a diamond film of thickness $\sim 100\mu$m with a surface area ~ 1 mm^2, as depicted in Fig. 61, gives $\sigma_y^{pulsed} \sim 6.7 \times 10^{-13}/\sqrt{\tau}$. Further increasing the defect density to 1 ppb would improve all values by another order of magnitude, but dephasing effects may start to arise owing to

interactions with other paramagnetic impurities [388]. Next, we will consider limitations of the NV frequency standard imposed by: dephasing, ensemble effects and temperature.

8.3.4 Dephasing and Inhomogenous Broadening

Dephasing. The coherent evolution of the NVC is strongly affected by interactions with its local environment, meaning that the $T^{-1/2}$ scaling of Eq. (8.29) cannot be maintained for all times. Unlike an atomic vapor, where collisions and stray magnetic fields dominate the dephasing, in the case of the NVC, impurities in the solid-state lattice limit the coherence. However, excellent material growth [45] and precision implantation [74, 75] can yield crystals, which are largely free of paramagnetic impurities. For a single NVC in an ultrapure diamond sample, spin echo (of duration $2T$) can further improve the observable coherence with a scaling, $e^{-(2T/T_2)^n}$, where the exponent $n \approx 3$ is related to the nuclear spin bath [44, 415]. In an ensemble of NVCs, where each center has a different bath, and hence, a different T_2 time, the net effect results in an "averaged" time constant, T_e, and $n = 1 - 2$, depending on the NV density [416]. We also note that owing to imperfect conversion efficiency, the NV density in the sample is a fraction of the total number of substitutional nitrogen impurities. Thus, a heavily doped sample, while improving the S/N, can reduce the overall ensemble coherence time T_e. Based on the estimates in Ref. [388], with an NV density of $10^{17}/\text{cm}^3$, a marginal modification can be expected; figure 66 shows the Allan deviation floor due to such dephasing considerations.

Inhomogenous Broadening. By taking advantage of spin echo, the pulsed NV frequency standard shows a favorable Allan deviation when compared to similarly sized atomic standards. As discussed above, considering an ensemble of defects provides a straightforward route to improving the Allan variance; however, the local strain field within the crystal may vary from center to center resulting in inhomogeneous broadening. Recent room temperature experiments on bulk diamond (defect fraction of $\sim 10^{-13}$) have observed $\sim 50 - 100$kHz variations in the NV D_{gs} of centers spaced at $\sim 1\mu$m [113]. Taking these

parameters would imply that for an NV-ensemble clock, the sensitivity is in fact, limited by the inhomogeneously broadened ensemble linewidth, $T_{2,\text{ens}} \sim 10 - 20\mu$s. This would reduce our estimated stability by nearly an order of magnitude and motivates the development of modern CVD growth and annealing techniques, which may be able to alleviate such local strain fluctuations [417].

8.3.5 Temperature Fluctuations

One of the most challenging aspects of an NV frequency standard is the fact that the resonance frequency corresponding to D_{gs} varies as function of temperature. At room-temperature, recent ensemble studies have observed $dD_{gs}/dT = -74.2(7)$ kHz/K [382] for mm-sized samples. Low temperature studies, down to 5K, show that this temperature dependence is, in fact, highly nonlinear; indeed, at liquid Nitrogen temperatures, linearizing yields a much weaker temperature dependence with, $dD_{gs}/dT \sim 100$ Hz/K [164]. Finally, at higher temperatures (up to 600K), recent work has observed $|dD_{gs}/dT| = 100$ kHz/K, consistent with room temperature measurements [418]. The microscopic mechanism which underlies this pronounced zero-field splitting (ZFS) temperature dependence is not yet fully understood, but is thought to be related to the thermal expansion of the diamond. In particular, as temperatures vary, the local lattice spacing of the NV center is distorted causing changes in orbital overlaps which determine D_{gs}. This picture is also consistent with very recent measurements of the room-temperature ZFS of single NV centers in bulk diamond, which also exhibits $dD_{gs}/dT \sim -75$ kHz/K [113]. Since the ensemble measurement is averaged over all NV orientations, the fact that it agrees identically with the single NV case suggests that crystallographic orientation does not affect dD_{gs}/dT, consistent with our proposed mechanism which owes to the overall thermal expansion of the lattice.

To further understand the effects of thermal expansion, we consider a schematic picture of the NV electronic orbitals; in particular, let us assume that the three orbitals associated

with the basal Carbon atoms are highly-localized wavefunctions (δ-function), which simply move with their respective atoms. The microscopic origin of the zero-field splitting is thought to be spin-spin interactions, meaning that a shifting of the wavefunctions will correspondingly alter the average magnetic dipole-dipole interaction, leading to a change in D_{gs}. The dipole-dipole interaction is generally characterized as,

$$V_{ij}S_iS_j = -\frac{\kappa}{2}\left\langle \frac{3\hat{r_i}\hat{r_j} - \delta_{ij}}{r^3} \right\rangle S_iS_j \tag{8.30}$$

where S_i is the magnetic dipole operator and κ is the scale of the interaction strength (2.88 GHz at 2.6 angstroms). To compute the above expectation value, we simply need to average over the displacements between each pair of carbon atoms. With a as the distance between nearest neighbor carbon atoms, the displacement vectors (without strain) are given by: $\mathbf{r^{(1)}} = a\hat{y}$, $\mathbf{r^{(2)}} = \frac{\sqrt{3}a}{2}\hat{x} - \frac{a}{2}\hat{y}$, and $\mathbf{r^{(3)}} = -\frac{\sqrt{3}a}{2}\hat{x} - \frac{a}{2}\hat{y}$. Thus, the spin Hamiltonian in the absence of strain is simply,

$$H = V_{ij}S_iS_j = \frac{3\kappa}{4a^3}(S_z^2 - 2/3). \tag{8.31}$$

Under strain ϵ_{kl}, the change in this Hamiltonian is,

$$\begin{aligned}
\Delta \quad & H = S_iS_j\Delta V_{ij} = -\frac{\kappa}{2}\left\langle \left(\frac{\partial}{\partial r_k}\frac{3\hat{r_i}\hat{r_j} - \delta_{ij}}{r^3}\right)\epsilon_{kl}\hat{r_l} \right\rangle S_iS_j \\
= \quad & \frac{3\kappa}{2a^3}[-\frac{3}{4}(\epsilon_{xx}+\epsilon_{yy})(S_z^2 - 2/3) + \frac{1}{8}(\epsilon_{xx}-\epsilon_{yy})(S_x^2 - S_y^2) \\
+ \quad & \frac{1}{8}(\epsilon_{xy}+\epsilon_{yx})(S_xS_y + S_yS_x) - \frac{1}{2}\epsilon_{zx}(S_xS_z + S_zS_x) \\
- \quad & \frac{1}{2}\epsilon_{zy}(S_yS_z + S_zS_y)].
\end{aligned} \tag{8.32}$$

Inspection reveals that the change in the ZFS is set by the coefficient of the first term, $\alpha = -\frac{3}{4}(\epsilon_{xx}+\epsilon_{yy})\frac{3\kappa}{2a^3}$. In order to reproduce the zero strain ZFS of $\frac{3\kappa}{4a^3} = 2.88$ GHz, we take $a = 2.38$Å, yielding $\alpha = -4.32\text{GHz}(\epsilon_{xx}+\epsilon_{yy})$. Assuming isotropic expansion

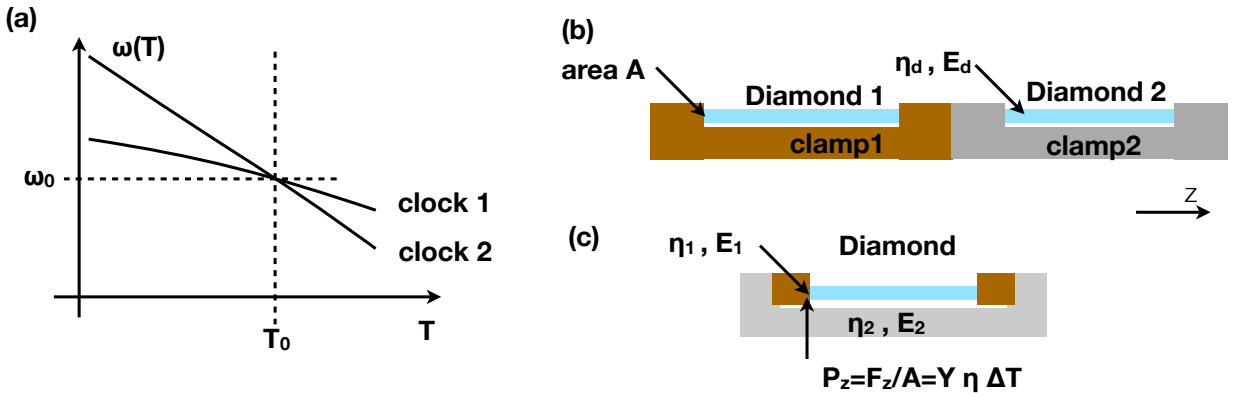

Figure 64: Temperature Stabilization using two clocks. (a) The two diamond clocks have differing dD_{gs}/dT since they are clamped to substrates with different thermal expansion coefficients, $\eta_{1,2}$ and different Young's moduli, $E_{1,2}$ (b) Schematic illustration of a synchronized composite clock setup. (c) Alternatively, using strain engineering, a single clamp may be designed to fully cancel the temperature dependence of the NV ZFS.

$\epsilon_{xx} = \epsilon_{yy} = \epsilon_{zz}$, our highly schematic model predicts a ZFS temperature dependence of,

$$\frac{dD_{gs}}{dT} = (-4.32 \times 2)\left(\frac{1.6 \times 10^{-6}}{1K}\right) \approx 15\text{kHz/K}, \tag{8.33}$$

which is a factor of 5 from the observed room-temperature dependence [382]. By adding in further details, e.g. taking p-orbitals instead of δ-function orbitals, one can refine our above results so that the predicted temperature dependence is within a factor of 3 of the observed. This suggests that our proposed picture where temperature simply serves to distort the defect geometry is likely the dominant factor underlying the observed $\frac{dD_{gs}}{dT}$. Such a temperature dependence under normal operating conditions makes this passive standard behave like a traditional crystal oscillator and poses a challenge for maintaining a precise operating temperature.

One can certainly envision stabilizing the temperature of the diamond chip to within 0.01K by using commercially available Peltier coolers with PID loops. This would, in principle, allow us to achieve ≈ 742 Hz uncertainty in the zero-field splitting, or a fractional frequency stability of 2.58×10^{-7} at room temperature. We note that ensemble

averaging would have no beneficial effect here, as all centers shift equally due to isotropic expansion. In the next section, building upon our discussions above, we will show that one might benefit by inducing anisotropy in the crystal's temperature response. Furthermore, if two different temperature dependences can be identified, locking them in a feedback loop may also enable enhanced temperature stability.

Temperature Stabilization Using Synchronization

Let us start by considering a scheme which utilizes two NV clocks. The zero-field splittings of the two clocks are assumed to have different temperature dependences, a fact which can be achieved by utilizing two distinct diamond slabs mounted on substrates with different thermal expansion coefficients.

In particular, let us assume that one diamond slab ('1') is clamped in a stiff material (Young's modulus E_1) with a high thermal expansion coefficient η_{c1} (e.g., brass), while the second slab ('2') is clamped in a different material with Young's modulus E_2 and a lower thermal expansion coefficient $\eta_{c2} < \eta_{c1}$, as illustrated in Fig. 64(b). Both diamond slabs and clamps are assumed to be at the same temperature, T. Assuming that the clamp's cross sectional area is much larger than that of the diamond slab, one finds that the change in strain imparted on the diamond can be approximated as $\Delta\epsilon_{1,2} \approx \eta_d(1 + \eta_{c1,2}E_{c1,2}/E_d)\Delta T$, where ΔT is the temperature difference from an initial set-point, T_0. This set-point should be chosen such that both clocks have the same initial frequency ω_0 and can be adjusted by pre-loading strain within the samples, as illustrated in Fig. 64(a).

A conventional thermal feedback system maintains the temperature T near T_0, but current thermistors only allow a long-term stability $\sim 10^{-2} - 10^{-3}$K. To compensate for even smaller temperature drifts, we employ a protocol, which exploits the different

temperature dependencies of the two diamond samples,

$$\omega_1(T) = \omega_0 + \beta_1 \Delta T \tag{8.34}$$

$$\omega_2(T) = \omega_0 + \beta_2 \Delta T \tag{8.35}$$

where $\beta_{1,2} = \frac{d\epsilon}{dT}\frac{dD_{gs}}{d\epsilon} = \eta_d(1 + \eta_{c1,2}E_{c1,2}/E_d)(dD_{gs}/d\epsilon)$. At time $\tau = 0$, both clocks are at the same temperature T_0, before the temperature is allowed to fluctuate within a small range around T_0. After time t, these clocks have acquired a phase

$$\phi_{1,2}(t) = \omega_0 t + \int_0^t \beta_{1,2}\Delta T(t')dt' \pm \Delta\phi_0, \tag{8.36}$$

where $\Delta\phi_0 = \xi\sqrt{t}/\sqrt{T_{2,\mathrm{ens}}N}$ is the phase uncertainty. The difference between the two phases may be recorded by mixing and low-pass filtering the two clock signals, giving $\Delta\phi(t) = \phi_2(t) - \phi_1(t) = \int_0^t \Delta\beta_{1,2}\Delta T(t')dt' \pm \sqrt{2}\Delta\phi_0$, where $\Delta\beta_{1,2} \equiv \beta_2 - \beta_1$ and we have assumed identical variances for $\phi_1(t)$ and $\phi_2(t)$.

Now, one can "correct" for temperature fluctuations in clock '1':

$$\begin{aligned}
\phi_1'(t) &= \phi_1(t) - \int_0^t \beta_1 \Delta T(t')dt' \\
&= \phi_1(t) - \left(\int_0^t \Delta\beta_{1,2}\Delta T(t')dt'\right)\cdot\frac{\beta_1}{\Delta\beta_{1,2}} \\
&= \phi_1(t) - \frac{\beta_1}{\Delta\beta_{1,2}}(\Delta\phi(t) \mp \sqrt{2}\Delta\phi_0).
\end{aligned} \tag{8.37}$$

Dividing by t yields the frequency, from which we then find the uncertainty of the new "synchronized composite" clock after a time t:

$$\begin{aligned}
\frac{\Delta\omega_1'}{\omega_1'} &= \frac{\xi}{\sqrt{T_2 N t}D_{gs}}\left(1 + 2\left(\frac{\beta_1}{\Delta\beta_{1,2}}\right)^2\right)^{1/2} \\
&= \left(\frac{\Delta\omega}{\omega}\right)_{T=T_0}\left(1 + 2\left(\frac{\beta_1}{\Delta\beta_{1,2}}\right)^2\right)^{1/2}.
\end{aligned} \tag{8.38}$$

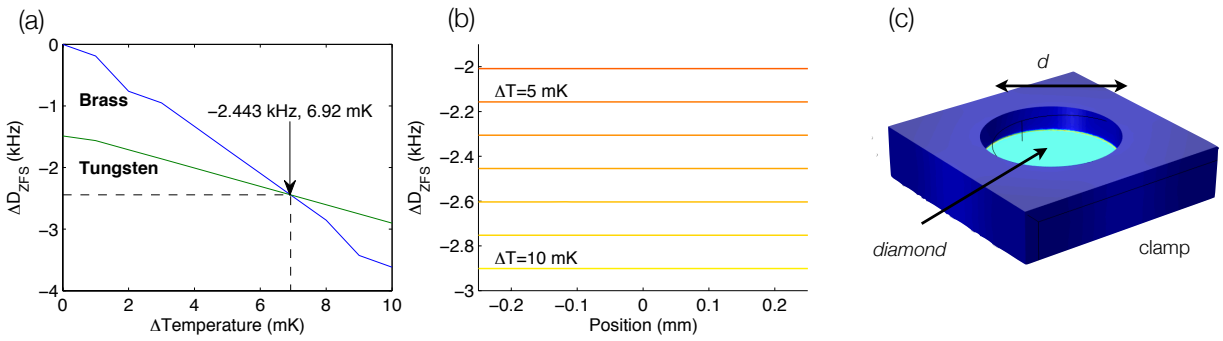

Figure 65: Simulated D_{gs} variation with temperature for tungsten (green) and brass (blue) clamps. (b) Spatial frequency variation as a function of position within the diamond disk. (c) Clamp and diamond geometry.

The expression provides an intuitive result: the uncertainty is minimized when the temperature dependencies of the two clocks can be large. In particular, Eq. (8.38) reveals that when $\Delta\beta_{1,2} \gg \beta_1$, then the performance of the composite clock is similar to that of a bare temperature-insensitive NV clock. While the phase difference can be directly computed and the clock frequency corrected digitally, in many cases, it will be easier to use the phase difference to stabilize the temperature. This stabilization is simplest if the two clocks are maintained at a frequency difference, $\nu_{beat} \sim 10$ kHz, so that the beat frequency can be locked to a high Q ($\sim 10^6$) quartz oscillator.

So far, we have approximated that the strain imparted on the diamond by the clamp is uniform across the sample. To check the validity of this assumption, we model the composite system by finite element analysis as a circular disk of diamond clamped within a brass or tungsten holder, as shown in Fig. 65(c). Fig. 65(a) depicts the calculated shift in D_{gs} as a function of temperature; the slopes agree with our previous expression for $\beta_{1,2} \sim \eta_d(1 + \eta_{c1,2}E_{c1,2}/E_d)/(-75$ kHz/K). Finally, Fig. 65(b) shows that the strain is nearly uniform for a large area within the disk across the relevant temperature range $\Delta T \sim 0.01$K. Building upon the notion of altering the temperature dependence of the NV ZFS, in the next section, we consider the possibility of fully canceling the dD_{gs}/dT.

Controlling Temperature Dependence with Engineered Strain

As previously discussed, the temperature response of the NV D_{gs} likely originates from changes in the local strain field; in particular, fluctuations in temperature modulate the lattice, altering the position of the basal carbon atoms and thereby changing the effective spin-spin interaction. Within the usual ground state Hamiltonian, the strain dependence is hidden in the effective electric field vector, $\vec{\sigma}$. In terms of actual components of the strain tensor ϵ, perturbations to the spin Hamiltonian take the form, $F_{ijkl}S_iS_j\epsilon_{kl}$, where F is the fourth order strain response tensor. Symmetries reduce the number of allowed terms to eight totally symmetric combinations, and of these, we are interested in only the ones with an S_z^2 coefficient. Thus, one finds that the strain dependence of the ZFS is most generally characterized as,

$$(D_{gs} + A_1(\epsilon_{xx} + \epsilon_{yy}) + A_2\epsilon_{zz})(S_z^2 - 2/3) \tag{8.39}$$

where A_1 and A_2 are parameters which require further experimental input. In the case of isotropic expansion, $\epsilon_{xx} = \epsilon_{yy} = \epsilon_{zz}$, one would expect $dD_{gs}/dT = 2A_1 + A_2$. By clamping the diamond along a specific direction, one can envision inducing an anisotropic lattice response which may significantly reduce the effective temperature dependence of the ZFS.

A schematic example is illustrated in Fig. 64b. Consider a small temperature shift ΔT, near T_0, which would cause a diamond slab of length L_d to expand by $\Delta L = L_d\eta_d\Delta T$. If the diamond slab were instead clamped, this expansion could easily be modulated. For instance, if material '2', which forms the bottom of the clamp, has a low thermal expansion coefficient and high Young's modulus, and material '1' has a high thermal expansion coefficient and high Young's modulus, then a pressure $P = E_d\Delta L_d/L = E_d\varepsilon_d = E_d\Delta T\eta_d$ may be exerted to compress the diamond slab by $-\Delta L$. For temperature changes $\Delta T \sim 0.01K$, this pressure is approximately 12.2 kPa. One possible material combination (among many), is to utilize brass for material '1' and silicon carbide for material '2'; tuning

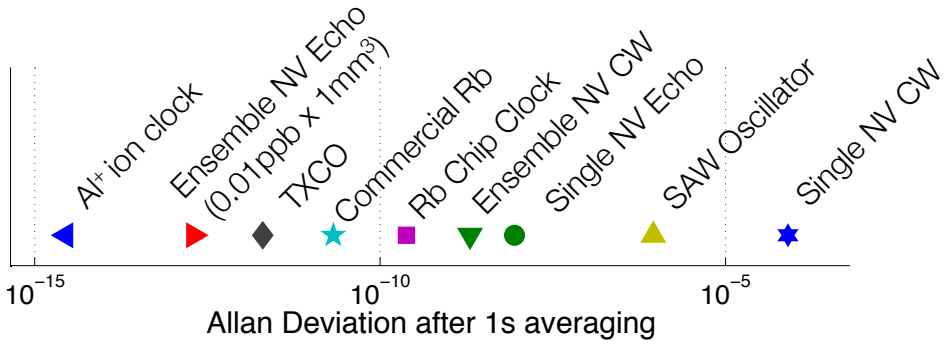

Figure 66: Allan Deviation for Atomic and Solid-state standards. Note that in moving from a CW scheme with a single NV center to an ensemble of centers with pulsed excitation and detection, we gain almost six decades of improvement. Cited deviations are as follows: Al-ion clock: [402, 405]; Cs Chip Clock [407]; TXCO and Commercial Rb figures available from Stanford Research Systems (www.thinksrs.com); SAW oscillator is quote from Epson Toyocom Corporation EG-4101/4121CA datasheet

of the modulated temperature can then be achieved by altering the width of the brass layer.

Looking forward, the diamond frequency standard promises a fully chip-integratable solid-state time-keeping platform whose performance rivals that of modern atomic clocks, both laboratory and chip-scale. Such miniaturized clocks can easily be integrated into scientific and consumer electronics and could be used in harsh external environments. Devices benefiting include those for wireless communication and GPS navigation (with improved tolerance to jamming) [419]. In addition, the clock's center-frequency of 2.870 GHz would enable a wide-bandwidth data rate in next-generation cellular communications ($f \geq 40$ GHz). At these frequencies, phase-sensitive data encoding is limited by the phase noise of the derived frequency source, which is usually a MHz range mechanical oscillator, whose frequency gets upconverted by a factor ≥ 1000. The low noise spectrum of the mechanical oscillator scales with N^2, thus degrading performance. By contrast, a low-power, portable, and stable on-board oscillator in the GHz range can avoid this quadratic stability loss (Fig. 66).

In summary, we have proposed a solid-state spin-optical frequency standard based on the

NV defect center in diamond. Due to the center's relatively long lifetime, high density of spins, and optical detection, we estimate a time stability exceeding $\sigma_y = 2 \times 10^{-12}\tau^{-1/2}$, rivaling that of the newest chip-scale Cs and Rb standards. Many of the technological advances, such as surface emitting lasers and chip-scale detectors, are readily deployable to this system, with the added benefit that the atomic system resides within the diamond substrate. We anticipate the ability to greatly improve upon this frequency standard using: repetitive readout [295], entanglement [58], IR absorption detection [366], and nanophotonics [420].

8.4 Nanometer scale thermometry in a living cell

In the previous section, we found that the main challenge for an NV-based frequency standard was the strong temperature dependence of the zero-field splitting. In this section, we turn this challenge on its head and demonstrate that NV centers in nanodiamonds can be effective nanoscale thermometers that can even be integrated inside living cells. Sensitive probing of temperature variations on nanometer scales represents an outstanding challenge in many areas of modern science and technology[421]. In particular, a thermometer capable of sub-degree temperature resolution over a large range of temperatures as well as integration within a living system could provide a powerful new tool for many areas of biological, physical and chemical research; possibilities range from the temperature-induced control of gene expression[422–425] and tumor metabolism[426] to the cell-selective treatment of disease[427, 428] and the study of heat dissipation in integrated circuits[421]. By combining local light-induced heat sources with sensitive nanoscale thermometry, it may also be possible to engineer biological processes at the sub-cellular level[422–425]. Here, we demonstrate a new approach to nanoscale thermometry that utilizes coherent manipulation of the electronic spin associated with nitrogen-vacancy (NV) color centers in diamond. We show the ability to detect temperature variations down to 1.8 mK (sensitivity of 9 mK/$\sqrt{\text{Hz}}$) in an ultra-pure bulk

diamond sample. Using NV centers in diamond nanocrystals (nanodiamonds), we directly measure the local thermal environment at length scales down to 200 nm. Finally, by introducing both nanodiamonds and gold nanoparticles into a single human embryonic fibroblast, we demonstrate temperature-gradient control and mapping at the sub-cellular level, enabling unique potential applications in life sciences.

Many promising approaches to local temperature sensing[421] are currently being explored. These include scanning probe microscopy[421, 429], Raman spectroscopy[430], and fluorescence-based measurements using nanoparticles[431, 432] and organic dyes[433, 434]. Fluorescent polymers[433] and green fluorescent proteins (GFPs)[434] have recently been used for temperature mapping within a living cell. However, many of these existing methods are limited by drawbacks such as low sensitivity and systematic errors owing to fluctuations in the fluorescence rate[431, 432]; such fluctuations result from a combination of changes to the local chemical environment[433] and to the optical properties of the surrounding medium[434]. Moreover, while promising, GFP-based methods rely on cellular transfection[434] that proves to be difficult to achieve in certain primary cell types[435]. Our new approach to nanoscale thermometry utilizes the quantum mechanical spin associated with nitrogen vacancy (NV) color centers in diamond. As illustrated in Fig. 67, in its electronic ground state, the NV center constitutes a spin-1 system. These spin states can be coherently manipulated using microwave pulses and efficiently initialized and detected via laser illumination (see SI). In the absence of an external magnetic field, the precise value of the transition frequency (Δ) between the $|m_s = 0\rangle$ and $|m_s = \pm 1\rangle$ states exhibits a temperature dependence ($d\Delta/dT = -(2\pi)77$ kHz/K) due to thermally induced lattice strains[164, 382, 418].

The operational principle of NV-based thermometry relies upon the accurate measurement of this transition frequency, which can be optically detected with high spatial resolution (Fig. 67). For a sensor containing N color centers, the temperature sensitivity is

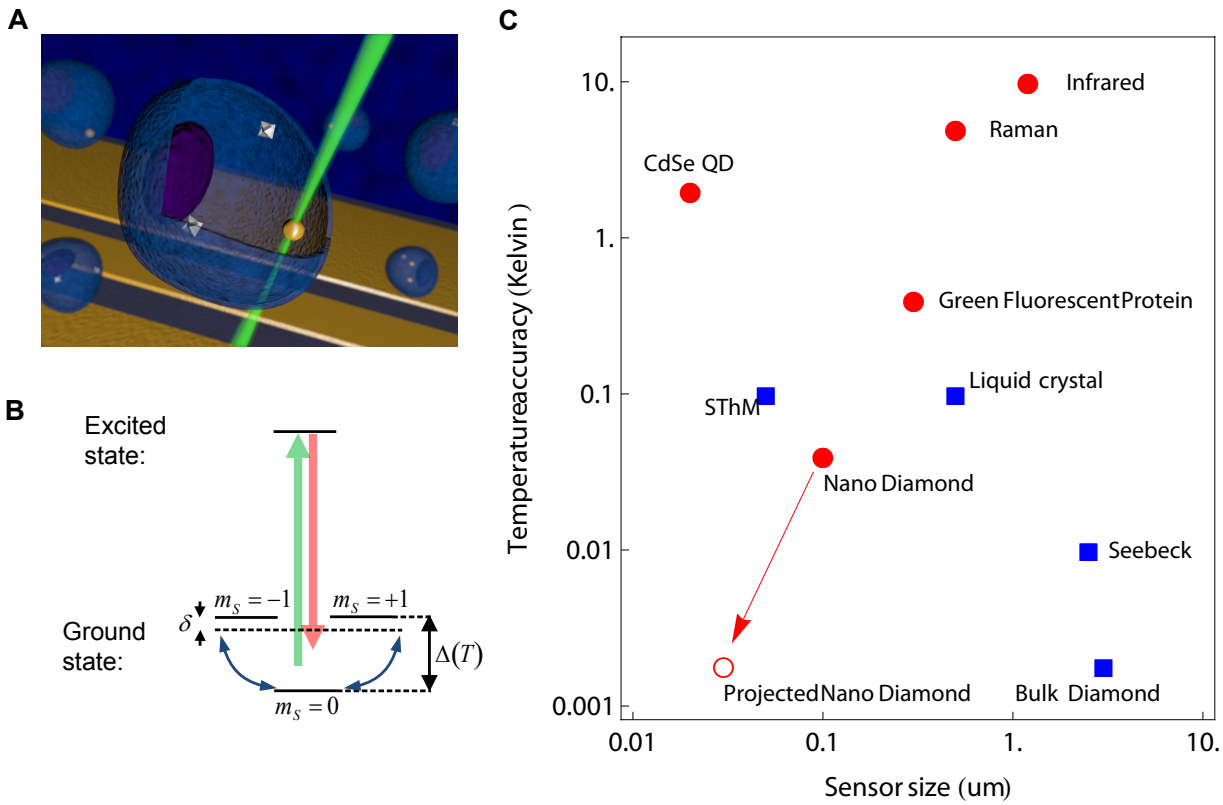

Figure 67: a, Schematic image depicting nanodiamonds and gold nanoparticles (Au NPs) within a living cell. The controlled application of local heat is achieved via laser illumination of the Au NP, while nanoscale thermometry is achieved via precision spectroscopy of the NV spins in nanodiamonds. b, Simplified NV level diagram showing a ground state spin triplet and an excited state. At zero magnetic field, the $|\pm 1\rangle$ sub-levels are split from the $|0\rangle$ state by a temperature-dependent zero field splitting $\Delta(T)$. Pulsed microwave radiation is applied (detuning δ) to perform Ramsey-type spectroscopy. c, Comparison between the NV quantum thermometer and other reported techniques as a function of sensor size and temperature accuracy. Red circles indicate methods that are biologically compatible. The red open circle indicates the ultimate expected accuracy for our measurement technique in solution (see Methods).

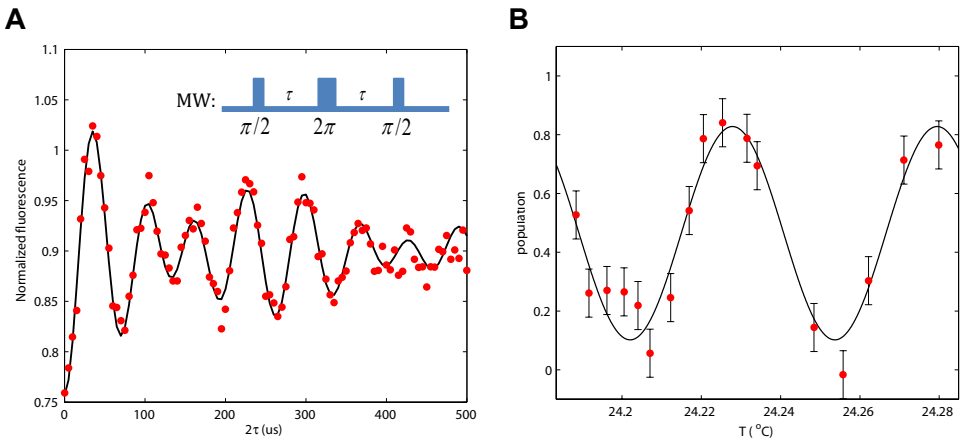

Figure 68: a, Measured fluorescence as a function of echo evolution time 2τ (red points); the black solid line indicates a fit corresponding to a damped cosine function with two distinct frequencies. The characteristic beating can be explained by fluctuating proximal charge traps located at distances of about 50 nm. The inset depicts the microwave 2π-echo-pulse sequence used to cancel unwanted external magnetic field fluctuations[437]. b, Measured fluorescence (red points), corresponding error bars (one standard deviation) and best fit line as function of temperature for an echo time of $2\tau = 250$ μs (bottom) and $2\tau' = 50$ μs (top). The fixed evolution times of 2τ and $2\tau'$ are indicated in (a) by red arrows. The overall temperature is controlled by a Peltier element at the sample mount, while the (local) x-axis temperature is determined via a thermistor located immediately next to the sample. The fluorescence is converted to population by normalizing to two reference measurements where the spin is prepared in $m_s = 0$ ($m_s = -1$).

given by

$$\eta = \frac{C}{d\Delta/dT}\frac{1}{\sqrt{T_{\text{coh}}Nt}}, \tag{8.40}$$

where T_{coh} is the NV-spin coherence time and t is the integration time. Here, we also introduce a factor C to account for imperfections in readout and initialization[388]. Assuming T_{coh} is on the order of a few milliseconds and $C \approx 0.03$[388], a single NV can potentially exhibit a sensitivity better than 1 mK/$\sqrt{\text{Hz}}$. Beyond high sensitivity, NV-based thermometry also offers several distinct advantages over existing methods in biological and chemical temperature sensing. First, owing to diamond's chemical inertness, it is generally robust to changes in the local chemical environment. Second, it can be applied over a wide range of temperatures, $200 - 600$ K[164, 418], which is of particular interest in the study of nanoscale chemical reactions[436].

As a first benchmark experiment, we demonstrate the high temperature sensitivity of NV-based thermometry in a bulk diamond sample. While the NV's magnetic sensitivity has rendered it a competitive magnetometer[287, 293], to accurately determine the temperature, it is necessary to decouple the NV electronic spin from fluctuating external magnetic fields. This is achieved via a modified spin-echo sequence that makes use of the spin-1 nature of the NV defect[437], allowing us to eliminate the effects of an external, slowly varying, magnetic field. Specifically, we apply a microwave pulse at frequency ω (Fig. 67b) to create a coherent superposition $\frac{1}{\sqrt{2}}(|0\rangle + |B\rangle)$, where $|B\rangle = \frac{1}{\sqrt{2}}(|+1\rangle + |-1\rangle)$. After half the total evolution time τ we apply a 2π echo-pulse that swaps the population of the $|+1\rangle$ and $|-1\rangle$ states (Fig. 68a). Following another period of free evolution for time τ, quasi-static, magnetic-field-induced shifts of these $|\pm 1\rangle$ levels are eliminated, allowing for accurate temperature sensing. In the experiment, we use a CVD-grown, isotopically pure diamond (99.99 % spinless ^{12}C isotope) sample[45] to further reduce magnetic-field fluctuations originating from the intrinsic ^{13}C nuclear spin bath. As shown in Fig. 68a, this allows us to observe coherence fringes approaching 0.5 ms. Interestingly, for all NVs tested, we observe a characteristic low-frequency beating of the fluorescence signal that varies from NV to NV, which is most likely due to locally fluctuating charge traps[381]. Despite this beating, for a fixed evolution time 2τ, the NV spin depends sensitively on the sample temperature (Fig. 68b). We observe a temperature sensitivity of $\eta = (9 \pm 1.8)$ mK/$\sqrt{\text{Hz}}$ for $2\tau = 250$ μs. With 30 seconds of integration, we achieve a measurement accuracy $\delta T = 1.8 \pm 0.3$ mK (see Methods). While the measurement sequence for a single value of 2τ allows us to determine the temperature only up to a multiple of $(2d\Delta/dT2\tau)^{-1}$, absolute temperature variations can be determined by repeating the measurement for $2\tau' < 2\tau$ as shown in Fig. 68b.

We now demonstrate the high spatial resolution of NV-based thermometry. This is achieved by using diamond nanocrystals (nanodiamonds, NDs). In most commercially available nanodiamonds, the NV coherence time is limited to approximately 1 μs due to

additional paramagnetic impurities. While this shortened coherence time reduces the intrinsic temperature sensitivity for a single defect, this decrease can be offset by using an ensemble of NVs to enhance the signal to noise ratio by a factor of $\sqrt{N}$. Note that unlike NV-based magnetometry, where the proximity to the source (often limited by nanodiamond size) is critical to the maximum sensitivity, NV thermometry is not subject to such a constraint; in fact, the excellent thermal conductivity of diamond ensures that all NV centers within a nanocrystal are in thermal equilibrium with the local heat environment. To maximize the number of NV centers and to minimize the lattice strain, our measurements are performed on single-crystalline nanodiamonds containing approximately 500 NV centers (Adamas Nanotechnologies). The zero-field splitting Δ of the NV ensemble, and thus the temperature, is determined by recording a continuous-wave electron spin resonance (ESR) spectrum. Specifically, we measure changes to the zero-field splitting by recording the fluorescence at four different frequencies centered around $\Delta = 2.87$ GHz (Fig. 69a). This procedure eliminates unwanted effects from fluctuations in the total fluorescence rate, ESR contrast, Rabi frequency and magnetic field, yielding a robust thermometer (see Methods).

Combining our nanodiamond thermometer with the laser heating of a gold nanoparticle (Au NP) allows us to both control and monitor temperature at nanometer length scales (Fig. 69). Both nanodiamonds and Au NPs (nominal diameter 100 nm) are initially spin-coated on a microscope coverslip. Using a confocal microscope with two independent scanning beams, we co-localize Au NPs and nanodiamonds with $\sim 100\ nm$ resolution (see SI). While locally heating the Au NP via continuous illumination with a variable-power green laser (focused to a diffraction limited spot), we simultaneously measure the temperature at the nanodiamond location using ESR spectroscopy.

The ability to measure temperature with NDs is verified by heating the substrate temperature over a range of 2.5 K and simultaneously monitoring the zero-field splitting (see Fig. 69c, inset). To demonstrate nano-scale temperature control Fig. 69c depicts the

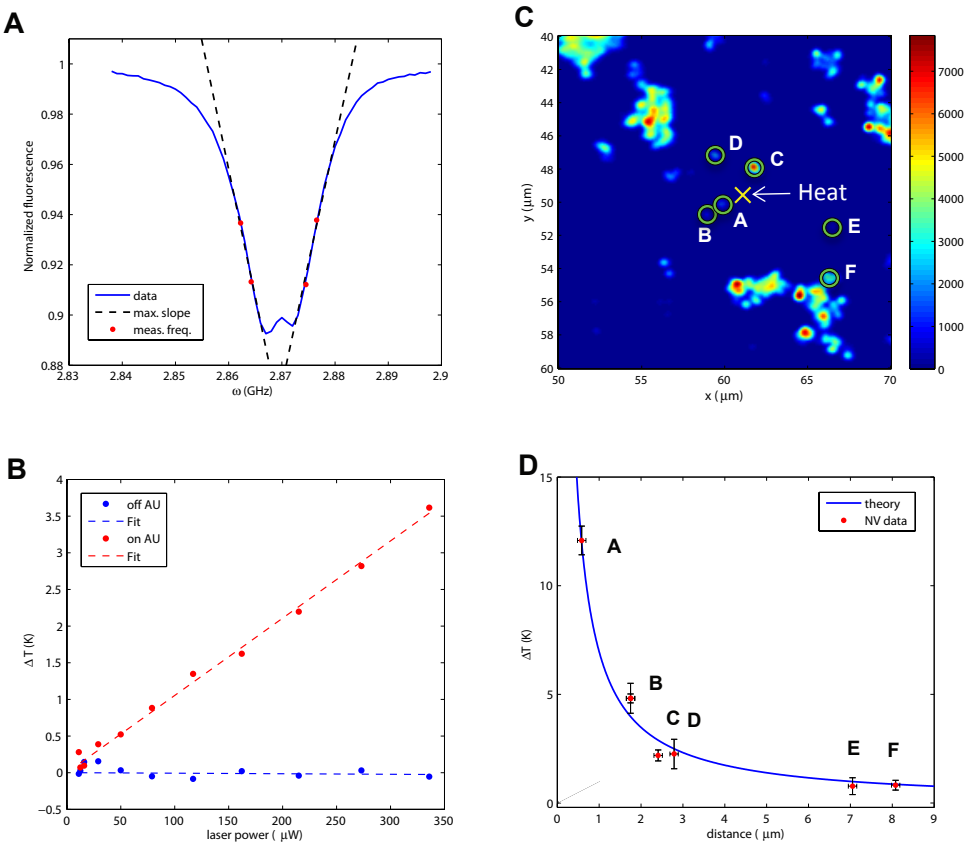

Figure 69: a, Frequency scan of a single nanodiamond containing approximately 500 NV centers. The four red points indicate the measurement frequencies used to extract the temperature as detailed in Methods. b, Two-dimensional confocal scan of nanodiamonds (circles) and Au NPs (cross) spin-coated onto a glass coverslip. The color bar represents fluorescence given in counts per second (cps). c, Temperature of a single nanodiamond as a function of laser power for two different laser-focus locations. The red data points depict the dramatic heating of a nanodiamond as a result of laser illumination on a nearby Au NP. The blue data points depict the same measurement with the laser focus displaced by 0.8 μm from the Au NP location; this results in the negligible heating of the nanodiamond as a function of laser power. The inset shows the measured temperature change of a nanodiamond. The surrounding temperature is controlled by a Peltier element. d, Temperature changes measured (red points) at the six nanodiamond locations in (b) as a function of distance from the illuminated Au NP (cross). The blue curve represents the theoretical temperature profile based upon a steady-state solution of the heat equation. All data in this figure are obtained on a glass coverslip, and all error bars correspond to one standard deviation.

temperature change recorded by the ND as a function of the green laser power applied to the Au NP at a distance of 0.8 ± 0.1 μm. To further verify that the temperature change originates from local heating, we repeat the measurement with the excitation laser displaced from the ND by 0.8 μm in the opposite direction. In this case, the temperature measured by the nanodiamond remained constant as a function of laser power (blue points), thereby confirming the locality of the heat source. From a linear fit to the data we estimate the accuracy of our ND sensor to be $\delta T = (44 \pm 10)$ mK. The measured temperature change is in excellent agreement with the theoretically expected temperature profile based upon a steady-state solution of the heat equation, $\Delta T(r) = \frac{\dot{Q}}{4\pi\kappa r}$, where $\dot{Q}$ is the heat dissipation, κ is the thermal conductivity of glass and r is the distance between the nanodiamond and the Au NP. As shown in Fig. 69b, by recording the temperature of six nanodiamonds at different distances from the laser-heated Au NP we find that the measured temperature profile (Fig. 69d) is in excellent agreement with the theoretical steady-state prediction (solid line). This allows us to directly estimate the temperature change at the location of the Au NP to be 72 ± 6 K.

To demonstrate that nanodiamond thermometry is compatible with living cells, we introduce nanodiamonds and Au NPs into human embryonic fibroblast WS1 cells via nanowire-assisted delivery[435]. Just as in the control experiments described above, we probe the temperature at two different locations (NV_1 and NV_2) within a single cell while locally heating an individual Au NP (Fig. 70a). As shown in Fig. 70b, NV_1, which is significantly closer to the heat source, exhibits a stronger temperature dependence as a function of laser power than NV_2. Varying the incident power allows us to generate controlled temperature gradients of up to 5 K over distances of approximately 7 μm. To ensure that this temperature gradient is created by the controlled illumination of the NP and does not result from heating of the cellular cytoplasm, we displace the laser spot from the Au NP; this then results in a negligible temperature change at the location of NV_1 with $\Delta T = (-20 \pm 50)$ mK (green square, Fig. 70b). The increased measurement uncertainty for

larger laser powers is the result of heating fluctuations from drift of the Au NP.

The experiments shown in Fig. 70b clearly demonstrate the sub-micron measurement of an intra-cellular heat gradient. However, the substantial heating induced by constant illumination for an extended period of time ultimately leads to the death of the cell, which is confirmed using a standard live/dead assay (Calcein AM/Ethidium Homodimer-1). To demonstrate that our technique can be employed within living cells, we increase the concentration of Au NPs to allow for heat generation at different locations by simply moving the laser focus. Then, we measured the temperature variation at a single nanodiamond (bar plot in Fig. 70c) while introducing a slight heating of Au NPs in two differing locations (crosses). After our measurement, the viability of the cell is confirmed (Fig. 70c).

Finally, we demonstrate that our method can be used to control cell viability. To start, we heat the cell with 12 μW of laser power and measure a temperature change of 0.5 ± 0.2 K at the nanodiamond location; this corresponds to a change of approximately 10K at the Au NP spot. At this point, the cell is still alive, as confirmed by the absence of ethidium homodimer-1 fluorescence inside the membrane (Fig. 70d). By increasing the laser power to 120μW, we induce a temperature change of 3.9 ± 0.1K at the nanodiamond location (approximately 80K at the location of the laser focus); in this case, the cell is flooded with fluorescence from the ethidium homodimer, thus signaling cell death. This proof-of-principle experiment indicates that nanodiamond thermometry may enable the optimization of NP-based photothermal therapies[428].

Our experiments demonstrate that NV centers in diamond can be used as robust temperature sensors that combine the virtues of sub-micron spatial resolution, sub-degree thermal sensitivity and bio-compatibility. The sensitivity of our current measurement can be enhanced by improving the relevant coherence time and by increasing the number of NV centers within the nanocrystal. Optimizing these factors should allow us to reach sensitivities of 80 $\mu\mathrm{K}/\sqrt{\mathrm{Hz}}$ (see Methods), yielding the ability to sense sub-kelvin

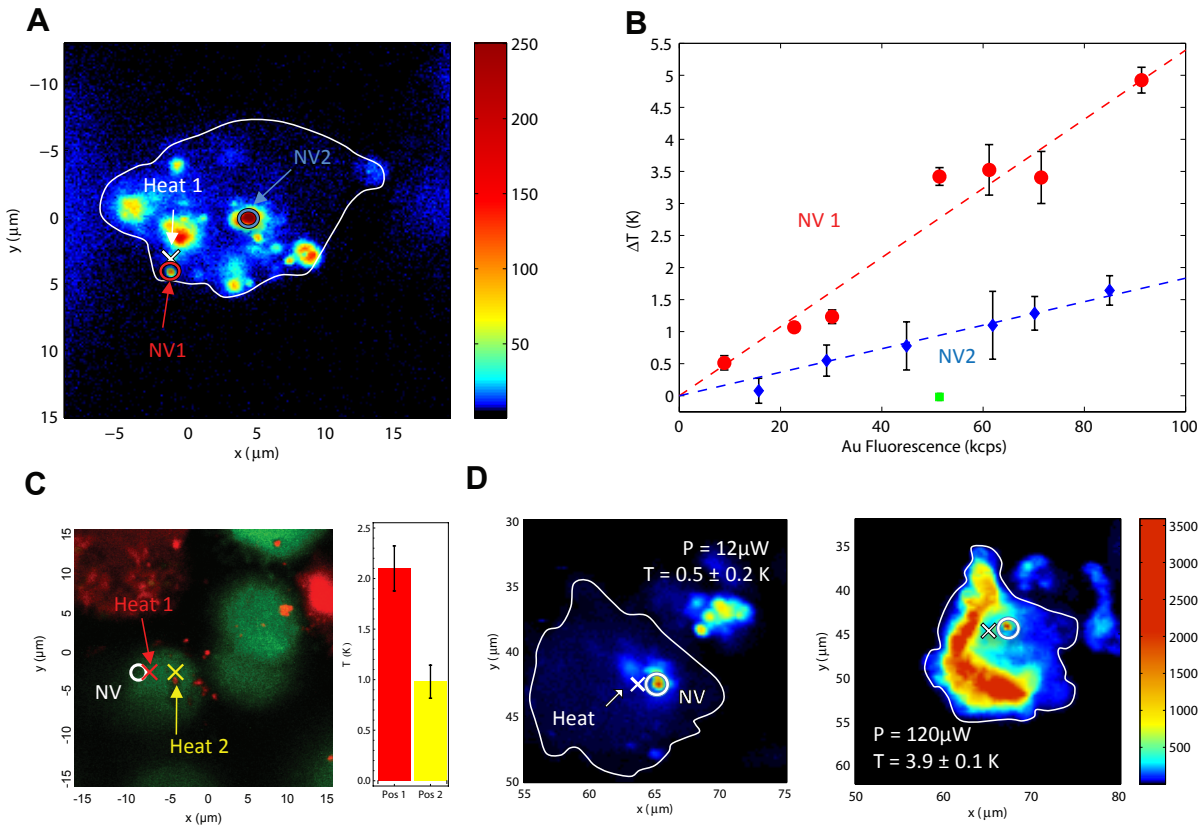

Figure 70: a, Confocal scan of a single cell under 532 nm excitation with collection above 638 nm. The cross corresponds to the position of the Au NP used for heating, while circles represent the location of the nanodiamonds (NV_1 and NV_2) used for thermometry. The dotted line provides a guide to the eye and outlines the cell membrane. Color bars indicate the fluorescence in cps. b, Measured change in temperature at the position of NV_1 and NV_2 relative to the incident laser power applied to the Au NP. Dashed lines are linear fits to the data. Each point consists of an average of 10-20 measurements with each individual measurement taking 4 seconds. The error bars (one standard deviation) are set by fluctuations in the laser heating of the Au NP. c, Fluorescence scan of stained cells (live/dead assay) with excitation at 494/528 nm and emission at 515 nm (green - cell alive) and 617 nm (red - cell dead). The bar plot depicts the temperature of a single nanodiamond (circle) with local heat applied at two different locations (cross). d, Confocal fluorescence scans of an individual cell under varying illumination power. Excitation occurs at 532 nm and collection is above 630 nm. Cell death is indicated by the penetration of ethidium homodimer-1 through the cell membrane, staining the nucleus. At low laser powers, the cell remains alive, while cell-death occurs as laser-induced heating is increased.

temperature variations with milli-second time resolution, thus opening the door to studying non-equilibrium nanoscale processes. In solution, the ultimate accuracy of our method will likely be limited by residual heating during the measurement process. As discussed in the Methods, this limit is in the range of 50 μK to 5 mK, depending on experimental conditions. While the present work focuses on monitoring temperature variations, the use of diamond samples with low strain or, alternatively, ensembles of NDs, should allow for the realization of an absolute thermometer (see Methods). The spatial resolution of our method can be further improved by using far-field sub-diffraction techniques[227].

The present observations open up a number of intriguing possibilities. For instance, the simultaneous real-time measurement and control of a sub-cellular thermal gradient could enable the accurate control of gene expression[438]. The large dynamic range of our quantum thermometer and it's intrinsic robustness may also allow for the direct microscopic monitoring and control of chemical reactions[436]. Moreover, combining our technique with two-photon microscopy[439, 440] may enable in vivo identification of local tumor activity by mapping atypical thermogenesis at the single-cell level[441]. Finally the combination of thermoablative therapy with our temperature sensor constitutes a potent tool for the selective identification and killing of malignant cells without damaging surrounding tissue [428, 442].

8.4.1 Nanodiamond measurement pulse sequence

As indicated in Fig. 69a, we record the fluorescence at four different frequencies centered around $\Delta = 2.87$ GHz:

$f^{1,2} \approx f(\omega_-) + \frac{\partial f}{\partial \omega}|_{\omega-} \left(\mp\delta\omega + \delta B + \delta T \frac{d\Delta}{dT}\right)$ and

$f^{3,4} \approx f(\omega_+) + \frac{\partial f}{\partial \omega}|_{\omega+} \left(\mp\delta\omega - \delta B + \delta T \frac{d\Delta}{dT}\right)$. This allows us to determine the change in temperature,

$$\delta T = \frac{\delta\omega}{d\Delta/dT} \frac{(f^1 + f^2) - (f^3 + f^4)}{(f^1 - f^2) + (f^3 - f^4)}, \tag{8.41}$$

where $\omega_\pm \mp \delta\omega$ are the four microwave carrier frequencies and δB is a unknown static

magnetic field. By averaging the fluorescence at these four frequencies as shown in equation (8.41), we are able to remove errors associated with changes in total fluorescence rate, ESR contrast, Rabi frequency and magnetic field.

8.4.2 Experimental apparatus, sensitivity and accuracy

Our experimental apparatus consists of a confocal microscope with two independent excitation/collection paths allowing measurement and heating at two independent locations simultaneously. The experiments use either a Nikon Plan Fluor 100x oil immersion, NA = 1.3, (nanodiamonds) or a Nikon Plan Apo 100x air, NA = 0.95, objective (bulk sample), resulting in $C \approx 0.03$, which can be further improved by employing a solid immersion lens or diamond nano patterning. Microwaves are delivered via a lithographically defined coplanar waveguide on top of a glass coverslip. For experiments with nanodiamonds we use neutral density filters in the collection path to avoid saturation of the APD. The temperature accuracy δT for bulk diamond is estimated from the measurement shown in Fig. 68b. Using the standard deviation σ (shown error bars) we evaluate the accuracy as $\delta T = \sigma/(c\ \frac{d\Delta}{dT}\ 2\tau)$, where c is the oscillation amplitude and 2τ is the free evolution time. We find that for integration times $t < 30\ s$ (limited by temperature stability) the temperature accuracy improves as $\sqrt{t}$, giving a sensitivity $\eta = \delta T\sqrt{t}$. A linear dependence of the dissipated heat as a function of laser power (Fig. 69b) is used to determine the measurement accuracy for NDs. A linear function, with slope m, is fitted to the data (red dashed line) and the measurement accuracy is given by $\delta T = \sqrt{\frac{1}{N-1}\Sigma_{i=1}^{N}\left(T_i - m\ P_i\right)^2}$, with T_i the measured temperature and P_i the corresponding laser power. The error bars are evaluated as $\sigma\left(\delta T\right) = \delta T\sqrt{1 - \frac{2}{N-1}\frac{\Gamma^2(n/2)}{\Gamma^2((n-1)/2)}}$, where $\Gamma(\cdot)$ indicates the Gamma distribution.

8.4.3 Ultimate sensitivity

The ultimate sensitivity of our method is limited by the NV coherence time and the number of defect centers. In our current experiment, we have demonstrated a sensitivity of 9 mK/$\sqrt{\text{Hz}}$ (with a free evolution time of 250 μs). Two natural extensions enable longer NV coherences: 1) decreasing the ^{13}C concentration to suppress the nuclear spin bath and 2) further dynamical decoupling. These methods can, in principle, allow us to extend the evolution time up to $T_1/2 \sim 3$ ms. In combination with a nanocrystal that contains ~ 1000 NV centers, this could yield an ultimate sensitivity limit of 80 μK/$\sqrt{\text{Hz}}$. Further improvement may be possible by employing spin squeezed states. Finally, we note that the absolute temperature sensitivity of our technique is limited by variations of the zero-field splitting due to spatially varying strain. For low strain diamond samples, we find that the variation in the zero-field splitting is on the order of 60 kHz. Thus, using an ensemble of NV centers in different NDs with uncorrelated strain values would allow for a further increase in absolute sensitivity by a factor $\sqrt{n}$, where n is the number of NDs.

8.4.4 Ultimate accuracy in solution

In cases where our method is used to probe a system that is in solution (e.g. cells, chemical reactions), the primary accuracy limit is set by heat dissipation during the measurement process. In particular, the microwave spectroscopy used to detect changes in the NV zero-field splitting also induces heating of the solution. In the present experiment, we utilize a lithographically fabricated microwave loop (diameter 200 μm) to generate an ac-magnetic field, $B \approx 10$ milli-gauss, for spin manipulations. Estimating the effective dipole field created by the microwave loop shows that the solution (water) absorbs 10^{-6} W of power yielding a temperature increase of 5 mK in the steady state. By using a smaller microwave loop (20 μm) and reducing the duty cycle, it could be possible to decrease the heating of the solution to approximately 50 μK.

8.4.5 Injection of nanodiamonds into cells

Nanodiamonds and Au NPs were introduced into WS1 cells via silicon nanowire-mediated delivery[435]. Silicon nanowires were treated with 3-amino- propyltrimethoxysilane to present NH_2 functionality on the surface, and nanodiamonds / Au NPs were subsequently attached via electrostatic binding. Afterwards, human embryonic fibroblast WS1 cells were plated on the silicon nanowire substrates and cultured overnight. The cells were removed by trypsin treatment and re-plated on a glass slide with lithographically defined strip lines for ESR measurements. The samples were stained with calcein-AM and ethidium homodimer-1 for the live/dead assay.

Appendix A

Many-body localization with power-laws

This appendix serves as a detailed derivation for certain results in Chapter 2 of this thesis. In particular, we derive the counting of pseudo-spin resonances for power-law interaction systems.

A.1 The Pseudo-spin Hamiltonian

We begin by isolating the Hamiltonian of a pair of spins, S_1, S_2, at some separation R,

$$H_{12} = \epsilon_1 S_1^z + \epsilon_2 S_2^z + t_{12}(S_1^+ S_2^- + S_1^- S_2^+) + V_{12} S_1^z S_2^z \tag{A.1}$$

where ϵ_i are local random fields of bandwidth W, t_{12}, V_{12} are the flip-flop and interaction piece of the Hamiltonian and we have temporarily absorbed the R-dependence into the couplings. For R large enough, we may assume that $t_{12}, V_{12} \ll |\epsilon_i| \sim W$. In this case, the perturbation t_{12} leads to resonance between the $|\Uparrow\rangle = |\uparrow\downarrow\rangle$ and $|\Downarrow\rangle = |\downarrow\uparrow\rangle$ states in the $S^z = 0$ manifold, precisely when the detuning $\delta_a = \epsilon_1 - \epsilon_2$ satisfies $|\delta_a| \lesssim t_a = t_{12}$. Somewhat more formally, we define a set of pseudospin Pauli operators τ_a^α with respect to the $|\Uparrow\rangle, |\Downarrow\rangle$ basis to get an effective pseudospin Hamiltonian restricted to the $S^z = 0$

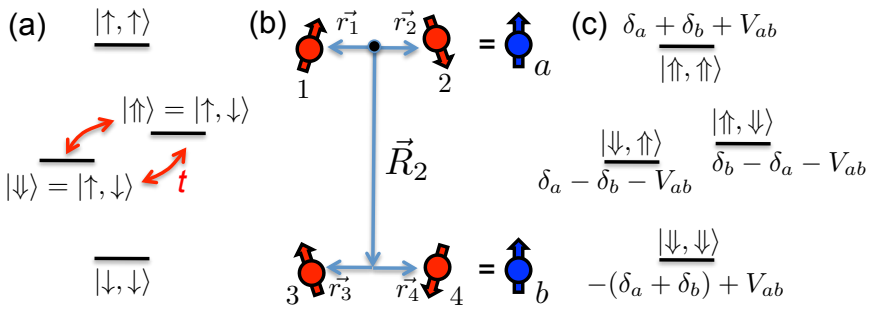

Figure 71: Schematic construction of pseudo-spin resonances. (a) Energy levels of an original pair of spins separated by a distance R_1. The spin flip-flop couples the central two energy levels which defines a new pseudo-spin degree of freedom. (b) Spatial structure of an interacting pseudo-spin pair. The original spins S_1 and S_2 form the new pseudo-spin a and spins S_3 and S_4 form the new pseudo-spin b. (c) Bare energy levels (neglecting t_a, t_b) of the pseudo-spin Hamiltonian H_{ab}.

subspace:

$$H_a = \delta_a \tau_a^z + t_a \tau_a^x \tag{A.2}$$

Resonance corresponds to the condition that the eigenstates of this Hamiltonian point predominantly in the τ_a^x direction. We note that V_{12} does not enter the pseudospin Hamiltonian as the Ising term $S_1^z S_2^z$ is constant on the $S^z = 0$ subspace.

We now consider the interaction of a pair of pseudospins $a = 12$, $b = 34$ each of size R_1 and at separation R_2 (Fig. S1). So long as $t(R_2) \ll |\epsilon_i| \sim W$, the hopping terms between a and b spins will be unable to resonantly move out of the $S_a^z = 0$, $S_b^z = 0$ subspaces, so we may again restrict attention to the joint pseudospin space. The effective Hamiltonian in this space is

$$H_{ab} = \delta_a \tau_a^z + t_a \tau_a^x + \delta_b \tau_b^z + t_b \tau_b^x + V_{ab} \tau_a^z \tau_b^z \tag{A.3}$$

where $V_{ab} = V_{13} - V_{14} - V_{23} + V_{24}$. This coupling formula follows most easily by noting that, within the pseudospin subspace, $\tau_a^z = S_1^z = -S_2^z$.

Within the effective Hamiltonian H_{ab}, pseudospin resonance corresponds to the condition that some set of eigenstates of H_{ab} are entangled of order unity (as a function of the

separations R_1, R_2). Clearly this requires the interaction $V_{ab} \neq 0$, but it further requires $t_{a/b} \neq 0$ or else the eigenstates will be product states in the τ^z basis. Assuming the original spins are resonant ($\delta_{a/b} \lesssim t_{a/b}$), we find pseudospin resonance for $\sqrt{t_a^2 + \delta_a^2}, \sqrt{t_b^2 + \delta_b^2} \gtrsim V_{ab} \gtrsim |t_a - t_b|$. This corresponds to the resonance condition quoted in chapter 2.

Finally, we turn to the next level of the hierarchical construction of resonances, i.e. pseudo-pseudo-spins. We define a new set of pseudo-pseudo-spin Pauli operators μ^α and take the μ^z eigenstates to label the two resonant central eigenstates of H_{ab}. Unlike the pseudospins τ, there is no natural quantization axis for μ. In particular, that the two central eigenstates are resonant ensures that the pseudo-pseudo-spins have $\mathcal{O}(1)$ transition matrix elements with respect to the underlying τ^x and τ^z operators. Thus, a pair of pseudo-pseudo-spins has a Hamiltonian of the form,

$$\begin{aligned} H &= H_{ab} + H_{cd} + H_{int} \\ &= \Delta_{ab}\mu^z_{ab} + \Delta_{cd}\mu^z_{cd} + \sum_{\alpha,\beta\in\{x,z\}} V_{\alpha\beta}\mu^\alpha_{ab}\mu^\beta_{cd}, \end{aligned} \tag{A.4}$$

where $H_{int} = V_{ac}\tau^z_a\tau^z_c + V_{ad}\tau^z_a\tau^z_d + V_{bc}\tau^z_b\tau^z_c + V_{bd}\tau^z_b\tau^z_d$ and in the second line, we have restricted to the resonant μ subspace.

A.2 Multipole expansion

The pseudospin resonance between two well-separated pairs of spins corresponds to correlated interaction-induced local charge rearrangements within each pair. If $V(r) \sim 1/r$ is pure Coulomb, this observation immediately suggests that the effective interactions between pairs should decay according to the next leading term in a multipole expansion — that is, as dipoles $1/r^3$. More generally, for homogenous, isotropic interactions

$V(r) \sim 1/r^\beta$, we have

$$\begin{aligned} V_{ab} &= V_{13} - V_{14} - V_{23} + V_{24} \\ &= \left(\frac{1}{R_{13}^\beta} - \frac{1}{R_{14}^\beta}\right) + \left(\frac{1}{R_{24}^\beta} - \frac{1}{R_{23}^\beta}\right) \\ &= \left(\frac{1}{|\vec{R}_2 + \vec{r_4} - \vec{r_1}|^\beta} - \frac{1}{|\vec{R}_2 + \vec{r_3} - \vec{r_1}|^\beta}\right) + \left(\frac{1}{|\vec{R}_2 + \vec{r_3} - \vec{r_2}|^\beta} - \frac{1}{|\vec{R}_2 + \vec{r_4} - \vec{r_2}|^\beta}\right) \\ &\approx \frac{1}{R_2^\beta}\frac{\beta}{2}\left(\frac{2r_3 \cdot r_1 + 2r_4 \cdot r_2 - 2r_4 \cdot r_1 - 2r_3 \cdot r_2}{R_2^2}\right) \sim \frac{R_1^2}{R_2^{\beta+2}}. \end{aligned} \tag{A.5}$$

where in the last step we have assumed that $R_1 < R_2/2$ in order to perform the multipole expansion. The factor of R_1^2 in the numerator corresponds to the scale of the multipole moment.

In general, the cancellation that produces the leading multipole decay fails unless the interactions are homogeneous and isotropic. An important special case is provided by uniformly aligned dipoles for which the interaction depends on the angle between the dipole axis and the displacements R_{ij}. The sum $V_{ab} = V_{13} - V_{14} - V_{23} + V_{24}$ can be reinterpreted as the interaction energy of the four dipoles where the dipole at site 2 and 4 has been reversed and thus the net dipole moment in a or b is zero and $V_{ab} \sim R_1^2/R_2^5$ becomes quadrupolar.

When the multipole form of V_{ab} Eq. (A.5) applies, the estimate of $N_2(R_1, R_2)$ presented in the main text Eq. (3) must be corrected by the replacement $V/R_2^\beta \to VR_1^2/R_2^{\beta+2}$. The resulting criteria for MBL (the "istotropic" case) are summarized in the last column of Table I. For completeness, we provide detailed derivations of these formulae below.

A.3 Pseudo-spin counting

A.3.1 Fixed pair size ("small pairs")

We fix the size of a central pseudo-spin to be R_1 and count the number of resonant pseudo-spins separated by a distance R_2 (using the multipole form of the interaction),

$$N_2(R_1, R_2) \sim (n_1(R_1)R_2^d) \cdot \frac{VR_1^2/R_2^{\beta+2}}{t/R_1^\alpha} \sim R_2^{d-(\beta+2)}, \tag{A.6}$$

where $n_1 = \rho N_1$ is the density of pseudo-spins. The first factor $(n_1(R_1)R_2^d)$ counts the total number of pseudo-spins in a volume shell between R_2 and $2R_2$ while the second factor $(\frac{VR_1^2/R_2^{\beta+2}}{t/R_1^\alpha})$ represents the probability that a given pseudospin is resonant with the central pseudospin. With R_1 fixed, we can take $R_2 \to \infty$ to check whether the number of resonant pseudo-spins diverges. This occurs when $d > \beta + 2$.

A.3.2 Growing pair size ("extended pairs")

A more stringent constraint arises when one allows the size of the central pseudospin to grow as R_2 grows. The optimum arises when $V(R_2) \sim t(R_1)$ such that the factor describing the probability of resonance in Eq. (A.6) is maximized (of order unity), $\frac{V(R_2)}{t(R_1)} \sim \frac{R_1^2/R_2^{\beta+2}}{1/R_1^\alpha} \sim 1/10$, yielding $R_2 \sim R_1^{\frac{\alpha+2}{\beta+2}}$ (again using the multipole form of the interaction) and

$$N_2(R_1, R_2) \sim R_1^{d+2}(R_1^{\frac{\alpha+2}{\beta+2}})^{d-(\beta+2)} = R_1^{d-\alpha+d\frac{\alpha+2}{\beta+2}}. \tag{A.7}$$

The number of resonant pseudo-spin pairs diverges at large scales, and hence delocalization occurs, for $d > \frac{\alpha(\beta+2)}{\alpha+\beta+4}$.

A.3.3 Iterating the construction of pseudo-spin pairs ("iterated pairs")

It is possible to continue iterating the hierarchical construction of resonant pairs (e.g. to create an effective pseudo-pseudo-spin from 4 original spin degrees of freedom). However, the resulting criteria for MBL saturate after the third level. The counting at this level is,

$$N_3(R_1, R_2, R_3) \sim (n_2(R_1, R_2)R_3^d) \cdot \frac{\tilde{V}/R_3^\beta}{\tilde{V}/R_2^\beta} = (n_2(R_1, R_2)R_3^d) \cdot \frac{\tilde{V}R_1^2/R_3^{\beta+2}}{\tilde{V}R_1^2/R_2^{\beta+2}}$$
$$= R_1^{2d-\alpha+2} \cdot R_2^d \cdot R_3^{d-\beta-2} \tag{A.8}$$

where $n_2 = n_1 N_2$ is the density of pseudo-pseudo-spins. As usual, we count the number of resonant pseudo-pseudo-spins as $R_3 \to \infty$. Holding R_1, R_2 fixed reproduces the small pairs criterion. Holding R_1 fixed but optimizing $R_2 \sim R_3$ (to saturate the probability of resonance) yields a new, "iterated pairs" criterion $d > (\beta + 2)/2$. Finally, optimizing both $R_1 \sim R_2^{(\beta+2)/(\alpha+2)}$ and $R_2 \sim R_3$ reproduces the extended pairs criterion. Physically, the reason that all MBL criteria saturate after N_3 is that no new length scales emerge; this occurs because both the numerator and denominator of the term describing the probability of resonance originate from V as all pseudo-pseudo-spins have transition dipole moments with respect to σ^z. The iterated pairs criterion supersedes Eq. (S6) only when $\alpha > \beta + 4$. We note that throughout section III we always assume $R_1 \leq R_2 \leq R_3$.

A.4 Nearby resonances

In the mixed power law regime, with $\alpha > \beta$, the distance R_2 between pairs of pseudospins is much larger than the scale of the both isotropic ($R_1 \sim R_2^{\beta+2/\alpha+2}$) and anisotropic ($R_1 \sim R_2^{\beta/\alpha}$) pseudospins. As the interactions V are generally much stronger, one might worry that pseudospins at distances $\tilde{R} < R_2$ might spoil the resonance condition for the pseudospin counting at the larger distance R_2.

When are there $\mathcal{O}(1)$ pseudospins of scale R_1 at distances $\tilde{R} < R_2$? First, we note that

the number of resonances at a distance $\tilde{R}$ is given by,

$$N_2(R_1, \tilde{R}) \sim \rho N_1(R_1) \tilde{R}^d \sim R_1^{d-\alpha} \tilde{R}^d. \tag{A.9}$$

Thus, there are $\mathcal{O}(1)$ resonances when $\tilde{R} \sim R_1^{\alpha/d-1}$. We should now compare this with R_2 as set by the condition $V(R_2) \sim t(R_1)$. There are three possible cases:

(A) When $\tilde{R} > R_2$, there are no "nearby" resonances.

(B) When $\tilde{R} = R_2$, pairs at scale R_1 find other pairs at scale $\tilde{R} = R_2$ which are resonant with respect to V.

(C) When $\tilde{R} < R_2$, there are many "nearby" resonances before distance R_2.

The critical case occurs when $\tilde{R} \sim R_2$ or when $R_1^{\alpha/d-1} \sim R_1^{\frac{\alpha}{\beta}}$, yielding $d_c = \frac{\alpha\beta}{\alpha+\beta}$. This result is especially nice since this condition matches with that obtained for the critical dimensions for MBL (middle column of Table I in the maintext). Thus, for $d < \frac{\alpha\beta}{\alpha+\beta}$, MBL is consistent with resonance counting of the form considered above; moreover, there are no "nearby" resonances to modify the counting.

A.5 Size of a resonant pseudo-spin pair

In numerical and experimental studies of finite size systems, pseudospin resonances only play a role when the system size becomes large enough to contain them. Thus, in this section, we estimate the typical scale R_2 at which any given extended pair finds $\mathcal{O}(1)$ resonant partners $N_2(R_2) \sim 1$. The typical size R_2 is measured in lattice units and thus has a microscopically detailed dependence on the microscopic couplings and disorder as we derive below.

A.5.1 Random field disorder

Let us first estimate R_2 in the case of a filled lattice where disorder arises from the underlying randomness of the on-site fields (e.g. the case of molecules with speckle). In the next subsection, we will consider the case where disorder arises from dilution (e.g. rotor or NV spin model).

We consider $N_2(R_1, R_2)$ and are interested in the smallest R_2 which harbors resonances. For concreteness, let us work with $\alpha = \beta$ and hence take $R_1 \sim R_2$. A central pseudo-spin is resonates with another pseudo-spin at scale R_2 if $N_2(R_2) \sim 1$, so we estimate,

$$1 \sim N_2(R_2) = \rho^2 \cdot R_2^{2d-\beta} \cdot \frac{V}{W} \implies R_2^{2d-\beta} = \frac{1}{\rho^2}\frac{W}{V} = \frac{1}{\rho^2}\frac{1}{a_0^\beta}\frac{W}{V/a_0^\beta} \tag{A.10}$$

We now define $D = \frac{W}{V/a_0^\beta}$ as the ratio between the disorder bandwidth and the nearest neighbor interaction strength; it is a dimensionless measure of the disorder strength and for an un-diluted lattice $\rho \sim 1/a_0^d$. Thus, one obtains

$$R_2 \approx a_0 D^{1/(2d-\beta)}, \tag{A.11}$$

which for $d = \beta = 3$ is $R_2 \approx a_0 \sqrt[3]{D}$ and for $d = 2$ is $R_2 \approx a_0 D$. For $\alpha = \beta = 3$ (e.g. dipoles), the expected upper critical dimension is $d_c = 1.5$ so as expected, the pair size diverges (in large disorder, such that $D > 1$) as one approaches d_c from above.

A.5.2 Disorder arising from dilution

We now consider the case where disorder arises from Poissonian (random) dilution on the lattice. For concreteness, let us consider the rotor example from the maintext ($\alpha = \beta = 3$). The effective on-site random fields generated by the dilution arise from the $d_i^z d_j^z$ (Ising) term of the dipolar interaction. Assuming that the rotors are oriented along the same

quantization axis, one finds

$$\sum_{i<j}\frac{d_i^z d_j^z}{r_{ij}^3}=\sum_{i<j}\frac{(d_i^s+d_i^a\sigma_i^z)(d_j^s+d_j^a\sigma_j^z)}{r_{ij}^3}=\sum_{i<j}\frac{(d^s)^2}{r_{ij}^3}+\sum_{i<j}\frac{d^a d^s}{r_{ij}^3}(\sigma_i^z+\sigma_j^z)+\sum_{i<j}\frac{(d^a)^2}{r_{ij}^3}\sigma_i^z\sigma_j^z, \tag{A.12}$$

where we have re-expressed the effective permanent dipole moment (diagonal component of the dipole moment operator) in terms of symmetric and antisymmetric pieces, e.g. $\langle\uparrow|\, d^z\,|\uparrow\rangle = d^s + d^a$ and $\langle\downarrow|\, d^z\,|\downarrow\rangle = d^a - d^s$.

Let us now estimate the width of the disorder distribution arising from random fields $\epsilon_i = \sum_{i\neq j}\frac{d^a d^s}{r_{ij}^3}$. The average field at site i is $\overline{\epsilon_i} = \sum_{j\neq i}\frac{d^a d^s}{r_{ij}^3}\overline{Q_j} = \nu\frac{d^a d^s}{a_0^3}\sum_{\ell\in lat}\frac{1}{\ell^3}$, where ν is the dilution probability and $Q_j = 1$ for a lattice site containing a spin and 0 otherwise; the last sum runs over the integer lattice and is the analog of the usual Madelung constant in electrostatics. The variance of the on-site field is $\overline{\delta\epsilon_i^2} = \overline{\epsilon_i^2} - \overline{\epsilon_i}^2$, where $\overline{\epsilon_i^2} = \overline{\sum_{j\neq i}\sum_{k\neq i}\left(\frac{d^a d^s}{r_{ij}^3}Q_j\right)\left(\frac{d^a d^s}{r_{ik}^3}Q_k\right)}$. Noting that $\overline{Q_jQ_k} = \nu\delta_{jk} + \nu^2(1-\delta_{jk})$ yields $\overline{\epsilon_i^2} = \left(\frac{d^a d^s}{a_0^3}\right)^2\left[(\nu-\nu^2)\sum_{\ell\in lat}\frac{1}{\ell^6} + \left(\nu\sum_{\ell\in lat}\frac{1}{\ell^3}\right)^2\right]$. Thus, one finds that

$$W = \sqrt{\overline{\epsilon_i^2}} = \sqrt{\overline{\epsilon_i^2} - \overline{\epsilon_i}^2} = \frac{d^a d^s}{a_0^3}\sqrt{(\nu-\nu^2)\sum_{\ell\in lat}\frac{1}{\ell^6}}, \tag{A.13}$$

which in the strong dilution limit ($\nu \ll 1$) scales as $W \sim \sqrt{\nu}\frac{d^a d^s}{a_0^3}$.

With the effective disorder bandwidth in hand, we now estimate the size of resonant pseudo-spin pairs. For the case of dilution, we note that $\rho \sim \nu/a_0^3$ and $W = \frac{d^a d^s}{a_0^3}\sqrt{(\nu-\nu^2)\sum_{\ell\in lat}\frac{1}{\ell^6}}$. Following the same analysis, one finds,

$$1 \sim N_2(R_2) = \rho^2\cdot R_2^{2d-\beta}\cdot\frac{V}{W} \implies R_2^{2d-3} = \frac{1}{\rho^2}\frac{W}{V} = \frac{1}{\rho^2}\frac{1}{a_0^3}\frac{\frac{d^a d^s}{a_0^3}\sqrt{(\nu-\nu^2)\sum_{\ell\in lat}\frac{1}{\ell^6}}}{V/a_0^3}. \tag{A.14}$$

The interaction strength $V \sim (d^a)^2$ and hence,

$$R_2 \approx a_0 \left(\frac{d^s}{d^a} \frac{1}{\nu^2} \sqrt{(\nu - \nu^2) \sum_{\ell \in lat} \frac{1}{\ell^6}} \right)^{\frac{1}{2d-3}} . \tag{A.15}$$

Working in the strong dilution limit $\nu \ll 1$ and ignoring the order 1 correction from the Madelung constant, one finds that in $d = 3$, $R_2 \approx \left(\frac{d_s}{d_a}\right)^{1/3} a_0/\sqrt{\nu}$ and in $d = 2$, $R_2 \approx \frac{d_s}{d_a} a_0/\nu^{3/2}$.

Appendix B

Topology from Polar Molecules

This appendix serves as a detailed derivation for the results in Chapter 3 of this thesis. In particular, we derive the effective Hamiltonian starting from the rotational physics of polar molecules.

B.1 Deriving the Effective Hamiltonian

Here, we derive the effective Hamiltonian, $H_B = -\sum_{ij} t_{ij} a_i^\dagger a_j + \frac{1}{2}\sum_{i\neq j} V_{ij} n_i n_j$. The molecules lie in the X-Y plane and the applied DC electric field has spherical coordinates (Θ_0, Φ_0) in this basis. To simplify the notation, we define $|\uparrow\rangle = s|1,-1\rangle + v|1,1\rangle + w|1,0\rangle$, where $s = \Omega_2\Omega_4/\tilde{\Omega}$, $v = \Omega_1\Omega_3/\tilde{\Omega}$, $w = -\Omega_1\Omega_4/\tilde{\Omega}$. Consider two dressed molecules at positions i and j separated by $\mathbf{R} = (R, \theta, \phi)$ (spherical coordinates in the $\{x, y, z\}$ basis). The dipolar interaction between these molecules can be written in spherical tensor form as:

$$H_{\rm dd} \;=\; -\frac{1}{4\pi\epsilon_0}\frac{\sqrt{6}}{R^3}\sum_{q=-2}^{2}(-1)^q C^2_{-q}(\theta,\phi)T^2_q(\mathbf{d}^{(i)},\mathbf{d}^{(j)}), \tag{B.1}$$

where $C^k_q(\theta,\phi)$ is the spherical harmonic of degree k and z angular momentum q. Here, T^2 is the rank 2 spherical tensor generated from the dipole operators; in particular, $T^2_{\pm 2}(\mathbf{d}^{(i)},\mathbf{d}^{(j)}) = d^{(i)}_\pm d^{(j)}_\pm$, $T^2_{\pm 1}(\mathbf{d}^{(i)},\mathbf{d}^{(j)}) = \left(d^{(i)}_z d^{(j)}_\pm + d^{(i)}_\pm d^{(j)}_z\right)/\sqrt{2}$,

$T_0^2(\mathbf{d}^{(i)}, \mathbf{d}^{(j)}) = \left(d_-^{(i)} d_+^{(j)} + 2 d_z^{(i)} d_z^{(j)} + d_+^{(i)} d_-^{(j)}\right)/\sqrt{6}$, and $d_\pm = \mp(d_x \pm i d_y)/\sqrt{2}$. Expressing the dipolar interaction in this form allows us to isolate energy conserving terms. We assume that the energy difference between $|1,0\rangle$ and $|1,\pm1\rangle$ is larger than the scale of the dipole-dipole interactions. Under this assumption, $T_{\pm1}^2$ terms of the dipolar interaction are energy non-conserving and thus highly suppressed.

We now consider the three resonant contributions to the hopping (t_{ij}) matrix elements,

$$\langle\uparrow_i\downarrow_j| T_0^2 |\downarrow_i\uparrow_j\rangle = \sqrt{\frac{2}{3}}[d_{00}^2 w_i^* w_j - \frac{1}{2} d_{01}^2 (v_i^* v_j + s_i^* s_j)], \tag{B.2}$$

$$\langle\uparrow_i\downarrow_j| T_{+2}^2 |\downarrow_i\uparrow_j\rangle = -d_{01}^2 (v_i^* s_j), \tag{B.3}$$

$$\langle\uparrow_i\downarrow_j| T_{-2}^2 |\downarrow_i\uparrow_j\rangle = -d_{01}^2 (s_i^* v_j), \tag{B.4}$$

where $d_{00} = \langle 1,0|d_z|0,0\rangle$ and $d_{01} = \langle 1,\pm1|d_\pm|0,0\rangle$. Combined with the spherical harmonic coefficients of Eq. B.1, these terms determine the directionally dependent hopping t_{ij} of the spin flips.

The interactions V_{ij} between the spin flips arise as a consequence of the induced dipole moment which each molecule acquires in an applied electric field. Thus, $V_{ij} = \langle\uparrow_i\uparrow_j| H_{dd} |\uparrow_i\uparrow_j\rangle + \langle\downarrow_i\downarrow_j| H_{dd} |\downarrow_i\downarrow_j\rangle - \langle\uparrow_i\downarrow_j| H_{dd} |\uparrow_i\downarrow_j\rangle - \langle\downarrow_i\uparrow_j| H_{dd} |\downarrow_i\uparrow_j\rangle$ can be calculated in a similar fashion. First, let us define the induced dipolar moment of a molecule on site i, $d_{\uparrow_i} = d_1(|s_i|^2 + |v_i|^2) + \mu_0 |w_i|^2$, where $d_1 = \langle 1,\pm1|d_z|1,\pm1\rangle$ and $\mu_0 = \langle 1,0|d_z|1,0\rangle$ that of the $|1,0\rangle$ state. The contributing terms to V_{ij} are then

(suppressing ij superscripts in $\mathbf{d}$):

$$\langle\downarrow_i\downarrow_j|\, d_z d_z + \frac{1}{2}(d_+ d_- + d_- d_+)\,|\downarrow_i\downarrow_j\rangle = d_0^2, \tag{B.5}$$

$$\langle\uparrow_i\downarrow_j|\, d_z d_z + \frac{1}{2}(d_+ d_- + d_- d_+)\,|\uparrow_i\downarrow_j\rangle = d_{\uparrow_i} d_0, \tag{B.6}$$

$$\langle\downarrow_i\uparrow_j|\, d_z d_z + \frac{1}{2}(d_+ d_- + d_- d_+)\,|\downarrow_i\uparrow_j\rangle = d_0 d_{\uparrow_j}, \tag{B.7}$$

$$\langle\uparrow_i\uparrow_j|\, d_z d_z + \frac{1}{2}(d_+ d_- + d_- d_+)\,|\uparrow_i\uparrow_j\rangle = d_{\uparrow_i} d_{\uparrow_j} - \frac{1}{2}\mu_{01}^2(s_i w_i^* w_j s_j^* + w_i v_i^* v_j w_j^* + \text{c.c.}) \tag{B.8}$$

$$\langle\uparrow_i\uparrow_j|\, d_+ d_+\,|\uparrow_i\uparrow_j\rangle = -\mu_{01}^2(s_i w_i^* w_j v_j^* + w_i v_i^* s_j w_j^*), \tag{B.9}$$

$$\langle\uparrow_i\uparrow_j|\, d_- d_-\,|\uparrow_i\uparrow_j\rangle = -\mu_{01}^2(w_i s_i^* v_j w_j^* + v_i w_i^* w_j s_j^*), \tag{B.10}$$

where $d_0 = \langle 0,0|d_z|0,0\rangle$ and $\mu_{01} = \langle 1,\pm 1|d_\pm|1,0\rangle$ is the transition dipole moment between $|1,0\rangle$ and $|1,\pm 1\rangle$. From H_{dd} there also exists an on-site potential $t_{ii} = \sum_{j\neq i}(\langle\downarrow_i\downarrow_j|\, H_{dd}\,|\downarrow_i\downarrow_j\rangle - \langle\uparrow_i\downarrow_j|\, H_{dd}\,|\uparrow_i\downarrow_j\rangle)$ which varies between sites; however, as we will see below, inhomogeneities in t_{ii} can be regulated using optical lattice tensor shifts. Finally, we note that we have dropped a uniform chemical potential term associated with the molecule's rotational constant $2B$.

To obtain topological flat bands, we adjust the optical radiation to generate four different types of sites $\{a, b, A, B\}$ (in relation to the M-scheme). By restricting the variation of $|\uparrow\rangle$ on (a vs. A) sites and on (b vs. B) sites, we ensure that both t_{ij} and V_{ij} are invariant under the direct lattice vectors $\vec{g}_1, \vec{g}_2$, enhancing the symmetry to that of a checkerboard lattice with a two-site translational unit cell. This small generalization from a two-site model provides an important minus-sign freedom in the choice of w between lowercase and uppercase letter sites, which we exploit in tuning the Chern band structures. The freedom can be seen by examining the constraints imposed by requiring t_{ij} and V_{ij} to be invariant under $a \leftrightarrow A$ and $b \leftrightarrow B$ (i.e. translation by $\mathbf{g}_2$). In particular, the relevant constraints allow $w_{a/b} = w_{A/B}$ or $w_{a/b} = -w_{A/B}$ as solutions.

B.2 Experimental Implementation in ^{40}K^{87}Rb

B.2.1 Molecular Hyperfine Structure:

In this section, we consider the complications in our scheme due to the hyperfine structure of diatomic polar molecules such as ^{40}K^{87}Rb. The molecular rotational degree of freedom is naturally coupled to the nuclear spins, $I_1 = 4$ and $I_2 = 3/2$ of potassium and rubidium. The hyperfine Hamiltonian is dominated by the nuclear quadrupole interaction, which has a typical strength $H_Q \sim 1$MHz (for ^{40}K^{87}Rb). This interaction splits the degeneracy between the $|1, \pm 1\rangle$ rotational states implying that our workhorse, the $T^2_{\pm 2}$ terms of H_{dd}, are off-resonant. To overcome this issue, one can simply ensure that the optical dressing Ω (in the M-scheme) is much stronger than H_{hf}. This ensures that the hyperfine interaction is unable to couple the dark state to other dressed eigenstates.

One final issue to consider is the particular choice of nuclear spin states. Since the composition of the dark state differs on the four types of lattice sites $\{a, b, A, B\}$, molecules on these sites are subject to slightly different hyperfine potentials; in particular, $\langle\uparrow_A| H_{hf} |\uparrow_A\rangle = \langle\uparrow_a| H_{hf} |\uparrow_a\rangle \neq \langle\uparrow_B| H_{hf} |\uparrow_B\rangle = \langle\uparrow_b| H_{hf} |\uparrow_b\rangle$. Furthermore, the appropriate nuclear eigenstates will also depend on whether we are considering the rovibrational ground state ($|\downarrow\rangle$) or the dark state ($|\uparrow\rangle$); this is because the decoupled nuclear spin basis (so-called Paschen-Bach regime) is only valid in the first case. One can solve this issue by applying a static magnetic field $\sim 10^3$ G along the direction of the DC electric field, ensuring that the decoupled basis is appropriate for both $|\downarrow\rangle$ and $|\uparrow\rangle$ (note that such a field is already present in experiments). Then, it only remains to choose a pair of nuclear eigenstates which have reasonable overlap and resonant energies. We have numerically verified that this is generically achievable.

B.2.2 Optical Lattice Tensor Shifts:

Similar to the hyperfine potential, A-type and B-type sites feel different tensor shifts from the optical lattice. As alluded to in the main text, these tensor shifts can be exploited to compensate for dipolar induced t_{ii} terms. To start, let us consider a single optical field, $E(R,t) = E(R)e^{-i\omega t} + \text{h.c.}$ which we use to create the lattice potential in the $\hat{X}$ direction. The optical potential is given by $H_{lattice} = -E(R)^* \alpha(\omega) E(R)$, where $E(R) = |E(R)| \sum_p \beta_p(R) e_p$, e_p is the polarization basis, and $\alpha(\omega)$ is the polarizability tensor of the molecule. Recasting the lattice potential in terms of spherical harmonics yields,

$$H_{lattice} = -E^2(R) \left[\frac{2\alpha_\perp - \alpha_\parallel}{3} + (\alpha_\parallel - \alpha_\perp) \sum_p C_p^2 \gamma_p \right] \tag{B.11}$$

where $\alpha_\parallel$ is the polarizability along the internuclear axis, $\alpha_\perp$ is the polarizability transverse to the internuclear axis, $\gamma_0 = |\beta_0|^2 - 1/3$, $\gamma_{\pm 1} = 1/\sqrt{3}(\beta_0^* \beta_\pm - \beta_\mp^* \beta_0)$, and $\gamma_{\pm 2} = -\sqrt{2/3}\beta_\mp^* \beta_\pm$.

In our case, the optical lattice potential seen by $|\downarrow\rangle$ is,

$$\langle\downarrow| H_{lattice} |\downarrow\rangle = -E^2(R) \left[\frac{2\alpha_\perp - \alpha_\parallel}{3} + (\alpha_\parallel - \alpha_\perp) \langle 0,0| C_0^2 |0,0\rangle \gamma_0 \right] \tag{B.12}$$

while the potential seen by $|\uparrow\rangle$ is,

$$\begin{aligned} \langle\uparrow| H_{lattice} |\uparrow\rangle &= -E^2(R)[\frac{2\alpha_\perp - \alpha_\parallel}{3} + (\alpha_\parallel - \alpha_\perp)\{\gamma_0(|s|^2 \langle 1,-1| C_0^2 |1,-1\rangle \\ &+ |v|^2 \langle 1,1| C_0^2 |1,1\rangle + |w|^2 \langle 1,0| C_0^2 |1,0\rangle) + \gamma_2 s v^* \langle 1,1| C_2^2 |1,-1\rangle \\ &+ \gamma_{-2} s^* v \langle 1,-1| C_{-2}^2 |1,1\rangle\}]. \end{aligned} \tag{B.13}$$

The energy difference $\delta E = \langle\uparrow| H_{lattice} |\uparrow\rangle - \langle\downarrow| H_{lattice} |\downarrow\rangle$ varies between A-type and B-type sites since the dressing parameters $\{s, v, w\}$ are site-dependent. The goal is to use this tunable tensor shift to compensate for dipolar induced t_{ii} terms. Note that we can achieve

propagation of the optical beams along any direction using only σ_+ and π light. Since our optical field never contains any σ_- polarization, we find that $\gamma_{\pm 2}$ terms are zero. Moreover, we have also dropped $\gamma_{\pm 1}$ terms, since $\Delta = E_{1,0} - E_{1,1} \gg H_{lattice}$. Combining the optical fields along the $\hat{x}$, $\hat{y}$ and $\hat{z}$ direction, we have numerically verified that by simply adjusting the intensities of the lattice light, we can fully compensate for any inhomogeneous on-site potential.

Finally, we demonstrate a simple configuration of Raman lasers (with wavelength λ_0), which generates the M-scheme for the $\{a, b, A, B\}$ checkerboard lattice shown in Fig. 2A. We take the lattice constant to be $\lambda_L = R_0$ (Fig. 2A) and assume that $\lambda_0 \leq \lambda_L$; this can always be accomplished by increasing λ_L (at the expense of weaker dipolar interactions). We can tilt the k-vectors propagating along $\hat{X}$ and along $\hat{Y}$ up or down out of the XY plane to give them a periodicity of λ_L (in the XY plane). Similarly, we can tilt the k-vectors propagating along $(\hat{X} \pm \hat{Y})$ up or down out to give them a periodicity of $\sqrt{2}\lambda_L$ (in the XY plane). By using only four out of these eight beams and linearly polarizing them along $\hat{k} \times \hat{z}$, we can obtain arbitrary Ω_2 and Ω_3 on A and B sites with $\Omega_1 = \Omega_4 = 0$. By utilizing the other four beams, we can obtain arbitrary $\Omega_1 = \Omega_4$ on A and B sites (and their negatives on a and b sites) with $\Omega_2 = \Omega_3 = 0$. This immediately enables us to construct the four-site M-scheme.

B.3 Many-Body Phases

Here, we provide a detailed description of the many-body phases which arise as one tunes the electric field parameters. First, we note that the field and dressing parameters for the phase diagram are different than those in Chapter 3. This is because the richest many-body phase diagram that we observe does not occur for the band structure with the largest flatness ratio. The band-structure depicted in Chapter 3 occurs at electric field tilt $\Theta_0 = 0.68, \Phi_0 = 5.83$, with optical dressing parameters:

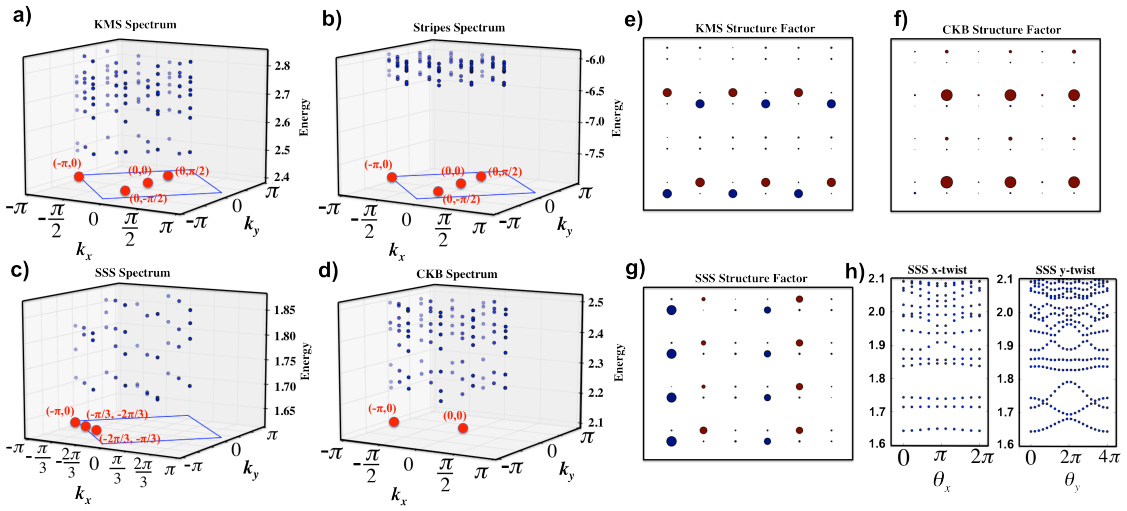

Figure 72: Many-body Phases. (A) Depicts the spectrum associated with the knight's move solid phase in the reduced Brillouin zone (k_x and k_y are crystal momenta). The electric field tilt is $\Theta_0 = 0.05$ and the field strength is $|E| \sim 32$kV/cm. (B) depicts the spectrum associated with the striped phase ($\Theta_0 = 1.05$ and $|E| \sim 28$kV/cm). (C) depicts the spectrum associated with the striped supersolid phase ($\Theta_0 = 0.68$ and $|E| \sim 36$kV/cm). (D) depicts the spectrum associated with the checkerboard phase ($\Theta_0 = 0.25$ and $|E| \sim 40$kV/cm). (E-G) depicts the structure factor of the KMS, CKB, SSS respectively for the same parameters as above (SS phase omitted). (H) depicts the spectral flow under magnetic flux insertion of the SSS phase.

$\{\theta_a, \theta_b, \phi_a, \phi_b, \alpha_a, \alpha_b, \gamma_a, \gamma_b\} = \{0.53, 0.97, 1.36, 3.49, 2.84, 2.03, 4.26, 3.84\}$, where we have parametrized: $s_i = \sin(\alpha_i)\sin(\theta_i)$, $v_i = \sin(\alpha_i)\cos(\theta_i)e^{i\phi_i}$ and $w_i = \cos(\alpha_i)e^{i\gamma_i}$. The phase diagram shown in Fig. 72 is computed by exact diagonalization for filling fraction $\nu = 1/2$ and a total of $N_s = 24$ sites (parameters:

$\{\Theta_0, \Phi_0, \theta_a, \theta_b, \phi_a, \phi_b, \alpha_a, \alpha_b, \gamma_a, \gamma_b\} = \{0.65, 3.68, 2.4, 2.97, 6.06, 4.1, 0.97, 2.74, 3.44, 1.74\}$). The associated band-structure has an optimized flatness ratio, $f \approx 7$. The dressing parameters on A-type and B-type sites are identical to those on a and b sites with the exception that $\gamma_A = \pi + \gamma_a$ and $\gamma_B = \pi + \gamma_b$ (ie. $w_{a/b} = -w_{A/B}$). At weak electric fields, $E \lesssim 8$ kV/cm, diagonalization reveals the $\nu = 1/2$ Fractional Chern Insulator. By changing both the strength and tilt (Θ_0) of the DC field, one can map out a phase diagram containing both conventional and topological phases. To isolate the effects of long-range interactions, we ensure that at each tilt, the flatness ratio remains the same for all DC field strengths. This can be achieved by re-optimizing the dressing parameters for each field

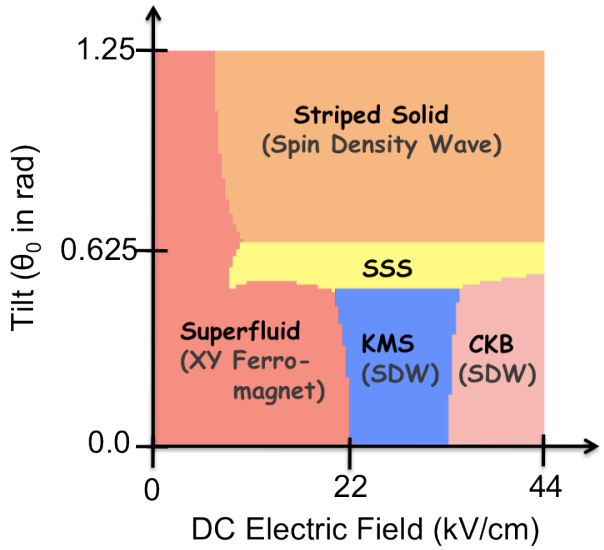

Figure 73: Variational Mean-field theory. Depicts the variational mean-field theory for ^{40}K^{87}Rb as a function of applied electric field strength and tilt angle Θ_0. We consider twelve variational ansatz's including all allowed solids up to a quadrupled unit cell. The superfluid ansatz is optimized with respect to its winding and a relative phase difference between A- and B-type sites.

strength. Alternatively, this corresponds to ensuring that $d_{00} = d_{01}$ as the field increases; experimentally, one can realize this by dressing the $|1, \pm 1\rangle$ states with a long-lived metastable excited state. Numerically, we implement this constraint by taking $s_i \to s_i d_{00}/d_{01}$ and $v_i \to v_i d_{00}/d_{01}$.

There exist four crystalline phases at strong DC electric fields whose diagnostics we depict in Fig. S1. At low and intermediate DC field strengths, we observe a large superfluid region. This phase is characterized by a unique ground state (typically in either the $(0, 0)$ or $(-\pi, 0)$ momentum sectors) and a fluid-like real space structure factor. The homogeneity of the superfluid changes as one adjusts the DC field strength and tilt. At very weak fields $|E| < 4$kV/cm, A-type and B-type sites are equally populated; however, as one increases the field strength, the anisotropy of the long-range dipolar interaction yields anisotropy in the structure factor. To verify the nature these non-topological phases in the thermodynamic limit, we perform a detailed variational mean-field study. As shown in Fig. 73, this study confirms not only the existence of these phases, but also the qualitative

location of the phase boundaries. Moreover, in the KMS, CKB and SS solids, the mean-field energies match nearly identically with the exact diagonalization energies. This suggests that product state wavefunctions are valid approximations in these regimes and hence, that one can easily prepare finite density, low-temperature states.

Appendix C

Yu-Shiba-Rusinov corrections to RKKY in a superconductor

This appendix serves as a detailed derivation for the results in Chapter 4 of this thesis. In particular, we derive the perturbative superconducting correction to RKKY and discuss the origin of the singular contribution to the Yu-Shiba-Rusinov interaction

C.1 Perturbative Superconducting Correction to RKKY

We provide the derivation for the perturbative (second order) superconducting correction to RKKY. In particular, we compute the exchange integral from the magnetization density,

$$I(r) = \frac{\beta^2}{4\pi}\int_0^\infty \mathrm{Tr}[G_0(r;z)G_0(r;z)]dx \tag{C.1}$$

where $G_0(r;z) = \int d^3k \frac{z+\epsilon\tau_z+\Delta\tau_x}{z^2-\epsilon^2-\Delta^2}$ is the superconducting Green's function. Calculation reveals,

$$G_0(r;z=ix) = \frac{2\pi\rho_0}{k_f r}\frac{e^{-\sqrt{\Delta^2+x^2}/v_f r}}{\sqrt{\Delta^2+x^2}}\left(\cos(k_f r)\sqrt{\Delta^2+x^2}\tau_z + \sin(k_f r)[ix+\Delta\tau_x]\right). \tag{C.2}$$

Computing $\mathrm{Tr}[G_0(r;z)G_0(r;z)]$ one finds,

$$I(r) = \int_0^\infty dx \frac{e^{-\frac{k_f r_0 \sqrt{x^2+\Delta^2}}{E_f}} \beta^2[\Delta^2 + x^2\cos(2k_f r_0)]}{\pi(k_f r_0)^2(x^2+\Delta^2)} \tag{C.3}$$

$$= \frac{\beta^2}{\pi(k_f r_0)^2}\left(\cos(2k_f r_0)\int_0^\infty dx\left[e^{-\frac{k_f r_0\sqrt{x^2+\Delta^2}}{E_f}}\right] + 2\Delta^2\sin^2(k_f r)\int_0^\infty dx\frac{e^{-\frac{k_f r_0\sqrt{x^2+\Delta^2}}{E_f}}}{(x^2+\Delta^2)}\right) \tag{C.4}$$

Changing the variables from $x \to \Delta x$ yields,

$$I(r) = \frac{\beta^2}{\pi(k_f r_0)^2}\left(\cos(2k_f r_0)\int_0^\infty \Delta dx\left[e^{-\frac{k_f r_0\Delta\sqrt{x^2+1}}{E_f}}\right] + 2\sin^2(k_f r)\int_0^\infty \Delta dx\frac{e^{-\frac{k_f r_0\Delta\sqrt{x^2+1}}{E_f}}}{(x^2+1)}\right) \tag{C.5}$$

Noting that $\int_1^\infty dx\left[e^{-\frac{k_f r_0 \Delta x}{E_f}}\right] = \frac{E_f}{k_f r_0 \Delta}e^{-\frac{k_f r_0\Delta}{E_f}}$, we can rewrite exactly,

$$\int_0^\infty dx\left[e^{-\frac{k_f r_0\Delta\sqrt{x^2+1}}{E_f}}\right] = \frac{E_f}{k_f r_0\Delta}e^{-\frac{k_f r_0\Delta}{E_f}}F_1\left[\frac{k_f r_0\Delta}{E_f}\right] \tag{C.6}$$

where F_1 is the integral defined as,

$$F_1[\alpha] = \alpha\int_0^\infty dx e^{-\alpha(\sqrt{x^2+1}-1)}. \tag{C.7}$$

The second integral can be recast in a similar fashion,

$$\int_0^\infty dx\frac{e^{-\frac{k_f r_0\Delta\sqrt{x^2+1}}{E_f}}}{(x^2+1)} = \frac{\pi}{2}e^{-\frac{k_f r_0\Delta}{E_f}}F_2\left[\frac{k_f r_0\Delta}{E_f}\right] \tag{C.8}$$

where F_2 is the integral defined as,

$$F_2\left[\alpha\right] = \frac{2}{\pi}\int_0^\infty dx \frac{e^{-\alpha(\sqrt{x^2+1}-1)}}{(x^2+1)}. \tag{C.9}$$

In combination, this yields the perturbative superconducting RKKY exchange (see Fig. 74 for agreement with full non-perturbative calculation) as,

$$\begin{aligned} I(r) &= \frac{E_f\beta^2}{\pi(k_f r_0)^3}\cos(2k_f r_0)e^{-\frac{k_f r_0 \Delta}{E_f}}F_1\left[\frac{k_f r_0\Delta}{E_f}\right] + \frac{\Delta\beta^2}{(k_f r_0)^2}\sin^2(k_f r)e^{-\frac{k_f r_0\Delta}{E_f}}F_2\left[\frac{k_f r_0\Delta}{E_f}\right] \\ &= \frac{E_f\beta^2}{\pi(k_f r_0)^3}\cos(2k_f r_0)e^{-\frac{2r_0}{\xi}}F_1\left[\frac{2r_0}{\xi}\right] + \frac{\Delta\beta^2}{(k_f r_0)^2}\sin^2(k_f r)e^{-\frac{2r_0}{\xi}}F_2\left[\frac{2r_0}{\xi}\right] \end{aligned} \tag{C.10}$$

While the integrals F_1 and F_2 cannot be performed analytically, by looking at the asymptotic behavior, one can provide a reasonable closed form approximation,

$$F_1\left[\alpha\right] = \alpha\int_0^\infty dx e^{-\alpha(\sqrt{x^2+1}-1)} \approx 1.25(\alpha+0.65)^{1/2} \tag{C.11}$$

$$F_2\left[\alpha\right] = \frac{2}{\pi}\int_0^\infty dx \frac{e^{-\alpha(\sqrt{x^2+1}-1)}}{(x^2+1)} \approx \frac{0.8}{(\alpha+0.65)^{1/2}}. \tag{C.12}$$

C.2 Dyson Expansion

Recall from the main-text that the Dyson expansion reveals

$$\mathrm{Tr}[G_{\mathrm{k,k'}}(z) - G^{(0)}_{\mathrm{k}}(z)] = \mathrm{Tr}[S\Pi + S\Pi SG + S\Pi SGSG + \dots] = \mathrm{Tr}[S\Pi(z)(1 - SG^{(0)}(z))^{-1}]. \tag{C.13}$$

We now establish that our above expression is consistent with the conventional linear response formalism in the small S limit. To check this, observe that at quadratic order in S

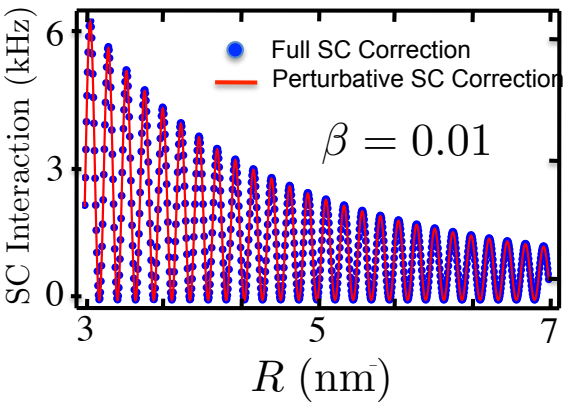

Figure 74: Depicts a comparison between the non-perturbative SC correction (blue circles) and the perturbative correction (red line) for small $\beta = 0.01$. The non-perturbative SC corrections are obtained by numerically integrating the full Green's function and then subtracting out the $\Delta = 0$ (metallic) portion.

(dropping the linear order S term, which does not contribute to interactions)

$$\mathrm{Tr}[S\Pi(z)(1 - SG^{(0)}(z))^{-1}] \approx \mathrm{Tr}[S\Pi(z)SG^{(0)}(z)]. \tag{C.14}$$

Expanding both $\Pi(z)$ and $G(z)$ in eigenstates, we obtain

$$\mathrm{Tr}[S\Pi(z)SG^{(0)}(z)] = \sum_{n,m} \frac{\langle\Psi_n|S|\Psi_m\rangle\langle\Psi_m|S|\Psi_n\rangle}{(z-\varepsilon_m)^2(z-\varepsilon_n)}. \tag{C.15}$$

The contribution of the above term to E_{tot} involves terms of the form

$$\begin{aligned}
&\int_0^{\infty+i\Lambda} \frac{d\epsilon}{4\pi} 2Re[\frac{i\epsilon}{(i\epsilon-\varepsilon_m)^2(i\epsilon-\varepsilon_n)}] \\
&= \int_{-\infty-i\Lambda}^{\infty-i\Lambda} -\frac{\epsilon d\epsilon}{4\pi i} \frac{\epsilon}{(i\epsilon-\varepsilon_m)^2(i\epsilon-\varepsilon_n)} \\
&= \int_{-\infty-i\Lambda}^{\infty-i\Lambda} -\frac{d\epsilon}{4\pi} \frac{\epsilon}{(\epsilon+i\varepsilon_m)^2(\epsilon+i\varepsilon_n)}.
\end{aligned} \tag{C.16}$$

The above integral can be computed via contour integration by closing the contour around either of $\pm i\infty$. If both $-i\varepsilon_{m,n}$ lie on the same side of $i\Lambda$ then the integral vanishes.

Otherwise we can close the integral on the side of $i\Lambda$ containing $-i\varepsilon_n$ so that

$$\begin{aligned}&\int_{-\infty-i\Lambda}^{\infty-i\Lambda} -\frac{d\epsilon}{4\pi}\frac{\epsilon}{(\epsilon+i\varepsilon_m)^2(\epsilon+i\varepsilon_n)}\\&=-\frac{1}{2}\frac{\varepsilon_n \mathrm{sgn}(\varepsilon_n-\Lambda)}{(\varepsilon_n-\varepsilon_m)^2}.\end{aligned} \tag{C.17}$$

Symmetrizing with respect to m, we obtain

$$\begin{aligned}&\int_{-\infty-i\Lambda}^{\infty-i\Lambda} -\frac{d\epsilon}{4\pi}\frac{\epsilon}{(\epsilon+i\varepsilon_m)^2(\epsilon+i\varepsilon_n)}\\&=-\frac{1}{4}\frac{\varepsilon_n \mathrm{sgn}(\varepsilon_n-\Lambda)+\varepsilon_m \mathrm{sgn}(\varepsilon_m-\Lambda)}{(\varepsilon_n-\varepsilon_m)^2} &\text{(C.18)}\\&=-\frac{1}{4}\frac{\mathrm{sgn}(\varepsilon_n-\Lambda)}{(\varepsilon_n-\varepsilon_m)} &\text{(C.19)}\\&=\frac{1}{4}\int_{-\infty-i\Lambda}^{\infty-i\Lambda} -\frac{d\epsilon}{2\pi}\frac{1}{(\epsilon+i\varepsilon_m)(\epsilon+i\varepsilon_n)}. &\text{(C.20)}\end{aligned}$$

Substituting back, we obtain that the correction to the total energy is also given by

$$\begin{aligned}4\delta E_{tot} &= 2\int_0^{\infty}\frac{d\epsilon}{4\pi}2\mathrm{Re}[i\mathrm{Tr}[SG^{(0)}(i\epsilon)SG^{(0)}(i\epsilon)]]\\&-\int_0^{\infty+i\Lambda}\frac{d\epsilon}{4\pi}2\mathrm{Re}[i\mathrm{Tr}[SG^{(0)}(i\epsilon)SG^{(0)}(i\epsilon)]]-\int_0^{\infty-i\Lambda}\frac{d\epsilon}{4\pi}2\mathrm{Re}[i\mathrm{Tr}[SG^{(0)}(i\epsilon)SG^{(0)}(i\epsilon)]],\end{aligned} \tag{C.21}$$

in agreement with the conventional linear response formalism.

C.3 Expressions for $G^{\sigma\sigma'}_{LL}(z)$, $G^{\sigma\sigma'}_{LR}(z)$, $\Pi^{\sigma\sigma'}_{LL}(z)$ and $\Pi^{\sigma\sigma'}_{LR}(z)$

Here, we provide the derivations for $G^{\sigma\sigma'}_{LL}(z)$, $G^{\sigma\sigma'}_{LR}(z)$,$\Pi^{\sigma\sigma'}_{LL}(z)$ and $\Pi^{\sigma\sigma'}_{LR}(z)$ as used in the numerics. First, let us note that L and R will denote the left and right impurities. From the symmetry of the expressions, one can immediately see that $G^{\sigma\sigma'}_{LL}(z)=G^{\sigma\sigma'}_{RR}(z)$ and that

$G^{\sigma\sigma'}_{LR}(z) = G^{\sigma\sigma'}_{RL}(z)$. Expressing the BCS Green's function yields,

$$G^{\sigma\sigma'}_{LL}(z) = \int d^3k \frac{1}{z^2 - \Delta^2 - \epsilon_k^2} \begin{pmatrix} z - \epsilon_k & \Delta \\ \Delta & z + \epsilon_k \end{pmatrix} = \frac{-\rho_0}{\sqrt{\Delta^2 - z^2}} \begin{pmatrix} z & \Delta \\ \Delta & z \end{pmatrix} \tag{C.22}$$

For $G^{\sigma\sigma'}_{LR}(z)$, the only difference is that the form factors do note cancel out. Instead, one finds

$$G^{\sigma\sigma'}_{LR}(z) = \int d^3k \frac{1}{z^2 - \Delta^2 - \epsilon_k^2} \begin{pmatrix} z - \epsilon_k & \Delta \\ \Delta & z + \epsilon_k \end{pmatrix} e^{ik\cdot r_0}, \tag{C.23}$$

where $\vec{r_0} = \vec{r_L} - \vec{r_R}$. Contour integration yields $G^{\sigma\sigma'}_{LR}(z) =$

$$\frac{-\rho_0}{k_f r_0} \frac{e^{-\frac{\sqrt{\Delta^2 - z^2}}{v_f} r_0}}{\sqrt{\Delta^2 - z^2}} \begin{pmatrix} z\sin(k_f r_0) + \sqrt{\Delta^2 - z^2}\cos(k_f r_0) & \Delta\sin(k_f r_0) \\ \Delta\sin(k_f r_0) & z\sin(k_f r_0) - \sqrt{\Delta^2 - z^2}\cos(k_f r_0) \end{pmatrix}. \tag{C.24}$$

A similar calculation for $\Pi^{\sigma\sigma'}_{LL}(z)$ yields,

$$\Pi^{\sigma\sigma'}_{LL}(z) = \frac{\rho_0 \Delta}{(\Delta^2 - z^2)^{3/2}} \begin{pmatrix} \Delta & z \\ z & \Delta \end{pmatrix}. \tag{C.25}$$

C.4 Singular YSR Contribution

Here, we explain the dominance of the YSR contribution relative to the bulk contribution (e.g. changes to the bulk DOS). In the limit $k_f r \gg 1$, we derive an analytic expression for

the YSR shifts in both the parallel and anti-parallel impurity configuration.

$$\eta_{\uparrow\downarrow} = E_{sh}\frac{\tan^2(2\delta)}{(2k_f r)^2}\left[\frac{1+\beta^2+(3\beta^2-1)\cos(2k_f r)}{1+\beta^2}\right]e^{-\frac{2r}{\xi}\sin(2\delta)} \tag{C.26}$$

$$= \Delta\frac{1-\beta^2}{1+\beta^2}\frac{1}{(2k_f r)^2}\left(\frac{2\beta}{1-\beta^2}\right)^2\left[\frac{1+\beta^2+(3\beta^2-1)\cos(2k_f r)}{1+\beta^2}\right]e^{-\frac{2r}{\xi}\sin(2\delta)} \tag{C.27}$$

$$= \Delta\frac{1}{1-\beta^2}\frac{1}{(2k_f r)^2}\frac{4\beta^2}{1+\beta^2}\left[\frac{1+\beta^2+(3\beta^2-1)\cos(2k_f r)}{1+\beta^2}\right]e^{-\frac{2r}{\xi}\sin(2\delta)} \tag{C.28}$$

$$\eta_{\uparrow\uparrow} = E_{sh}\frac{\sin^2(2\delta)}{(2k_f r)^2}\left[\frac{-1+\beta^2+(1-5\beta^2)\cos(2k_f r)}{1-\beta^2} + \frac{2r}{\xi}\sin(2\delta)\sin^2(k_f r)\right]e^{-\frac{2r}{\xi}\sin(2\delta)} \tag{C.29}$$

As one can see the singular contribution to the YSR interaction comes from the divergence of $\eta_{\uparrow,\downarrow}$ as $\beta \to 1$ ($E_{sh} \to 0$). The form for this singular portion of the YSR interaction is given by,

$$J_{YSR}^{singular} = \Delta\frac{1}{1-\beta}\frac{\cos^2(k_f r)}{2(k_f r)^2}e^{-\frac{2r}{\xi}}. \tag{C.30}$$

Appendix D

Yao-Kivelson model and Quantum State Transfer

This appendix serves as a detailed derivation for the results in Chapter 7 of this thesis.

D.1 Gauge Projection to the Spin Subspace

Having demonstrated topologically protected state transfer by working in the extended Hilbert space in the main text, here, we consider the gauge projection back to the physical subspace. We ultimately illustrate the SWAP gate associated with TPST in the language of physical spin states. Recall that the 4-Majorana representation of the spin algebra $\sigma^\alpha = i\gamma^\alpha\gamma^0$ (for spins $\alpha \in \{x, y, z\}$ and correspondingly for Majoranas $\alpha \in \{1, 2, 3\}$) only holds under the constraint that $D = \gamma^1\gamma^2\gamma^3\gamma^0 = 1$. This defines the two dimensional physical subspace of the four dimensional Hilbert space associated to four Majorana fermions. More generally, for N spins σ_i^α, the 2^N dimensional physical space is defined by the N constraints $D_i = 1$ in the 2^{2N} dimensional extended Hilbert space. We may impose these constraints by using the physical (gauge) projector

$$P = \prod_i \frac{1 + D_i}{2} \tag{D.1}$$

which simply annihilates any state not satisfying the local constraint.

The gauge projector P has several important properties. It commutes with any physical operator built out of spin operators: $[P, \sigma_i^\alpha] = 0$. Furthermore, P absorbs gauge transformations D_i, with $PD_i = D_i P = P$. This gives us the freedom to understand the evolution of physical states $|\psi\rangle$ under any physical operation $\mathcal{O}$, which is a function of spin operators σ_i^α, by lifting this operation to the extended Hilbert space $\mathcal{O}^\gamma = \mathcal{O}(i\gamma_i^\alpha \gamma_0^\alpha)$, applying any gauge transformations D_i which may simplify the analysis, and projecting back only at the end. That is, if we can find a state $|\psi^\gamma\rangle$ in the extended Hilbert space such that $|\psi\rangle = P|\psi^\gamma\rangle$ then $\mathcal{O}|\psi\rangle = P\mathcal{O}^\gamma|\psi^\gamma\rangle$. In particular, if $|\psi^\gamma\rangle$ is an eigenstate of $\mathcal{O}^\gamma$, the physical state $|\psi\rangle$ is an eigenstate of $\mathcal{O}$. This is particularly useful for identifying energy and spin eigenstates in the extended Hilbert space. One must always ensure that $P|\psi^\gamma\rangle \neq 0$.

D.1.1 Decorated Honeycomb Lattice

We now focus on the decorated honeycomb lattice model along with two additional spin registers. The full Hamiltonian, $H_T = H_0 + H_L + H_R + H_{int}$ is composed of

$$\begin{aligned} H_0 &= \frac{1}{2}\sum_{\substack{x,x' \\ links}} \sigma_i^x \sigma_j^x + \frac{1}{2}\sum_{\substack{y,y' \\ links}} \sigma_i^y \sigma_j^y + \frac{1}{2}\sum_{\substack{z,z' \\ links}} \sigma_i^z \sigma_j^z \\ H_{L/R} &= -\frac{\Delta_S}{2}\sigma_L^z - \frac{\Delta_S}{2}\sigma_R^z, \quad H_{int} = g_L \sigma_L^x \sigma_a^x + g_R \sigma_R^x \sigma_b^x \end{aligned} \tag{D.2}$$

where we have chosen units in which $\kappa = 1$. The extension of the Hamiltonian to the Majorana Hilbert space results in a model of Majorana fermions γ_i^0 coupled to a static $\mathbb{Z}_2$

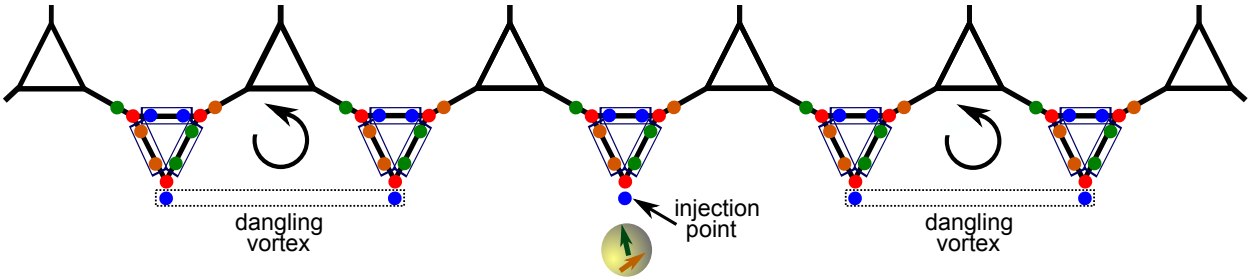

Figure 75: A schematic microscopic edge of the decorated honeycomb with the injection point explicitly labeled. Other pairs of dangling edge spins are paired into decoupled dangling vortices. It is these dangling vortices which lead to the large degeneracy found in the exactly solvable model.

gauge field $\hat{U}_{i,j}$ residing on the lattice links:

$$H_0^\gamma = \frac{i}{4}\sum_{ij}\hat{U}_{i,j}\gamma_i^0\gamma_j^0 \tag{D.3}$$

$$H_{L/R}^\gamma = -\frac{\Delta_S}{2}i\gamma_L^3\gamma_L^0 - \frac{\Delta_S}{2}i\gamma_R^3\gamma_R^0 \tag{D.4}$$

$$H_{int}^\gamma = -ig_L\hat{U}_{L,a}\gamma_L^0\gamma_a^0 - ig_R\hat{U}_{R,b}\gamma_R^0\gamma_b^0 \tag{D.5}$$

where $\hat{U}_{i,j} = i\gamma_i^\alpha\gamma_j^\alpha$ and $\alpha = x, y, z$ is the link type of $\langle ij\rangle$, or $\hat{U}_{i,j} = 0$ if i and j are not connected. We extend the definition of the gauge field $\hat{U}_{i,j}$ to the paired dangling edge spins on the boundary as in Fig. 75, and to $\hat{U}_{L,R} = i\gamma_L^2\gamma_R^2$. With this choice of pairings, all $\hat{U}_{i,j}$ are conserved by the total Hamiltonian and thus time evolution may be understood in each $\hat{U}_{i,j}$ sector. We label the sectors of $\hat{U}_{i,j}$ by field configurations $\{U_{i,j} = \pm 1\}$. Due to the antisymmetry of $U_{i,j}$, there is some subtlety in correctly labeling sectors: in all our formulae, we take ij to be oriented according to the arrows in chapter 7. Thus, $U_{i.j} = 1$ corresponds to a ground state gauge sector. Finally, we define $c_{L/R} = \frac{1}{2}(\gamma_{L/R}^0 + i\gamma_{L/R}^3)$ as in the main text so that we may think of $H_{L/R}^\gamma$ as measuring the occupation of left and right register fermions.

The $U_{i,j}$ are gauge dependent quantities as $\{D_i, \hat{U}_{i,j}\} = 0$, but the net flux around any closed loop $w(C) = \prod_{ij\in C}\hat{U}_{i,j}$ is gauge invariant; thus $w(C)$ is physical and conserved. The extended Hilbert space may be divided into conserved gauge sectors while the physical

Hilbert space splits into conserved flux sectors after projection. As usual, we say that any plaquette P such that $w(\partial P) = -1$ contains a vortex; here, we additionally extend this definition of vortices to include the dangling plaquettes defined by the $U_{i,j}$ links between dangling edges, as shown in Fig. 75. These dangling vortices are completely decoupled from the fermions and lead to a large degeneracy of the model with open boundaries ($2^{N_e/4}$ where N_e is the number of dangling edge spins).

D.1.2 Spin states on the Decorated Honeycomb

Let us consider the physical ground state of the system in the absence of interaction g between the registers and the decorated honeycomb. The spin registers both point up, disentangled from the rest of the system, while the lattice spins sit in their collective ground state: $\left|\left|\uparrow\right\rangle\right\rangle_L \left|GS\right\rangle_0 \left|\left|\uparrow\right\rangle\right\rangle_R$. We seek a reference ground state $|\Omega\rangle$ in a fixed gauge sector of the extended Hilbert space such that $\left|\left|\uparrow\right\rangle\right\rangle_L \left|GS\right\rangle_0 \left|\left|\uparrow\right\rangle\right\rangle_R = P\left|\Omega\right\rangle$ up to normalization. We choose $U_{i,j} = +1$ (i.e. the flux configuration of the ground state sector as described in the main text) and we choose $|\Omega\rangle$ to be annihilated by c_L, c_R and c_k for $k > 0$ of $H_0^\gamma(U) + H_{L/R}^\gamma$. This state is, by construction, a lowest energy eigenstate of the system, but it may not survive projection. The norm of $P\left|\Omega\right\rangle$ is $\left\langle\Omega\right| PP \left|\Omega\right\rangle = \frac{1}{2^N}\left\langle\Omega\right| 1 + \prod_i D_i \left|\Omega\right\rangle$ where we have exploited the orthogonality of states with different gauge configurations $U_{i,j}$. The product over all gauge transformations D_i measures the product of all $U_{i,j}$ and the parity of the $\gamma_1^0\gamma_2^0\cdots\gamma_N^0$ fermionic state. Thus, by flipping the choice of $U_{L,R}$ in $|\Omega\rangle$, we may guarantee that $P\left|\Omega\right\rangle$ survives projection. In general, in any fixed gauge sector related to our reference sector by an even (odd) number of flipped $U_{i,j}$'s, P will annihilate states with odd (even) fermionic parity.

We now construct an explicit representation of the 4 possible register states coupled to the

intermediate ground state $|GS\rangle_0$ by acting with $\sigma^x_{L/R}$:

$$
\begin{aligned}
||\uparrow\rangle\rangle_L |GS\rangle_0 ||\uparrow\rangle\rangle_R &= P|\Omega\rangle \\
||\downarrow\rangle\rangle_L |GS\rangle_0 ||\uparrow\rangle\rangle_R &= -iPc_L^\dagger \gamma_L^1 |\Omega\rangle \\
||\uparrow\rangle\rangle_L |GS\rangle_0 ||\downarrow\rangle\rangle_R &= -iPc_R^\dagger \gamma_R^1 |\Omega\rangle \\
||\downarrow\rangle\rangle_L |GS\rangle_0 ||\downarrow\rangle\rangle_R &= -iPc_L^\dagger c_R^\dagger |\Omega\rangle
\end{aligned}
\tag{D.6}
$$

where in the last line we have used $U_{L,R} = 1$ acting on $|\Omega\rangle$. More generally, degenerate and/or low energy states may be found in either the same flux sector with (pairs of) extra edge fermions, e.g. $Pc_p^\dagger c_{p'}^\dagger |\Omega\rangle$ or in degenerate flux sectors (containing dangling vortices), e.g. $Pc_k^\dagger \gamma_i^\alpha |\Omega\rangle$ where γ_i^α is a dangling edge Majorana. We note that since $H_0^\gamma(U)$ does not depend on the dangling edge $U_{i,j}$'s, neither do the fermionic eigenmodes c_k in these degenerate sectors nor the fermionic vacuum.

D.1.3 SWAP Gate in the Physical Subspace

Let us now consider time evolution $\mathcal{U}(t)$ in the presence of the coupling H^γ_{int}. The gauge field $U_{i,j}$ remains conserved and the time evolution of the Majorana field γ_i^0 within each gauge sector is that of noninteracting fermions. The full Hamiltonian in our chosen ground state gauge sector is given by equation (7.5). In general, ϵ_k, $Q_{k,a}$, and c_k depend on the gauge field but not on the dangling pieces of it, so the following analysis applies identically in each sector containing dangling vortices so long as the gauge is chosen the same way in the bulk and on $U_{L,a}$, $U_{R,b}$. Assuming that $g \ll \Delta_S$, we may use the secular approximation

to eliminate the c-fermion number non-conserving terms in equation (7.5),

$$\begin{aligned} H^{\gamma}(U) \approx & \sum_{k>0} \epsilon_k (c_k^\dagger c_k - \frac{1}{2}) + \Delta_S (c_L^\dagger c_L - \frac{1}{2}) + \Delta_S (c_R^\dagger c_R - \frac{1}{2}) \\ & - \frac{i}{\sqrt{2}} g_L (c_L^\dagger \sum_k Q_{k,a}^* c_k + c_L \sum_k Q_{k,a} c_k^\dagger) \\ & - \frac{i}{\sqrt{2}} g_R (c_R^\dagger \sum_k Q_{k,b}^* c_k + c_R \sum_k Q_{k,b} c_k^\dagger). \end{aligned} \tag{D.7}$$

This Hamiltonian leaves the c-fermion vacuum $|\Omega\rangle$ invariant and evolves the modes as usual non-interacting Dirac fermions: $\mathcal{U} c_{k_1}^\dagger c_{k_2}^\dagger \cdots c_{k_m}^\dagger |\Omega\rangle = c_{k_1(t)}^\dagger c_{k_2(t)}^\dagger \cdots c_{k_m(t)}^\dagger |\Omega\rangle$, where $k_i(t)$ denotes the time evolved wavefunction of the k_i mode according to the single particle Schrödinger equation. We note that the most general Majorana evolution would mix the $c^\dagger$ and c modes and accordingly the instantaneous c-vacuum would evolve in time.

To enable state transfer, we now tune $\Delta_S = \epsilon_{\tilde{k}}$ for an edge mode $\tilde{k}$. In the dot regime, we further require $|g_L Q_{\tilde{k},a}|, |g_R Q_{\tilde{k},b}| \ll |\epsilon_{\tilde{k}} - \epsilon_{\tilde{k}\pm 1}|$. This condition enables single-mode resolution of the edge eigenmodes and state transfer proceeds by resonant fermionic tunneling in an effective three mode model (dropping constants and the uninvolved modes):

$$H_{eff} = -\frac{i}{\sqrt{2}} g_L Q_{\tilde{k},a}^* c_L^\dagger c_{\tilde{k}} - \frac{i}{\sqrt{2}} g_R Q_{\tilde{k},b}^* c_R^\dagger c_{\tilde{k}} + h.c. \tag{D.8}$$

Since the individual quantum registers are fully controllable, we tune g_L and g_R to ensure that the effective tunneling rate $t_{\tilde{k}} = |\frac{g_L}{\sqrt{2}} Q_{\tilde{k},a}| = |\frac{g_R}{\sqrt{2}} Q_{\tilde{k},b}|$ between the modes is equivalent. Re-expressing $-iQ_{\tilde{k},a}^* = e^{i\phi_{\tilde{k},a}} |Q_{\tilde{k},a}|$ and $-iQ_{\tilde{k},b}^* = e^{i\phi_{\tilde{k},b}} |Q_{\tilde{k},b}|$, subsequent evolution under H_{eff} for a time $\tau = \frac{\pi}{\sqrt{2} t_{\tilde{k}}}$ results in mode evolution,

$$\begin{aligned} c_L^\dagger &\longrightarrow -e^{-i\phi} c_R^\dagger \\ c_{\tilde{k}}^\dagger &\longrightarrow -c_{\tilde{k}}^\dagger \\ c_R^\dagger &\longrightarrow -e^{i\phi} c_L^\dagger \end{aligned} \tag{D.9}$$

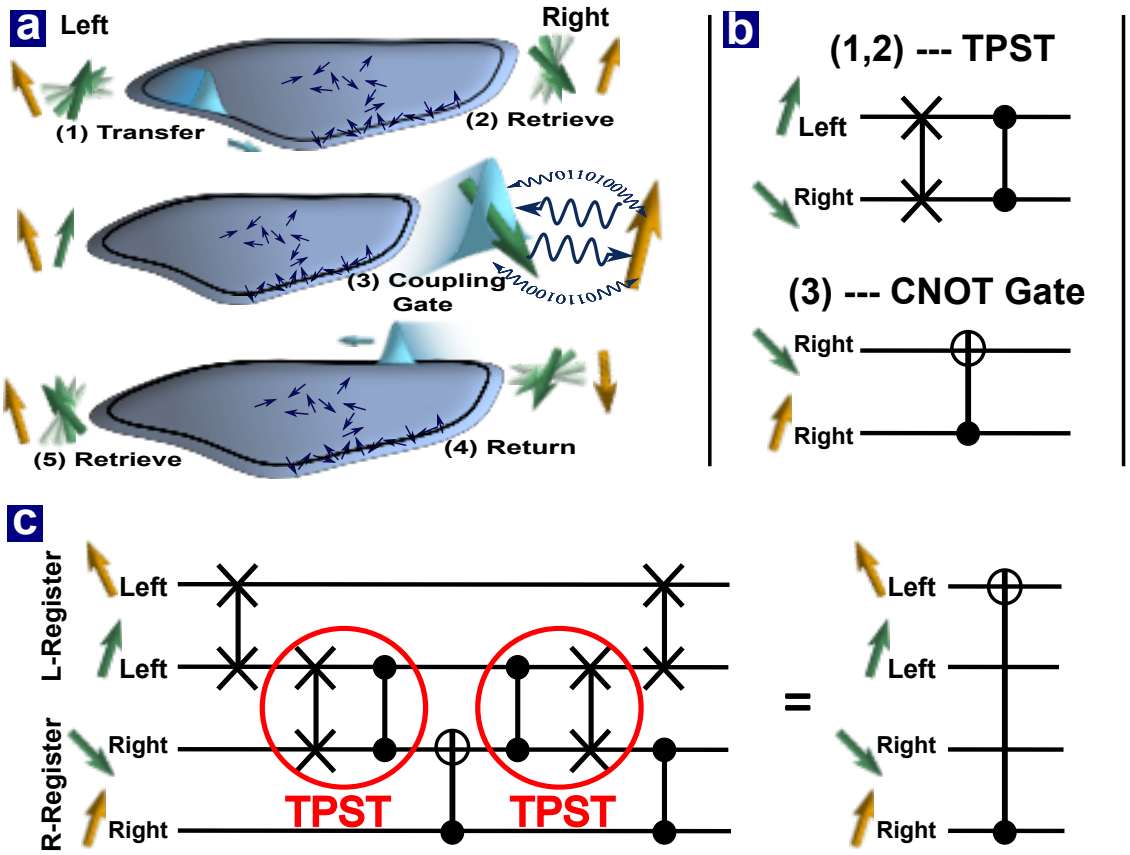

Figure 76: (a) The quantum registers L and R each contain two spins with the gold spin corresponding to the memory qubit. A single step of evolution SWAPs the information between the green spins of the left and right register. However, in addition to the SWAP gate, it also creates entanglement in the form of a controlled phase gate between these spins. To perform a remote CNOT gate between the memory qubits, we first perform an intra-register operation to SWAP the quantum information between the green and gold qubit of the left spin. (b) Next, the first step of TPST is performed (corresponding to a SWAP gate and a controlled phase gate). Afterwards, an intra-register CNOT gate between the green and gold qubit of the right register is performed. (c) The second step of TPST is then performed to return the information to the left register. Finally, intra-register gates are performed to yield a remote CNOT between the memory qubits. This enables universal computation.

where $\phi = \phi_{\tilde{k},a} - \phi_{\tilde{k},b}$. Using these relations to evolve the states from equation (D.6), we find

$$
\begin{aligned}
&||\uparrow\rangle\rangle_L |GS\rangle_0 ||\uparrow\rangle\rangle_R \longrightarrow ||\uparrow\rangle\rangle_L |GS'\rangle_0 ||\uparrow\rangle\rangle_R \\
&||\downarrow\rangle\rangle_L |GS\rangle_0 ||\uparrow\rangle\rangle_R \longrightarrow -ie^{-i\phi} ||\uparrow\rangle\rangle_L |GS'\rangle_0 ||\downarrow\rangle\rangle_R \\
&||\uparrow\rangle\rangle_L |GS\rangle_0 ||\downarrow\rangle\rangle_R \longrightarrow ie^{i\phi} ||\downarrow\rangle\rangle_L |GS'\rangle_0 ||\uparrow\rangle\rangle_R \\
&||\downarrow\rangle\rangle_L |GS\rangle_0 ||\downarrow\rangle\rangle_R \longrightarrow - ||\downarrow\rangle\rangle_L |GS'\rangle_0 ||\downarrow\rangle\rangle_R .
\end{aligned}
\tag{D.10}
$$

up to known dynamical phases. The time evolution presented above generates our desired SWAP gate in addition to a controlled phase gate between the register modes (up to single qubit rotations). Here $|GS'\rangle_0$ indicates a state which evolves from $|GS\rangle_0$ independent of the state of the two register qubits. As depicted in Fig. 76, in combination with intra-register manipulations, the gate described by equation (D.10) enables universal computation between the memory qubits of the remote spin registers.

This schematic evolution holds identically for any initial state of the intermediate system $|GS\rangle_0$ containing extra fermions or dangling vortices, since such states may be represented in a gauge sector where all bulk $U_{i,j} = 1$. Furthermore, in flux sectors in which there are an even number of bulk vortices, it is possible to choose a gauge in which $U_{i,j} = 1$ for all links near the edge. The evolution proceeds nearly identically in this case as well. On the other hand, in flux sectors where there are an odd number of bulk vortices, the energy of the edge modes is shifted by $\sim \kappa/L$ implying that the spin registers are off-resonant. This can be corrected for through tomography and subsequent retuning.

D.2 Shaping the Traveling Fermionic Wavepacket

Here, we describe the shaping of the fermionic wavepacket in the droplet regime of TPST. The edge mode energies ϵ_k of a finite-sized droplet are split at order $1/\ell$. As discussed in the main text, since single mode energy resolution becomes impossible in the macroscopic

limit, we encode the spin register's quantum information into a fermionic wavepacket traveling along the chiral edge of the 2D droplet. This requires the shaping of $g_L(t)$ and $g_R(t)$ in order to ensure the sending and receiving of the packet. Let us first consider the shaping of the initial wavepacket at the left register, so $g_R(t) = 0$. As described in Sec. IC, here, it is sufficient for us to consider the single particle problem since the modes evolve as usual non-interacting Dirac fermions. By tuning Δ_S to an energy in the middle of the edge dispersion and restricting $|g_L| \ll \Delta_S$, we have (assuming a plane wave description of the low energy chiral edge modes)

$$H_{wp} = \sum_k E_k |k\rangle\langle k| + \frac{g_L}{\sqrt{l}} \sum_k (|k\rangle\langle L| + |L\rangle\langle k|), \tag{D.11}$$

where $|k\rangle$ is the edge mode with momentum k, we have absorbed all numerical factors into g_L and $E_k = vk$ is shifted by Δ_S (here, we have correspondingly shifted the definition of zero energy and the indexing of k to begin at the state with energy Δ_S). We choose this notation for the Hamiltonian to be consistent with the literature regarding photonic wavepacket storage and retrieval, where an analogous problem is solved; thus, in this section, c_i, rather than being fermionic operators, will represent the amplitude of the $|i\rangle$ mode. Initially, we consider a state $|\psi\rangle$ whose amplitude is fully localized on the left spin register, $|\psi\rangle = c_L|L\rangle + \sum c_k|k\rangle$, where $c_L(t=0) = 1$ and $c_k(t=0) = 0$. After making a continuum approximation in both position and momentum, we formally solve the Schrödinger equation to obtain $\dot{c}_L(t) = -\frac{1}{2v}|g_L(t)|^2 c_L(t)$, yielding $c_L(t) = e^{h(t)}$ where $h(t) = \frac{1}{2v}\int_0^t dt' |g_L(t')|^2$. Substituting this result into the formal solution of $c_k(t)$ yields

$$c_k(t) = -i \int_0^t dt' e^{-ivk(t-t')} \frac{1}{\sqrt{l}} g_L(t') e^{-h(t')}. \tag{D.12}$$

Thus, the shape of the outgoing wavepacket is

$$c(x,t) = \frac{1}{\sqrt{l}}\sum_k e^{ikx}c_k(t) \approx \frac{\sqrt{l}}{2\pi}\int dk e^{ikx}c_k(t) = \frac{-i}{2\pi}\int dk e^{ikx}\int_0^t dt' e^{-ivk(t-t')}g_L(t')e^{-h(t')} \tag{D.13}$$

$$= -i\int_0^t dt'\delta(x - v(t-t'))g_L(t')e^{-h(t')} = -i\frac{1}{v}g_L(t-x/v)e^{-h(t-x/v)}\theta(t-x/v).$$

where θ is the Heaviside step function and we have assumed linear dispersion with group velocity v. Here, we note that in converting from a k sum to an integral, we have assumed that the amplitude on both $k < 0$ and bulk modes will be negligible since $|g_L| \ll \Delta_S$. As previously discussed, this assumption is crucial to ensure that the vacuum does not undergo time evolution.

It is natural to think of the wave-packet in the time domain and evaluate $c(x,t)$ at $x = 0$. Thus, the solution to the problem of shaping any desired wavepacket, $f(t)$, simplifies to deriving the requisite $g_L(t)$ control function that satisfies $\frac{1}{v}g_L(t)e^{-h(t)} = f(t)$ where $h(t) = \frac{1}{2v}\int_0^t dt'|g_L(t')|^2$; such a solution then yields,

$$g_L(t) = \frac{\sqrt{v}f(t)}{\sqrt{\int_t^\infty dt'|f(t')|^2}}. \tag{D.14}$$

The subsequent retrieval of the wave-packet at the location of the right spin register can be understood by using time-reversal; indeed, the control function $g_R(t)$ should be the time-reversed form of the control used to generate the time-reversed form of the sent wavepacket. While, for simplicity, we have considered $g_L, g_R \in \mathbb{R}$ above, generalizing to complex $g_{L/R}$ can easily be achieved, for example, by employing a Λ-configuration spin register.

D.3 The Edge — Injection and Interactions

There are two types of excitations on the edge: Majorana fermions and $\mathbb{Z}_2$ vortices. The topology of the bulk guarantees the existence of gapless chiral Majorana edge-modes, as described in a low energy theory by,

$$H_e = v \int dx \gamma(x)(i\partial)\gamma(x) \tag{D.15}$$

where $\gamma(x)$ is a continuum Majorana field and v is the group velocity. Generically all vortices are gapped; however, details of the lattice edge can lead to the existence of decoupled and/or low energy vortices. While the Hamiltonian (D.15) does not capture these degrees of freedom, the presence of these additional states in the low energy Hilbert space cannot be ignored. Indeed, the degeneracy of the exactly solved model follows from the presence of zero-energy dangling vortices formed by pairs of dangling Majoranas, as depicted in Fig. 75. Away from the injection point: 1) zero energy vortices are decoupled and hence irrelevant to TPST, 2) low energy vortices scatter only weakly, and 3) high energy vortices are suppressed by temperature. The presence of a low-energy vortex degree of freedom at the injection point is critical to enable spin-edge coupling, which occurs at a dangling spin. Crucially, this dangling spin contains a decoupled Majorana operator γ_a^3 (dangling Majorana), as shown in Fig. 75. Keeping track of this mode in the low-energy Hilbert space allows us to couple as follows,

$$H_c = v \int dx \gamma(x)(i\partial)\gamma(x) - \frac{\Delta_S}{2}\sigma^z + ig\sigma^x\gamma(0)\gamma_{decoupled}. \tag{D.16}$$

This is the continuum formulation of the microscopic coupling illustrated in the main text. To further elucidate the importance of the vortex degree of freedom at the injection point, we consider three possibilities. First, in the case when the dangling injection Majorana is completely decoupled, the injection vortex (corresponding to the flipped $U_{i,j}$ at the

injection point) is zero energy and the procedure for TPST remains identical. Second, in the case when the injection Majorana is weakly interacting with a single nearby Majorana (respecting the interaction symmetry), the injection vortex is low-energy. In this case, the splitting of the spin-register will need to be retuned to account for the creation of this low-energy vortex and TPST will then naturally create both a fermion and an injection vortex. Crucially, tunneling of the injection vortex into the bulk will be energetically disallowed since $\Delta_v^{injection} \ll \Delta_v^{bulk}$. Problems only arise in the third case, when the injection Majorana is interacting strongly (order κ) with a single nearby Majorana, and the injection vortex is hence high-energy. In this case, spin-edge coupling will create an injection vortex which can diffuse into the bulk; thus, upon the return of the traveling fermion, the injection vortex may no longer be localized near the injection point, causing dephasing when the quantum information is recaptured.

Next, we consider the role of interactions between edge modes. The fidelity of topological state transfer will be dependent on these interactions as they induce decay of the Majorana quasiparticles. Here, we begin by estimating the lifetime of such excitations in the continuum edge setting by taking into account the leading order interaction term. We consider, at $T = 0$, the situation where we tunnel a single quasiparticle excitation into the chiral edge from an associated spin register. The Hamiltonian is,

$$H = H_e + H_e' \tag{D.17}$$
$$H_e' = \lambda \int dx\, \gamma(x)(i\partial)\gamma(x)(i\partial)^2\gamma(x)(i\partial)^3\gamma(x).$$

To evaluate the interaction induced decay rate of the quasiparticles, we use Fermi's golden rule and consider the relevant interaction matrix elements coupling an incoming excitation $\gamma_p|\Omega\rangle$ with three outgoing (decayed) excitations $\gamma_{p_1}\gamma_{p_2}\gamma_{p_3}|\Omega\rangle$. The associated decay rate

takes the form,

$$\Gamma = 2\pi \int \frac{dp_1}{2\pi}\frac{dp_2}{2\pi}\frac{dp_3}{2\pi}|\langle\Omega|\gamma_{-p_1}\gamma_{-p_2}\gamma_{-p_3}H'_e\gamma_p|\Omega\rangle|^2\delta(\epsilon_p - \epsilon_{p_1} - \epsilon_{p_2} - \epsilon_{p_3}) \tag{D.18}$$

where the delta-function imposes energy conservation and the integrals are one dimensional because the quasiparticle is confined to the droplet edge. To evaluate the decay rate, we begin by considering the interaction matrix element,

$$M = \lambda \int \frac{dk_1}{2\pi}\frac{dk_2}{2\pi}\frac{dk_3}{2\pi}\frac{dk_4}{2\pi}k_2k_3^2k_4^3(2\pi)\delta(k_1+k_2+k_3+k_4)\langle\gamma_{-p_1}\gamma_{-p_2}\gamma_{-p_3}\gamma_{k_1}\gamma_{k_2}\gamma_{k_3}\gamma_{k_4}\gamma_p\rangle \tag{D.19}$$

where we have represented the interaction Hamiltonian in momentum space; by employing Wick's theorem, we can contract the matrix element into a function of two point Majorana correlators. The only terms from this contraction which contribute are connected terms of the form $\langle\gamma_{-p_1}\gamma_{k_1}\rangle\langle\gamma_{-p_2}\gamma_{k_2}\rangle\langle\gamma_{-p_3}\gamma_{k_3}\rangle\langle\gamma_{k_4}\gamma_p\rangle$ and such terms yield, $\Gamma \sim \lambda^2 p^{13}/v$. The leading order temperature correction in the limit $|vp| \gg kT$, is obtained from a Sommerfeld type expansion and yields,

$$\Gamma \sim \frac{\lambda^2 p^{13}}{v} + \frac{\lambda^2 p^{11}T^2}{v} + \mathcal{O}(T^4). \tag{D.20}$$

References

[1] A. M. Zagoskin, Quantum theory of many-body systems (Springer, 1998).

[2] S. Gopalakrishnan (private communication) (2014).

[3] D. Basko, I. Aleiner, B. Altshuler, Ann. Phys. 321, 1126 (2006).

[4] I. V. Gornyi, A. D. Mirlin, D. G. Polyakov, Phys. Rev. Lett. 95, 206603 (2005).

[5] V. Oganesyan, D. A. Huse, Phys. Rev. B 75, 155111 (2007).

[6] M. Žnidarič, T. Prosen, P. Prelovšek, Phys. Rev. B 77, 064426 (2008).

[7] C. Monthus, T. Garel, Phys. Rev. B 81, 134202 (2010).

[8] A. Pal, D. A. Huse, Phys. Rev. B 82, 174411 (2010).

[9] E. Cuevas, M. Feigel'man, L. Ioffe, M. Mezard, Nat. Commun. 3, 1128 (2012).

[10] J. H. Bardarson, F. Pollmann, J. E. Moore, Phys. Rev. Lett. 109, 017202 (2012).

[11] R. Vosk, E. Altman, Phys. Rev. Lett. 110, 067204 (2013).

[12] S. Iyer, V. Oganesyan, G. Refael, D. A. Huse, Phys. Rev. B 87, 134202 (2013).

[13] M. Serbyn, Z. Papić, D. A. Abanin, Phys. Rev. Lett. 110, 260601 (2013).

[14] M. Serbyn, Z. Papić, D. A. Abanin, Phys. Rev. Lett. 111, 127201 (2013).

[15] D. A. Huse, V. Oganesyan, arXiv preprint arXiv:1305.4915 (2013).

[16] D. A. Huse, R. Nandkishore, V. Oganesyan, A. Pal, S. Sondhi, Phys. Rev. B 88, 014206 (2013).

[17] B. Bauer, C. Nayak, J. Stat. Mech. Theor. Exp. 2013, P09005 (2013).

[18] B. Swingle, arXiv preprint arXiv:1307.0507 (2013).

[19] D. Pekker, G. Refael, E. Altman, E. Demler, V. Oganesyan, Phys. Rev. X 4, 011052 (2014).

[20] R. Vosk, E. Altman, arXiv preprint arXiv:1307.3256 (2013).

[21] Y. Bahri, R. Vosk, E. Altman, A. Vishwanath, arXiv preprint arXiv:1307.4092 (2013).

[22] A. Chandran, V. Khemani, C. R. Laumann, S. L. Sondhi, Phys. Rev. B 89, 144201 (2014).

[23] P. W. Anderson, Phys. Rev. 109, 1492 (1958).

[24] R. Roy, S. L. Sondhi, Physics 4, 46 (2011).

[25] S. Parameswaran, R. Roy, S. Sondhi, Phys. Rev. B 85, 241308 (2012).

[26] G. Möller, N. R. Cooper, Phys. Rev. Lett. 108, 045306 (2012).

[27] N. Regnault, B. A. Bernevig, Phys. Rev. X 1, 021014 (2011).

[28] D. Sheng, Z.-C. Gu, K. Sun, L. Sheng, Nat. Commun. 2, 389 (2011).

[29] Z. Liu, E. J. Bergholtz, H. Fan, A. M. Läuchli, Phys. Rev. Lett. 109, 186805 (2012).

[30] Y.-F. Wang, Z.-C. Gu, C.-D. Gong, D. Sheng, Phys. Rev. Lett. 107, 146803 (2011).

[31] J. McGreevy, B. Swingle, K.-A. Tran, Phys. Rev. B 85, 125105 (2012).

[32] D. C. Tsui, H. L. Stormer, A. C. Gossard, Phys. Rev. Lett. 48, 1559 (1982).

[33] R. B. Laughlin, Phys. Rev. Lett. 50, 1395 (1983).

[34] M. Ruderman, C. Kittel, Phys. Rev. 96, 99 (1954).

[35] T. Kasuya, Prog. Theor. Phys. 16, 45 (1956).

[36] K. Yosida, Phys. Rev. 106, 893 (1957).

[37] L. Yu, Acta Phys. Sin. 21, 75 (1965).

[38] H. Shiba, Progr. Theor. Phys. 40, 435 (1968).

[39] A. I. Rusinov, Sov. Phys. JETP 29, 1101 (1969).

[40] D. Loss, D. P. DiVincenzo, Phys. Rev. A 57, 120 (1998).

[41] L.-M. Duan, B. B. Blinov, D. L. Moehring, C. Monroe, Quantum Info. Comput. 4, 165 (2004).

[42] S. C. Benjamin, D. E. Browne, J. Fitzsimons, J. J. Morton, New J. Phys. 8, 141 (2006).

[43] Y. Makhlin, G. Schön, A. Shnirman, Rev. Mod. Phys. 73, 357 (2001).

[44] L. Childress, J. M. Taylor, A. S. S rensen, M. D. Lukin, Phys. Rev. Lett. 96, 070504 (2006).

[45] G. Balasubramanian, et al., Nature Mater. 8, 383 (2009).

[46] J. R. Weber, et al., Proc. Natl. Acad. Sci. 107, 8513 (2010).

[47] G. D. Fuchs, et al., Nature Phys. 6, 668 (2010).

[48] P. Cappellaro, L. Jiang, J. Hodges, M. Lukin, Phys. Rev. Lett. 102, 210502 (2009).

[49] L. Fleishman, P. Anderson, Phys. Rev. B 21, 2366 (1980).

[50] B. L. Altshuler, Y. Gefen, A. Kamenev, L. S. Levitov, Phys. Rev. Lett. 78, 2803 (1997).

[51] A. L. Burin, arXiv preprint cond-mat/0611387 (2006).

[52] M. Schiulaz, M. Müller, arXiv preprint arXiv:1309.1082 (2013).

[53] S. Korenblit, et al., New J. Phys. 14, 095024 (2012).

[54] I. Ryabtsev, D. Tretyakov, I. Beterov, V. Entin, Phys. Rev. Lett. 104, 073003 (2010).

[55] J. Nipper, et al., Phys. Rev. Lett. 108, 113001 (2012).

[56] M. De Miranda, et al., Nature Phys. 7, 502 (2011).

[57] K.-K. Ni, et al., Science 322, 231 (2008).

[58] P. Neumann, et al., Nature Phys. 6, 249 (2010).

[59] M. V. G. Dutt, et al., Science 316, 1312 (2007).

[60] P. Neumann, et al., Science 320, 1326 (2008).

[61] L. Levitov, Phys. Rev. Lett. 64, 547 (1990).

[62] L. Levitov, Ann. Phys. 8, 697 (1999).

[63] A. Burin, I. Y. Polishchuk, arXiv preprint arXiv:0707.2596 (2007).

[64] M. White, et al., Phys. Rev. Lett. 102, 055301 (2009).

[65] J. M. Brown, A. Carrington, Rotational spectroscopy of diatomic molecules (Cambridge University Press, 2003).

[66] B. Yan, et al., Nature 501, 521 (2013).

[67] A. Chotia, et al., Phys. Rev. Lett. 108, 080405 (2012).

[68] J. Deiglmayr, et al., Phys. Rev. Lett. 101, 133004 (2008).

[69] K. Aikawa, et al., Phys. Rev. Lett. 105, 203001 (2010).

[70] A. J. Kerman, J. M. Sage, S. Sainis, T. Bergeman, D. DeMille, Phys. Rev. Lett. 92, 153001 (2004).

[71] T. Takekoshi, et al., Phys. Rev. A 85, 032506 (2012).

[72] N. Bar-Gill, L. M. Pham, A. Jarmola, D. Budker, R. L. Walsworth, Nat. Commun. 4, 1743 (2013).

[73] T. M. Babinec, et al., Nature Nanotech. 5, 195 (2010).

[74] P. Spinicelli, et al., New J. Phys. 13, 025014 (2011).

[75] D. M. Toyli, C. D. Weis, G. D. Fuchs, T. Schenkel, D. D. Awschalom, Nano Lett. 10, 3168 (2010).

[76] L. M. K. Vandersypen, I. L. Chuang, Rev. Mod. Phys. 76, 1037 (2005).

[77] O. Mandel, et al., Phys. Rev. Lett. 91, 010407 (2003).

[78] J. Guzman, et al., Phys. Rev. A 84, 063625 (2011).

[79] M. Knap, et al., Phys. Rev. X 2, 041020 (2012).

[80] M. Knap, et al., Phys. Rev. Lett. 111, 147205 (2013).

[81] P.-K. Wang, C. P. Slichter, J. H. Sinfelt, Phys. Rev. Lett. 53, 82 (1984).

[82] A. Milov, A. Ponomarev, Y. Tsvetkov, Chem. Phys. Lett. 110, 67 (1984).

[83] R. G. Larsen, D. J. Singel, J. Chem. Phys. 98, 5134 (1993).

[84] M. Pasienski, D. McKay, M. White, B. DeMarco, Nature Phys. 6, 677 (2010).

[85] C. D'Errico, et al., New J. Phys. 15, 045007 (2013).

[86] N. Strohmaier, et al., Phys. Rev. Lett. 104, 080401 (2010).

[87] S. Trotzky, et al., Science 319, 295 (2008).

[88] T. Fukuhara, et al., Nature Phys. 9, 235 (2013).

[89] N. Y. Yao, et al., arXiv preprint arXiv:1311.7151 (2013).

[90] K. Sun, Z. Gu, H. Katsura, S. D. Sarma, Phys. Rev. Lett. 106, 236803 (2011).

[91] E. Tang, J.-W. Mei, X.-G. Wen, Phys. Rev. Lett. 106, 236802 (2011).

[92] T. Neupert, L. Santos, C. Chamon, C. Mudry, Phys. Rev. Lett. 106, 236804 (2011).

[93] M. Trescher, E. J. Bergholtz, Phys. Rev. B 86, 241111 (2012).

[94] S. Yang, Z.-C. Gu, K. Sun, S. D. Sarma, Phys. Rev. B 86, 241112 (2012).

[95] Y.-F. Wang, H. Yao, C.-D. Gong, D. Sheng, Phys. Rev. B 86, 201101 (2012).

[96] A. Micheli, G. Brennen, P. Zoller, Nature Phys. 2, 341 (2006).

[97] A. Micheli, G. Pupillo, H. P. Büchler, P. Zoller, Phys. Rev. A 76, 043604 (2007).

[98] J. Aldegunde, B. A. Rivington, P. S. Żuchowski, J. M. Hutson, Phys. Rev. A 78, 033434 (2008).

[99] A. V. Gorshkov, et al., Phys. Rev. Lett. 107, 115301 (2011).

[100] H. Schempp, et al., Phys. Rev. Lett. 104, 173602 (2010).

[101] J. Pritchard, et al., Phys. Rev. Lett. 105, 193603 (2010).

[102] L. Tagliacozzo, A. Celi, A. Zamora, M. Lewenstein, Ann. Phys. 330, 160 (2013).

[103] M. Lu, S. H. Youn, B. L. Lev, Phys. Rev. Lett. 104, 063001 (2010).

[104] D. R. Hofstadter, Phys. Rev. B 14, 2239 (1976).

[105] N. R. Cooper, Phys. Rev. Lett. 106, 175301 (2011).

[106] Y.-J. Lin, et al., Nature Phys. 7, 531 (2011).

[107] J. Dalibard, F. Gerbier, G. Juzeliūnas, P. Öhberg, Rev. Mod. Phys. 83, 1523 (2011).

[108] G. Juzeliūnas, J. Ruseckas, P. Öhberg, M. Fleischhauer, Phys. Rev. A 73, 025602 (2006).

[109] J. Abo-Shaeer, C. Raman, J. Vogels, W. Ketterle, Science 292, 476 (2001).

[110] I. Spielman, Phys. Rev. A 79, 063613 (2009).

[111] D. Thouless, M. Kohmoto, M. Nightingale, M. Den Nijs, Phys. Rev. Lett. 49, 405 (1982).

[112] Y. Hatsugai, Phys. Rev. Lett. 71, 3697 (1993).

[113] P. C. Maurer, et al., Science 336, 1283 (2012).

[114] J. Dalibard, C. Cohen-Tannoudji, J. Opt. Soc. Am. B 6, 2023 (1989).

[115] N. Y. Yao, et al., Phys. Rev. Lett. 110, 185302 (2013).

[116] N. Y. Yao, et al., Phys. Rev. Lett. 106, 040505 (2011).

[117] D. A. Abanin, T. Kitagawa, I. Bloch, E. Demler, Phys. Rev. Lett. 110, 165304 (2013).

[118] A. S. Sørensen, et al., Phys. Rev. A 81, 061603 (2010).

[119] X.-G. Wen, Phys. Rev. B 65, 165113 (2002).

[120] A. M. Essin, M. Hermele, Phys. Rev. B 87, 104406 (2013).

[121] V. Kalmeyer, R. Laughlin, Phys. Rev. Lett. 59, 2095 (1987).

[122] V. Kalmeyer, R. B. Laughlin, Phys. Rev. B 39, 11879 (1989).

[123] A. E. Nielsen, J. I. Cirac, G. Sierra, Phys. Rev. Lett. 108, 257206 (2012).

[124] I. Spielman, Physics 4, 35 (2011).

[125] D. Wang, et al., Phys. Rev. A 81, 061404 (2010).

[126] S. Ospelkaus, et al., Phys. Rev. Lett. 104, 030402 (2010).

[127] S. R. Manmana, E. Stoudenmire, K. R. Hazzard, A. M. Rey, A. V. Gorshkov, Phys. Rev. B 87, 081106 (2013).

[128] E. Andrew, A. Bradbury, R. Eades, Nature 182, 1659 (1958).

[129] B. A. Bernevig, N. Regnault, Phys. Rev. B 85, 075128 (2012).

[130] M. Greiter, R. Thomale, Phys. Rev. Lett. 102, 207203 (2009).

[131] M. Barkeshli, J. McGreevy, arXiv preprint arXiv:1201.4393 (2012).

[132] N. Goldman, J. Beugnon, F. Gerbier, Phys. Rev. Lett. 108, 255303 (2012).

[133] J. A. Kjäll, J. E. Moore, Phys. Rev. B 85, 235137 (2012).

[134] H. Guo, C.-C. Chien, K. Levin, Phys. Rev. Lett. 105, 120401 (2010).

[135] C.-H. Wu, J. W. Park, P. Ahmadi, S. Will, M. W. Zwierlein, Phys. Rev. Lett. 109, 085301 (2012).

[136] S. Kotochigova, E. Tiesinga, Phys. Rev. A 73, 041405 (2006).

[137] J. H. V. Vleck, Rev. Mod. Phys. 34, 681 (1962).

[138] A. V. Balatsky, I. Vekhter, J.-X. Zhu, Rev. Mod. Phys. 78, 373 (2006).

[139] M. N. Baibich, et al., Phys. Rev. Lett. 61, 2472 (1988).

[140] G. Binasch, P. Grünberg, F. Saurenbach, W. Zinn, Phys. Rev. B 39, 4828 (1989).

[141] C. P. Moca, E. Demler, B. Jankó, G. Zaránd, Phys. Rev. B 77, 174516 (2008).

[142] D. Poilblanc, D. J. Scalapino, W. Hanke, Phys. Rev. Lett. 72, 884 (1994).

[143] M. E. Flatté, J. M. Byers, Phys. Rev. B 56, 11213 (1997).

[144] M. E. Flatté, J. M. Byers, Phys. Rev. Lett. 78, 3761 (1997).

[145] M. E. Flatté, D. E. Reynolds, Phys. Rev. B 61, 14810 (2000).

[146] A. V. Balatsky, M. I. Salkola, A. Rosengren, Phys. Rev. B 51, 15547 (1995).

[147] M. I. Salkola, A. V. Balatsky, J. R. Schrieffer, Phys. Rev. B 55, 12648 (1997).

[148] S. H. Pan, et al., Nature 403, 746 (2000).

[149] Y. V. Fominov, M. Houzet, L. I. Glazman, Phys. Rev. B 84, 224517 (2011).

[150] A. Yazdani, B. A. Jones, C. P. Lutz, M. F. Crommie, D. M. Eigler, Science 275, 1767 (1997).

[151] S.-H. Ji, et al., Phys. Rev. Lett. 100, 226801 (2008).

[152] M. Iavarone, et al., J. Phys.: Condens. Matter 22(1), 015501 (2010).

[153] L. Faoro, L. B. Ioffe, Phys. Rev. Lett. 100, 227005 (2008).

[154] S. Sendelbach, et al., Phys. Rev. Lett. 100, 227006 (2008).

[155] V. Galitski, A. Larkin, Phys. Rev. B 66, 064526 (2002).

[156] D. Aristov, S. Maleyev, A. Yashenkin, Z. Phys. B Con. Mat. 102, 467 (1997).

[157] A. A. Abrikosov (1988).

[158] W. Chung, M. Jarrell, Phys. Rev. Lett. 77, 3621 (1996).

[159] R. Bulla, T. A. Costi, T. Pruschke, Rev. Mod. Phys. 80, 395 (2008).

[160] K. Satori, H. Shiba, O. Sakai, Y. Shimizu, J. Phys. Soc. Jpn. 61, 3239 (1992).

[161] O. Sakai, Y. Shimizu, H. Shiba, K. Satori, J. Phys. Soc. Jpn. 62, 3181 (1993).

[162] J. R. Schrieffer, Theory of Superconductivity (Advanced Book Program, Perseus Books, 1999).

[163] R. J. Donnelly, Cryogenics (Physics Vade Mecum, AIP, 1981).

[164] X.-D. Chen, et al., Appl. Phys. Lett. 99, 161903 (2011).

[165] H. B. Heersche, P. Jarillo-Herrero, J. B. Oostinga, L. M. Vandersypen, A. F. Morpurgo, Nature 446, 56 (2007).

[166] K. F. Mak, C. Lee, J. Hone, J. Shan, T. F. Heinz, Physical Review Letters 105, 136805 (2010).

[167] B. Radisavljevic, A. Radenovic, J. Brivio, V. Giacometti, A. Kis, Nature Nanotech. 6, 147 (2011).

[168] A. Hewson, The Kondo Problem to Heavy Fermions (Cambridge University Press, New York, N.Y., 1993).

[169] P. Nozieres, J. Low Temp. Phys. 17, 31 (1974).

[170] H. Tsunetsugu, M. Sigrist, K. Ueda, Rev. Mod. Phys. 69, 809 (1997).

[171] S. Doniach, Physica B+C 91, 231 (1977).

[172] B. A. Jones, C. M. Varma, Phys. Rev. Lett. 58, 843 (1987).

[173] I. Affleck, A. W. W. Ludwig, Phys. Rev. Lett. 68, 1046 (1992).

[174] T. Hecht, A. Weichselbaum, J. von Delft, R. Bulla, J. Phys.: Condens. Matter 20, 275213 (2008).

[175] T. Meng, S. Florens, P. Simon, Phys. Rev. B 79, 224521 (2009).

[176] P. Stadler, C. Holmqvist, W. Belzig, Phys. Rev. B 88, 104512 (2013).

[177] J. Bauer, A. Oguri, A. C. Hewson, J. Phys.: Condens. Matter 19, 486211 (2007).

[178] R. Žitko, O. Bodensiek, T. Pruschke, Phys. Rev. B 83, 054512 (2011).

[179] R. S. Deacon, et al., Phys. Rev. Lett. 104, 076805 (2010).

[180] L. Hofstetter, S. Csonka, J. Nygard, C. Schonenberger, Nature 461, 960 (2009).

[181] L. G. Herrmann, et al., Phys. Rev. Lett. 104, 026801 (2010).

[182] F. H. L. Essler, H. Frahm, F. G hmann, A. Kl mper, V. E. Korepin, The One-Dimensional Hubbard Model (Cambridge University Press, 2005).

[183] N. Y. Yao, L. I. Glazman, E. A. Demler, M. D. Lukin, J. D. Sau, arXiv:1309.2633v1 (2013).

[184] F. Pientka, L. I. Glazman, F. von Oppen, Phys. Rev. B 88, 155420 (2013).

[185] S.-H. Ji, et al., Appl. Phys. Lett. 96, 073113 (2010).

[186] C. H. Bennett, et al., Phys. Rev. Lett. 70, 1895 (1993).

[187] N. Gisin, G. Ribordy, W. Tittel, H. Zbinden, Rev. Mod. Phys. 74, 145 (2002).

[188] S. Lloyd, Science 261, 1569 (1993).

[189] A. D. Greentree, J. H. Cole, A. Hamilton, L. C. Hollenberg, Phys. Rev. B 70, 235317 (2004).

[190] B. B. Blinov, D. L. Moehring, L.-M. Duan, C. Monroe, Nature 428, 153 (2004).

[191] D. Moehring, et al., Nature 449, 68 (2007).

[192] E. Togan, et al., Nature 466, 730 (2010).

[193] D. Kielpinski, C. Monroe, D. J. Wineland, Nature 417, 709 (2002).

[194] S. Bose, Phys. Rev. Lett. 91, 207901 (2003).

[195] D. Petrosyan, G. M. Nikolopoulos, P. Lambropoulos, Phys. Rev. A 81, 042307 (2010).

[196] M. Christandl, N. Datta, A. Ekert, A. J. Landahl, Phys. Rev. Lett. 92, 187902 (2004).

[197] D. Burgarth, V. Giovannetti, S. Bose, Phys. Rev. A 75, 062327 (2007).

[198] M.-H. Yung, S. Bose, Phys. Rev. A 71, 032310 (2005).

[199] C. Di Franco, M. Paternostro, M. Kim, Phys. Rev. Lett. 101, 230502 (2008).

[200] A. Kay, Phys. Rev. Lett. 98, 010501 (2007).

[201] E. Fel dman, E. Kuznetsova, A. Zenchuk, Phys. Rev. A 82, 022332 (2010).

[202] S. Clark, C. M. Alves, D. Jaksch, New J. Phys. 7, 124 (2005).

[203] L. C. Venuti, S. Giampaolo, F. Illuminati, P. Zanardi, Phys. Rev. A 76, 052328 (2007).

[204] G. Gualdi, V. Kostak, I. Marzoli, P. Tombesi, Phys. Rev. A 78, 022325 (2008).

[205] M. Paternostro, G. Palma, M. Kim, G. Falci, Phys. Rev. A 71, 042311 (2005).

[206] D. Tsomokos, M. Hartmann, S. Huelga, M. Plenio, New J. Phys. 9, 79 (2007).

[207] A. Wójcik, et al., Phys. Rev. A 72, 034303 (2005).

[208] L. Banchi, T. J. G. Apollaro, A. Cuccoli, R. Vaia, P. Verrucchi, Phys. Rev. A 82, 052321 (2010).

[209] J. Gong, P. Brumer, Phys. Rev. A 75, 032331 (2007).

[210] N. Y. Yao, et al., Nature Commun. 3 (2012).

[211] V. S. Malinovsky, D. J. Tannor, Phys. Rev. A 56, 4929 (1997).

[212] E. Fel'Dman, A. Zenchuk, Phys. Lett. A 373, 1719 (2009).

[213] P. Karbach, J. Stolze, Phys. Rev. A 72, 030301 (2005).

[214] P. Cappellaro, C. Ramanathan, D. G. Cory, Phys. Rev. Lett. 99, 250506 (2007).

[215] J. Zhang, et al., Phys. Rev. A 80, 012316 (2009).

[216] J. Fitzsimons, J. Twamley, Phys. Rev. Lett. 97, 090502 (2006).

[217] M. Stoneham, Physics 2, 34 (2009).

[218] F. Evers, A. D. Mirlin, Rev. Mod. Phys. 80, 1355 (2008).

[219] E. Lieb, T. Schultz, D. Mattis, Ann. Phys. 16, 407 (1961).

[220] A. V. Gorshkov, J. Otterbach, E. Demler, M. Fleischhauer, M. D. Lukin, Phys. Rev. Lett. 105, 060502 (2010).

[221] M. Markiewicz, M. Wieśniak, Phys. Rev. A 79, 054304 (2009).

[222] M. A. Nielsen, Phys. Lett. A 303, 249 (2002).

[223] E. H. Lieb, D. W. Robinson, Commun. Math. Phys. 28, 251 (1972).

[224] Y. Zou, R. Barnett, G. Refael, Phys. Rev. B 82, 224205 (2010).

[225] D. Burgarth, K. Maruyama, F. Nori, Phys. Rev. A 79, 020305 (2009).

[226] E. Rittweger, K. Y. Han, S. E. Irvine, C. Eggeling, S. W. Hell, Nature Photon. 3, 144 (2009).

[227] P. C. Maurer, et al., Nature Phys. 6, 912 (2010).

[228] A. G. Fowler, A. M. Stephens, P. Groszkowski, Phys. Rev. A 80, 052312 (2009).

[229] D. S. Wang, A. G. Fowler, L. C. Hollenberg, Phys. Rev. A 83, 020302 (2011).

[230] A. Zwick, G. A. Álvarez, J. Stolze, O. Osenda, Phys. Rev. A 85, 012318 (2012).

[231] L. Banchi, A. Bayat, P. Verrucchi, S. Bose, Phys. Rev. Lett. 106, 140501 (2011).

[232] L. Banchi, T. J. G. Apollaro, A. Cuccoli, R. Vaia, P. Verrucchi, New. J. Phys. 13, 123006 (2011).

[233] J. Fitzsimons, L. Xiao, S. C. Benjamin, J. A. Jones, Phys. Rev. Lett. 99, 030501 (2007).

[234] K. Kim, et al., New J. Phys. 13, 105003 (2011).

[235] S. Mostame, R. Schützhold, Phys. Rev. Lett. 101, 220501 (2008).

[236] P. Jordan, E. Wigner, Z. Physik 47, 631 (1928).

[237] A. Y. Kitaev, Phys.-Usp. 44, 131 (2001).

[238] C. Nayak, S. H. Simon, A. Stern, M. Freedman, S. Das Sarma, Rev. Mod. Phys. 80, 1083 (2008).

[239] P. Cappellaro, L. Viola, C. Ramanathan, Phys. Rev. A 83, 032304 (2011).

[240] C. Ogden, E. Irish, M. Kim, Phys. Rev. A 78, 063805 (2008).

[241] S. Bose, D. G. Angelakis, D. Burgarth, J. Mod. Opt. 54, 2307 (2007).

[242] G. de Moraes Neto, M. de Ponte, M. Moussa, Phys. Rev. A 84, 032339 (2011).

[243] S.-B. Shim, M. Imboden, P. Mohanty, Science 316, 95 (2007).

[244] K. Brown, et al., Nature 471, 196 (2011).

[245] F. Cataliotti, et al., Science 293, 843 (2001).

[246] S. Teitel, C. Jayaprakash, Phys. Rev. Lett. 51, 1999 (1983).

[247] A. H. Safavi-Naeini, et al., Nature 472, 69 (2011).

[248] T. D. Ladd, et al., Nature 464, 45 (2010).

[249] D. Burgarth, Eur. Phys. J. Spec. Top. 151, 147 (2007).

[250] A. Zwick, O. Osenda, J. Phys. A: Mathematical and Theoretical 44, 105302 (2011).

[251] A. Jarmola, V. M. Acosta, K. Jensen, S. Chemerisov, D. Budker, Phys. Rev. Lett. 108, 197601 (2012).

[252] H. Weimer, R. Löw, T. Pfau, H. P. Büchler, Phys. Rev. Lett. 101, 250601 (2008).

[253] T. Pohl, E. Demler, M. Lukin, Phys. Rev. Lett. 104, 043002 (2010).

[254] J. Schachenmayer, I. Lesanovsky, A. Micheli, A. Daley, New J. Phys. 12, 103044 (2010).

[255] R. van Bijnen, S. Smit, K. van Leeuwen, E. Vredenbregt, S. Kokkelmans, J. Phys. B 44, 184008 (2011).

[256] P. Neumann, et al., Science 329, 542 (2010).

[257] H. Weimer, H. P. Büchler, Phys. Rev. Lett. 105, 230403 (2010).

[258] E. Sela, M. Punk, M. Garst, Phys. Rev. B 84, 085434 (2011).

[259] J. Roland, N. J. Cerf, Phys. Rev. A 65, 042308 (2002).

[260] Q. Quan, P. Deotare, M. Loncar, Appl. Phys. Lett. 96, 203102 (2010).

[261] M. Saffman, T. Walker, K. Mølmer, Rev. Mod. Phys. 82, 2313 (2010).

[262] G. de Lange, Z. H. Wang, D. Rist , V. V. Dobrovitski, R. Hanson, Science 330, 60 (2010).

[263] S. Inouye, et al., Science 285, 571 (1999).

[264] R. Heidemann, et al., Phys. Rev. Lett. 99, 163601 (2007).

[265] A. Gaëtan, et al., Nature Phys. 5, 115 (2009).

[266] E. Urban, et al., Nature Phys. 5, 110 (2009).

[267] F. Brennecke, et al., Nature 450, 268 (2007).

[268] Y. Colombe, et al., Nature 450, 272 (2007).

[269] M. Bartenstein, et al., Phys. Rev. Lett. 92, 203201 (2004).

[270] J. Simon, H. Tanji, J. K. Thompson, V. Vuletić, Phys. Rev. Lett. 98, 183601 (2007).

[271] X. Zhu, et al., Nature 478, 221 (2011).

[272] W. F. Koehl, B. B. Buckley, F. J. Heremans, G. Calusine, D. D. Awschalom, Nature 479, 84 (2011).

[273] J. J. Pla, et al., Nature p. doi:10.1038/nature11449 (2012).

[274] T. Chanier, C. Pryor, M. E. Flatté, arXiv:1112.4436 (2011).

[275] F. Jelezko, T. Gaebel, I. Popa, A. Gruber, J. Wrachtrup, Phys. Rev. Lett. 92, 076401 (2004).

[276] A. Bermudez, F. Jelezko, M. B. Plenio, A. Retzker, Phys. Rev. Lett. 107, 150503 (2011).

[277] H. Weimer, N. Y. Yao, C. R. Laumann, M. D. Lukin, Phys. Rev. Lett. 108, 100501 (2012).

[278] J. F. Sherson, et al., Nature p. doi:10.1038/nature05136 (2006).

[279] D. Jaksch, et al., Phys. Rev. Lett. 85, 2208 (2000).

[280] M. D. Lukin, et al., Phys. Rev. Lett. 87, 037901 (2001).

[281] B. J. M. Hausmann, et al., CLEO/QELS 2011 (2011).

[282] J. Isoya (private communication).

[283] D. A. Redman, S. Brown, R. H. Sands, S. C. Rand, Phys. Rev. Lett. 67, 3420 (1991).

[284] J. Harrison, M. Sellars, N. Manson, Diam. Relat. Mater. 15, 586 (2006).

[285] S. Takahashi, R. Hanson, J. van Tol, M. S. Sherwin, D. D. Awschalom, Phys. Rev. Lett. 101, 047601 (2008).

[286] J. S. Waugh, L. M. Huber, U. Haeberlen, Phys. Rev. Lett. 20, 180 (1968).

[287] J. R. Maze, et al., Nature 455, 644 (2008).

[288] S. Felton, et al., Phys. Rev. B 79, 075203 (2009).

[289] R. Raussendorf, J. Harrington, Phys. Rev. Lett. 98, 190504 (2007).

[290] L. Jiang, J. M. Taylor, A. S. Sørensen, M. D. Lukin, Phys. Rev. A 76, 062323 (2007).

[291] B. E. Kane, Fortschr. Phys - Prog. Phys. 48(9-11), 1023 (2000).

[292] R. J. Epstein, F. M. Mendoza, Y. K. Kato, D. D. Awschalom, Nature Phys. 1, 94 (2005).

[293] G. Balasubramanian, et al., Nature 455, 648 (2008).

[294] L. Jiang, et al., Phys. Rev. Lett. 100, 073001 (2008).

[295] L. Jiang, et al., Science 326, 267 (2009).

[296] A. Tallaire, et al., Diam. Relat. Mater. 15, 1700 (2006).

[297] E. Reynhardt, G. High, J. Van Wyk, J. Chem. Phys. 109, 8471 (1998).

[298] S. Haroche, J.-M. Raimond, Exploring the quantum: atoms, cavities, and photons (oxford graduate texts) (Oxford University Press, USA, 2013).

[299] W. M. Itano, D. J. Heinzen, J. Bollinger, D. Wineland, Physical Review A 41, 2295 (1990).

[300] H. Lee, Y. Liu, D. Ham, R. M. Westervelt, Lab Chip 7, 331 (2007).

[301] L. Balents, M. P. Fisher, Phys. Rev. B 56, 12970 (1997).

[302] J. Loubser, W. Van Ryneveld, British J. Appl. Phys. 18, 1029 (1967).

[303] C. Kedkaew, P. Limsuwan, K. Thongcham, S. Meejoo, Intl. J. Mod. Phys. B 22, 4740 (2008).

[304] T. Caneva, et al., Phys. Rev. Lett. 103, 240501 (2009).

[305] A. Messiah, Quantum mechanics (1962).

[306] S. B. Bravyi, A. Y. Kitaev, Quantum Computers and Computing 2, 43 (2001).

[307] N. C. Jones, et al., Phys. Rev. X 2, 031007 (2012).

[308] N. Khaneja, R. Brockett, S. J. Glaser, Phys. Rev. A 63, 032308 (2001).

[309] H. Yuan, R. Zeier, N. Khaneja, Phys. Rev. A 77, 032340 (2008).

[310] M. Grace, et al., J. Phys. B 40, S103 (2007).

[311] P. Rabl, et al., Phys. Rev. B 79, 041302 (2009).

[312] I. L. Chuang, R. Laflamme, P. W. Shor, W. H. Zurek, Science 270, 1633 (1995).

[313] M. A. Nielsen, I. L. Chuang, Quantum Computation and Quantum Information. (Cambridge University Press: New York, 2000).

[314] H.-J. Briegel, W. Dür, J. I. Cirac, P. Zoller, Phys. Rev. Lett. 81, 5932 (1998).

[315] H. J. Kimble, Nature 453, 1023 (2008).

[316] J. Preskill, Proc. Roy. Soc. Lond. A 454, 385 (1998).

[317] D. Gottesman, Phys. Rev. A 57, 127 137 (1998).

[318] E. Dennis, A. Kitaev, A. Landahl, Preskill, J. Math. Phys. 43, 4452 (2002).

[319] A. Y. Kitaev, Annals Phys. 303, 2 (2003).

[320] L. B. Ioffe, M. V. Feigel'man, Phys. Rev. B 66, 224503 (2002).

[321] S. Das Sarma, M. Freedman, C. Nayak, Phys. Today 7, 32 (2006).

[322] J. J. Morton, et al., Nature 455, 1085 (2008).

[323] Z. Kurucz, M. W. Sørensen, J. M. Taylor, M. D. Lukin, M. Fleischhauer, Physical review letters 103, 010502 (2009).

[324] J. Taylor, et al., Nature Physics 1, 177 (2005).

[325] A. Kitaev, Ann. of Phys. 321, 2 (2006).

[326] M. Hermele, V. Gurarie, A. M. Rey, Phys. Rev. Lett. 103, 135301 (2009).

[327] H. Yao, S. A. Kivelson, Phys. Rev. Lett. 99, 247203 (2007).

[328] M. Kohmoto, Y. Hasegawa, Phys. Rev. B 76, 205402 (2007).

[329] T. J. Osborne, N. Linden, Phys. Rev. A 69, 052315 (2004).

[330] M. Lukin, S. Yelin, M. Fleischhauer, Phys. Rev. Lett. 84, 4232 (2000).

[331] A. V. Gorshkov, A. André, M. D. Lukin, A. S. Sørensen, Phys. Rev. A 76, 033804 (2007).

[332] P. Fendley, M. Fisher, C. Nayak, Ann. Phys. 324, 1547 (2009).

[333] K.-M. C. Fu, et al., Phys. Rev. Lett. 330, 60 (2009).

[334] J. Taylor, M. Lukin, Quantum Inf. Processing 5, 503 (2006).

[335] L.-M. Duan, E. Demler, M. Lukin, Phys. Rev. Lett. 91, 090402 (2003).

[336] C. Zhang, V. Scarola, S. Tewari, S. D. Sarma, Proc. Natl. Acad. Sci. 104, 18415 (2007).

[337] S. Sugawa, et al., Nature Phys. 7, 642 (2011).

[338] H. Büchler, A. Micheli, P. Zoller, Nature Phys. 3, 726 (2007).

[339] S. Gladchenko, et al., Nature Phys. 5, 48 (2009).

[340] J. Q. You, X.-F. Shi, X. Hu, F. Nori, Phys. Rev. B 81, 014505 (2010).

[341] I. Buluta, F. Nori, Science 326, 108 (2009).

[342] W.-B. Gao, et al., Nature Phys. 6, 331 (2010).

[343] M. Johnson, et al., Nature 473, 194 (2011).

[344] R. Islam, et al., Nat. Commun. 2, 377 (2011).

[345] T. Monz, et al., Phys. Rev. Lett. 106, 130506 (2011).

[346] C. L. Lee, E. Gu, M. D. Dawson, I. Friel, G. A. Scarsbrook, Diam. Relat. Mater. 17, 1292 (2008).

[347] L. Balents, Nature 464, 199 (2010).

[348] Y. Machida, S. Nakatsuji, S. Onoda, T. Tayama, T. Sakakibara, Nature 463, 210 (2010).

[349] S. Wiesner, ACM SIGACT News 15, 78 (1983).

[350] W. K. Wootters, W. H. Zurek, Nature 299, 802 (1982).

[351] D. B. Hume, T. Rosenband, D. J. Wineland, Phys. Rev. Lett. 99, 120502 (2007).

[352] G. Wendin, Philosophical Transactions of the Royal Society of London. Series A: Mathematical, Physical and Engineering Sciences 361, 1323 (2003).

[353] S. Aaronson, 24th Annual IEEE Conference on Computational Complexity (IEEE, 2009), pp. 229–242.

[354] A. Lutomirski, arXiv:1010.0256 (2010).

[355] E. Farhi, et al., Phys. Rev. Lett. 105, 190503 (2010).

[356] A. Lutomirski, arxiv:1107.0321 (2011).

[357] D. Gavinsky, arXiv:1109.0372 (2011).

[358] R. F. Werner, Phys. Rev. A 58, 1827 (1998).

[359] G. Gutoski, J. Watrous, Proceedings of the thirty-ninth annual ACM symposium on Theory of computing, STOC '07 (ACM, New York, NY, USA, 2007), pp. 565–574.

[360] R. Impagliazzo, V. Kabanets, Constructive proofs of concentration bounds, Tech. Rep. 072 (2010).

[361] D. Bruss, M. Cinchetti, G. Mauro D'Ariano, C. Macchiavello, Phys. Rev. A 62, 012302 (2000).

[362] C. Langer, et al., Phys. Rev. Lett. 95, 060502 (2005).

[363] C. H. Bennet, G. Brassard, International Conference on Computers, Systems & Signal Processing (1984). Bangalore, India.

[364] D. Gottesman, H. Lo, IEEE Trans. Inf. Theory. 49, 457 (2003).

[365] V. Scarani, R. Renner, Phys. Rev. Lett. 100, 200501 (2008).

[366] V. M. Acosta, A. Jarmola, E. Bauch, D. Budker, Phys. Rev. B 82, 201202 (2010).

[367] L. M. Pham, et al., arXiv:1201.5686 (2012).

[368] D. Englund, et al., Nano Lett. 10, 3922 (2010).

[369] A. Faraon, P. E. Barclay, C. Santori, K.-M. C. Fu, R. G. Beausoleil, Nature Photon. 5, 301 (2011).

[370] P. Rabl, et al., Nature Phys. 6, 602 (2010).

[371] O. Arcizet, P.-F. Cohadon, T. Briant, M. Pinard, A. Heidmann, Nature 444, 71 (2006).

[372] S. Kolkowitz, et al., Science 335, 1603 (2012).

[373] M. K. Zalalutdinov, et al., Nano Lett. 11, 4304 (2011).

[374] M. J. Burek, et al., Nano Lett. 12, 6084 (2012).

[375] B. Hausmann, et al., Phys. Status Sol. (a) 209, 1619 (2012).

[376] P. Ovartchaiyapong, L. Pascal, B. Myers, P. Lauria, A. B. Jayich, App. Phys. Lett. 101, 163505 (2012).

[377] Y. Tao, J. M. Boss, B. A. Moores, C. L. Degen, Nat. Commun. 5 (3638) (2014).

[378] J. Maze, et al., New J. Phys. 13, 025025 (2011).

[379] M. W. Doherty, et al., Phys. Rev. B 85, 205203 (2012).

[380] E. Van Oort, M. Glasbeek, Chem. Phys. Lett. 168, 529 (1990).

[381] F. Dolde, et al., Nature Phys. 7, 459 (2011).

[382] V. M. Acosta, et al., Phys. Rev. Lett. 104, 070801 (2010).

[383] L. D. Landau, E. Lifshitz, Course of Theoretical Physics Vol 7: Theory and Elasticity (Pergamon Press, 1959).

[384] S. Habraken, K. Stannigel, M. Lukin, P. Zoller, P. Rabl, New J. Phys. 14, 115004 (2012).

[385] Ö. Soykal, R. Ruskov, C. Tahan, Physical review letters 107, 235502 (2011).

[386] I. Wilson-Rae, P. Zoller, A. Imamoglu, Phys. Rev. Lett. 92, 075507 (2004).

[387] M. Kitagawa, M. Ueda, Phys. Rev. A 47, 5138 (1993).

[388] J. M. Taylor, et al., Nature Phys. 4, 810 (2008).

[389] D. Wineland, J. Bollinger, W. Itano, F. Moore, D. Heinzen, Phys. Rev. A 46, R6797 (1992).

[390] J. Ma, X. Wang, C. Sun, F. Nori, Phys. Rep. 509, 89 (2011).

[391] M. H. Schleier-Smith, I. D. Leroux, V. Vuletić, Phys. Rev. A 81, 021804 (2010).

[392] I. D. Leroux, M. H. Schleier-Smith, V. Vuletić, Phys. Rev. Lett. 104, 073602 (2010).

[393] I. D. Leroux, M. H. Schleier-Smith, H. Zhang, V. Vuletić, Phys. Rev. A 85, 013803 (2012).

[394] D. Marcos, et al., Phys. Rev. Lett. 105, 210501 (2010).

[395] U. Haeberlen, J. Waugh, Phys. Rev. 175, 453 (1968).

[396] J. M. Martinis, S. Nam, J. Aumentado, K. Lang, C. Urbina, Phys. Rev. B 67, 094510 (2003).

[397] G. S. Uhrig, Phys. Rev. Lett. 98, 100504 (2007).

[398] Ł. Cywiński, R. M. Lutchyn, C. P. Nave, S. D. Sarma, Phys. Rev. B 77, 174509 (2008).

[399] R. Sousa, Electron Spin Resonance and Related Phenomena in Low-Dimensional Structures, M. Fanciulli, ed. (Springer Berlin Heidelberg, 2009), vol. 115 of Topics in Applied Physics, pp. 183–220.

[400] M. Rudner, L. Vandersypen, V. Vuletić, L. Levitov, Phys. Rev. Lett. 107, 206806 (2011).

[401] J. Camparo, Phys. Today 60, 33 (2007).

[402] T. Rosenband, et al., Science 319, 1808 (2008).

[403] M. Takamoto, F.-L. Hong, R. Higashi, H. Katori, Nature 435, 321 (2005).

[404] A. D. Ludlow, et al., Science 319, 1805 (2008).

[405] C. W. Chou, D. B. Hume, T. Rosenband, D. J. Wineland, Science 329, 1630 (2010).

[406] F. Riehle, Frequency Standards: Basics and Applications (Wiley-VCH, 2004).

[407] S. Knappe, et al., Appl. Phys. Lett. 85, 1460 (2004).

[408] D. Youngner, et al., Solid-State Sensors, Actuators and Microsystems Conference, 2007. TRANSDUCERS 2007. International (2007), pp. 39 –44.

[409] V. Shah, S. Knappe, P. D. D. Schwindt, J. Kitching, Nat Photon 1, 649 (2007).

[410] C. White, A. Hajimiri, Frequency Control Symposium and Exposition, 2005. Proceedings of the 2005 IEEE International (2005).

[411] N. B. Manson, J. P. Harrison, M. J. Sellars, Phys. Rev. B 74, 104303 (2006).

[412] A. Dreau, et al., Phys. Rev. B 84, 195204 (2011).

[413] C. A. Meriles, et al., J. Chem. Phys. 133, 124105 (2010).

[414] D. Le Sage, et al., Phys. Rev. B 85, 121202 (2012).

[415] C. P. Slichter, Principles of Magnetic Resonance (Springer, 1996), third edn.

[416] P. Stanwix, et al., Phys. Rev. B 82, 201201 (2010).

[417] P. M. Martineau, et al., Journal of Physics: Condensed Matter 21, 364205 (2009).

[418] D. Toyli, et al., Physical Review X 2, 031001 (2012).

[419] J. Vig, Ultrasonics, Ferroelectrics and Frequency Control, IEEE Transactions on 40, 522 (1993).

[420] P. E. Barclay, K.-M. C. Fu, C. Santori, R. G. Beausoleil, Appl. Phy. Lett. 95, 191115 (2009).

[421] Y. Yue, X. Wang, Nano Rev pp. – (2012).

[422] E. Lucchetta, J. Lee, L. Fu, N. Patel, R. Ismagilov, Nature 434, 1134 (2005).

[423] S. V. Kumar, P. A. Wigge, Cell 140, 136 (2010).

[424] V. M. Lauschke, C. D. Tsiairis, P. Francois, A. Aulehla, Nature 493, 101 (2012).

[425] Y. Kamei, et al., Nature Methods 6, 79 (2009).

[426] T. Vreugdenburg, C. Willis, L. Mundy, J. Hiller, Breast Cancer Res. Treat. 137, 665 (2013).

[427] A. Schroeder, et al., Nature Reviews Cancer 12, 39 (2012).

[428] D. P. O/'Neal, L. R. Hirsch, N. J. Halas, J. D. Payne, J. L. West, Cancer Lett. 209, 171 (2004).

[429] A. Majumdar, Annu. Rev. Mater. Sci. 29, 505 (1999).

[430] S. H. Kim, et al., Journal of Micromechanics and Microengineering 16, 526 (2006).

[431] J. Yang, H. Yang, L. Lin, ACS Nano 5, 5067 (2011).

[432] F. Vetrone, et al., ACS Nano 4, 3254 (2010).

[433] K. Okabe, et al., Nature Commun. 3, 705 (2012).

[434] J. Donner, S. Thompson, M. Kreuzer, G. Baffou, R. Quidant, Nano Lett. 12, 2107 (2012).

[435] A. K. Shalek, et al., Proceedings of the National Academy of Sciences 107, 1870 (2010).

[436] C. Jin, Z. Li, R. Williams, K. Lee, I. Park, Nano Lett. 11, 4818 (2011).

[437] J. S. Hodges, et al., Physical Review A 87, 032118 (2013).

[438] G. Xu, et al., PloS one 7, e49021 (2012).

[439] F. Helmchen, W. Denk, Nature Methods 2, 932 (2005).

[440] T.-L. Wee, et al., The Journal of Physical Chemistry A 111, 9379 (2007).

[441] M. Tsoli, et al., Cancer research 72, 4372 (2012).

[442] T. Schroeder, F. G deke, M. J. Banholzer, O. Benson, New J. Phys. 13, 055017 (2011).